

# Electronic structures of nickel(II)-bis(indanyloxazoline)-dihalide catalysts: Understanding ligand field contributions that promote C(sp<sup>2</sup>)-C(sp<sup>3</sup>) cross-coupling

Brendon J. McNicholas<sup>†,1</sup>, Z. Jaron Tong<sup>†,2</sup>, Daniel Bím<sup>1</sup>, Raymond F. Turro<sup>2</sup>, Nathanael P. Kazmierczak<sup>1</sup>, Jakub Chalupský<sup>3</sup>, Sarah E. Reisman<sup>2</sup>, and Ryan G. Hadt<sup>1,\*</sup>

<sup>1</sup>Division of Chemistry and Chemical Engineering, Arthur Amos Noyes Laboratory of Chemical Physics, California Institute of Technology, Pasadena, California 91125, United States

<sup>2</sup>Division of Chemistry and Chemical Engineering, The Warren and Katherine Schlinger Laboratory for Chemistry and Chemical Engineering, California Institute of Technology, Pasadena, California 91125, United States

<sup>3</sup>J. Heyrovský Institute of Physical Chemistry, The Czech Academy of Sciences, Dolejškova 3, Prague 8, Czech Republic

<sup>4</sup>Institute of Organic Chemistry and Biochemistry, Academy of Sciences of the Czech Republic, Flemingovo náměstí 2, 166 10 Prague 6, Czech Republic

<sup>†</sup>Co-first author

\*Corresponding Author: rghadt@caltech.edu

Table of Contents	Page Number
<b>S1. General</b>	<b>2</b>
<b>S2. NMR Spectra</b>	<b>5</b>
<b>S3. UV-vis-NIR Spectra</b>	<b>7</b>
<b>S4. Circular Dichroism and Magnetic Circular Dichroism Spectra</b>	<b>19</b>
<b>S5. Electrochemistry</b>	<b>33</b>
<b>S6. Spectroelectrochemistry Spectra</b>	<b>53</b>
<b>S7. X-Ray Crystallographic Data</b>	<b>67</b>
<b>S8. DFT/CASSCF+NEVPT2 Inputs and Results</b>	<b>70</b>
<b>S9. References</b>	<b>141</b>

## S1. General

Anhydrous zinc(II) chloride (Millipore Sigma) and electrochemical grade tetrabutylammonium hexafluorophosphate (Millipore Sigma) were used as received. Anhydrous N,N-dimethylacetamide (Millipore Sigma) and *d*<sup>2</sup>-dichloromethane (Cambridge Isotope Laboratories, Inc.) were stored in a nitrogen-filled glove box over activated 3 Å molecular sieves. Acetonitrile and dichloromethane were taken from degassed, dry solvent systems and stored over activated 3 Å molecular sieves in a nitrogen-filled glove box. Nickel(II) dichloride (3*aR*,3*a'R*,8*aS*,8*a'S*)-2,2'-(cyclopropane-1,1-diyl)bis(3*a*,8*a*-dihydro-8*H*-indeno[1,2-*d*]oxazole) [**Ni(II)Cl<sub>2</sub>**] and nickel(II) dibromide (3*aR*,3*a'R*,8*aS*,8*a'S*)-2,2'-(cyclopropane-1,1-diyl)bis(3*a*,8*a*-dihydro-8*H*-indeno[1,2-*d*]oxazole) [**Ni(II)Br<sub>2</sub>**] were synthesized according to literature precedent and doubly recrystallized from a mixture of DCM/hexanes.<sup>1,2</sup> All solvents were dried and stored over activated 3 Å molecular sieves in a nitrogen-filled glove box. All NMR spectra were collected on a Varian 400 MHz or Bruker 400 MHz spectrometer ( $\delta$  in ppm, m: multiplet). <sup>13</sup>C NMR spectra were <sup>1</sup>H decoupled.

UV-vis-NIR spectra were acquired using a Varian Cary 500 spectrophotometer, while electronic CD and MCD spectra were acquired using a Jasco J1700 CD spectrometer and 1.4 T permanent magnet. MCD spectra were generated by taking the difference between spectra with field direction parallel and field direction antiparallel to the direction of light propagation. Vibrational circular dichroism data (VCD) were collected using a ChiralIR-2X (BioTools, Inc.) spectrometer. Spectra were background-corrected for both cell and solvent signals. All spectra were collected in a 0.1 mm path length calcium fluoride cell. Variable temperature UV-vis-NIR spectra were acquired using a Varian Cary 50 spectrophotometer equipped with a USP-203 series cryostat (UNISOKU Co.) cooled with liquid nitrogen. Samples were equilibrated at each temperature for five minutes prior to acquisition. Spectroelectrochemical measurements were performed in a nitrogen-filled glovebox with a quartz spectroelectrochemical cell with a 0.17 cm path length from Pine Research Instrumentation (AKSTCKIT3), a gold honeycomb electrode (Pine Instruments), and a platinum wire counter electrode. Measurements were recorded using an Analytical Instrument Systems, Inc. DT2000 deuterium-tungsten UV-vis-NIR light source coupled to Stellarnet Black Comet UV-vis and DWARF-Star NIR spectrometers. All room-temperature UV-vis-NIR spectra and low-temperature magnetic circular dichroism spectra were deconvolved simultaneously using Gaussian

functions with fixed absorption maxima if possible or by letting values float within 10% for each set of spectra. All deconvolutions were performed in Matlab 2018b.

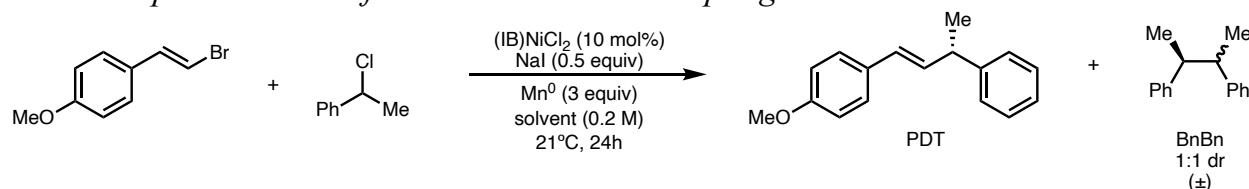
Homogeneous voltammetry experiments were conducted in a nitrogen-filled glove box using either a 3 mm diameter glassy carbon (CH Instruments) or an 11  $\mu\text{m}$  carbon fiber microdisk working electrode (Gamry Instruments). The real surface areas of these electrodes were determined using averaged values of decay currents from chronoamperometry (macro-disk) or steady-state currents from low scan rate linear sweep voltammetry (micro-disk) in acetonitrile with 0.1 M TBAPF<sub>6</sub> and ferrocene as the redox-active standard ( $D_0 = 2.24 \times 10^{-5} \text{ cm}^2 \text{ s}^{-1}$ ).<sup>3</sup> Based on the Cottrell equation (macroelectrode) or the steady-state current equation (microelectrode), the real surface areas were determined to be 0.0877 cm<sup>2</sup> and  $1.79 \times 10^{-6} \text{ cm}^2$ , respectively.<sup>4</sup> A 0.01 M Ag<sup>+/0</sup> non-aqueous reference electrode and platinum wire counter electrode were used for all voltammetry experiments. 0.01 M AgNO<sub>3</sub>/0.1 M TBAPF<sub>6</sub> in MeCN was used as the filling solution for the non-aqueous reference electrode (Bioanalytical Systems, Inc.). Linear fitting to the intercept of a Nyquist plot obtained from potentiostatic electrochemical impedance spectroscopy at the open circuit potential was used to determine the uncompensated resistance, and 95% of this value was compensated. All voltammetry was internally referenced to the Fc<sup>+/0</sup> redox couple. All experiments utilized a Gamry Reference 600 or Biologic SP-200 potentiostat. Low-temperature voltammetry was conducted using a temperature-controlled 50:50 ethylene glycol:water bath. Solutions were degassed with N<sub>2</sub> prior to measurement. A silver wire pseudo-reference electrode was used in place of Ag<sup>+/0</sup>.

*Zinc(II) bis(chloride) (3aR,3a'R,8aS,8a'S)-2,2'-(cyclopropane-1,1-diyl)bis(3a,8a-dihydro-8H-indeno[1,2-d]oxazole) [Zn(II)(Cl)<sub>2</sub>]:*

Previous syntheses of Ni(II) complexes were used as a template. (3aR,3a'R,8aS,8a'S)-2,2'-(cyclopropane-1,1-diyl)bis(3a,8a-dihydro-8H-indeno[1,2-d]-oxazole) (0.126 g, 0.354 mmol) and zinc(II) chloride (0.056 g, 0.412 mmol) were dissolved in 6.5 mL MeCN/0.1 mL H<sub>2</sub>O in a 20 mL scintillation vial under N<sub>2</sub>. The solution was heated at 80 °C for six hours and then cooled to room temperature. The solvent was evaporated *in vacuo*, and the resulting solid was redissolved in dichloromethane. The solution was filtered through a microfiber pipet filter, and the complex was precipitated with excess pentane. The solid was filtered, dried, and weighed to yield the product as a colorless powder (137.8 mg, 79% yield). <sup>13</sup>C NMR (100 MHz, CD<sub>2</sub>Cl<sub>2</sub>)  $\delta$  169.0, 139.5, 138.7,

130.1, 128.3, 127.5, 125.5, 86.1, 74.9, 39.3, 21.8, 19.3;  $^1\text{H}$  NMR (400 MHz,  $\text{CD}_2\text{Cl}_2$ )  $\delta$  7.95 (m, 2H), 7.34 (m, 6H), 5.89 (m, 2H), 5.52 (m, 2H), 3.48 (m, 2H), 3.28 (m, 2H), 1.96 (m, 2H), 1.76 (m, 2H).

### *Solvent-dependent Yields for Reductive Heterocoupling*



Procedure: To an oven-dried 1 dram vial equipped with a stir bar was added (*E*)-1-(2-bromovinyl)-4-methoxybenzene (21.3 mg, 0.10 mmol, 1 equiv), Mn<sup>0</sup> powder (7.5 mg, 0.30 mmol, 3 equiv), and Ni<sup>II</sup>(IB)Cl<sub>2</sub> (4.9 mg, 0.010 mmol, 0.1 equiv). The vial was then brought into a N<sub>2</sub>-filled glovebox where NaI (7.5 mg, 0.050 mmol, 0.5 equiv) was added followed by a careful (as to not disturb Mn<sup>0</sup> powder) addition of 500  $\mu\text{L}$  (0.2 M) of the appropriate solvent. 1-chloroethylbenzene (13.3  $\mu\text{L}$ , 0.10 mmol, 1 equiv) was then added followed by *n*-dodecane internal standard. The vial was sealed with a Teflon-lined cap and further sealed with electrical tape then removed from the glovebox where it was allowed to stir at 1500 rpm for 24 h. Upon completion, the reaction was quenched with 1 mL of H<sub>2</sub>O and extracted with 1 mL EtOAc then filtered through a MgSO<sub>4</sub> plug where the filtrate was further diluted with EtOAc and analyzed by GC-FID. Procedure was repeated 3x for each solvent.



## S2. NMR Spectra

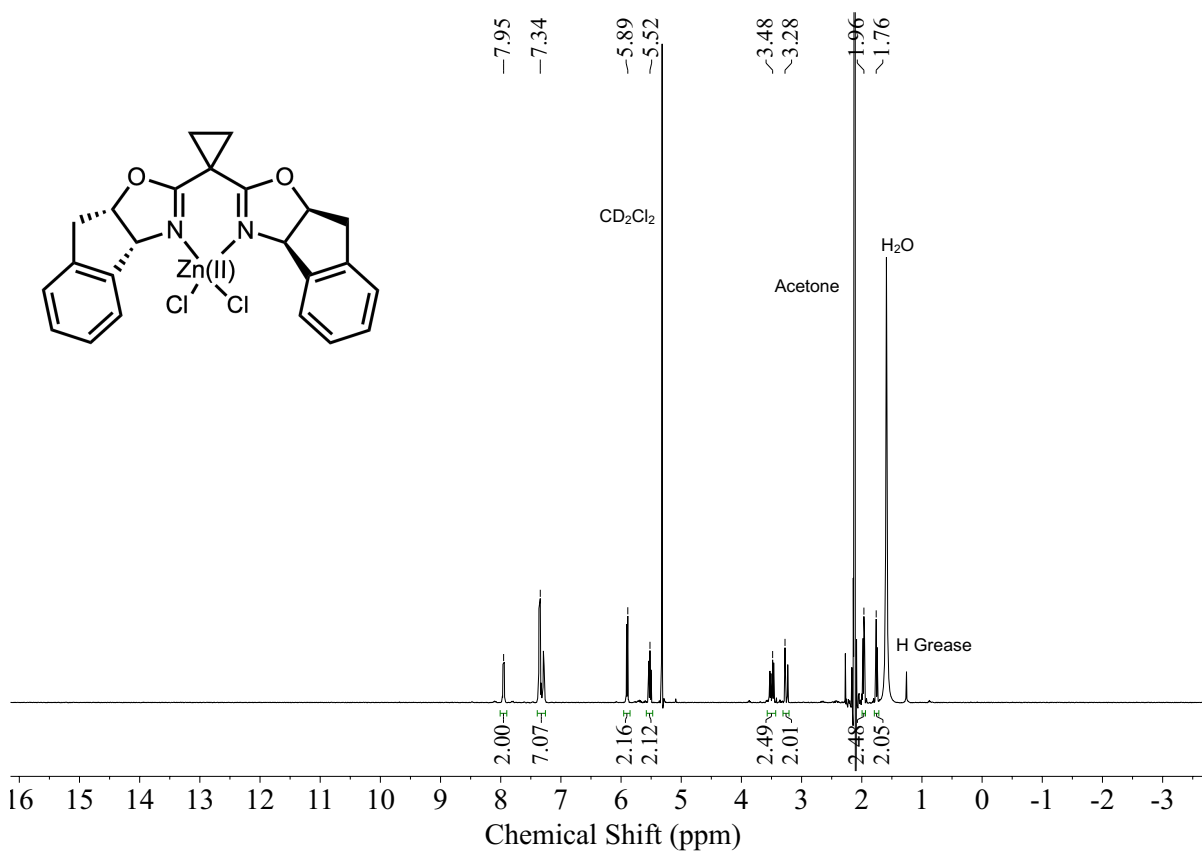


**Figure S1.**  $^1\text{H}$  NMR of  $\text{Zn}(\text{IB})\text{Cl}_2$  in  $d^2$ -dichloromethane.

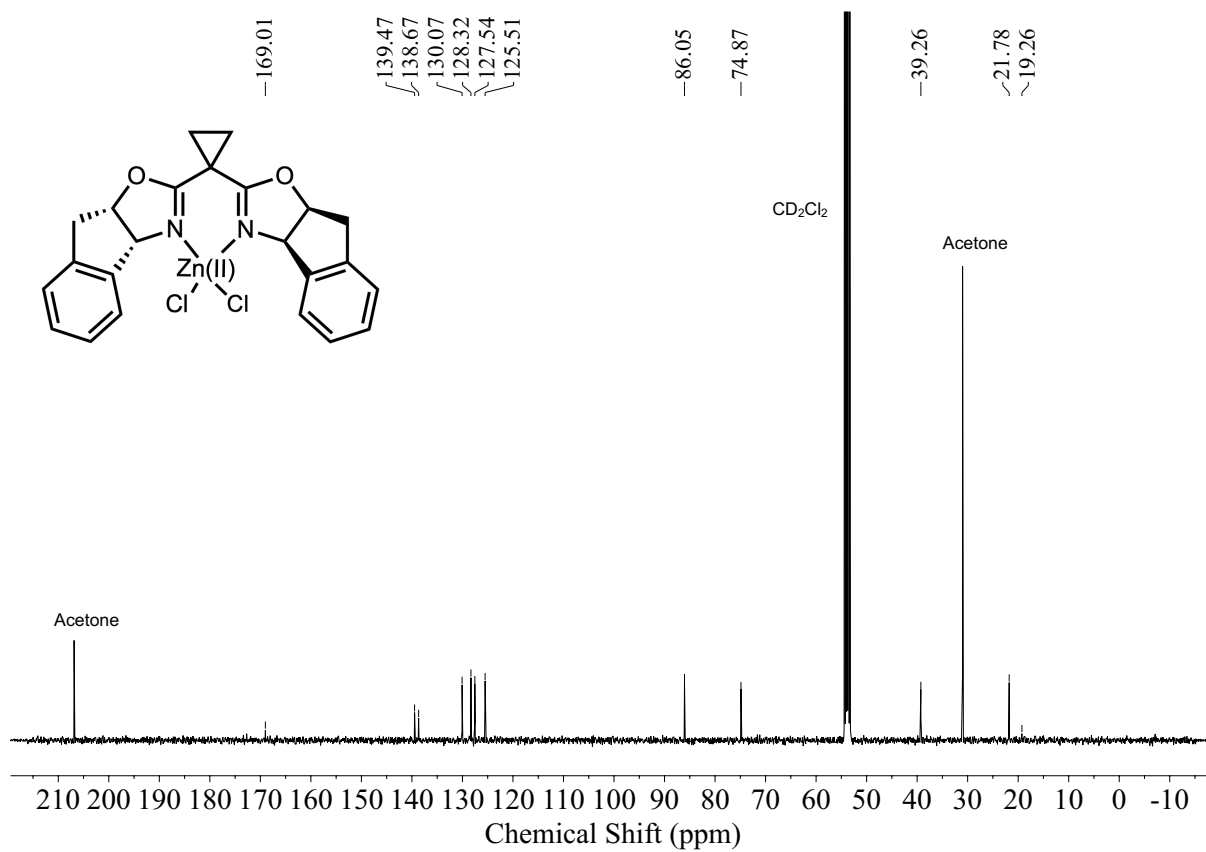


**Figure S2.**  $^{13}\text{C}$  NMR of  $\text{Zn(II)Cl}_2$  in  $d^2$ -dichloromethane.

### S3. UV-vis-NIR Spectra and Expanded Main Text Discussion

Briefly, MCD spectroscopy relies on the differential absorption of left- and right-circularly polarized light in the presence of a longitudinal magnetic field. The general intensity of an MCD spectrum can be defined by **Equation 1**:

$$I \propto \left[ A_1 \left( \frac{-\partial f(E)}{\partial E} \right) + \left( B_0 + \frac{C_0}{kT} \right) f(E) \right] \quad (1)$$

where  $A$ -terms and  $B$ -terms are temperature independent, while  $C$ -terms are temperature dependent. Based on the magnitude of low-symmetry distortions from ideal  $T_d$ , consideration of first-order spin-orbit coupling on the  $\text{Ni}^{\text{II}}$  center, and acquisition temperature, the observed MCD intensity is tentatively assigned to  $B$ -term intensity due to magnetic field-induced mixing of excited states. A future study utilizing variable-temperature variable-field MCD will be used to define this, along with the nature of the ground state zero-field splittings in these and other  $\text{Ni}^{\text{II}}$  cross-coupling catalysts.

Full Gaussian resolutions obtained from collective fits of the absorption, CD, and MCD spectra of  $\text{Ni}^{\text{II}}(\text{IB})\text{Cl}_2$  and  $\text{Ni}^{\text{II}}(\text{IB})\text{Br}_2$  in DCM are given in **Figure 1** and summarized in **Table 1**. Both complexes are pseudo- $T_d$ , a geometry that has been studied extensively for high-spin  $\text{Ni}^{\text{II}}$  complexes using ligands spanning a range of ligand field strengths.<sup>5-7</sup> Chloride and bromide are weak  $\sigma$  donors and  $\pi$  donors, while the bidentate **IB** is a moderate  $\sigma$  donor. Thus, these four-coordinate complexes are expected to follow a weak-field excited state ordering. Band assignments in idealized  $T_d$  and  $C_{2v}$  symmetry are provided in **Figure 1** and **Table 1**.

By group theory, the  $^3T_1(\text{F})$  ground state (in  $T_d$ ) will split due to low symmetry distortions. Descending in symmetry, and depending on the specific distortion angles and bond compression/elongation, the ground state can be  $^3A_2$ ,  $^3B_1$ , or  $^3B_2$  in  $C_{2v}$ .<sup>8</sup> Based on multiconfigurational calculations and previous assignments for complexes with similar primary ligand coordination spheres, the low symmetry distorted ground state is tentatively assigned as  $^3B_1$  in both complexes. For this assignment, transitions to  $^3B_2$  excited states are forbidden by group theory; transitions to  $^3A_1$ ,  $^3A_2$ , or  $^3B_1$  excited states are electric dipole allowed.<sup>5</sup> Based on calculations and assigned  $^3B_1$  ground state, the two holes lie in the  $d(x^2-y^2)$  and  $d(xz)$   $3d$  orbitals, consistent with previous angular overlap calculations on similar complexes.<sup>9</sup> We assign states for  $\text{Ni}^{\text{II}}(\text{IB})\text{Cl}_2$  from low to high energy; these assigned states correlate directly with those in  $\text{Ni}^{\text{II}}(\text{IB})\text{Br}_2$ . Bands 2, 3, and 4 fall in the  $\sim 5000 - 11\,000\text{ cm}^{-1}$  region (**Figure 1**). Note band 1 is

observed at low energy in vibrational CD (Main Text, **Section 2.2**). Bands 2 and 3 are assigned as the  $^3B_1$  and  $^3A_1$  components (in  $C_{2v}$ ), respectively, of the parent  $^3T_1(F) \rightarrow ^3T_2$  (in  $T_d$ ) excited state. One component from the  $^3T_1(F) \rightarrow ^3T_2$  (i.e., the  $^3B_2$ ) does not seem to be observed, consistent with its electric dipole forbidden nature and proximity to other transitions. Assignment of these transitions can be made with more certainty based on calculations (**Section 8.2**), which suggest both states should yield negative differential CD and MCD intensity. This is the case for band 3. Since  $^3B_1 \rightarrow ^3B_2$  is electric dipole forbidden, the higher oscillator strength observed for band 3 is consistent with calculated values, supporting assignment of this band as the  $^3B_1 \rightarrow ^3A_1$  transition. Band 4, the most intense transition in this lower energy manifold, is assigned to the  $^3A_2(F)$  term (in  $T_d$ ) ( $^3B_1(F) \rightarrow ^3A_2$  in  $C_{2v}$ ), consistent with previously reported spectra for a large number of high-spin, pseudo-tetrahedral  $Ni^{II}$  complexes.<sup>5</sup>

A sharp spin-forbidden ligand field transition is observed at  $\sim 12\,100\text{ cm}^{-1}$  (band i) and can be assigned to a component of the  $^3T_1(F) \rightarrow ^1E, ^1T_2$  (in  $T_d$ ) spin-flip transitions. This region consists of additional intensity (band ii), which is tentatively ascribed to additional overlapping spin-forbidden components that are broadened due to low-symmetry distortions. This assignment is also consistent with the additional structure present in this spectral region in the MCD spectrum (**Figure 1C**).

The higher energy manifold of components ( $\sim 14\,000 - \sim 22\,000\text{ cm}^{-1}$ ) is assigned to the next orbital triplet,  $^3T_1(F) \rightarrow ^3T_1(P)$  (in  $T_d$ ), which is comprised of bands at  $14\,940\text{ cm}^{-1}$  [band 5 ( $^3B_1(F) \rightarrow ^3B_1(P)$ )],  $18\,210\text{ cm}^{-1}$  [band 6 ( $^3B_1(F) \rightarrow ^3B_2(P)$ )], and  $20\,130\text{ cm}^{-1}$  [band 7 ( $^3B_1(F) \rightarrow ^3A_2(P)$ )]. The oscillator strengths for these bands track with electric dipole selection rules predicted by theory (i.e., bands 7, 6 > band 5).

The similarity in the signs of vibrational CD (*vide infra*), CD, and MCD signals between  $Ni^{II}(IB)Cl_2$  and  $Ni^{II}(IB)Br_2$  lead us to conclude that they exhibit the same state orderings for observed spin-allowed ligand field transitions. All assignments are also self-consistent based on differential intensity in CD and MCD. For example,  $^3B_1 \rightarrow ^3A_2$  transitions all display positive CD intensity and negative MCD intensity. For  $Ni^{II}(IB)Cl_2$ , additional bands are present at  $12\,400\text{ cm}^{-1}$  (band ii, UV-vis-NIR/CD),  $15\,890\text{ cm}^{-1}$  (band iii, UV-vis-NIR/CD/MCD),  $19\,050\text{ cm}^{-1}$  (band iv, CD), and  $23\,740\text{ cm}^{-1}$  (band v, UV-vis-NIR/CD/MCD). As partially described above, these are tentatively ascribed to the geometric and spin-orbit splitting of spin-forbidden transitions that broaden components ( $12\,400$  and  $19\,050\text{ cm}^{-1}$ ) and small amounts of trimer formation ( $23\,740$

cm<sup>-1</sup>) (Main text, **Section 2.4**). Note the band at 19 050 cm<sup>-1</sup> in CD is required to adequately fit the CD data. However, the UV-vis-NIR and MCD data are fit well without inclusion of the 19 050 cm<sup>-1</sup> band. Therefore, this band has not been included in the UV-vis-NIR and MCD fits.

The ligand field transitions of **Ni<sup>II</sup>(IB)Cl<sub>2</sub>** relative to **Ni<sup>II</sup>(IB)Br<sub>2</sub>** are blueshifted by ~120 – 710 cm<sup>-1</sup> in DCM (overlaps in **Figure S17**), consistent with stronger donation from chloride relative to bromide.  $10Dq$  in idealized  $T_d$  is given by the gap between the <sup>3</sup>A<sub>2</sub>(F) and the center of gravity of the <sup>3</sup>T<sub>2</sub>(F) manifold.<sup>7</sup> Using band 4 and the average of bands 2 and 3 for these energies, respectively, provides values of 2830 cm<sup>-1</sup> and 3085 cm<sup>-1</sup> for **Ni<sup>II</sup>(IB)Cl<sub>2</sub>** and **Ni<sup>II</sup>(IB)Br<sub>2</sub>**. While these estimates are consistent with previous  $10Dq$  values of < 4000 cm<sup>-1</sup> for various pseudo- $T_d$  Ni(II) complexes with weak  $\sigma$  donor ligands,<sup>10</sup> this approach does not provide a meaningful result for the **Ni<sup>II</sup>(IB)X<sub>2</sub>** comparison here. For highly distorted complexes, greater configuration interaction between states due to lower symmetry can lead to significant splitting of orbital triplets, which can make it difficult to extract accurate values of  $10Dq$ . To estimate the relative ligand field strength, we average the assigned spin-allowed transitions (bands 1 – 7). Doing so provides relative ligand field strengths of ~12 365 cm<sup>-1</sup> and ~11 975 cm<sup>-1</sup> ( $\Delta$  = ~390 cm<sup>-1</sup>) for **Ni<sup>II</sup>(IB)Cl<sub>2</sub>** and **Ni<sup>II</sup>(IB)Br<sub>2</sub>**, respectively, in better accord with the greater ligand field strength in the chloride complex relative to bromide. For one of the first times in this field, we demonstrate the direct connection of ligand field transitions exciting into the Ni<sup>II</sup>-based redox active molecular orbitals (RAMOs), which allows for correlations between transition energies and redox potentials to be made (Main text, **Section 3.3**).

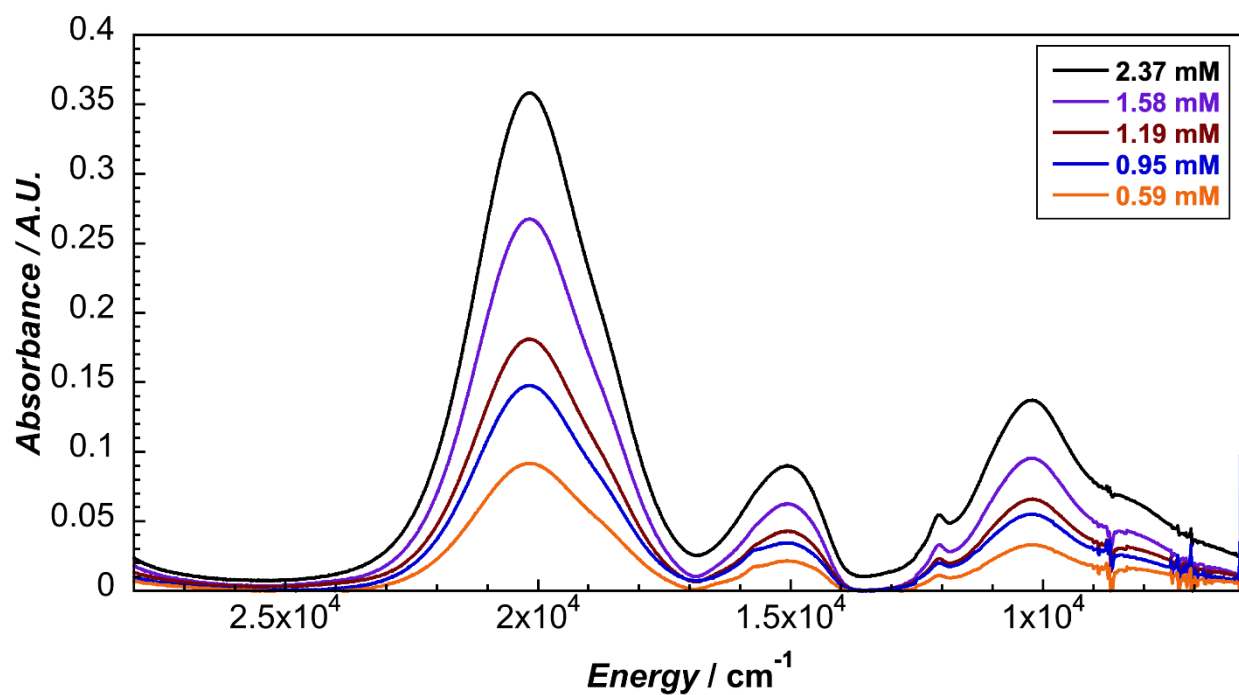


**Figure S3.** UV-vis-NIR spectra of  $\text{Ni}^{\text{II}}(\text{1B})\text{Cl}_2$  in  $\text{DCM}$ .

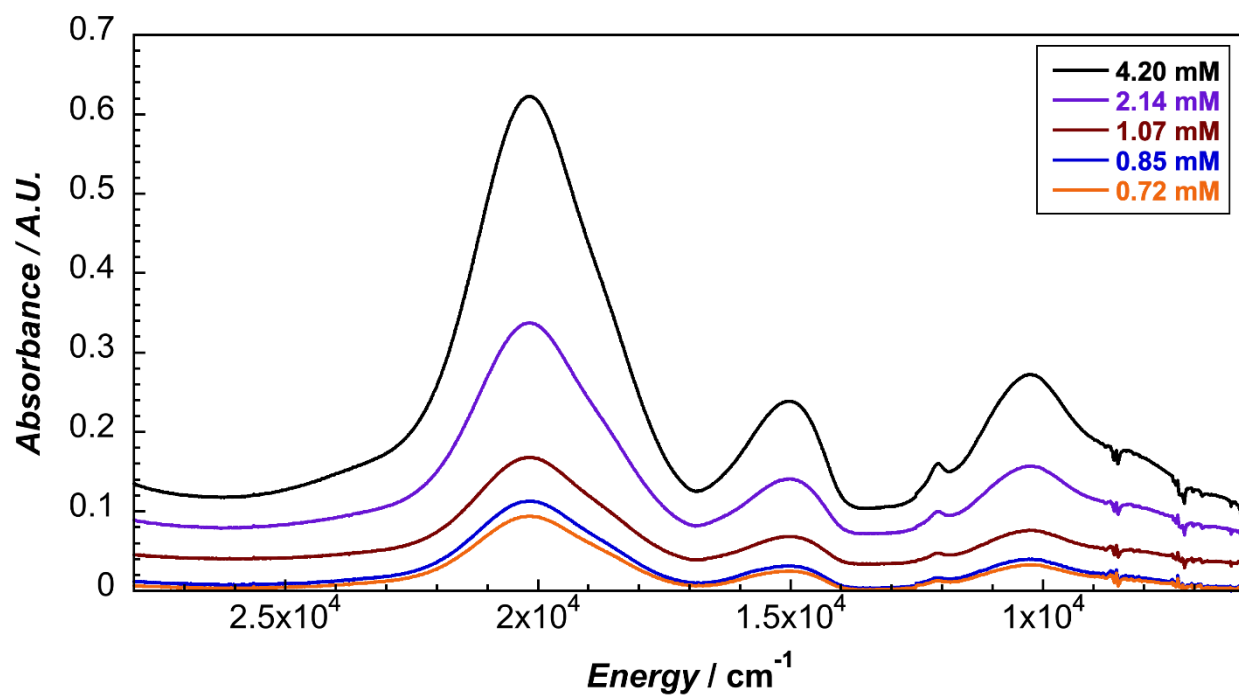


**Figure S4.** UV-vis-NIR spectra of  $\text{Ni}^{\text{II}}(\text{1B})\text{Cl}_2$  in  $\text{MeCN}$ .

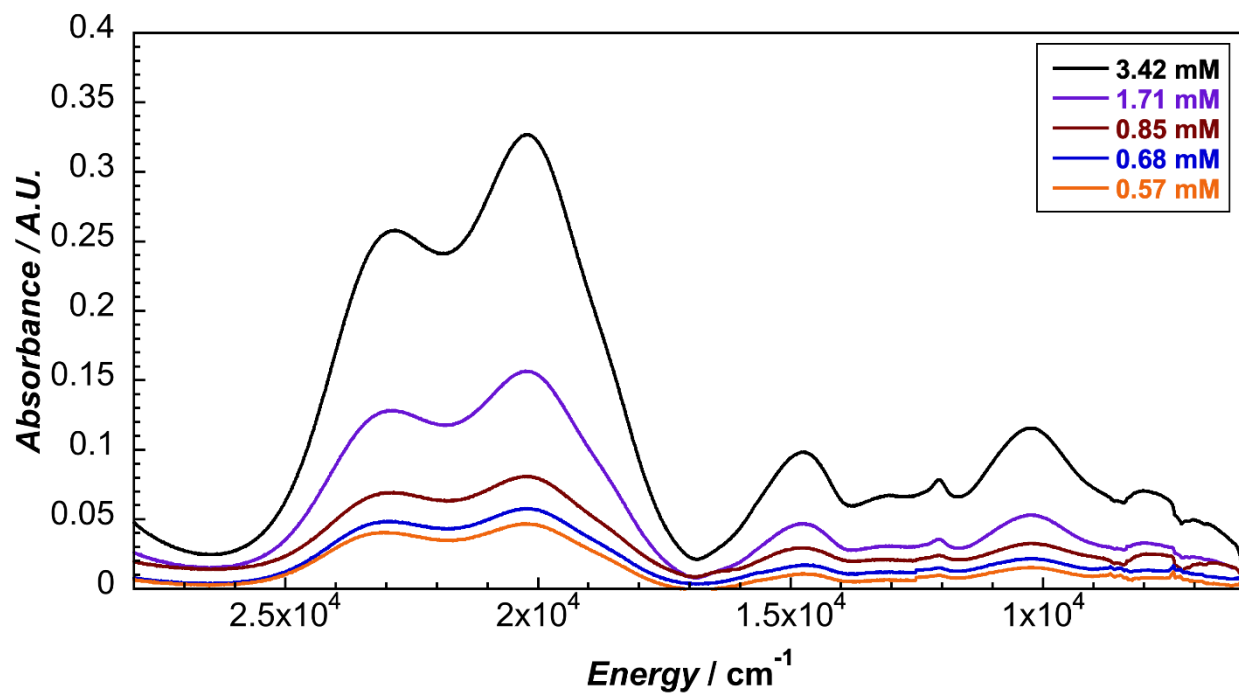


Figure S5. UV-vis-NIR spectra of  $\text{Ni}^{\text{II}}(\text{1B})\text{Cl}_2$  in DMA.

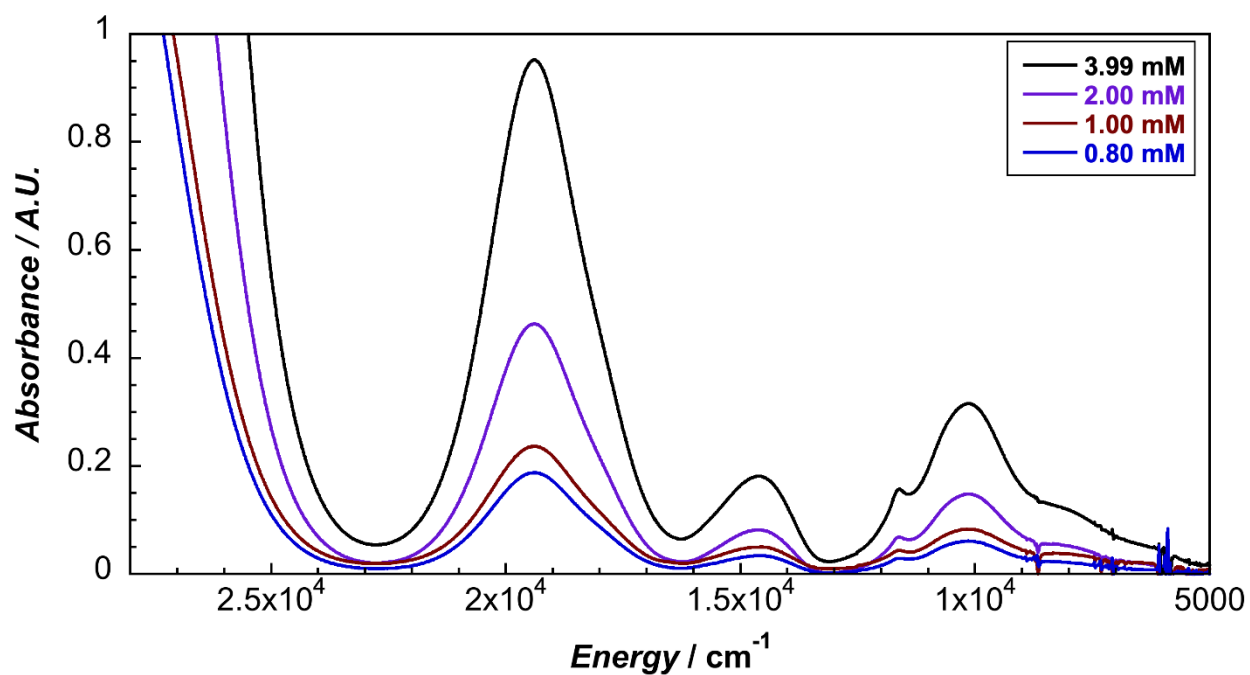


Figure S6. UV-vis-NIR spectra of  $\text{Ni}^{\text{II}}(\text{1B})\text{Br}_2$  in DCM.

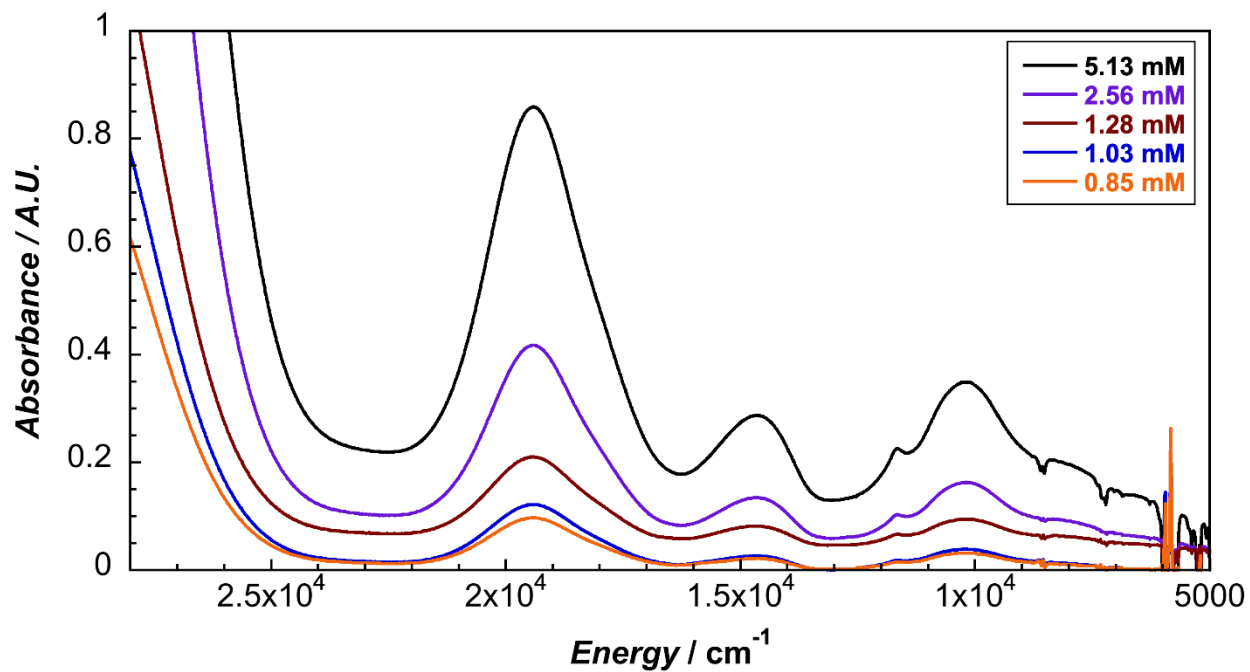


Figure S7. UV-vis-NIR spectra of  $\text{Ni}^{\text{II}}(\text{1B})\text{Br}_2$  in MeCN.

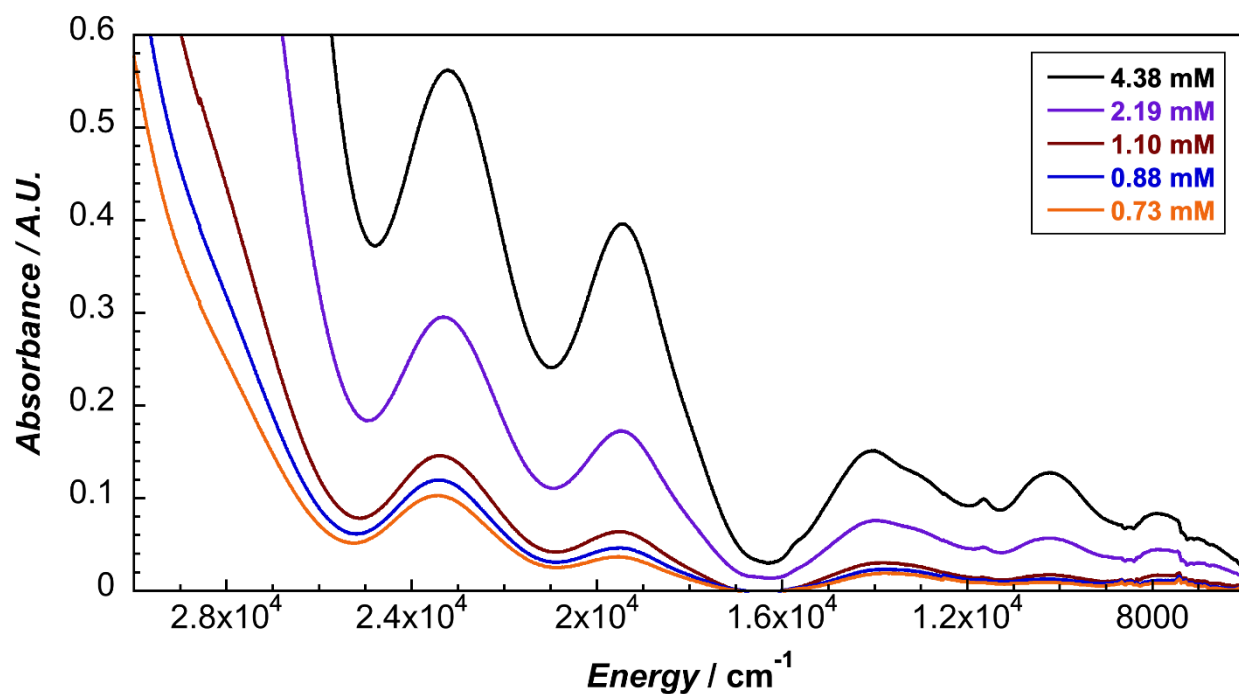
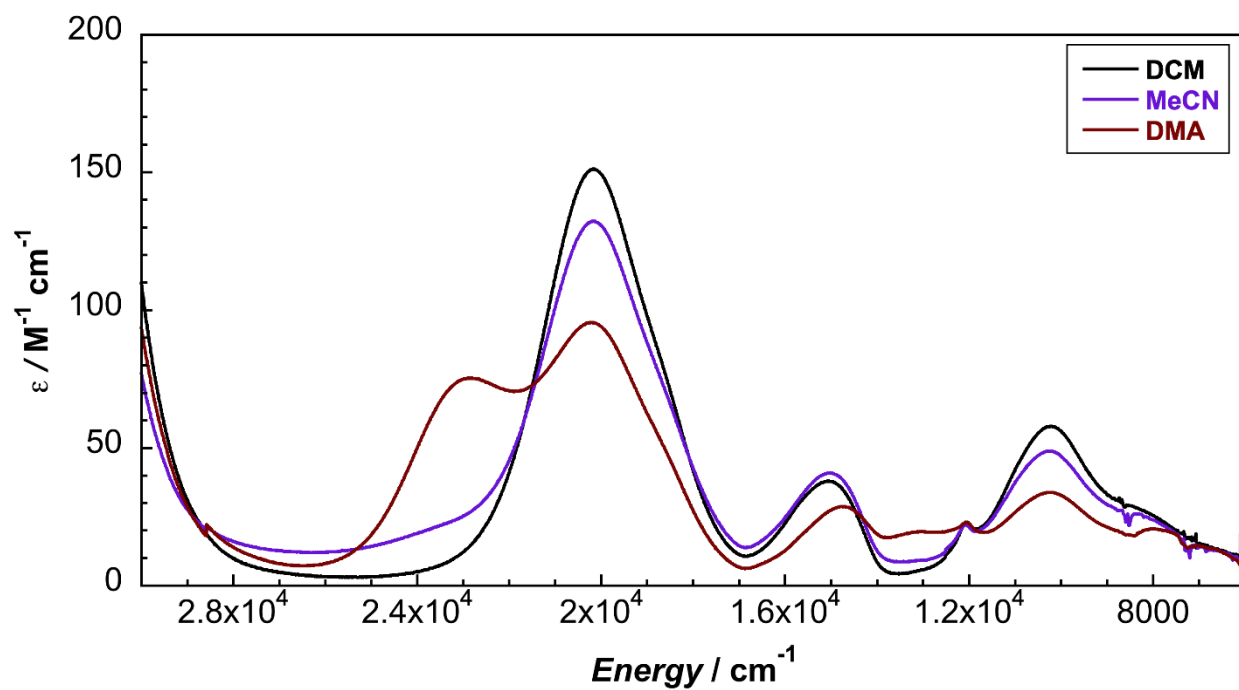
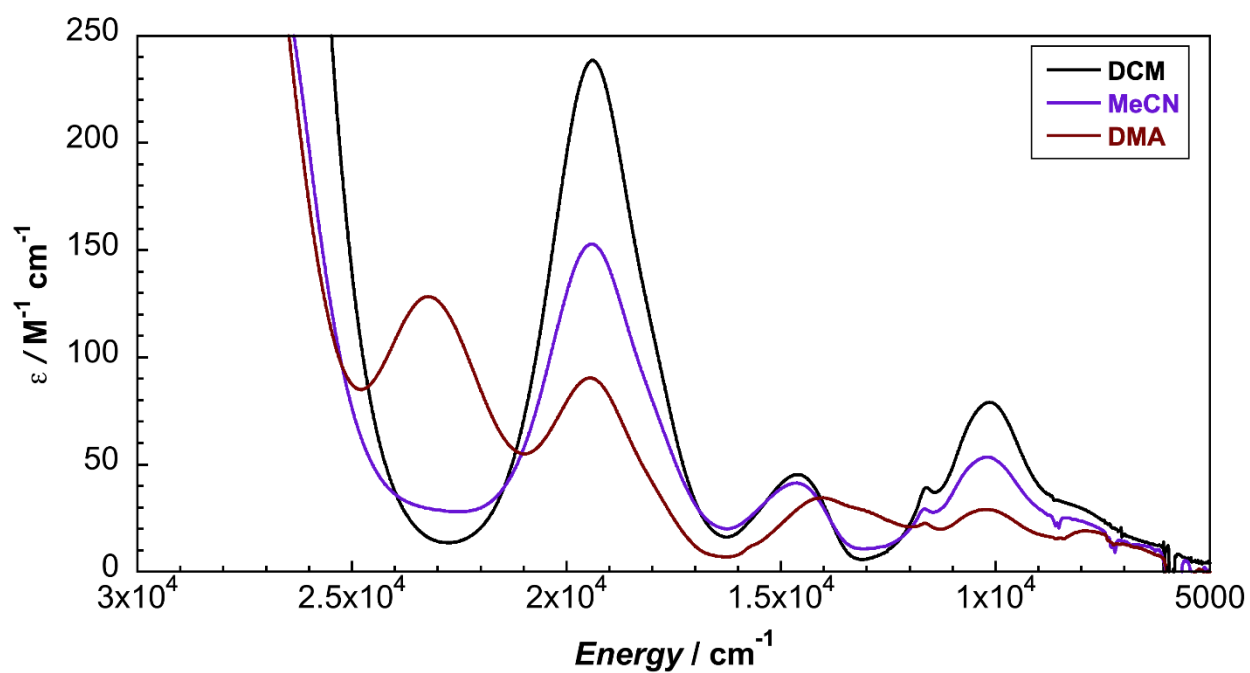


Figure S8. UV-vis-NIR spectra of  $\text{Ni}^{\text{II}}(\text{1B})\text{Br}_2$  in DMA.





**Figure S9.** Solvent comparison of UV-vis-NIR spectra of  $\text{Ni}^{\text{II}}(\text{1B})\text{Cl}_2$ .



**Figure S10.** Solvent comparison of UV-vis-NIR spectra of  $\text{Ni}^{\text{II}}(\text{1B})\text{Br}_2$ .

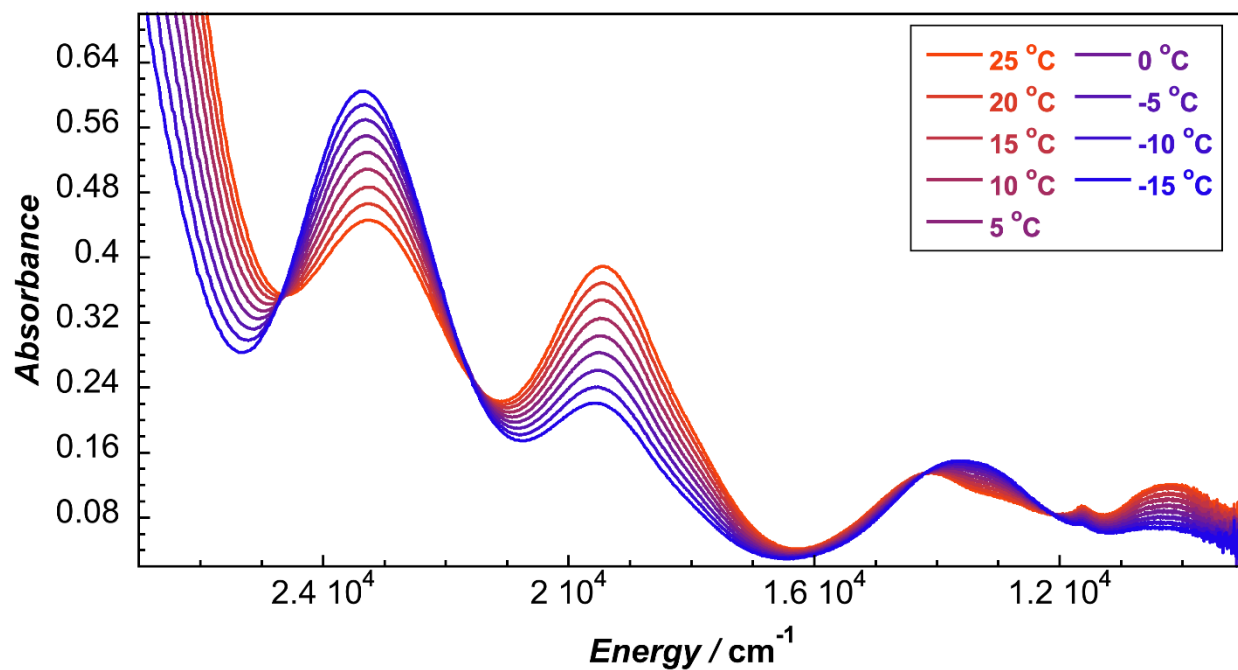


**Figure S11.** Variable-temperature UV-vis-NIR spectra of 3.5 mM  $\text{Ni}^{\text{II}}(\text{IB})\text{Br}_2$  in DMA.

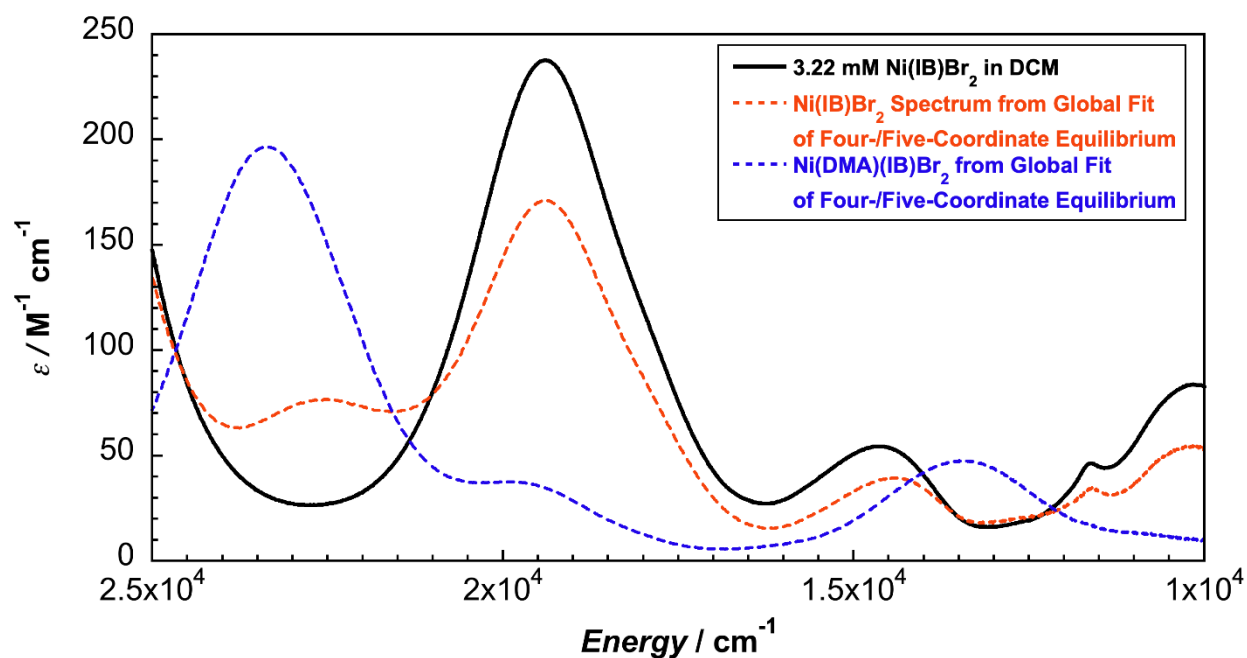


**Figure S12.** Global fitting and deconvolution into four- and five-coordinate species of the UV-vis-NIR spectra of  $\text{Ni}^{\text{II}}(\text{IB})\text{Br}_2$  in DMA.

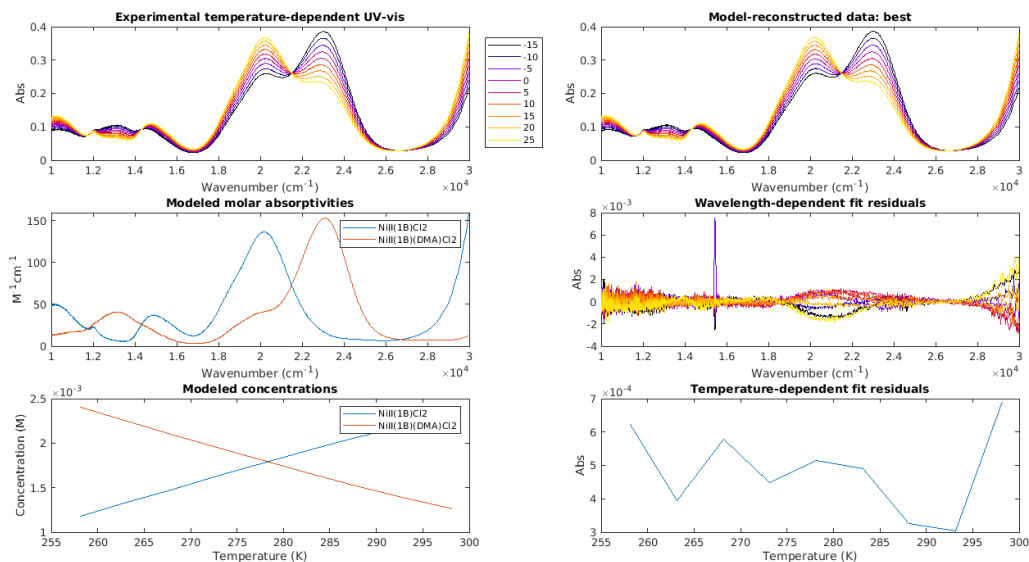


**Figure S13.** Global fitting and deconvolution into four- and five-coordinate species of the UV-vis-NIR spectra of 3.6 mM  $\text{Ni}^{\text{II}}(\text{1B})\text{Cl}_2$  in DMA.

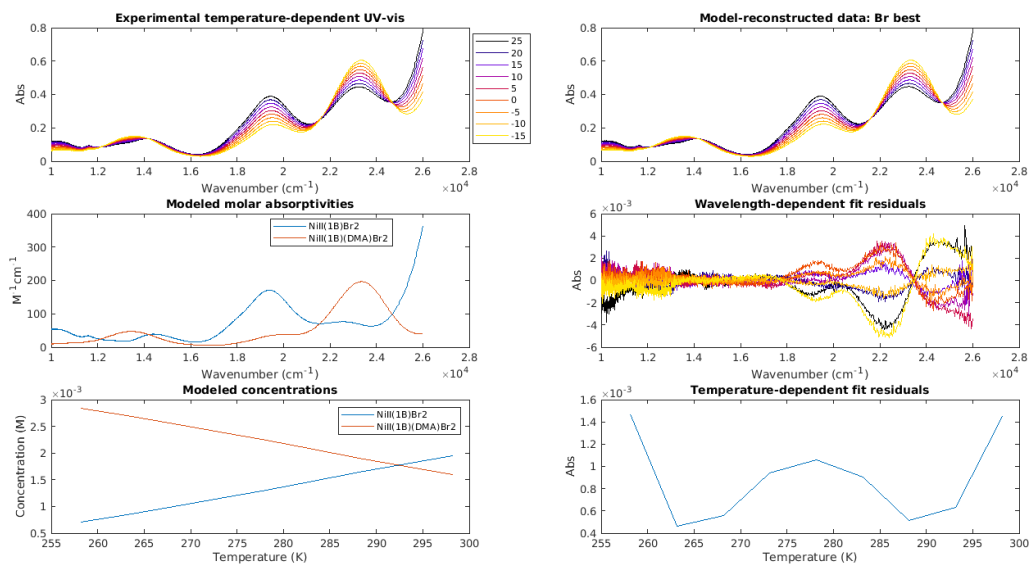


**Figure S14.** Global fitting and deconvolution into four- and five-coordinate species of the UV-vis-NIR spectra of 3.5 mM  $\text{Ni}^{\text{II}}(\text{1B})\text{Br}_2$  in DMA.

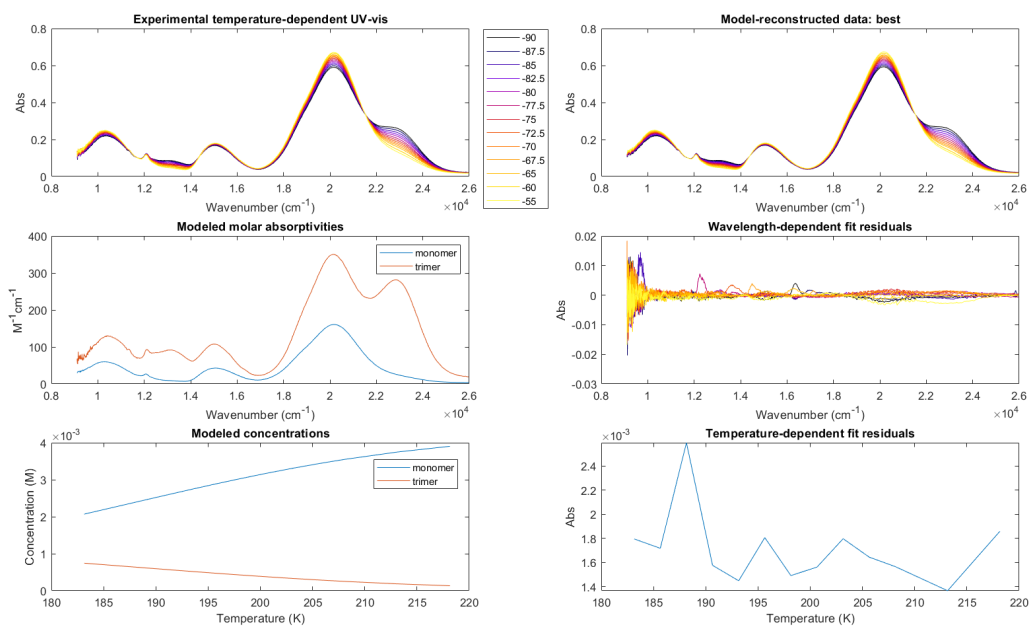


**Figure S15.** Global fitting and deconvolution into monomer and trimer species of the UV-vis-NIR spectra of 4.3 mM  $\text{Ni}^{\text{II}}(\text{1B})\text{Cl}_2$  in DCM.

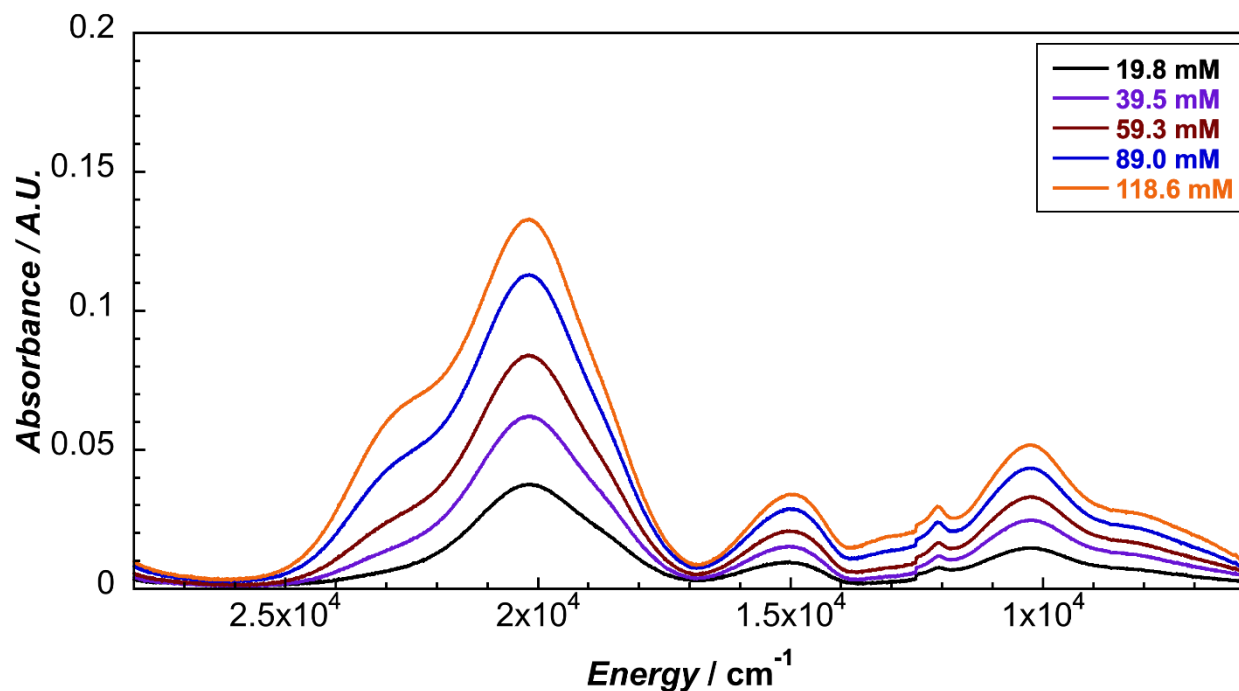


**Figure S16.** Variable-concentration UV-vis-NIR spectra of  $\text{Ni}^{\text{II}}(\text{1B})\text{Cl}_2$  in  $d^2$ -dichloromethane in a 0.1 mM calcium fluoride optical cell.

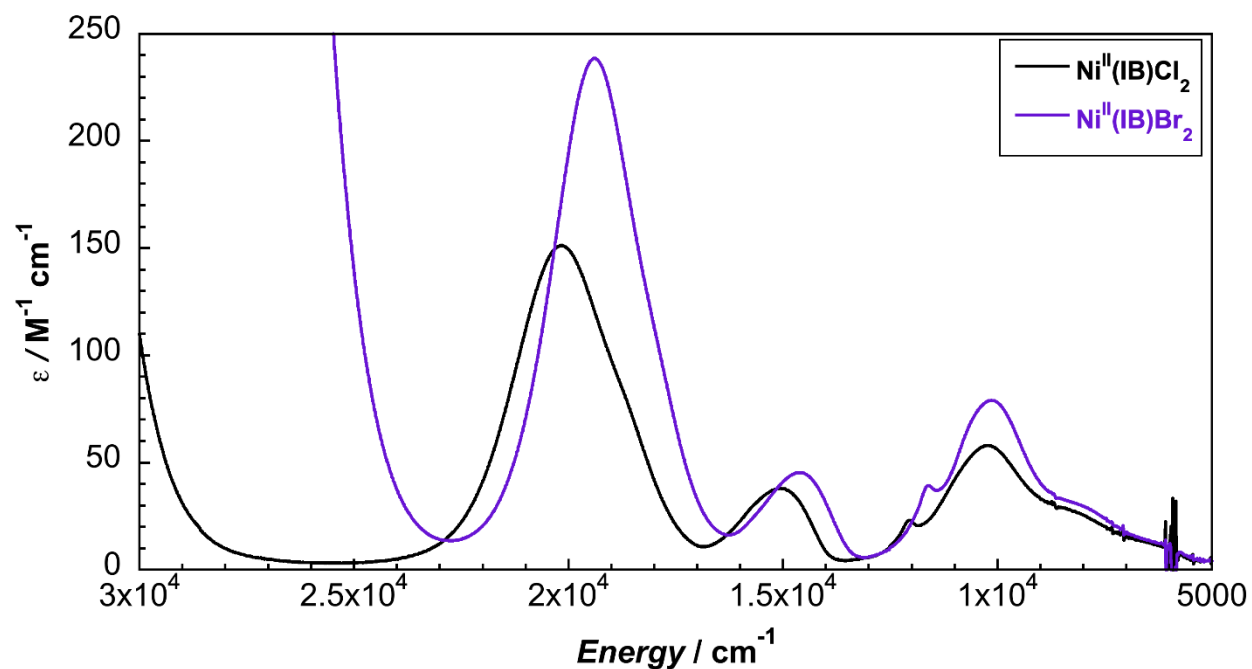


Figure S17. Comparison of UV-vis-NIR spectra of  $\text{Ni}^{\text{II}}(\text{1B})\text{Cl}_2$  and  $\text{Ni}^{\text{II}}(\text{1B})\text{Br}_2$  in DCM.

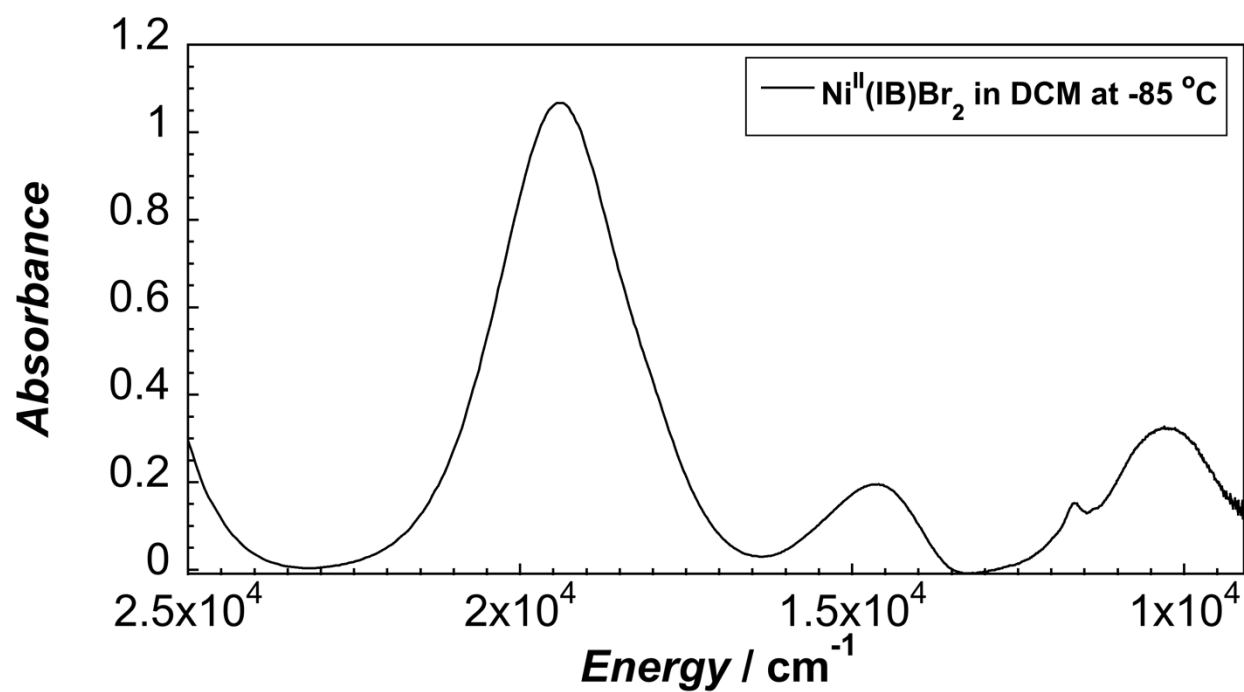
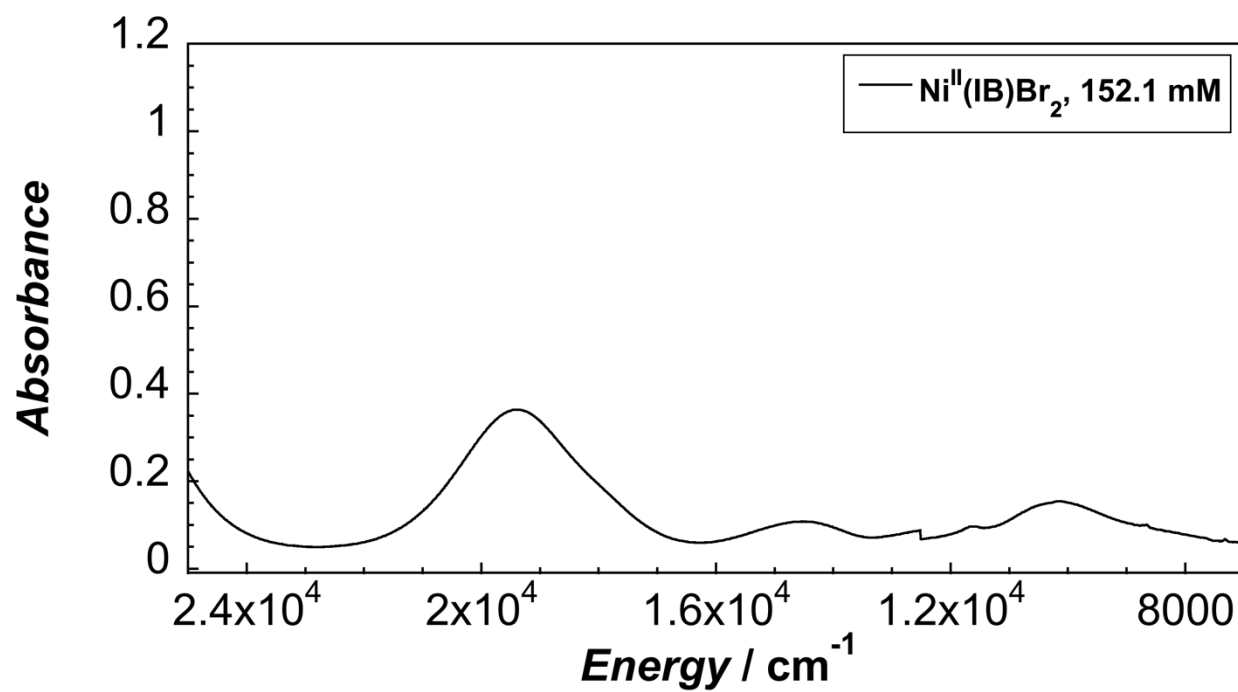


Figure S18. UV-vis-NIR spectra of  $\text{Ni}^{\text{II}}(\text{1B})\text{Br}_2$  at  $-85^\circ\text{C}$  in DCM solution.



**Figure S19.** UV-vis-NIR spectra of 152.1 mM  $\text{Ni}^{\text{II}}(\text{1B})\text{Br}_2$  in DCM solution.

#### S4. Circular Dichroism and Magnetic Circular Dichroism Spectra

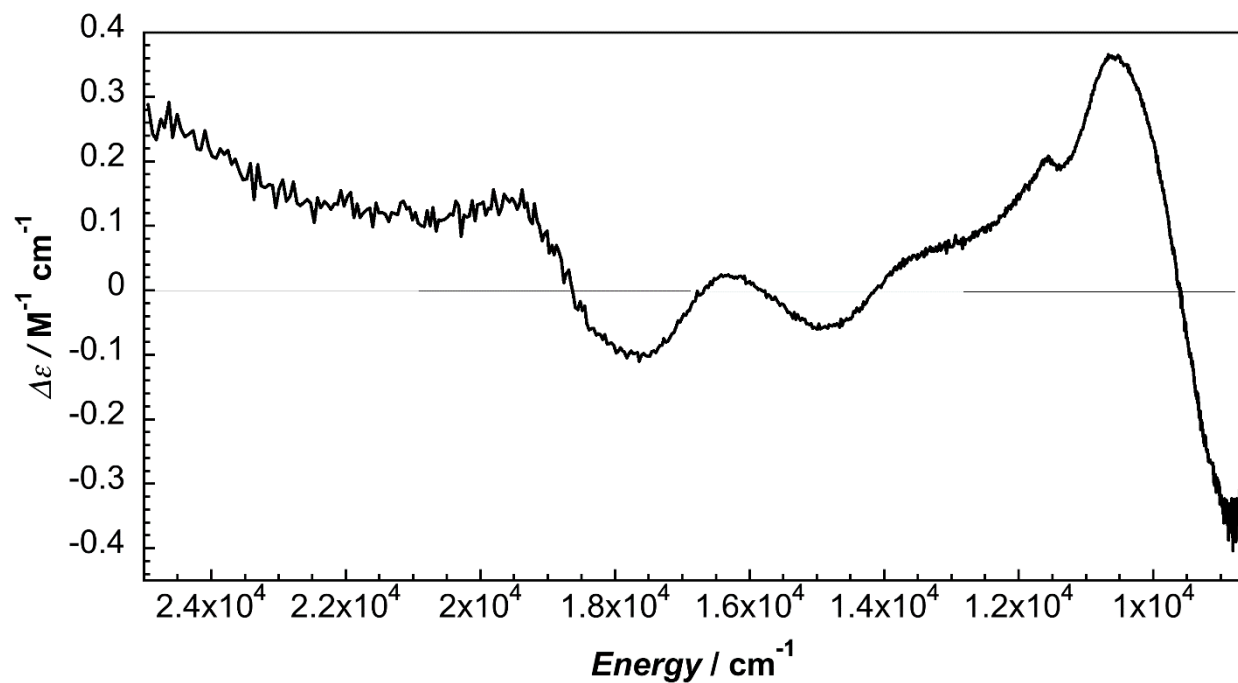


Figure S20. Circular dichroism of  $\text{Ni}^{\text{II}}(\text{1B})\text{Br}_2$  in DCM at 294 K.

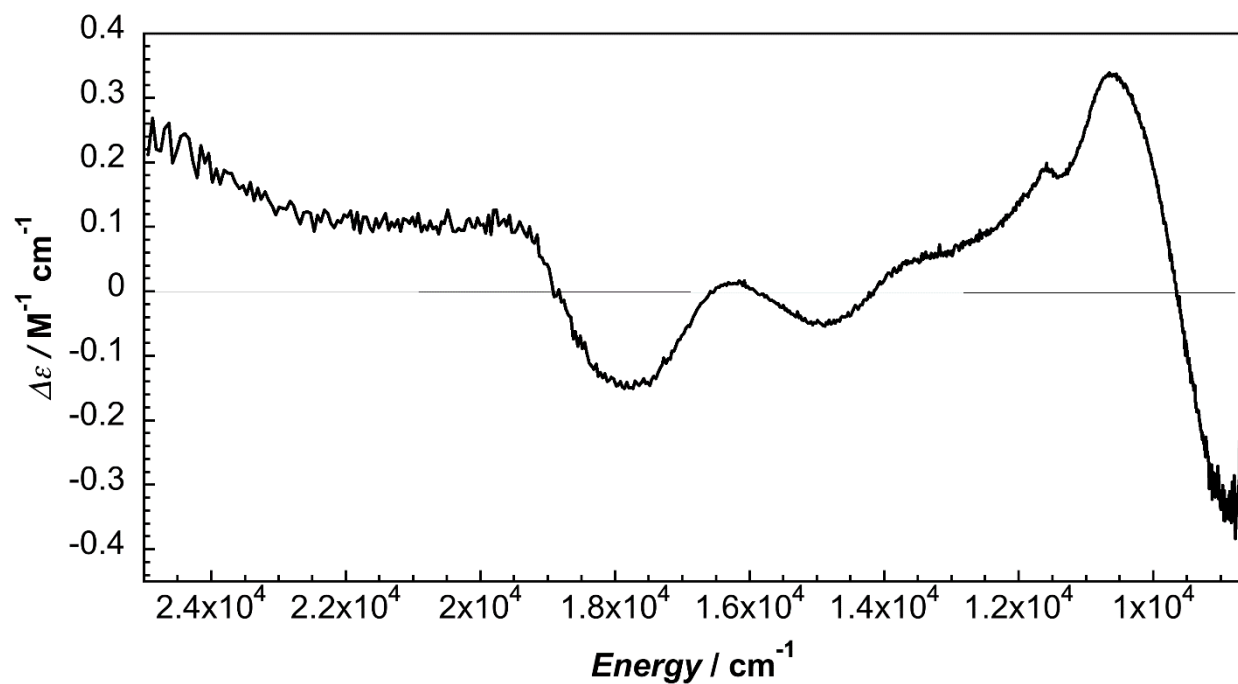
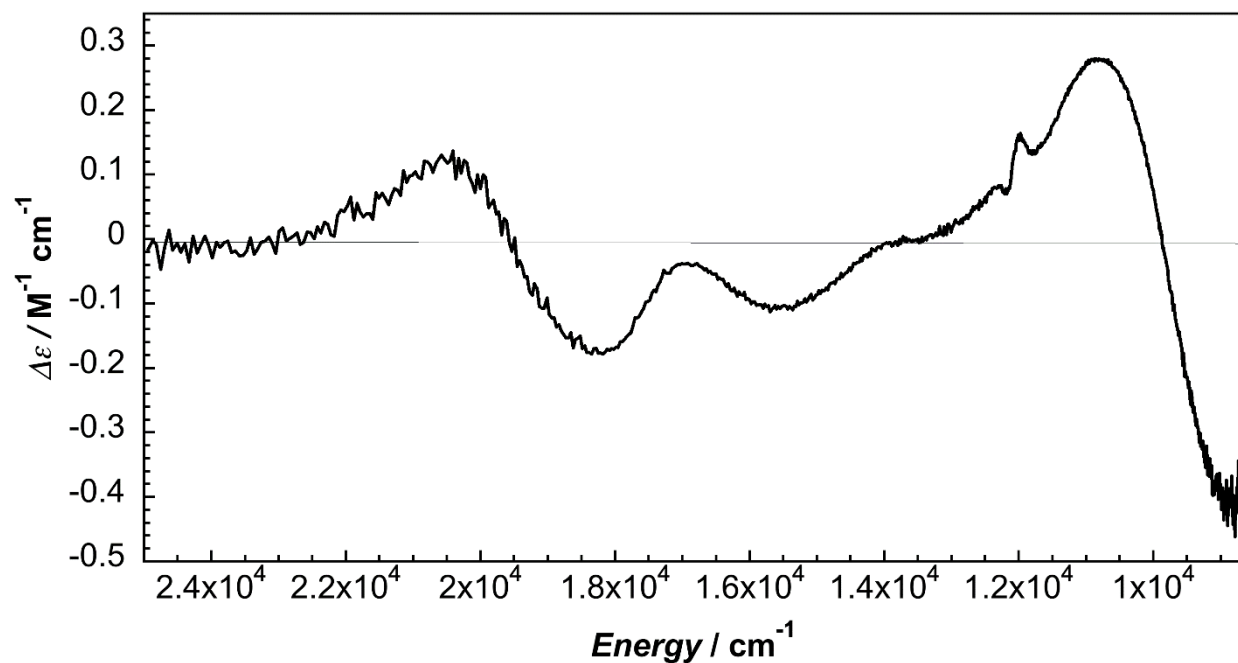
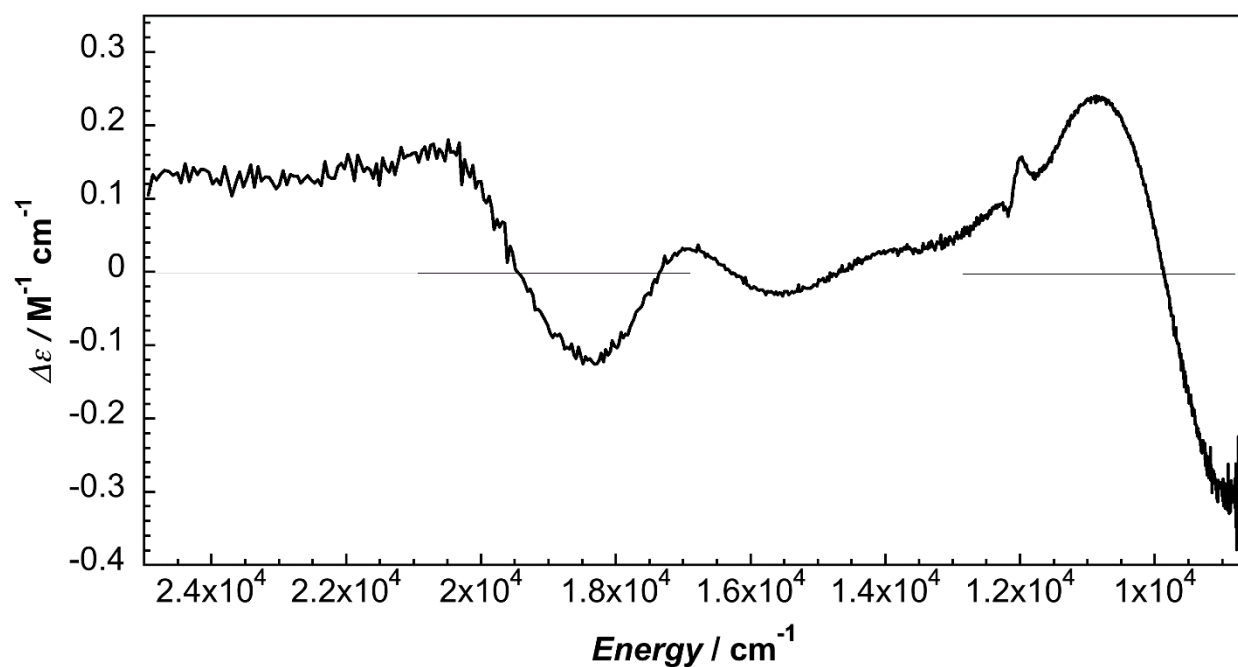


Figure S21. Circular dichroism of  $\text{Ni}^{\text{II}}(\text{1B})\text{Br}_2$  in 0.1 M  $\text{TBAPF}_6$  in DCM solution at 294 K.



**Figure S22.** Circular dichroism of  $\text{Ni}^{\text{II}}(\text{1B})\text{Cl}_2$  in DCM at 294 K.



**Figure S23.** Circular dichroism of  $\text{Ni}^{\text{II}}(\text{1B})\text{Cl}_2$  in 0.1 M  $\text{TBAPF}_6$  in DCM solution at 294 K.



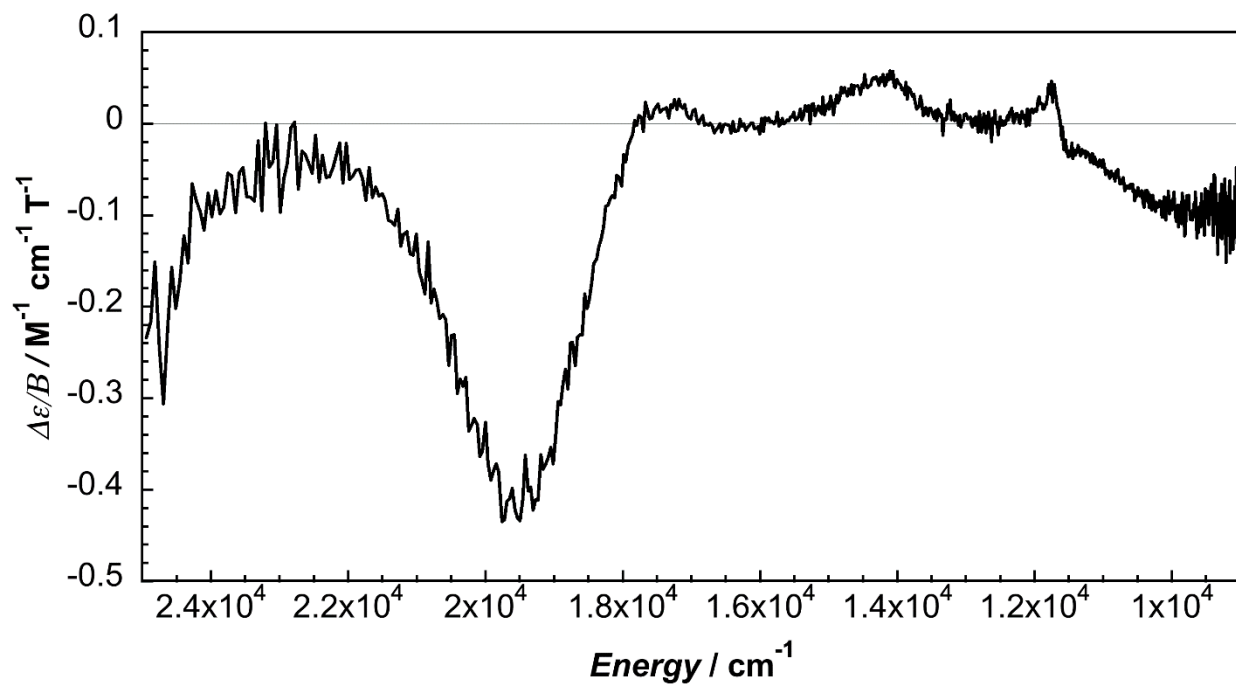


**Figure S24.** Magnetic circular dichroism of  $\text{Ni}^{\text{II}}(\text{IB})\text{Br}_2$  in DCM at 294 K.

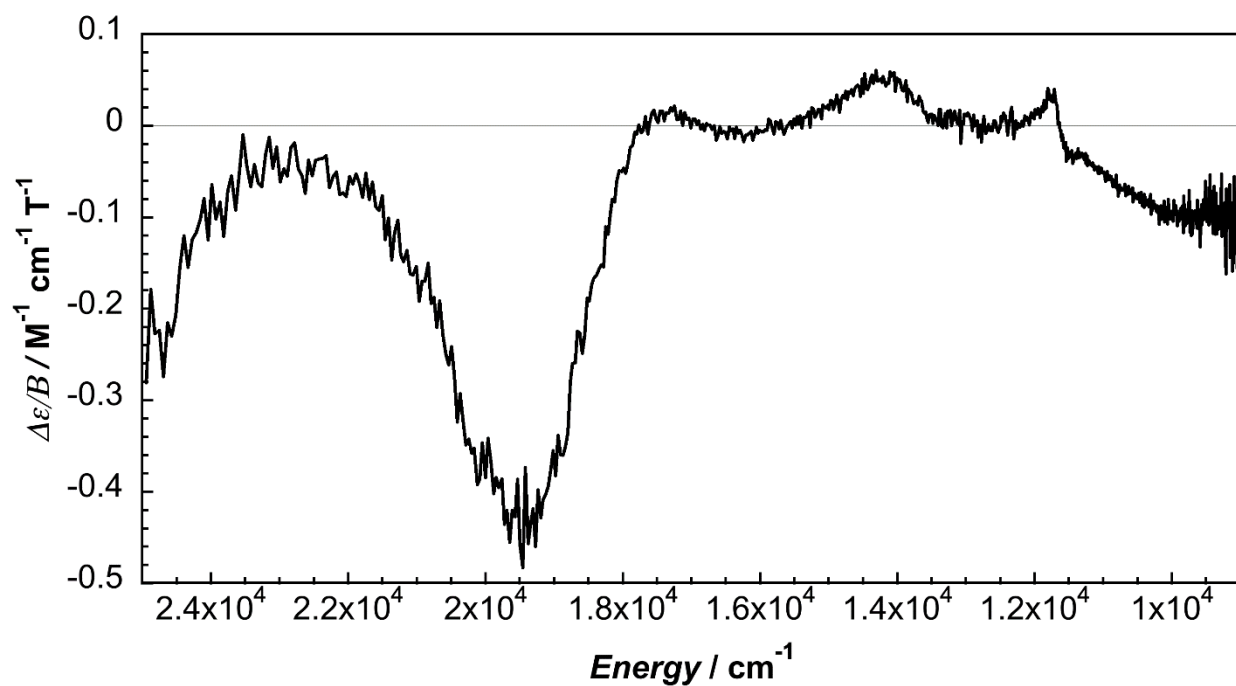


**Figure S25.** Magnetic circular dichroism of  $\text{Ni}^{\text{II}}(\text{IB})\text{Br}_2$  in 0.1 M  $\text{TBAPF}_6$  in DCM solution at 294 K.

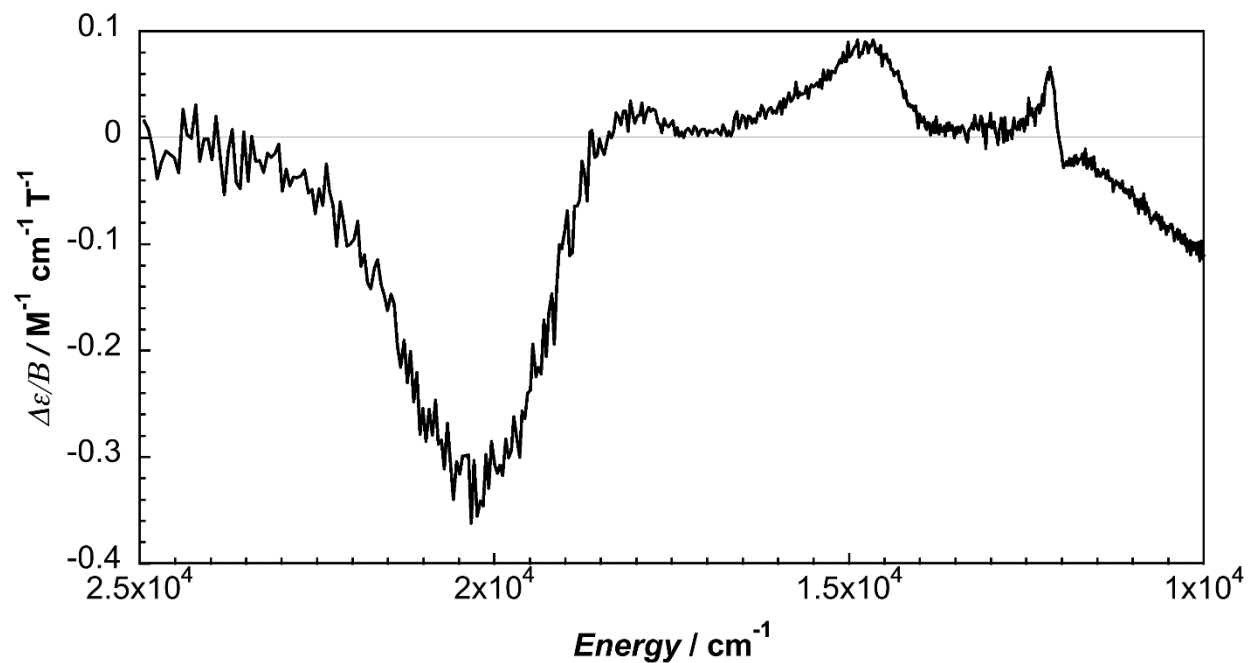


**Figure S26.** Magnetic circular dichroism of  $\text{Ni}^{\text{II}}(\text{1B})\text{Cl}_2$  in DCM at 294 K.

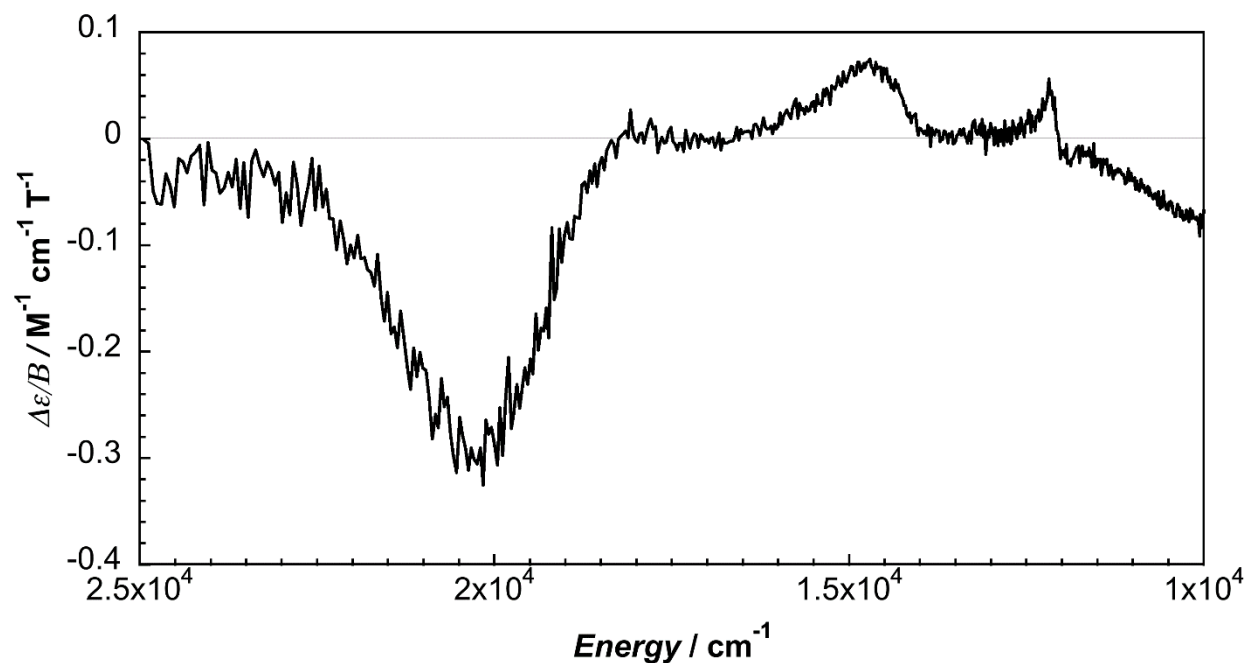


**Figure S27.** Magnetic circular dichroism of  $\text{Ni}^{\text{II}}(\text{1B})\text{Cl}_2$  in 0.1 M  $\text{TBAPF}_6$  in DCM solution at 294 K.

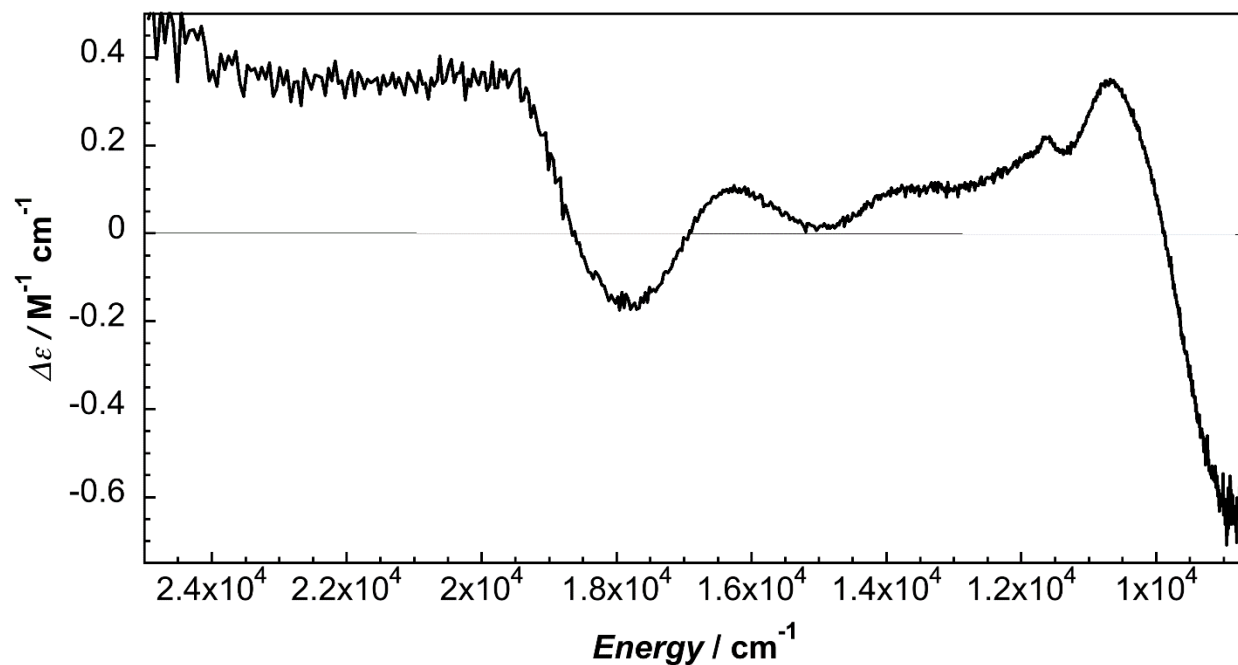


**Figure S28.** Circular dichroism of  $\text{Ni}^{\text{II}}(\text{1B})\text{Br}_2$  in MeCN at 294 K.

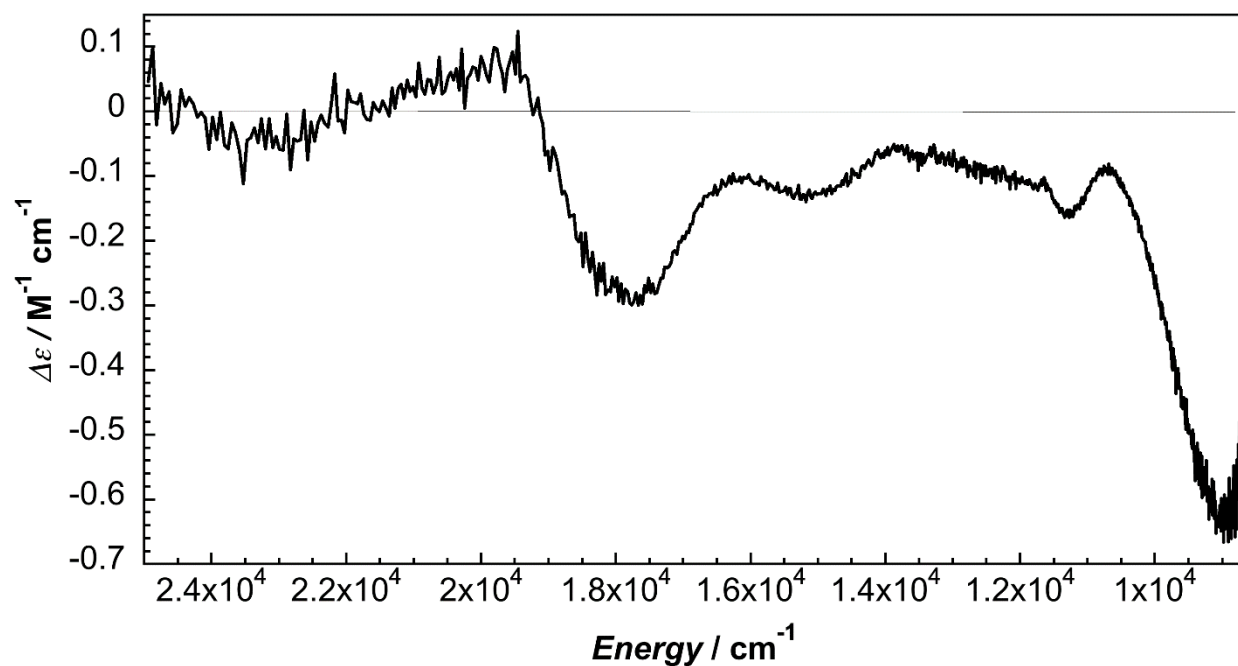


**Figure S29.** Circular dichroism of  $\text{Ni}^{\text{II}}(\text{1B})\text{Br}_2$  in 0.1 M TBAPF<sub>6</sub> in MeCN at 294 K.

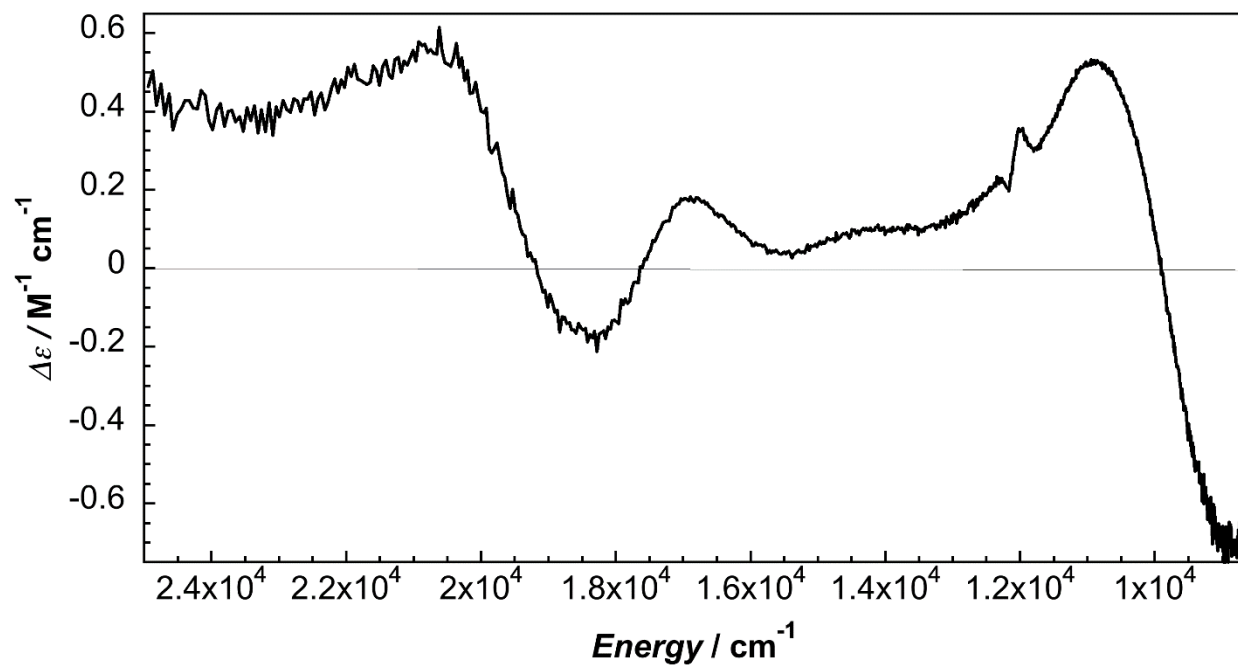


**Figure S30.** Circular dichroism of  $\text{Ni}^{\text{II}}(\text{1B})\text{Cl}_2$  in MeCN at 294 K.

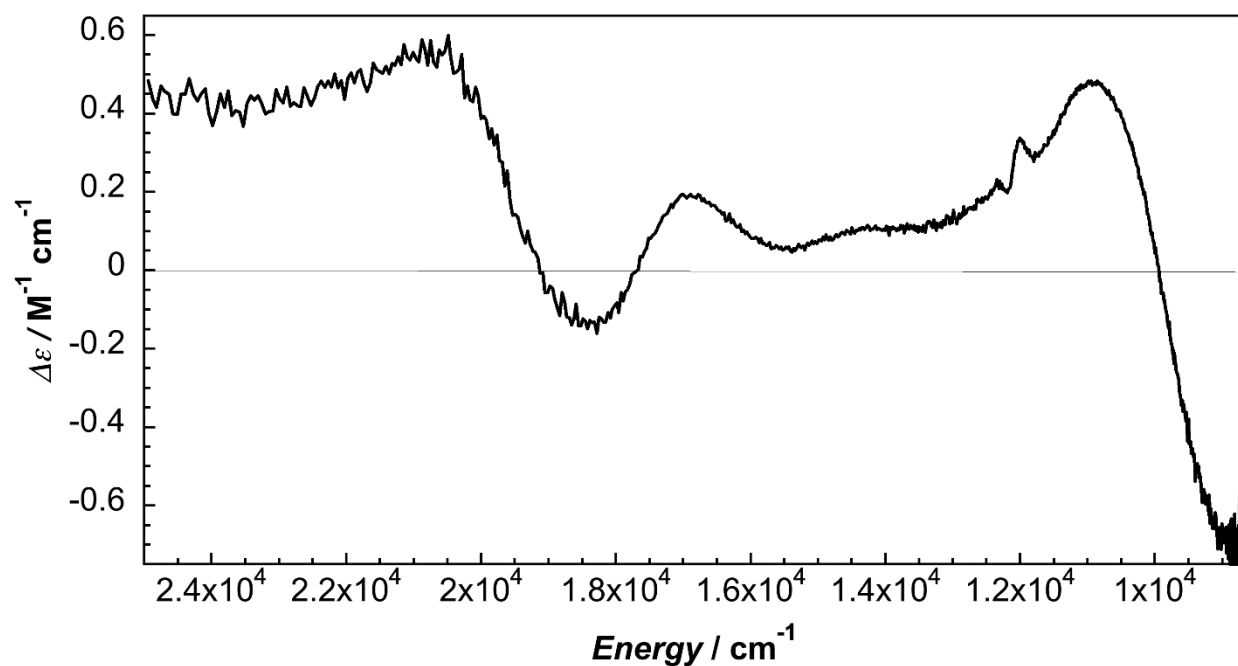


**Figure S31.** Circular dichroism of  $\text{Ni}^{\text{II}}(\text{1B})\text{Cl}_2$  in 0.1 M  $\text{TBAPF}_6$  in MeCN solution at 294 K.

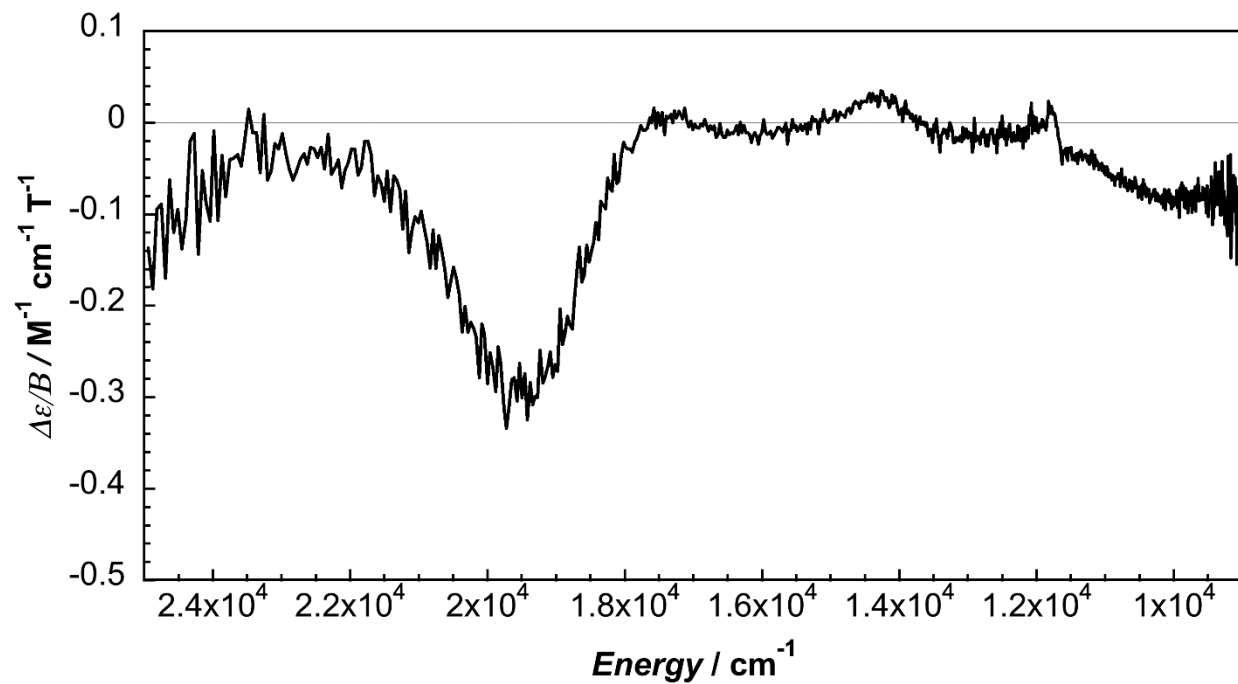


**Figure S32.** Magnetic circular dichroism of  $\text{Ni}^{\text{II}}(\text{1B})\text{Br}_2$  in MeCN.

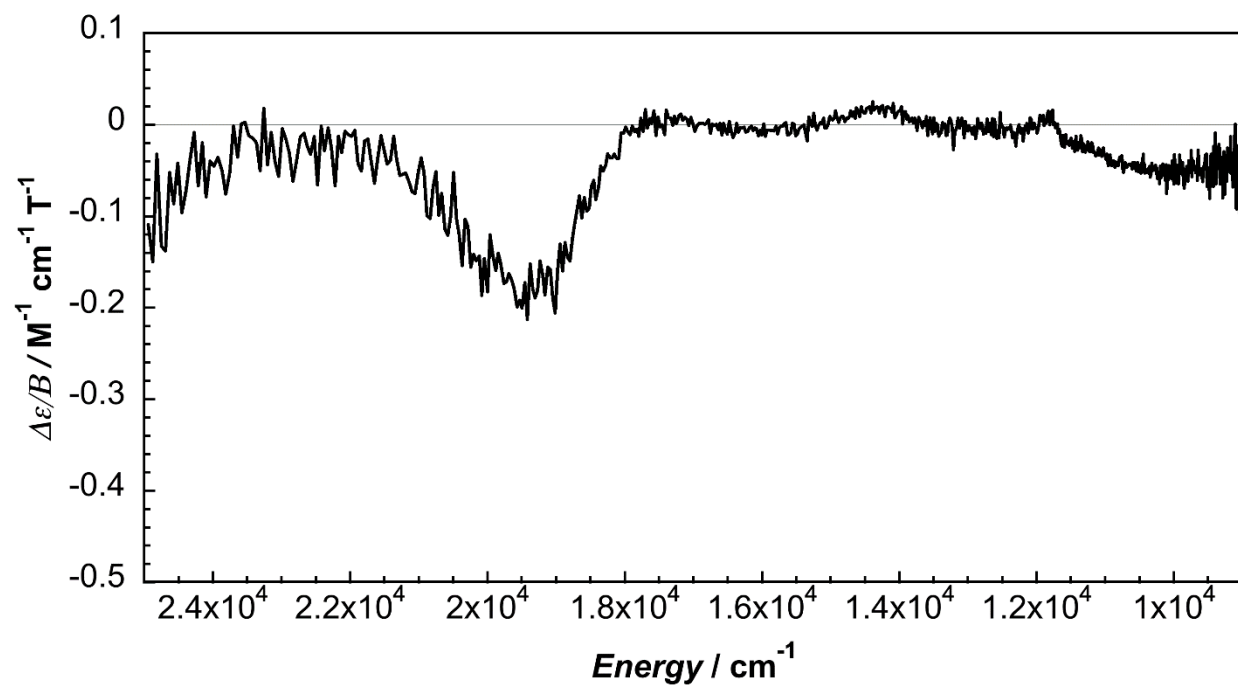


**Figure S33.** Magnetic circular dichroism of  $\text{Ni}^{\text{II}}(\text{1B})\text{Br}_2$  in 0.1 M TBAPF<sub>6</sub> in MeCN solution at 294 K.

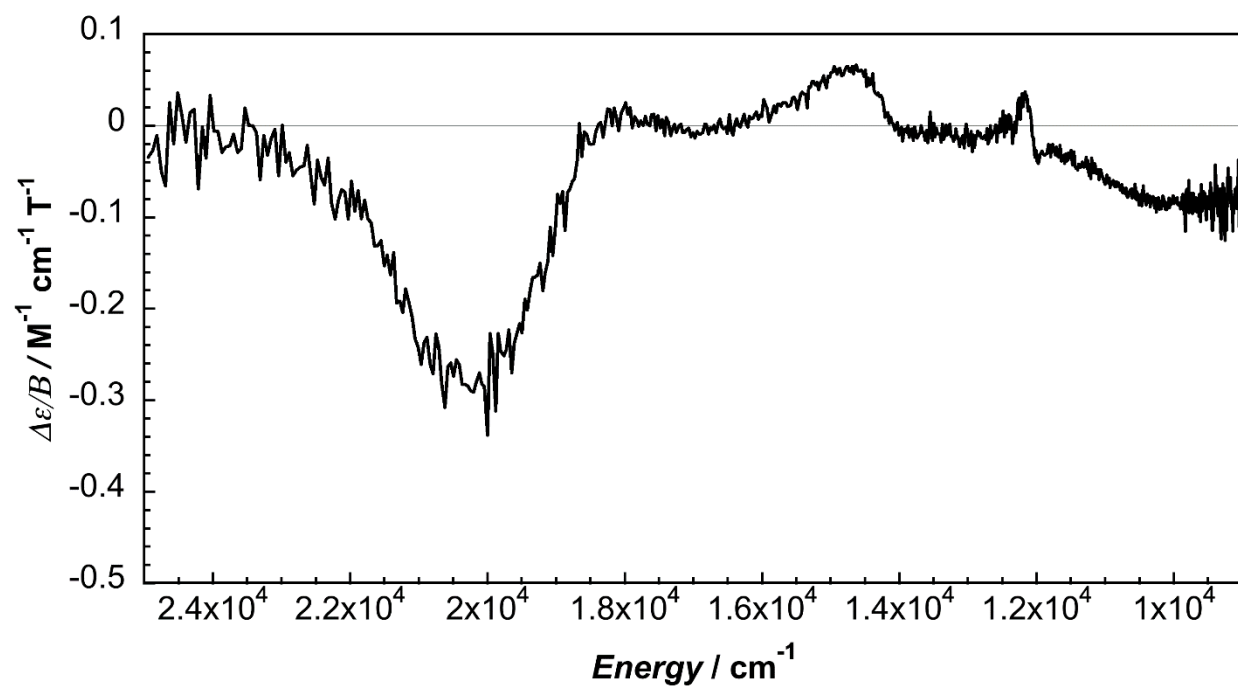


**Figure S34.** Magnetic circular dichroism of  $\text{Ni}^{\text{II}}(\text{1B})\text{Cl}_2$  in MeCN.

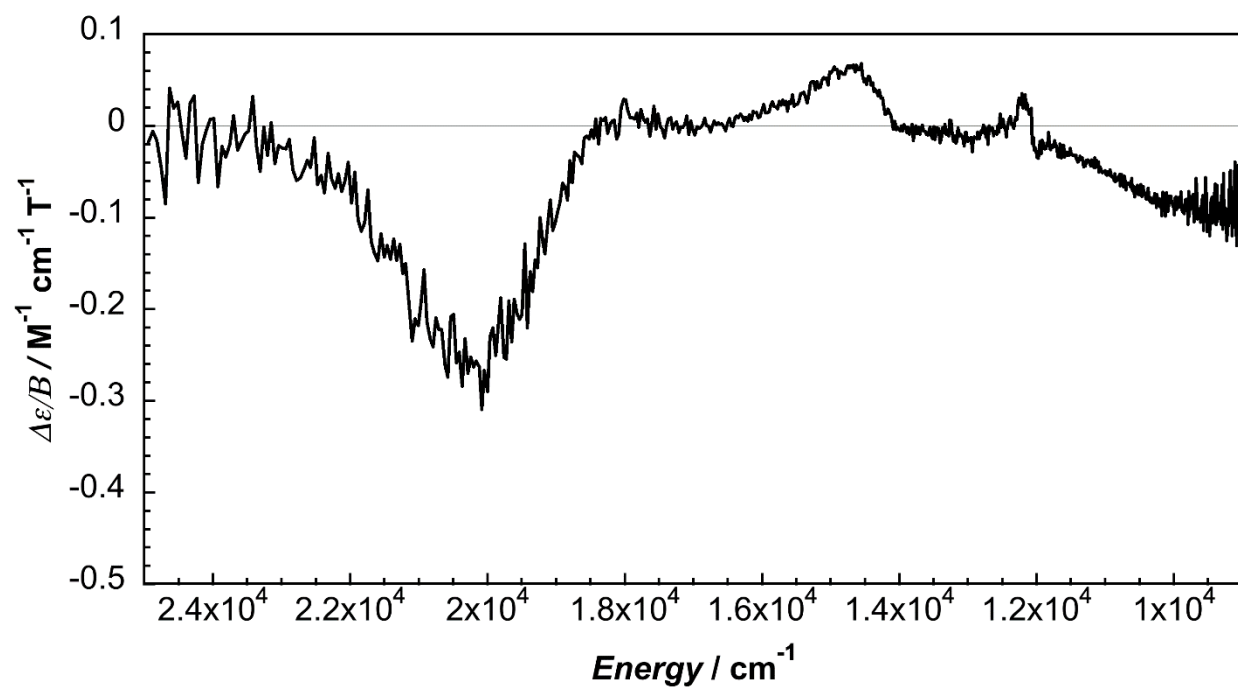


**Figure S35.** Magnetic circular dichroism of  $\text{Ni}^{\text{II}}(\text{1B})\text{Cl}_2$  in 0.1 M  $\text{TBAPF}_6$  in MeCN solution at 294 K.

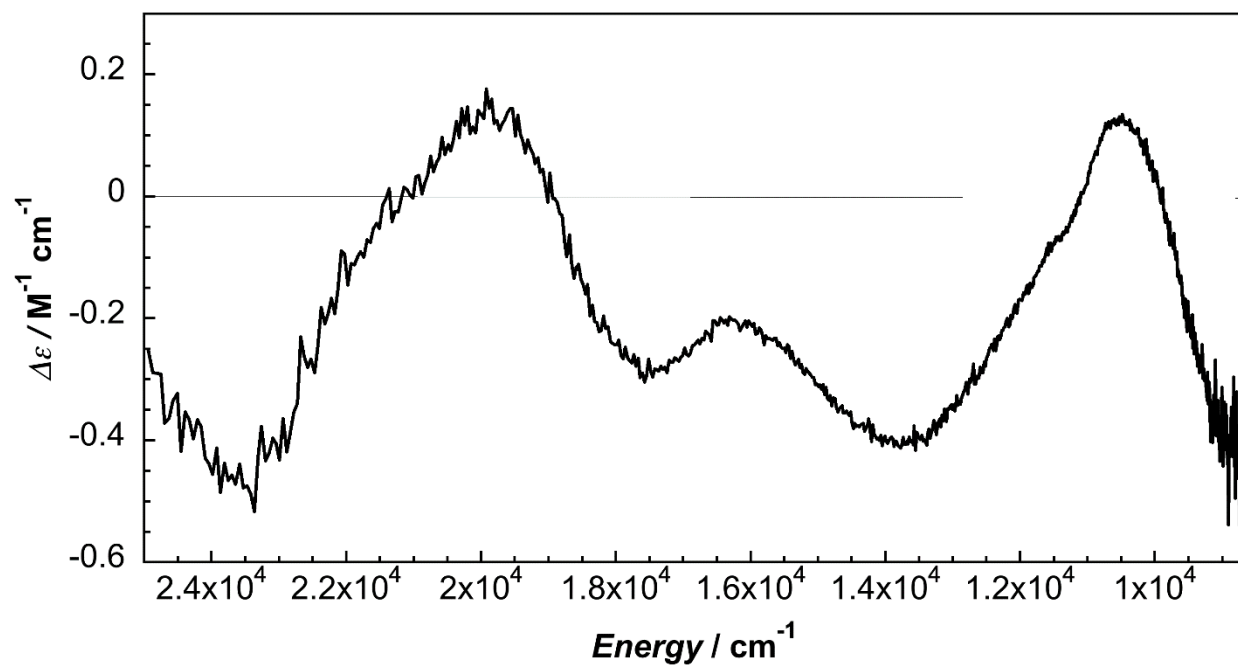


**Figure S36.** Circular dichroism of  $\text{Ni}^{\text{II}}(\text{1B})\text{Br}_2$  in DMA at 294 K.

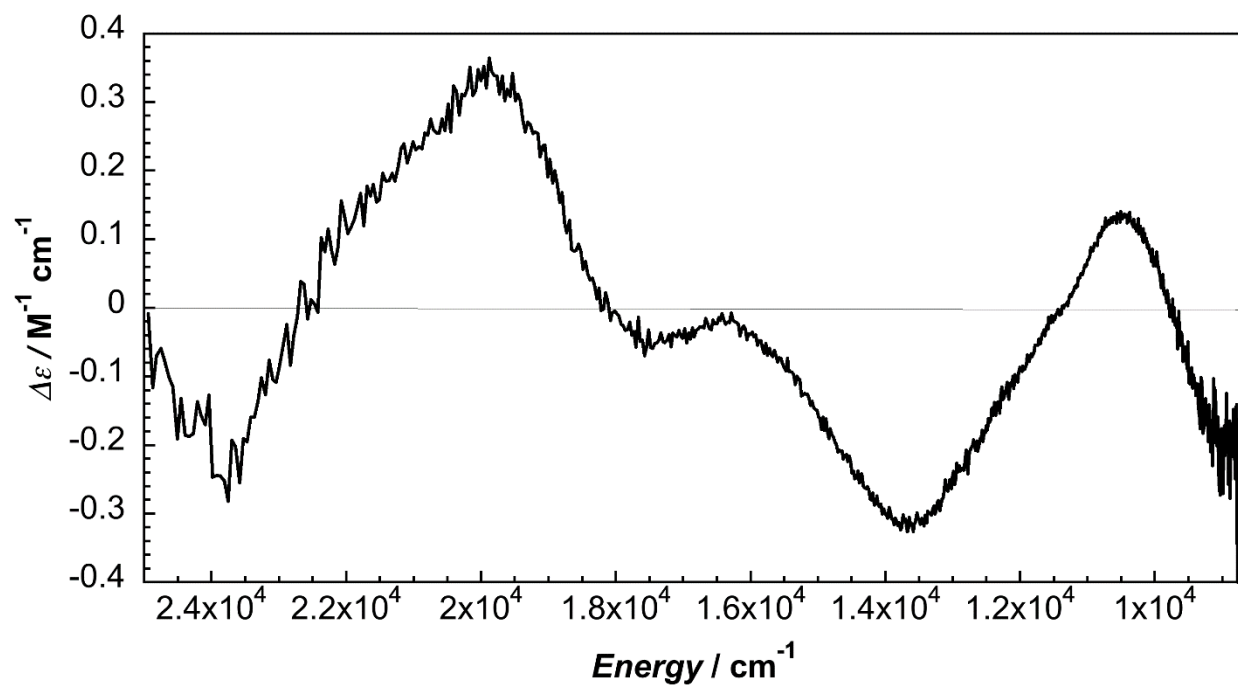


**Figure S37.** Circular dichroism of  $\text{Ni}^{\text{II}}(\text{1B})\text{Br}_2$  in 0.1 M  $\text{TBAPF}_6$  in DMA solution at 294 K.

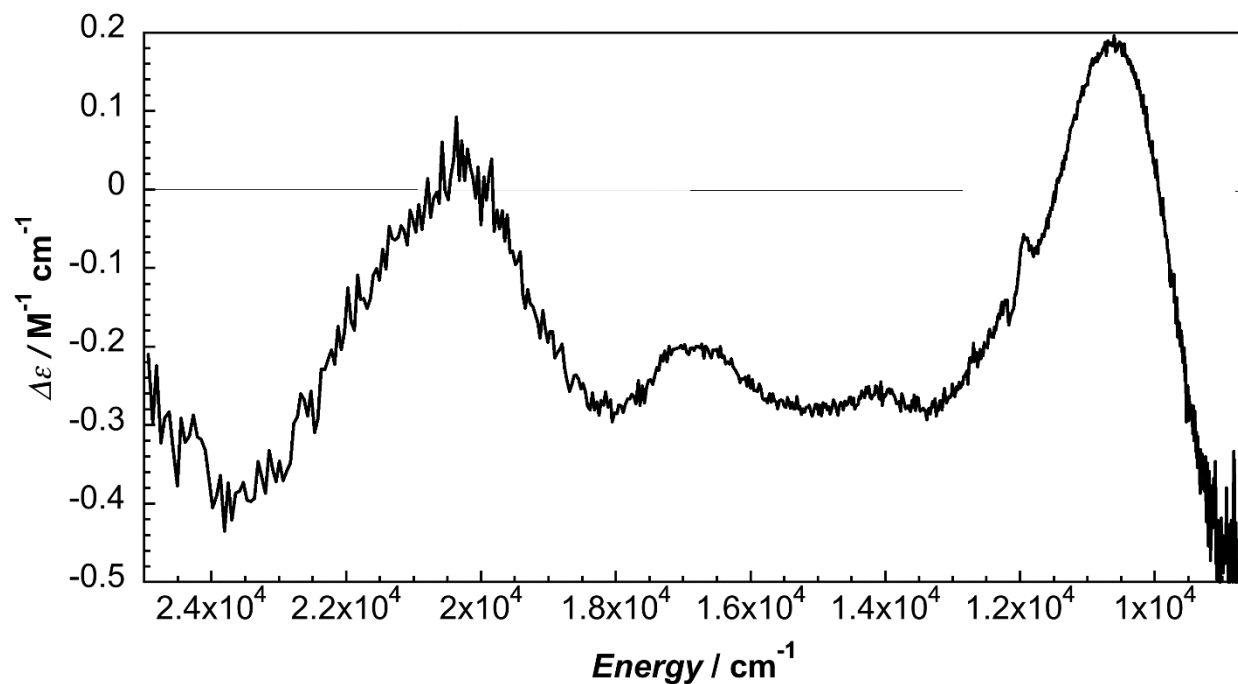


**Figure S38.** Circular dichroism of  $\text{Ni}^{\text{II}}(\text{1B})\text{Cl}_2$  in DMA at 294 K.

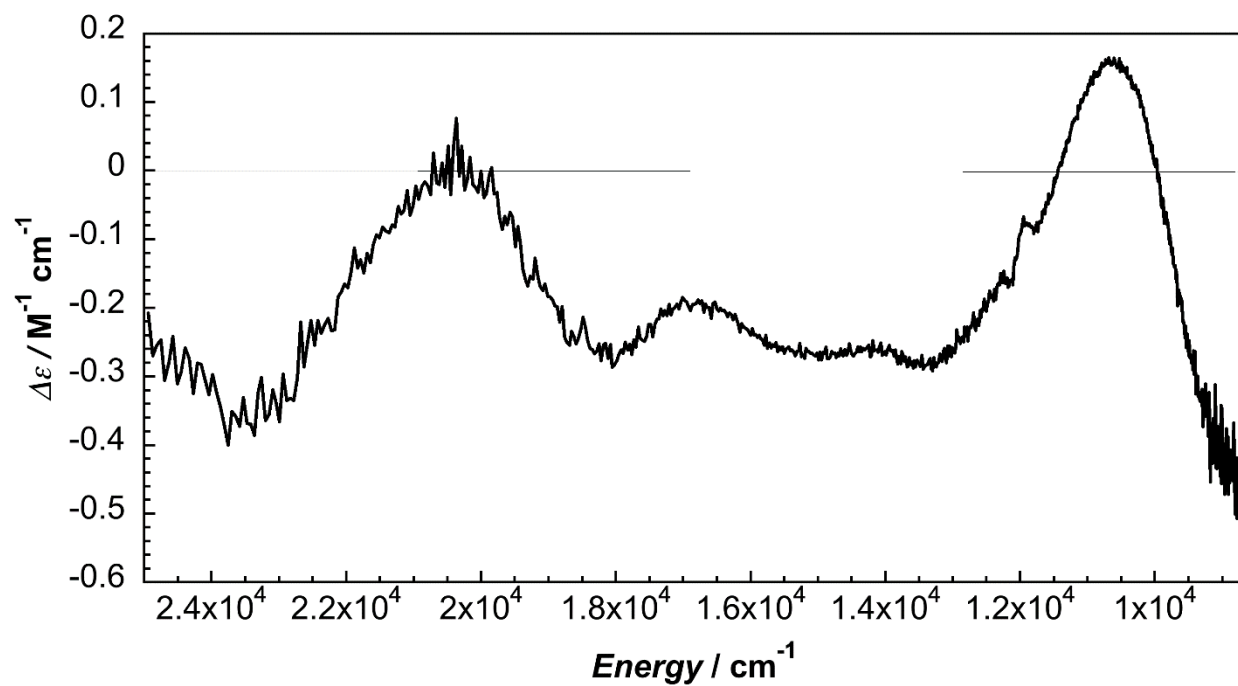


**Figure S39.** Circular dichroism of  $\text{Ni}^{\text{II}}(\text{1B})\text{Cl}_2$  in 0.1 M  $\text{TBAPF}_6$  in DMA solution at 294 K.



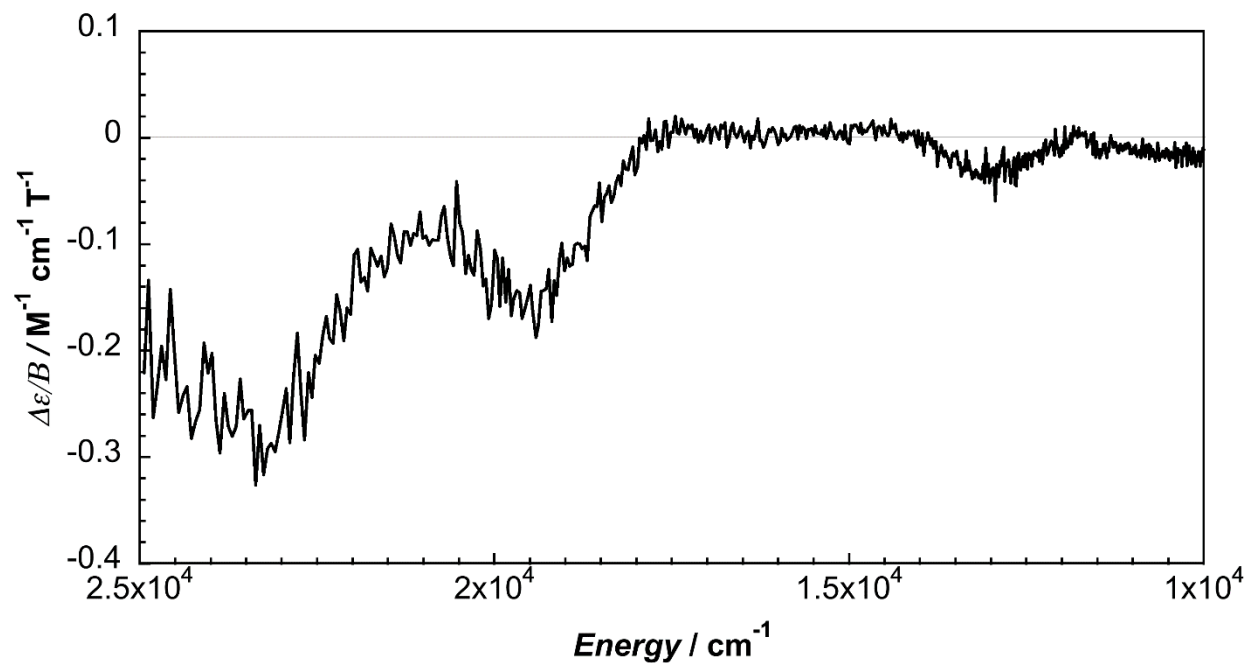


**Figure S40.** Magnetic circular dichroism of  $\text{Ni}^{\text{II}}(\text{IB})\text{Br}_2$  in DMA at 294 K.

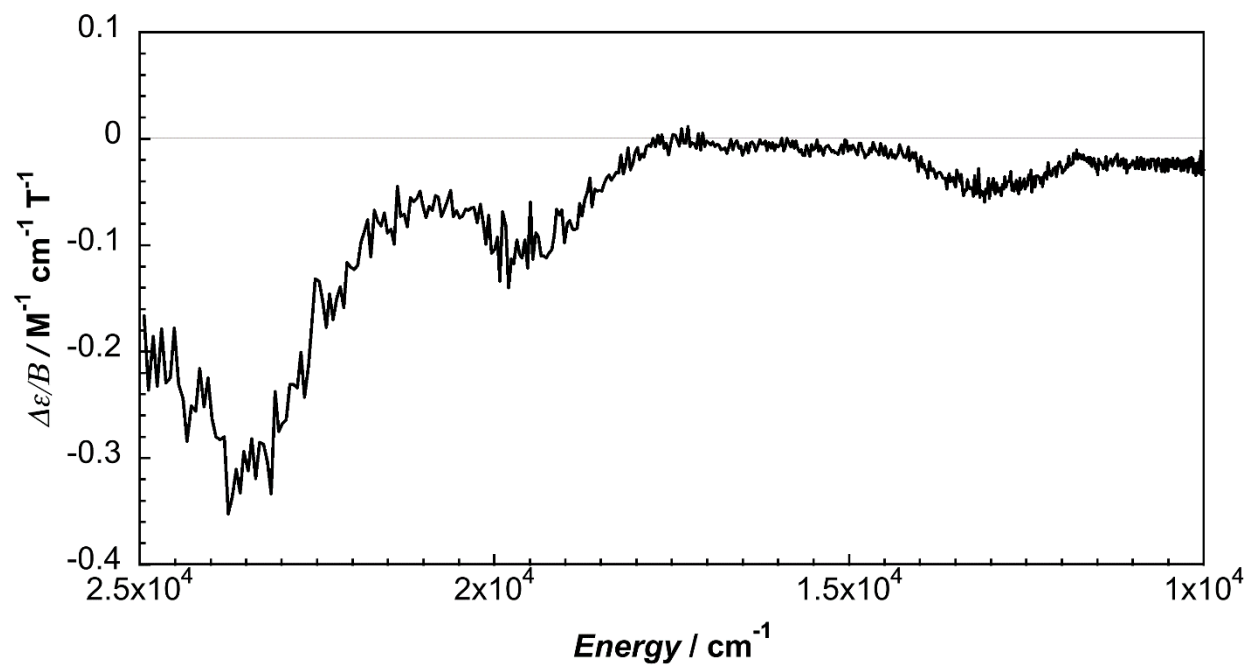


**Figure S41.** Magnetic circular dichroism of  $\text{Ni}^{\text{II}}(\text{IB})\text{Br}_2$  in 0.1 M  $\text{TBAPF}_6$  in DMA solution at 294 K.

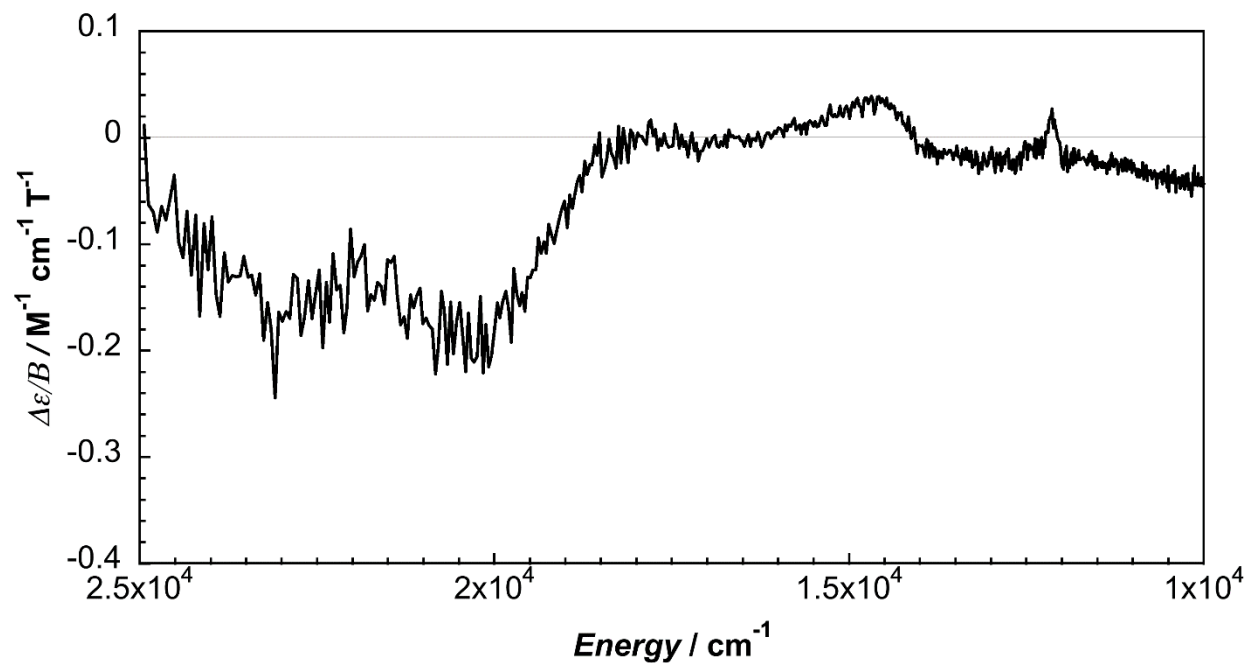


**Figure S42.** Magnetic circular dichroism of  $\text{Ni}^{\text{II}}(\text{1B})\text{Cl}_2$  in DMA at 294 K.

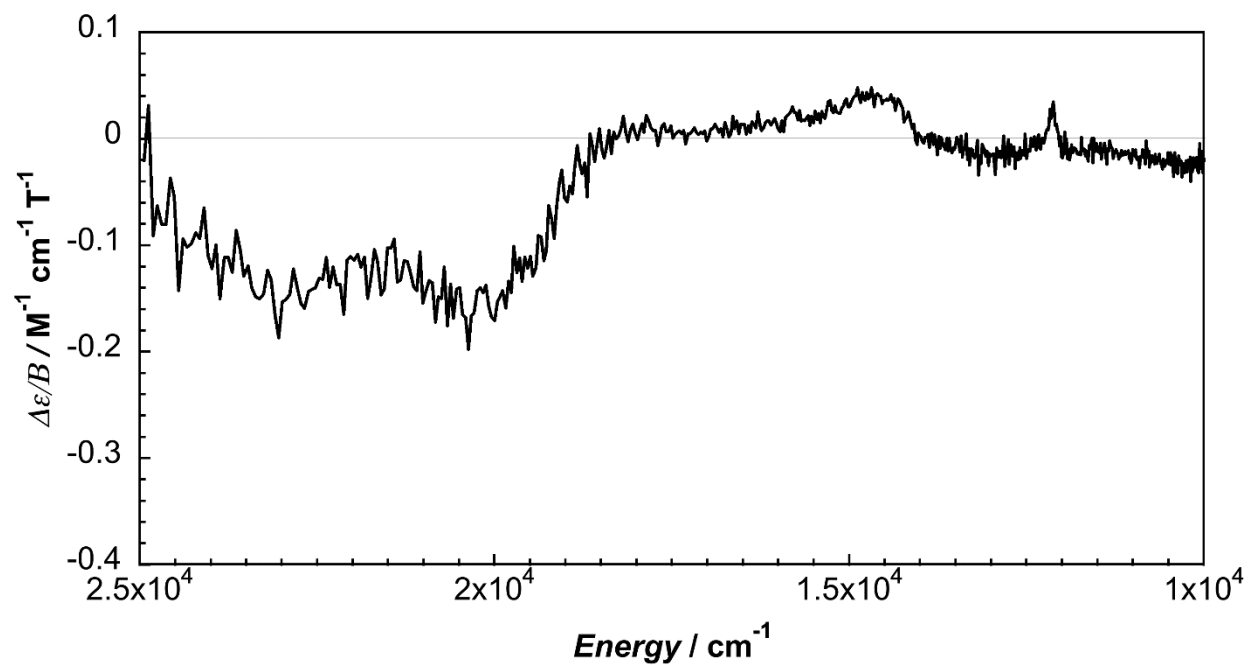


**Figure S43.** Magnetic circular dichroism of  $\text{Ni}^{\text{II}}(\text{1B})\text{Cl}_2$  in 0.1 M  $\text{TBAPF}_6$  in DMA solution at 294 K.

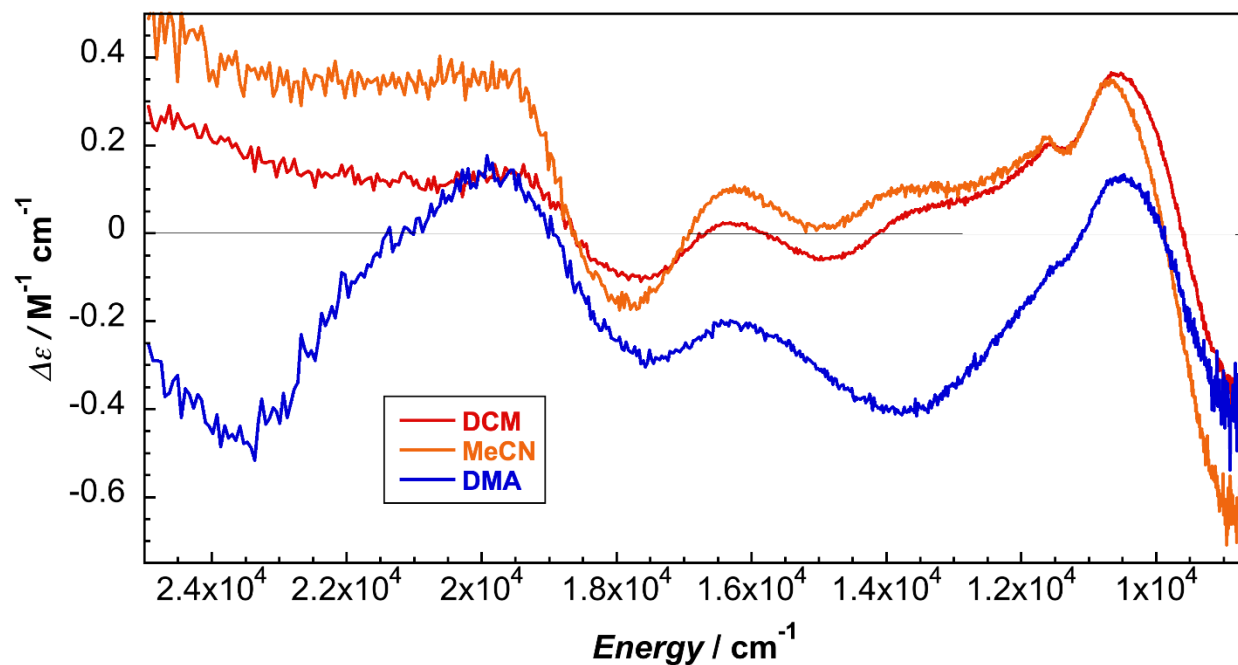


**Figure S44.** Solvent comparison of circular dichroism of  $\text{Ni}^{\text{II}}(\text{1B})\text{Br}_2$  at 294 K.

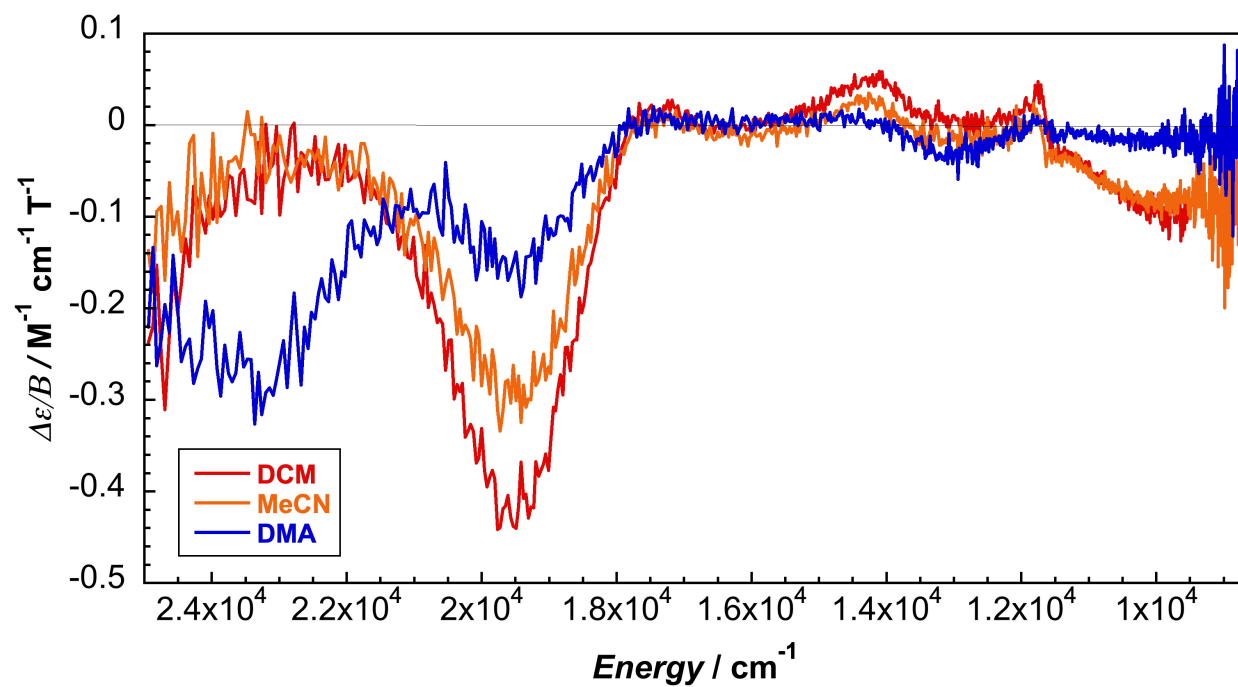


**Figure S45.** Solvent comparison of magnetic circular dichroism of  $\text{Ni}^{\text{II}}(\text{1B})\text{Br}_2$  at 294 K.

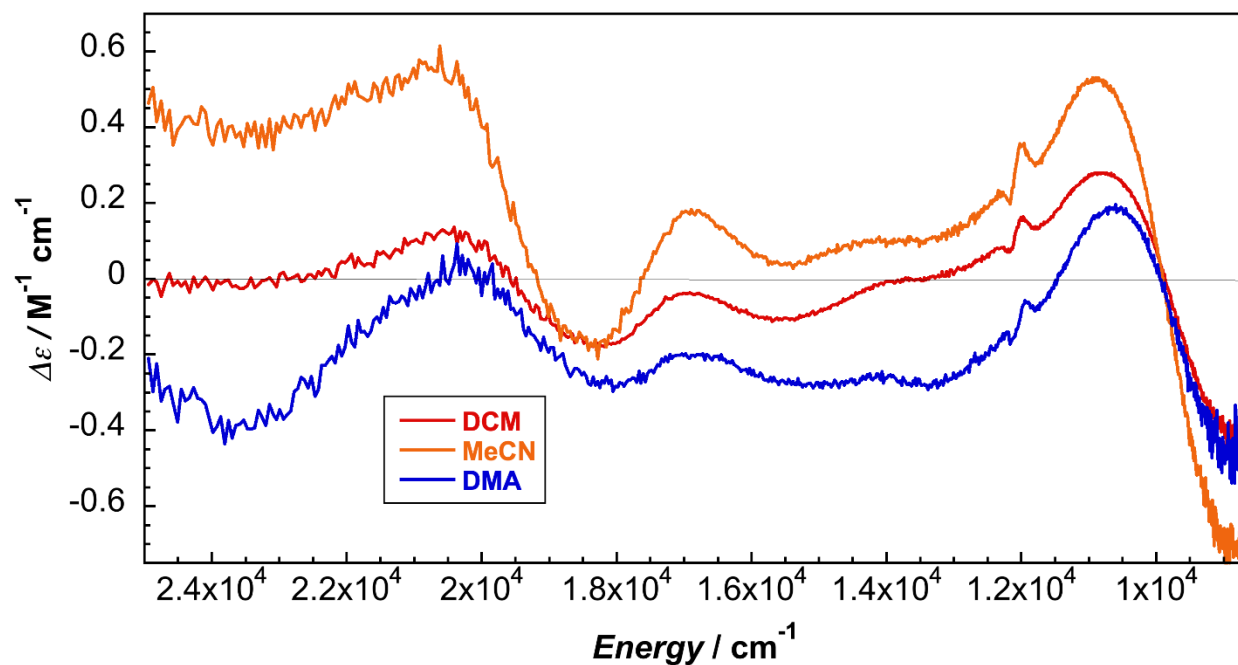


**Figure S46.** Solvent comparison of circular dichroism of  $\text{Ni}^{\text{II}}(\text{1B})\text{Cl}_2$  at 294 K.

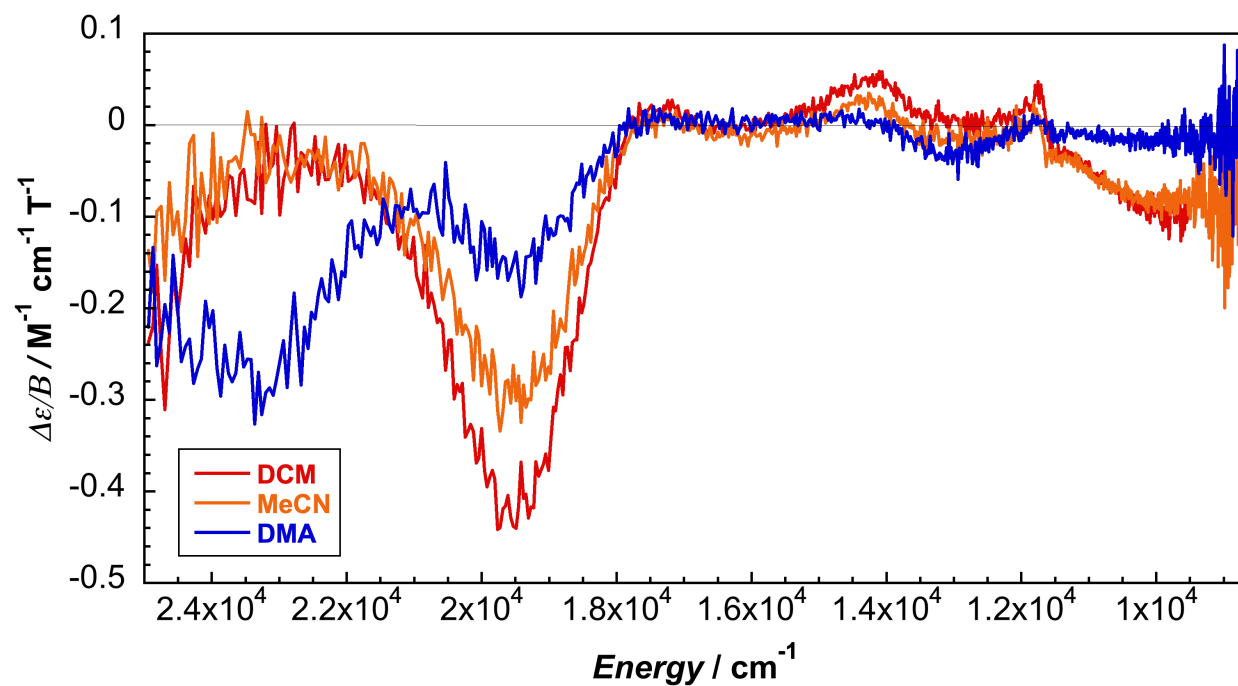


**Figure S47.** Solvent comparison of magnetic circular dichroism of  $\text{Ni}^{\text{II}}(\text{1B})\text{Cl}_2$  at 294 K.

## S5. Electrochemistry

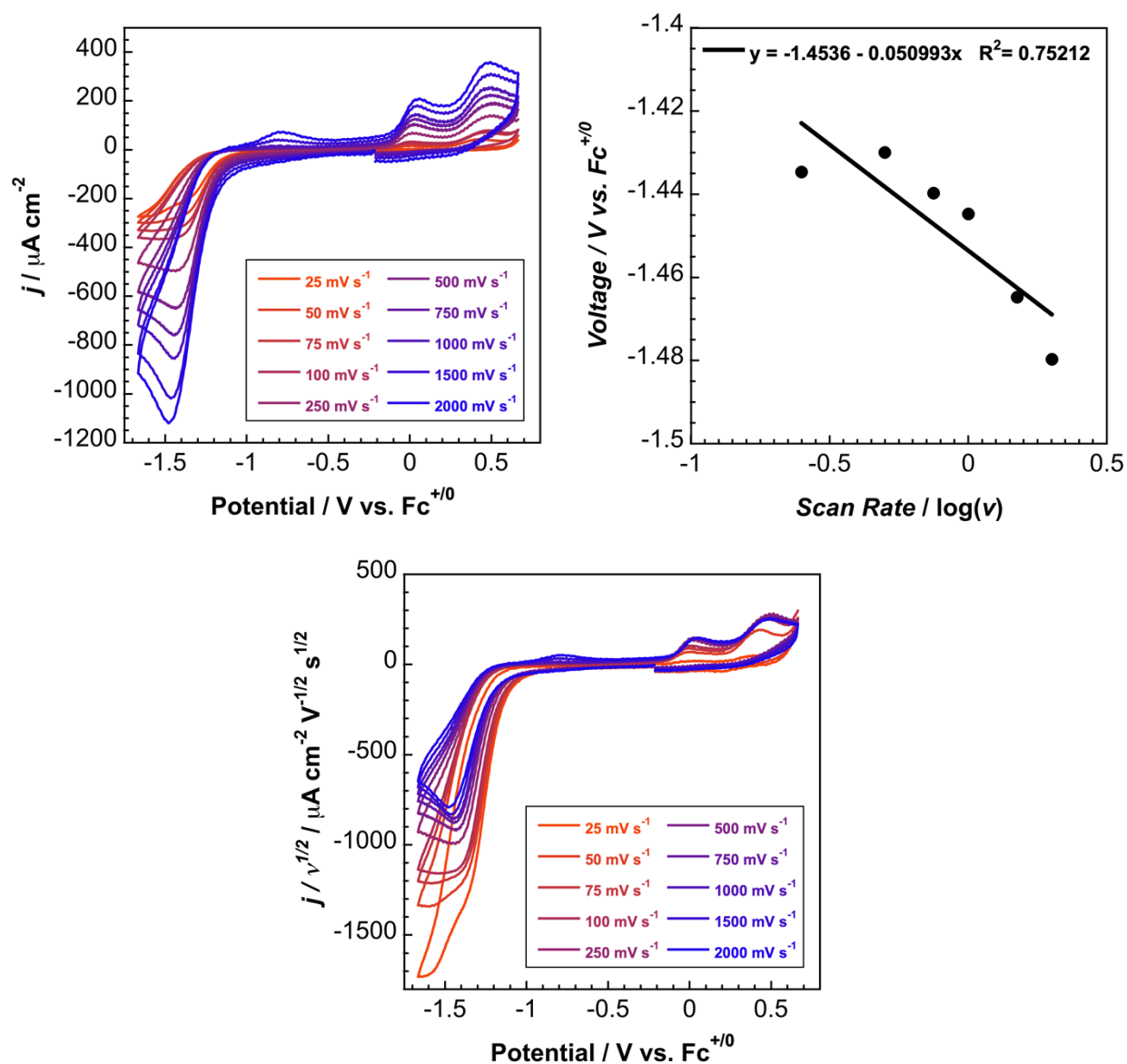


**Figure S48.** (Upper Left) Scan-rate dependence of reduction of  $1.64 \text{ mM Ni}^{\text{II}}(\text{IB})\text{Br}_2$  in  $0.1 \text{ M TBAPF}_6$  in DCM solution. (Upper Right) Peak reduction potential versus the logarithm of the scan rate ( $\text{V s}^{-1}$ ). (Lower) Scan rate normalized voltammetry of  $1.64 \text{ mM Ni}^{\text{II}}(\text{IB})\text{Br}_2$  in  $0.1 \text{ M TBAPF}_6$  in DCM solution.

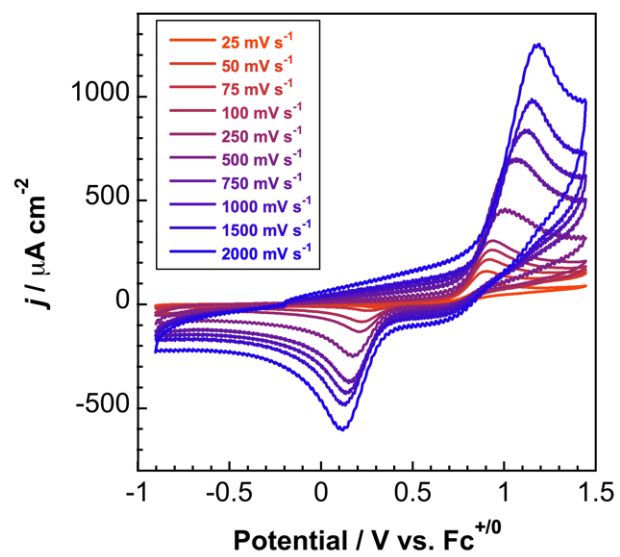


**Figure S49.** Scan-rate dependence of oxidation of  $1.0 \text{ mM Ni}^{\text{II}}(\text{1B})\text{Br}_2$  in DCM in  $0.1 \text{ M TBAPF}_6$  solution.

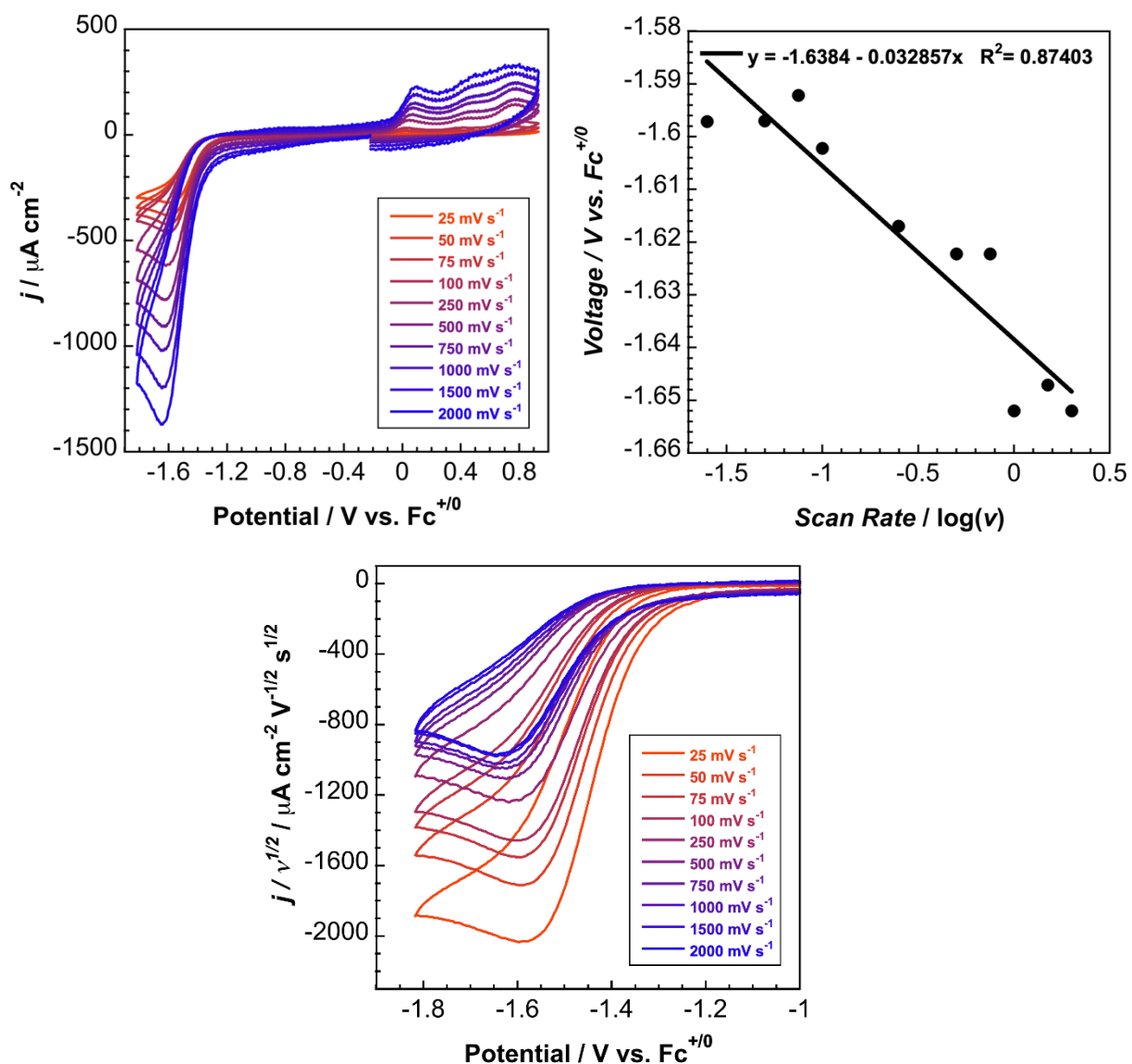


**Figure S50.** (Upper Left) Scan-rate dependence of reduction of 1.69 mM  $\text{Ni}^{\text{II}}(\text{IB})\text{Cl}_2$  in 0.1 M TBAPF<sub>6</sub> in DCM solution. (Upper Right) Peak reduction potential versus the logarithm of the scan rate ( $\text{V s}^{-1}$ ). (Lower) Scan rate normalized voltammetry of 1.69 mM  $\text{Ni}^{\text{II}}(\text{IB})\text{Cl}_2$  in 0.1 M TBAPF<sub>6</sub> in DCM solution.

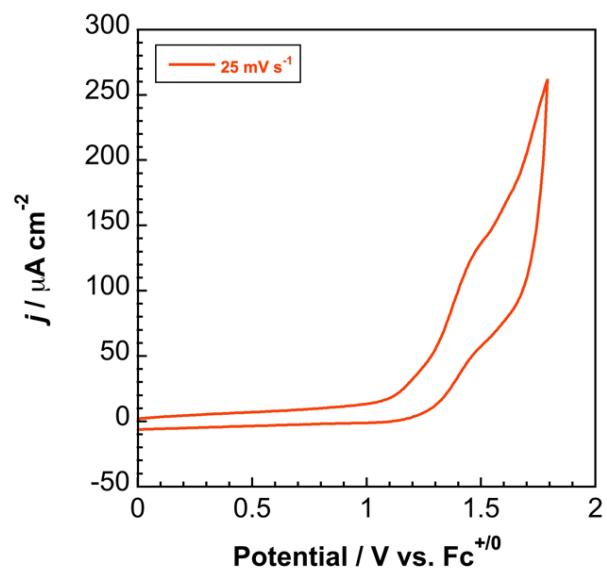


**Figure S51.**  $25 \text{ mV s}^{-1}$  scan of oxidation of  $1.21 \text{ mM Ni}^{\text{II}}(\text{IB})\text{Cl}_2$  in  $0.1 \text{ M TBAPF}_6$  in DCM solution.



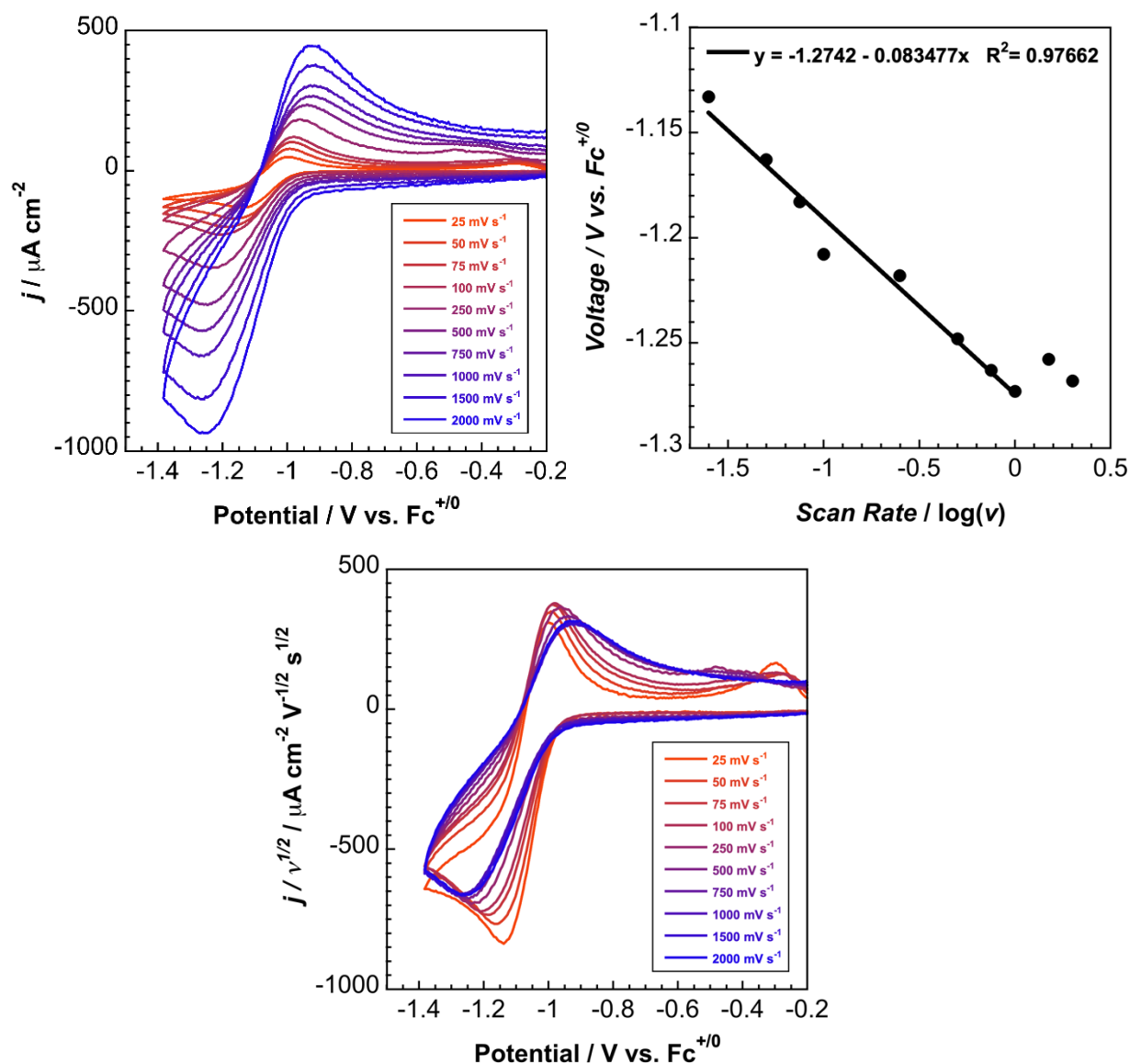


**Figure S52.** (Upper Left) Scan-rate dependence of reduction of  $1.46 \text{ mM Ni}^{\text{II}}(\text{IB})\text{Br}_2$  in  $0.1 \text{ M TBAPF}_6$  in MeCN solution. (Upper Right) Peak reduction potential versus the logarithm of the scan rate ( $\text{V s}^{-1}$ ). (Lower) Scan rate normalized voltammetry of  $1.46 \text{ mM Ni}^{\text{II}}(\text{IB})\text{Br}_2$  in  $0.1 \text{ M TBAPF}_6$  in MeCN solution.

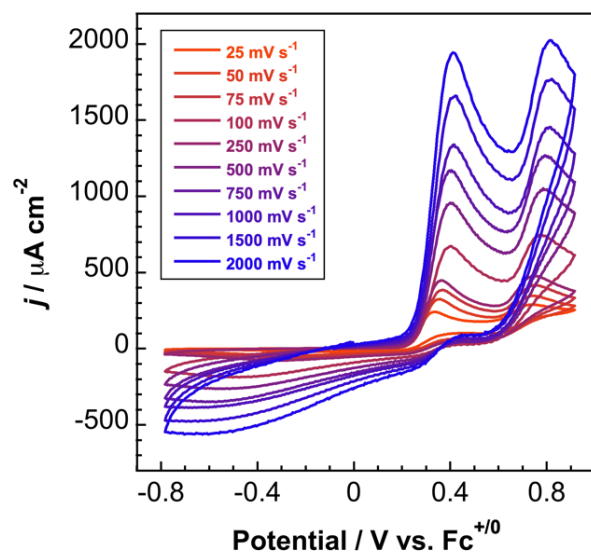


**Figure S53.** Scan-rate dependence of oxidation of 1.46 mM  $\text{Ni}^{\text{II}}(\text{IB})\text{Br}_2$  in 0.1 M  $\text{TBAPF}_6$  in  $\text{MeCN}$  solution.

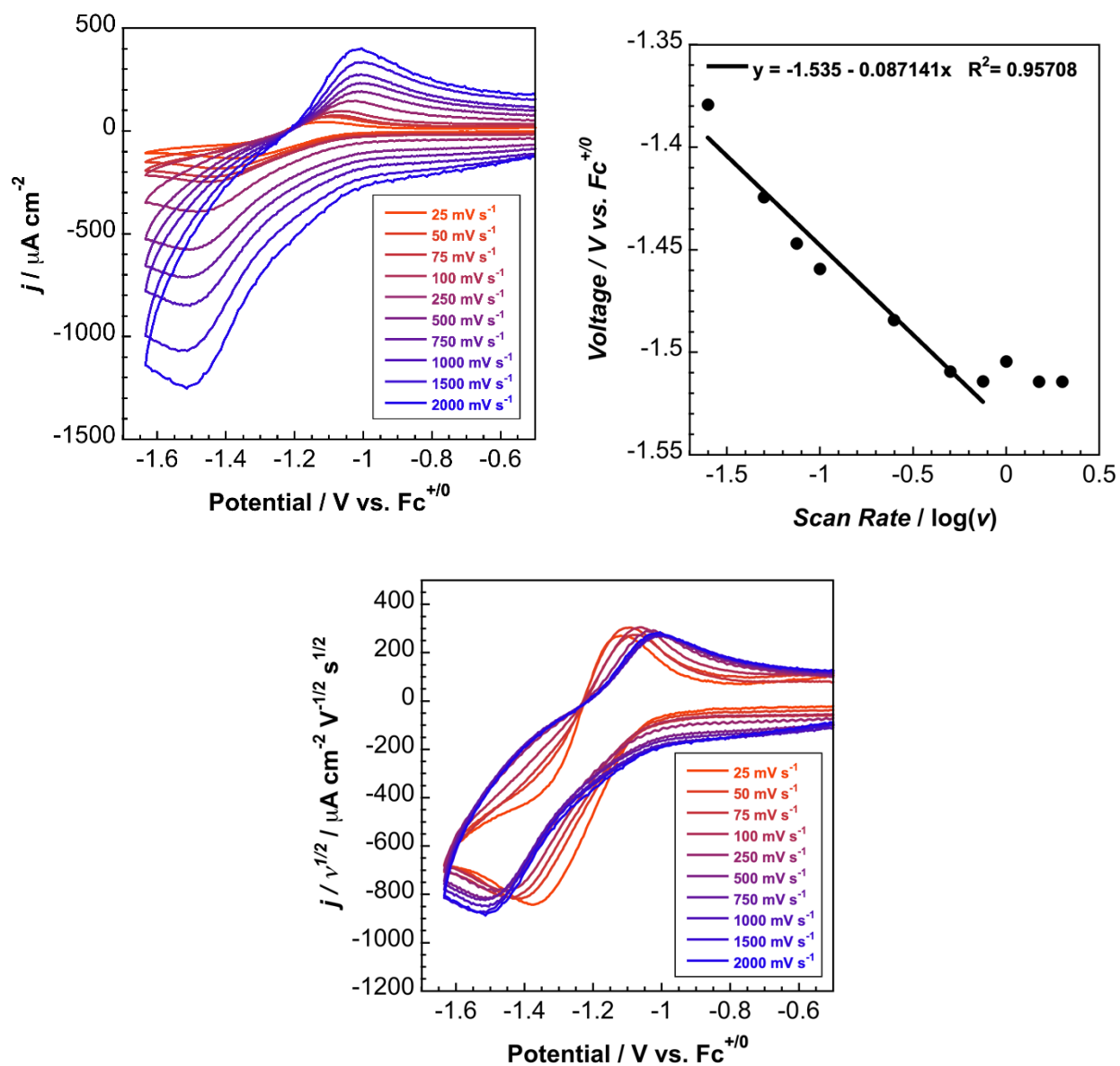


**Figure S54.** (Upper Left) Scan-rate dependence of reduction of 1.44 mM  $\text{Ni}^{\text{II}}(\text{IB})\text{Cl}_2$  in 0.1 M TBAPF<sub>6</sub> in MeCN solution. (Upper Right) Peak reduction potential versus the logarithm of the scan rate ( $\text{V s}^{-1}$ ). (Lower) Scan rate normalized voltammetry of 1.44 mM  $\text{Ni}^{\text{II}}(\text{IB})\text{Cl}_2$  in 0.1 M TBAPF<sub>6</sub> in MeCN solution.

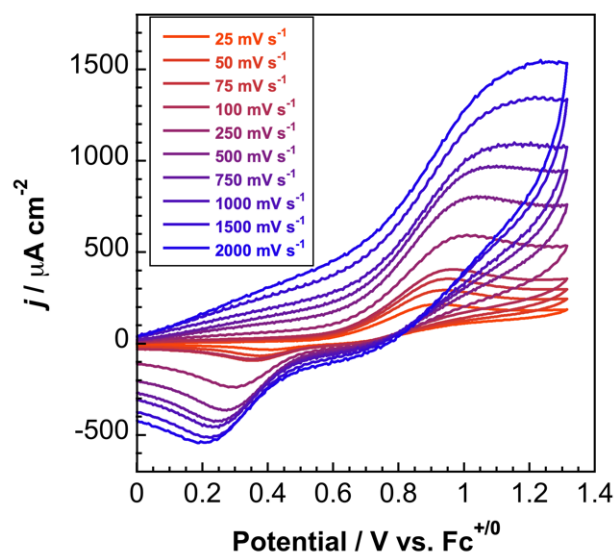


**Figure S55.** Scan-rate dependence of oxidation of  $1.44 \text{ mM Ni}^{\text{II}}(\text{1B})\text{Cl}_2$  in  $0.1 \text{ M TBAPF}_6$  in  $\text{MeCN}$  solution.

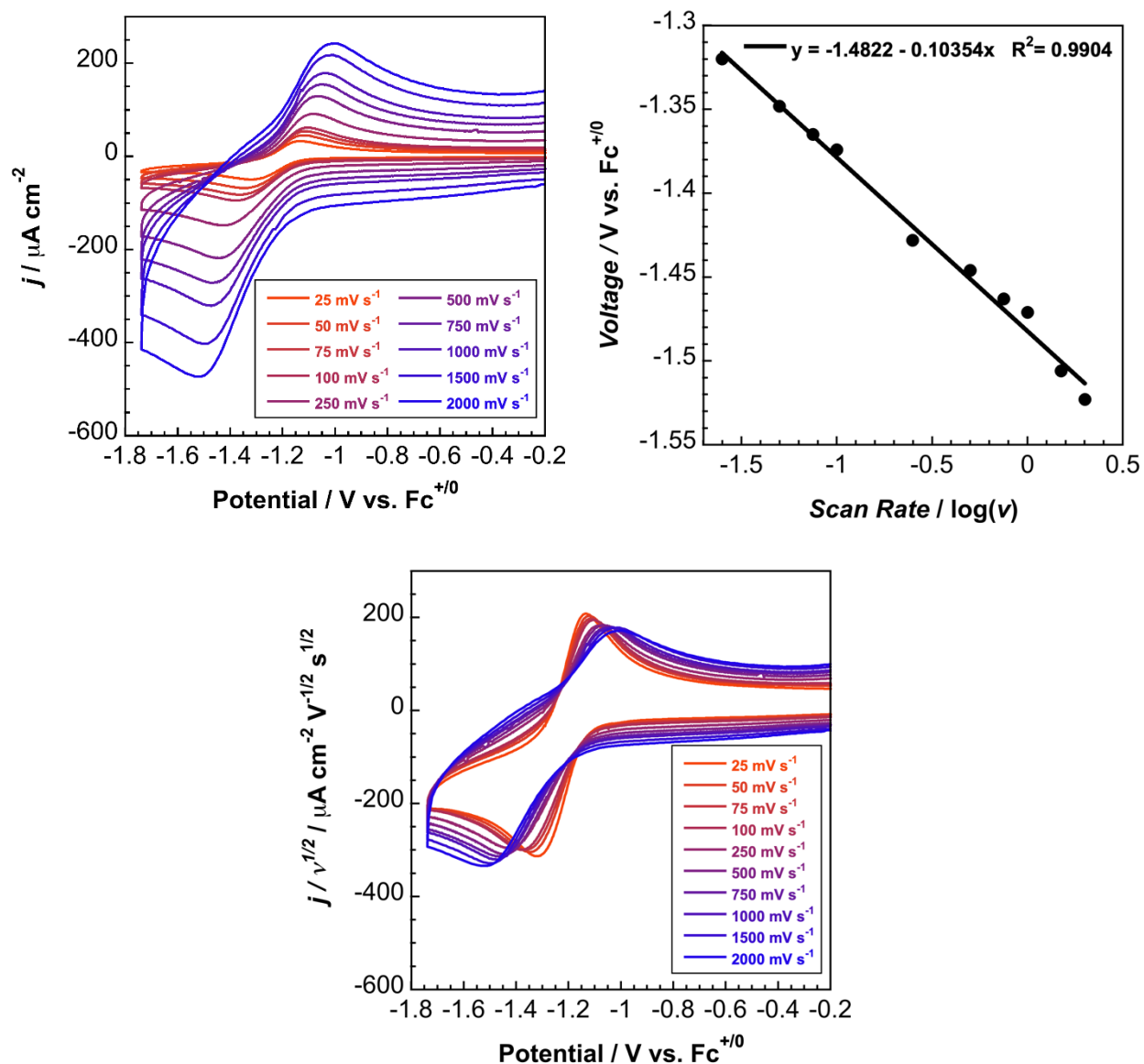


**Figure S56.** (Upper Left) Scan-rate dependence of reduction of 1.00 mM  $\text{Ni}^{\text{II}}(\text{1B})\text{Br}_2$  in 0.1 M TBAPF<sub>6</sub> in DMA solution. (Upper Right) Peak reduction potential versus the logarithm of the scan rate ( $\text{V s}^{-1}$ ). (Lower) Scan rate normalized voltammetry of 1.00 mM  $\text{Ni}^{\text{II}}(\text{1B})\text{Br}_2$  in 0.1 M TBAPF<sub>6</sub> in DMA solution.

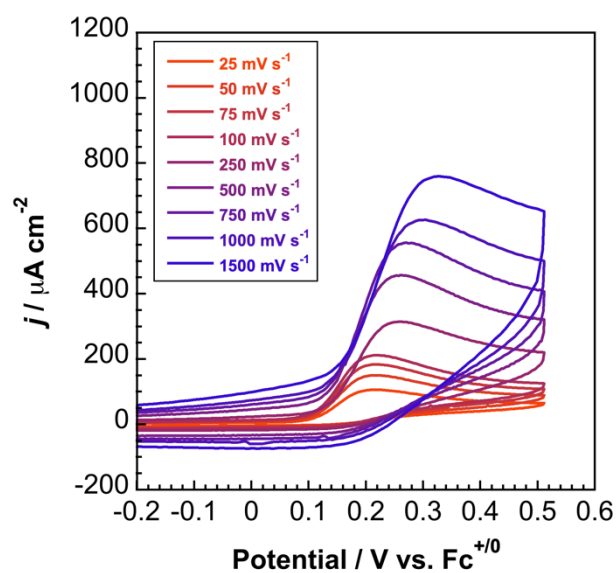


**Figure S57.** Scan-rate dependence of oxidation of 1.00 mM  $\text{Ni}^{\text{II}}(\text{IB})\text{Br}_2$  in 0.1 M  $\text{TBAPF}_6$  in DMA solution.

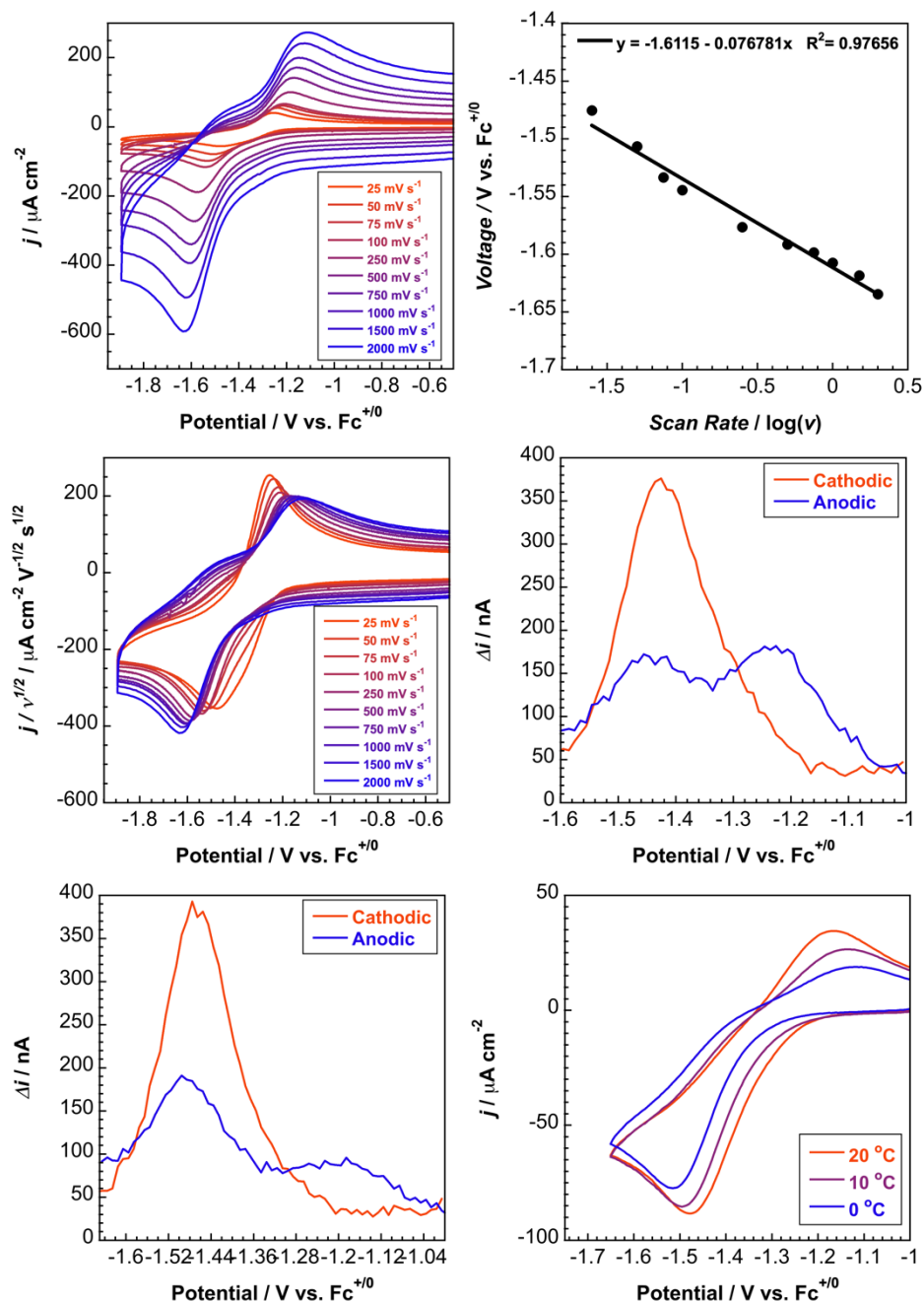


**Figure S58.** (Upper Left) Scan-rate dependence of reduction of 1.39 mM  $\text{Ni}^{\text{II}}(\text{IB})\text{Cl}_2$  in 0.1 M  $\text{TBAPF}_6$  in DMA solution. (Upper Right) Peak reduction potential versus the logarithm of the scan rate ( $\text{V s}^{-1}$ ). (Middle Left) Scan rate normalized voltammetry of 1.39 mM  $\text{Ni}^{\text{II}}(\text{IB})\text{Cl}_2$  in 0.1 M  $\text{TBAPF}_6$  in DCM solution. (Middle Right) Cathodic and return anodic differential pulse voltammetry of 1.79 mM  $\text{Ni}(\text{IB})\text{Cl}_2$  in 0.1 M  $\text{TBAPF}_6$  in DMA solution at 20 °C . (Bottom Left) Cathodic and return anodic differential pulse voltammetry of 1.79 mM  $\text{Ni}^{\text{II}}(\text{IB})\text{Cl}_2$  in 0.1 M  $\text{TBAPF}_6$  in DMA solution at 0 °C . (Bottom Right) Variable temperature voltammetry of the first reduction and re-oxidation of 1.79 mM  $\text{Ni}^{\text{II}}(\text{IB})\text{Cl}_2$  in 0.1 M  $\text{TBAPF}_6$  in DMA solution. Potentials shifted to the peak potential of  $\text{Ni}^{\text{II}}(\text{IB})\text{Cl}_2$  in DMA at 25  $\text{mV s}^{-1}$  from scan rate dependent voltammetry. DPV Parameters: 10 mV step size, 0.5 s sample period, 0.1 s pulse time, 5 mV pulse height.

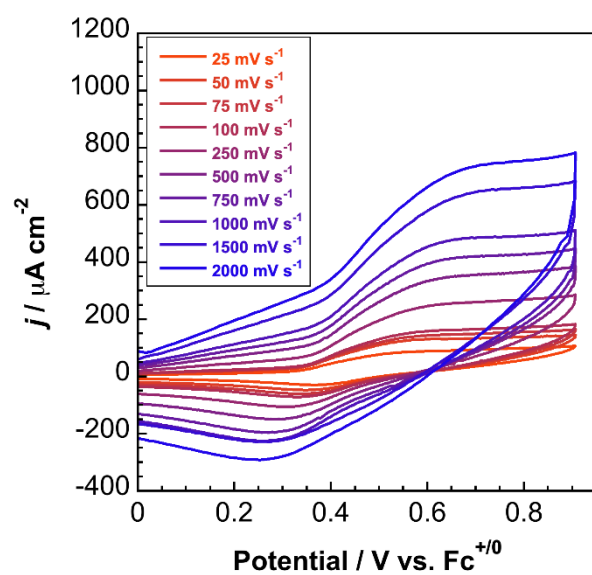


**Figure S59.** Scan-rate dependence of oxidation of 1.39 mM  $\text{Ni}^{\text{II}}(\text{IB})\text{Cl}_2$  in 0.1 M  $\text{TBAPF}_6$  in DMA solution.



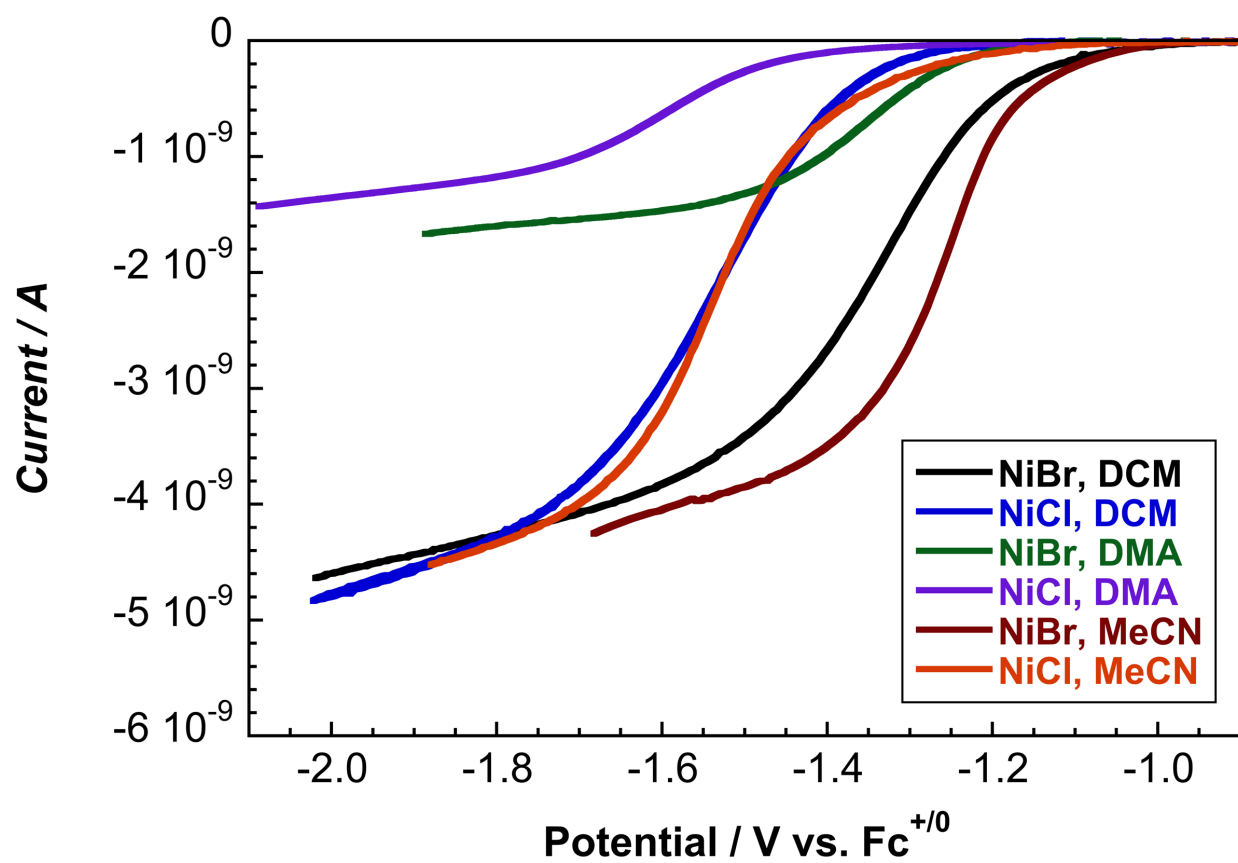


**Figure S60.** Summary overlay of microelectrode scans for determination of diffusion coefficients of  $\text{Ni}^{\text{II}}(\text{IB})\text{Br}_2$  and  $\text{Ni}^{\text{II}}(\text{IB})\text{Cl}_2$  in DCM, MeCN, and DMA solution.

**Table S1.** Return electrochemical parameters (upper, oxidation; lower, reduction) for  $\text{Ni}^{\text{II}}(\text{IB})\text{Cl}_2$  and  $\text{Ni}^{\text{II}}(\text{IB})\text{Br}_2$  and electrochemical parameters (oxidation) for tetrabutylammonium bromide (TBABr) in 0.1 M TBAPF<sub>6</sub> electrolyte solution using a glassy carbon working electrode, 0.01 M Ag<sup>+/0</sup> non-aqueous reference electrode, and platinum wire counter electrode. All peak and formal potentials are given in volts, obtained using a 1000 mV s<sup>-1</sup> scan rate (unless otherwise stated), and referenced to Fc<sup>+/0</sup>.

Complex	Solvent	$E_{p,an.,1}$	$E_{p,an.,2}$	$E_{p,an.,3}$	$E_{p,an.,4}$	$E_{an.,1}^{0'}$ <sup>a</sup>	$E_{an.,2}^{0'}$ <sup>a</sup>	$E_{an.,3}^{0'}$ <sup>a</sup>	$E_{an.,4}^{0'}$ <sup>a</sup>
$\text{Ni}^{\text{II}}(\text{IB})\text{Cl}_2$	DCM	-0.78 <sup>b</sup>	0.09	0.42 <sup>c</sup>	0.78	-0.95 <sup>b</sup>	0.00	0.33	0.63
$\text{Ni}^{\text{II}}(\text{IB})\text{Br}_2$	DCM	-0.79 <sup>b</sup>	0.04	---	0.48	-0.85 <sup>b</sup>	-0.02	---	0.38
$\text{Ni}^{\text{II}}(\text{IB})\text{Cl}_2$	MeCN	-1.01	-0.44 <sup>d</sup>	---	---	-1.10	-0.55	---	---
$\text{Ni}^{\text{II}}(\text{IB})\text{Br}_2$	MeCN	-0.92	---	---	---	-1.02	-0.36 <sup>c</sup>	---	---
$\text{Ni}^{\text{II}}(\text{IB})\text{Cl}_2$	DMA	-1.15	---	---	---	-1.24	---	---	---
$\text{Ni}^{\text{II}}(\text{IB})\text{Br}_2$	DMA	-1.03	---	---	---	-1.15	---	---	---
TBABr	DCM	---	---	0.24 <sup>c</sup>	0.56 <sup>c</sup>	---	---	0.18 <sup>c</sup>	0.48 <sup>c</sup>

<sup>a</sup>Taken from the inflection potential of the redox process at 1000 mV s<sup>-1</sup>, which approximates the formal potential. <sup>b</sup>Values at 2000 mV s<sup>-1</sup>. <sup>c</sup>Values at 100 mV s<sup>-1</sup>. <sup>d</sup>Values at 75 mV s<sup>-1</sup>.

Complex	Solvent	$E_{p,cat.,1}$	$E_{p,cat.,2}$	$E_{p,cat.,3}$	$E_{cat.,1}^{0'}$ <sup>a</sup>	$E_{cat.,2}^{0'}$ <sup>a</sup>	$E_{cat.,3}^{0'}$ <sup>a</sup>
$\text{Ni}^{\text{II}}(\text{IB})\text{Cl}_2$	DCM	---	---	---	---	1.38	---
$\text{Ni}^{\text{II}}(\text{IB})\text{Br}_2$	DCM	0.16	---	---	0.24	---	0.86
$\text{Ni}^{\text{II}}(\text{IB})\text{Cl}_2$	MeCN	0.24	---	---	0.36	0.86	---
$\text{Ni}^{\text{II}}(\text{IB})\text{Br}_2$	MeCN	-0.61	---	---	-0.45	0.35	0.72
$\text{Ni}^{\text{II}}(\text{IB})\text{Cl}_2$	DMA	0.27	---	---	0.41	---	---
$\text{Ni}^{\text{II}}(\text{IB})\text{Br}_2$	DMA	0.00	---	---	0.26	---	---
TBABr	DCM	-0.06 <sup>b</sup>	---	0.36 <sup>c</sup>	0.00	0.20	0.52 <sup>b</sup>

<sup>a</sup>Taken from the inflection potential of the redox process at 1000 mV s<sup>-1</sup>, which approximates the formal potential. <sup>b</sup>Values at 100 mV s<sup>-1</sup>.

**Table S2.** Electrochemical parameters for  $\text{Ni}^{\text{II}}(\text{IB})\text{Cl}_2$  and  $\text{Ni}^{\text{II}}(\text{IB})\text{Br}_2$  in 0.1 M TBAPF<sub>6</sub> electrolyte solution using a glassy carbon working electrode, 0.01 M Ag<sup>+/0</sup> non-aqueous reference electrode, and platinum wire counter electrode. All peak and formal potentials are given in volts, obtained using a 1000 mV s<sup>-1</sup> scan rate (unless otherwise stated), and referenced to Fc<sup>+/0</sup>.

Complex	Solvent	$E_{p,a,1}$	$E_{p,a,2}$	$E_{p,c}$	$E_{p/2,c}$	$E_c^{0'a}$	$E_a^{0'a}$	$D_0$ (cm <sup>2</sup> s <sup>-1</sup> ) <sup>b</sup>
$\text{Ni}^{\text{II}}(\text{IB})\text{Cl}_2$	DCM	1.51 <sup>d</sup>	---	-1.62	-1.49	-1.53	1.38	9.25 x 10 <sup>-6</sup>
$\text{Ni}^{\text{II}}(\text{IB})\text{Br}_2$	DCM	1.11	---	-1.45	-1.30	-1.32	1.00	9.25 x 10 <sup>-6</sup>
$\text{Ni}^{\text{II}}(\text{IB})\text{Cl}_2$	MeCN	1.10	---	-1.50	-1.34	-1.40	0.93	1.05 x 10 <sup>-5</sup>
$\text{Ni}^{\text{II}}(\text{IB})\text{Br}_2$	MeCN	0.42	0.82	-1.26	-1.10	-1.10	0.34/0.74	9.55 x 10 <sup>-6</sup>
$\text{Ni}^{\text{II}}(\text{IB})\text{Cl}_2$	DMA	0.75 <sup>d,e</sup>	---	-1.63	-1.52	-1.56	0.62	2.81 x 10 <sup>-6</sup>

<b>Ni<sup>II</sup>(IB)Br<sub>2</sub></b>	DMA	0.33 <sup>d,e</sup>	0.44 <sup>e</sup>	−1.45	−1.31	−1.34	0.24/0.39	3.06 x 10 <sup>−6</sup>
<b>Ni<sup>II</sup>(<sup>di</sup>Bn<sup>bi</sup>Ox)Br<sub>2</sub><sup>c</sup></b>	1,2-DFB	---	---	−1.90	−1.55	---	---	---
<b>Ni<sup>II</sup>(<sup>i</sup>Pr<sup>bi</sup>Ox)Br<sub>2</sub><sup>c</sup></b>	1,2-DFB	---	---	−1.64	−1.46	---	---	---
<b>Ni<sup>II</sup>(<sup>di</sup>Me<sup>bi</sup>Ox)(Dipp)Br<sup>c</sup></b>	THF	---	---	−2.39	−2.12	---	---	---

<sup>a</sup>From the inflection potential of the redox process at 1000 mV s<sup>−1</sup>, which approximates the formal potential. <sup>b</sup>Derived from mass transport-controlled current at a disk microelectrode. <sup>c</sup>See reference <sup>11</sup>. <sup>d</sup>Estimated from the local minimum of  $dj/dV$ . <sup>e</sup>Values at 75 mV s<sup>−1</sup>.  $E_{p/2,c}$  is the potential at half of the peak current.

In DCM, four re-oxidations are observed for **Ni<sup>II</sup>(IB)Cl<sub>2</sub>** and **Ni<sup>II</sup>(IB)Br<sub>2</sub>** after initial one-electron reduction. The first re-oxidation only appears at fast scan rates, indicative of a transient species that quickly decays on the CV time scale, and is tentatively assigned as the four-coordinate Ni<sup>I</sup> species that has not yet lost a halide. Experimental re-oxidation potentials for **Ni<sup>I/II</sup>(IB)Cl<sub>2</sub>** and **Ni<sup>I/II</sup>(IB)Br<sub>2</sub>** are −0.95 V and −0.85 V vs. Fc<sup>+0</sup>, respectively, indicating the former species is easier to oxidize, consistent with relative initial reduction potentials. The second re-oxidation (0.00 V (Cl) and −0.02 V (Br) vs. Fc<sup>+0</sup>) is assigned to the three-coordinate Ni<sup>I</sup> complexes (i.e., **Ni<sup>I/II</sup>(IB)X**) (**Figures S48 and S50**). The third and fourth re-oxidations are assigned to bromide/chloride re-oxidations that ultimately lead to the dihalide. Anodically, the complexes in DCM exhibit the most positive formal potentials, consistent with solvent-assisted oxidation that is likely coupled to a follow-up chemical reaction. The waveform and peak-to-peak separation are consistent with oxidation of bromide to tribromide, as evidenced by previous mechanistic studies on this complex reaction, specifically the observed return reduction at 0.24 V vs. Fc<sup>+0</sup>.

In DMA, the anodically shifted re-oxidation is likely associated with a one-electron reduced, halide-dissociated, solvent-associated species, as evidenced by the potentials for **Ni<sup>I</sup>(IB)Cl(DMA)** and **Ni<sup>I</sup>(IB)Br(DMA)** of −1.15 V and −1.14 V vs. Fc<sup>+0</sup>, respectively. This behavior is supported by the subtle shifts in anodic peak potential as a function of scan rate that are observed in **Figures S56 and S58**. Similarly, the potentials for **Ni<sup>I</sup>(IB)Cl(MeCN)** and **Ni<sup>I</sup>(IB)Br(MeCN)** are −1.10 V and −1.02 V vs. Fc<sup>+0</sup>. Behavior similar to re-oxidation in DMA is observed in **Figures S52 and S54**. Less return current at the more anodic wave suggests weaker binding of MeCN relative to DMA, consistent with the spectroscopic data.

Anodically, the normalized voltammetry in **Figure 6** indicates that oxidation in both solvents removes multiple electrons, which suggests formation of elemental bromine or bromine speciation. The return reduction in MeCN further supports this behavior. The oxidation of bromide

to bromine on a platinum electrode in MeCN occurs at 0.12, 0.72 V vs.  $\text{Fc}^{+/0}$ , while oxidations of  $\text{Ni}^{\text{II}}(\text{IB})\text{Br}_2$  occur at 0.34, 0.74 V vs.  $\text{Fc}^{+/0}$ .

To assess the effects of solvent donicity and dielectric constant on the electrochemical properties of  $\text{Ni}^{\text{II}}(\text{IB})\text{X}_2$  complexes, scan rate-dependent cyclic voltammetry data were acquired in DCM, MeCN, and DMA (**Figure 6** and **Figures S48-S59**). **Table 3** provides peak and formal potentials for initial redox events, while **Table S1** provides peak and formal potentials for unique re-oxidation and re-reduction events that result from chemical reactions following initial electron transfers.

To minimize unknown parameters for the analysis given below, real surface areas of a 3-mm diameter glassy carbon electrode and an 11- $\mu\text{m}$  diameter carbon fiber disk microelectrode were determined by measuring ferrocene ( $\text{Fc}$ ) voltammetry. To ensure consistent mass transport behavior, diffusion coefficients were measured for  $\text{Ni}^{\text{II}}(\text{IB})\text{X}_2$  complexes in the three solvents using the steady-state current for a disk microelectrode. This current can be used to determine the diffusion coefficients for both reversible and irreversible processes.<sup>12</sup> Since both complexes are neutral, the diffusion coefficients approximately follow the Stokes-Einstein equation, which inversely correlates the diffusion coefficient of a spherical particle and the viscosity of the solvating medium, as given by **Equation 2**:

$$D_0 = \frac{k_B T}{6\pi\eta r} \quad (2)$$

where  $D_0$  is the particle diffusion coefficient,  $k_B$  is Boltzmann's constant,  $T$  is temperature,  $\eta$  is the viscosity of the solvent, and  $r$  is the hydrodynamic radius of the diffusing particle. Slightly smaller diffusion coefficients are observed for both complexes in DCM ( $\eta = 0.40 \text{ mPa s}$ )<sup>13</sup> relative to MeCN ( $\eta = 0.34 \text{ mPa s}$ ),<sup>14</sup> consistent with small differences in solvent viscosity and comparable hydrodynamic radii for both complexes. Consistent results are also obtained for coefficients in DMA ( $\eta = 0.94 \text{ mPa s}$ ), which has a viscosity nearly three times that of MeCN.<sup>15</sup> With accurate  $D_0$  values, the voltammetry data can be normalized to provide a more meaningful comparison between solvent and scan rate-dependent effects (**Figure 6**).

Previous studies have provided formal potentials for both aromatic and non-aromatic  $\text{Ni}(\text{II})$  diimine systems, with many reports providing kinetic analyses with substrate present.<sup>16,17</sup> However,

to our knowledge, this is one of the first examples of detailed solvent-dependent electroanalytical chemistry for non-aromatic Ni(II) cross-coupling catalysts, with findings here rationalizing the parameters optimized through methodological studies. In general, precatalyst electrochemical responses are remarkably solvent dependent. In all three solvents, **Ni<sup>II</sup>(IB)Cl<sub>2</sub>** and **Ni<sup>II</sup>(IB)Br<sub>2</sub>** both exhibit single, electrochemically irreversible reduction events with significantly shifted oxidative waves (**Figures 6**, and **S50, S54, S58**). The general irreversibility required use of peak potentials ( $E_{p,a}$  or  $E_{p,c}$ ), potentials at half of the peak current value ( $E_{p/2}$ ), and inflection potentials (accurate estimate of formal potential,  $E^{0'}$ ) for analysis.<sup>12</sup> These data are analyzed with a caveat that the ferrocene (Fc) formal potential exhibits solvent dependence. However, Our measured Fc formal potentials in DMA and MeCN are 85 and 91 mV vs 0.01 M Ag<sup>+/0</sup>, respectively, indicating accurate conclusions can be drawn regarding solvent effects on measured formal potentials of the Ni complexes in these solvents. In DCM, the measured Fc formal potential is 215 mV. Therefore, measured formal potentials in DCM will appear negatively shifted relative to values in DMA and MeCN.

Based on shifts in peak potential as a function of scan rate and scan rate normalized voltammetry (current function) in all three solvents (**Figures S48-S58**), as well as differential pulse voltammetry and variable temperature voltammetry in DMA for **Ni<sup>II</sup>(IB)Cl<sub>2</sub>** (**Figure S58**), we can draw some insightful conclusions regarding the reduction mechanism, as the current function and shift in peak potential are dictated by the particular chemical and electrochemical mechanism. These conclusions also apply to **Ni<sup>II</sup>(IB)Cl<sub>2</sub>**. We ascribe the reduction of both complexes to a concerted  $E_qC_i$  (in DMA and MeCN, solvent coordination and/or halide loss occur in concert) or step-wise  $E_iC_i$  mechanism (DCM), where slow electron transfer is followed by rapid halide loss. In DCM, three-coordinate **Ni<sup>I</sup>(IB)X** will be generated upon reduction, with no subsequent solvent coordination. The lack of return current, shift in peak potential as a function of the logarithm of the scan rate near 29.6 mV, with ~33 mV observed here, and decrease in the current function toward a limiting value as the scan rate is increased supports a kinetically-controlled, stepwise reduction followed by rapid halide loss (**Figures S48 and S50**). Activation of DCM by other nickel complexes supported by naphthyridine-diimine ligands has been observed previously.<sup>18</sup> However, spectroelectrochemical data obtained in DCM do not support reactivity of the **Ni<sup>I</sup>(IB)X** with solvent (**Figures S73 - S75**). Overall, this analysis featuring electron transfer coupled to rapid halide loss is consistent with halide dissociation observed previously using extended X-ray

absorption fine structure (EXAFS) for a low-spin  $\text{Ni}^{\text{II}}$  biOx aryl halide complex upon chemical reduction with potassium graphite.<sup>17</sup>

Experimental formal potentials for chemically-coupled reduction of  $\text{Ni}^{\text{II}}(\text{IB})\text{Cl}_2$  and  $\text{Ni}^{\text{II}}(\text{IB})\text{Br}_2$  to  $\text{Ni}^{\text{I}}(\text{IB})\text{Cl}$  and  $\text{Ni}^{\text{I}}(\text{IB})\text{Br}$  in DCM are  $-1.47$  V and  $-1.26$  V vs.  $\text{Fc}^{+/0}$ , respectively (**Table 3**). It is therefore  $\sim 0.21$  V ( $\sim 1695$   $\text{cm}^{-1}$ ) harder to reduce  $\text{Ni}^{\text{II}}(\text{IB})\text{Cl}_2$  relative to  $\text{Ni}^{\text{II}}(\text{IB})\text{Br}_2$ . This observation is consistent with the energetic shifts in the spin-allowed ligand field bands in DCM in experiment (Main text, **Section 2.1**) and calculations (**Section 3.1** and **3.2**). In MeCN and DMA,  $\text{Ni}^{\text{II}}(\text{IB})\text{Cl}_2$  (**Figures S54** and **S58**) and  $\text{Ni}^{\text{II}}(\text{IB})\text{Br}_2$  (**Figure 6**, left) both exhibit superficially quasi-reversible voltammetry for the reduction. Experimental formal potentials for chemically-coupled reduction in MeCN/DMA of  $\text{Ni}^{\text{II}}(\text{IB})\text{Cl}_2$  and  $\text{Ni}^{\text{II}}(\text{IB})\text{Br}_2$  are  $-1.32/-1.47$  V and  $-1.05/-1.23$  V vs.  $\text{Fc}^{+/0}$ , respectively ( $\Delta = \sim 0.27/\sim 0.24$  V ( $\sim 2180/1935$   $\text{cm}^{-1}$ )). Thus, for all solvents used here, it is harder to reduce  $\text{Ni}^{\text{II}}(\text{IB})\text{Cl}_2$  relative to  $\text{Ni}^{\text{II}}(\text{IB})\text{Br}_2$ .

Based on the VT UV-vis-NIR data in DMA (**Section 2.4**), both the  $\text{Ni}^{\text{II}}$  four-coordinate and five-coordinate solvent adducts exist in equilibrium, and this can potentially influence the electrochemistry measured in this solvent. One possibility for the reduction mechanism for these species is reduction followed by halide loss and, for the four-coordinate portion of the complex, coordination of DMA to the  $\text{Ni}^{\text{I}}$  center, which could occur in a concerted or stepwise fashion. For a concerted mechanism, the anticipated shift in peak potential as a function of  $\log(\nu)$  is  $29.6/\alpha$  mV, where  $\alpha$  is the transfer coefficient for electron transfer.<sup>12</sup> Based on the observation of only one differential pulsed voltammetry wave on the forward scan and the shift in peak potential with  $\log(\nu)$  ( $\sim 77$ - $104$  mV), we propose that the reduction and chemical follow up reaction in both MeCN and DMA (i.e., solvent coordination at  $\text{Ni}^{\text{I}}$ ) is a concerted process. The two return waves observed scanning oxidatively suggest generation of a halide-dissociated species that is re-oxidized at more positive potentials. This conclusion is supported by VT differential pulse voltammetry (**Figure S58**), where the differential current at the more positive wave decreases as temperature is decreased, while the differential current at the wave ascribed to re-oxidation of five-coordinate  $\text{Ni}^{\text{I}}$  increases. Based on behavior previously observed for these systems and our computed formal potentials,<sup>17</sup> the more positive re-oxidation could arise from re-oxidation of a  $\text{Ni}^{\text{I}}/\text{Ni}^{\text{I}}$  dimer that forms after the initial reduction. However, we favor the interpretation featuring re-oxidation of the halide-dissociated species based on computed formal potentials (**Table 5**) and lack of return oxidation near the reduction event in DCM, where  $\text{Ni}^{\text{I}}$  is anticipated to dimerize rapidly. Further

supporting our hypothesis, an additional wave near where three-coordinate  $\text{Ni}^{\text{I}}$  is predicted to oxidize is present in MeCN, but not in DMA (**Figures S52 and S54**), supporting the weaker coordination affinity of MeCN and our assignment of the species generated upon reduction.

Potentials for chemically-coupled reductions in DMA are more cathodic relative to MeCN by  $\sim 200$  mV for both complexes. As discussed in **Section 3.3** of the main text, this difference is ascribed to DMA being a higher donicity solvent and coordinating to the  $\text{Ni}^{\text{II}}$  center. Note that solvent coordination is not observed in DCM and only weakly so in MeCN. Indeed, DFT calculations suggest the chemically-coupled reductions of DMA-coordinated  $\text{Ni}^{\text{II}}(\text{IB})\text{Cl}_2$  and  $\text{Ni}^{\text{II}}(\text{IB})\text{Br}_2$  are  $\sim 0.17$  V and  $\sim 0.05$  V more negative. It is further interesting to note that the reduction potential for  $\text{Ni}^{\text{II}}(\text{IB})\text{Cl}_2$  in both DCM and DMA is  $-1.47$  V vs.  $\text{Fc}^{+/0}$ , respectively; for  $\text{Ni}^{\text{II}}(\text{IB})\text{Br}_2$ , these are  $-1.26$  V and  $-1.23$  V vs.  $\text{Fc}^{+/0}$ , respectively. The similarity in reduction potentials in DCM and DMA is ascribed to the relative Fc formal potentials in DCM vs. DMA and the role of solvent in facilitating the Ni–X bond rupture upon one-electron reduction, with the anionic halide loss more facile in DMA relative to DCM. Because of these considerations and the electronic structure calculations presented in **Section 3.3**, the more quantitative comparison of potentials for the reduction with and without coordinated solvent is that between MeCN and DMA. Furthermore, the temperature-dependent cyclic voltammetry demonstrates a cathodically shifted reduction potential as the temperature is lowered, which may be due to increasing the relative amount of five-coordinate species. Thus, overall, solvent coordination results in a harder to reduce  $\text{Ni}^{\text{II}}$  center. By extension, this can be further translated to a more reducing  $\text{Ni}^{\text{I}}$  species, which, under catalytic conditions, can facilitate oxidative addition (see **Discussion** in the main text).<sup>19</sup>

Ligand field and bonding effects on  $\text{Ni}^{\text{II}}$ -based redox potentials can be further elucidated using electronic structure calculations (**Section 3.3**) and through correlations to electronic spectroscopy, as transitions to the RAMO are also observed experimentally. Differences in measured redox potentials correlate directly with specific structural influences on the energy of the RAMO.

Finally, based on the measured formal potentials, proposed electrochemical mechanisms, and additional electronic structure calculations of redox potentials (**Section 3.3**), we do not believe  $\text{Ni}^0(\text{IB})\text{X}_2$  (or  $\text{Ni}^0$  in any form) is thermodynamically accessible in the electrochemical window of common electrochemistry solvents, which supports a  $\text{Ni}^{\text{I/III}}$  catalytic cycle for reductive alkenylation and potentially related reactions involving bis(oxazoline)–Ni complexes.<sup>17</sup> No

additional reduction beyond  $\text{Ni}^{\text{I}}$  is required for oxidative addition of substrates for which this catalyst has been previously demonstrated to be competent.



## S6. Spectroelectrochemistry

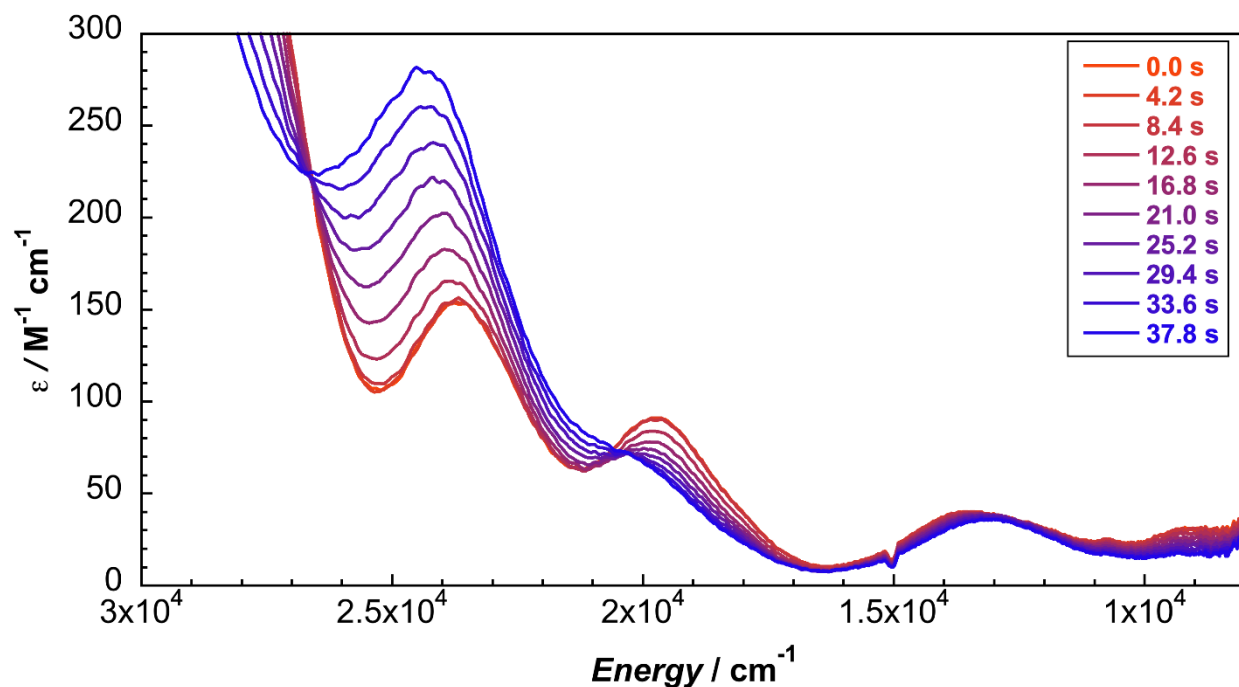


**Figure S61.** UV-vis-NIR spectral changes during the first 40 s of controlled potential electrolysis at 0.24 V vs.  $\text{Fc}^{+/0}$  of  $\text{Ni}^{\text{II}}(\text{IB})\text{Br}_2$  in 0.1 M TBAPF<sub>6</sub> in DMA solution.

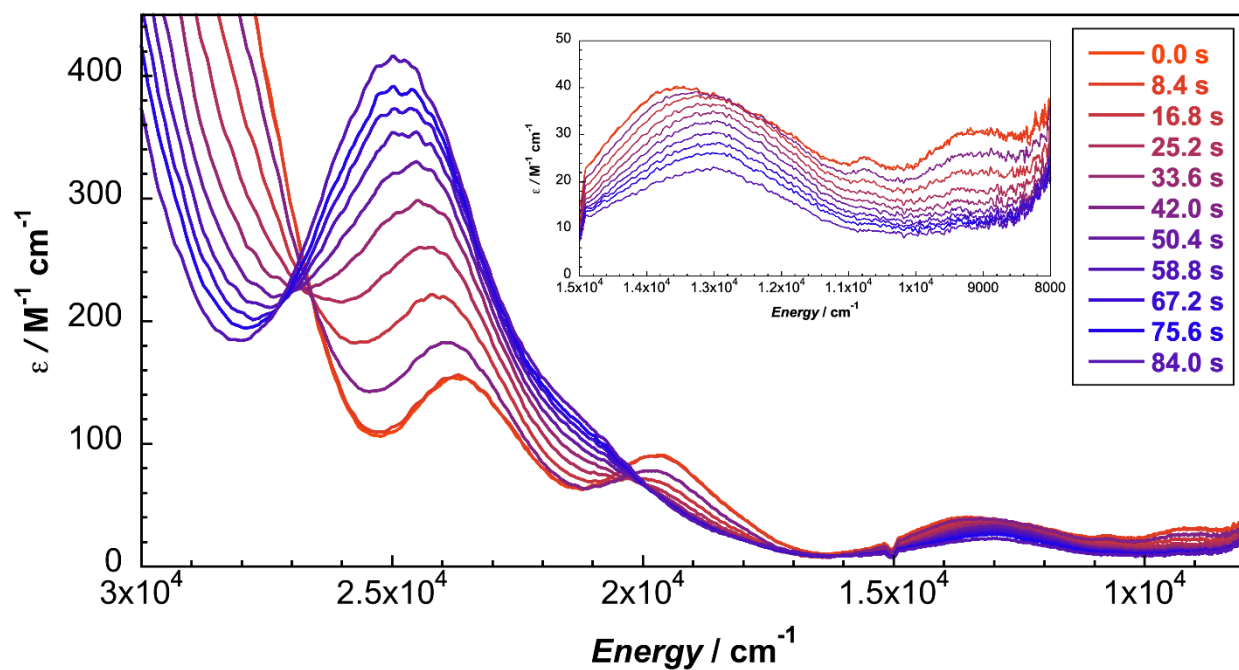


**Figure S62.** UV-vis-NIR spectral changes during the first 80 s of controlled potential electrolysis at 0.24 V vs.  $\text{Fc}^{+/0}$  of  $\text{Ni}^{\text{II}}(\text{IB})\text{Br}_2$  in 0.1 M TBAPF<sub>6</sub> in DMA solution.

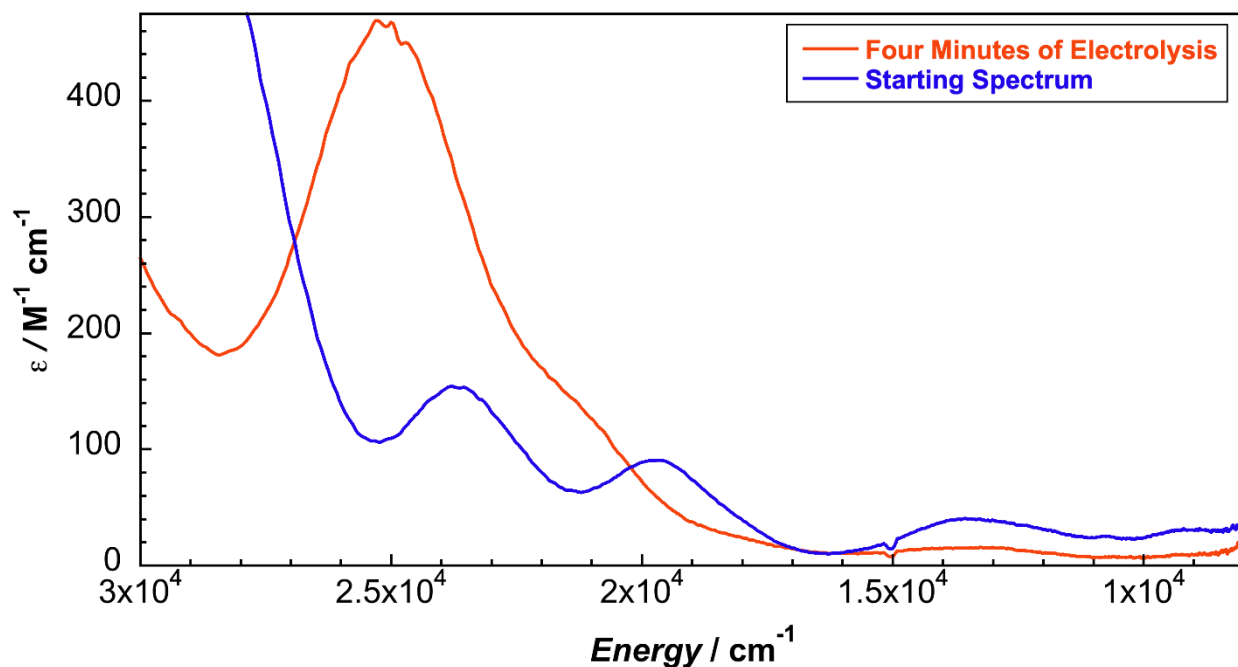


**Figure S63.** Starting and ending UV-vis-NIR spectra for four minutes of controlled potential electrolysis at 0.24 V vs.  $\text{Fc}^{+/0}$  of  $\text{Ni}^{\text{II}}(\text{1B})\text{Br}_2$  in 0.1 M TBAPF<sub>6</sub> in DMA solution.

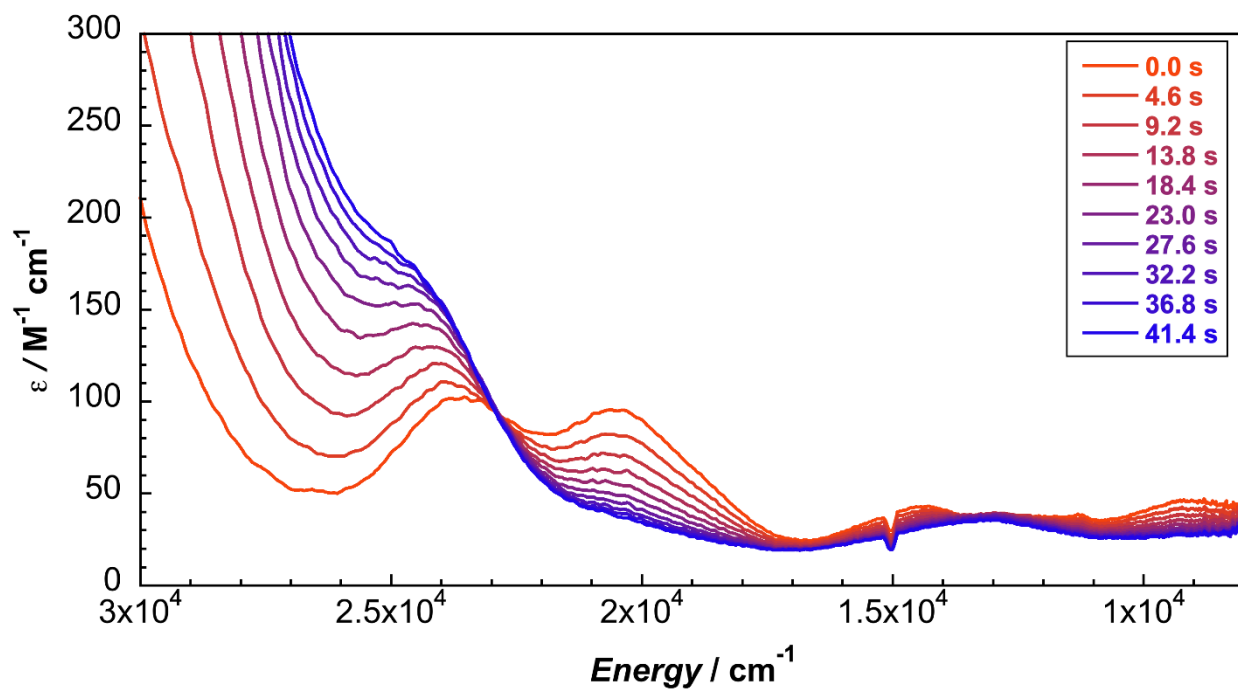


**Figure S64.** UV-vis-NIR spectral changes during the first 40 s of controlled potential electrolysis at 0.70 V vs.  $\text{Fc}^{+/0}$  of  $\text{Ni}^{\text{II}}(\text{1B})\text{Cl}_2$  in 0.1 M TBAPF<sub>6</sub> in DMA solution.

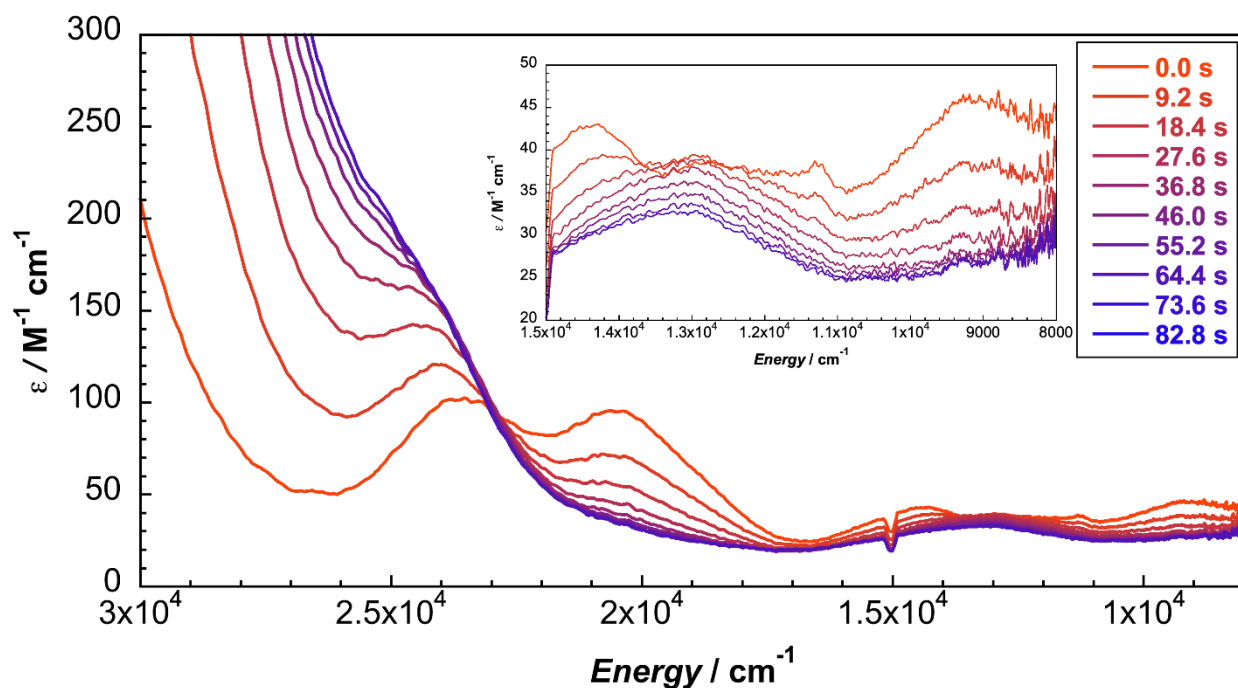


**Figure S65.** UV-vis-NIR spectral changes during the first 80 s of controlled potential electrolysis at 0.70 V vs.  $\text{Fc}^{+/0}$  of  $\text{Ni}^{\text{II}}(\text{IB})\text{Cl}_2$  in 0.1 M TBAPF<sub>6</sub> in DMA solution.

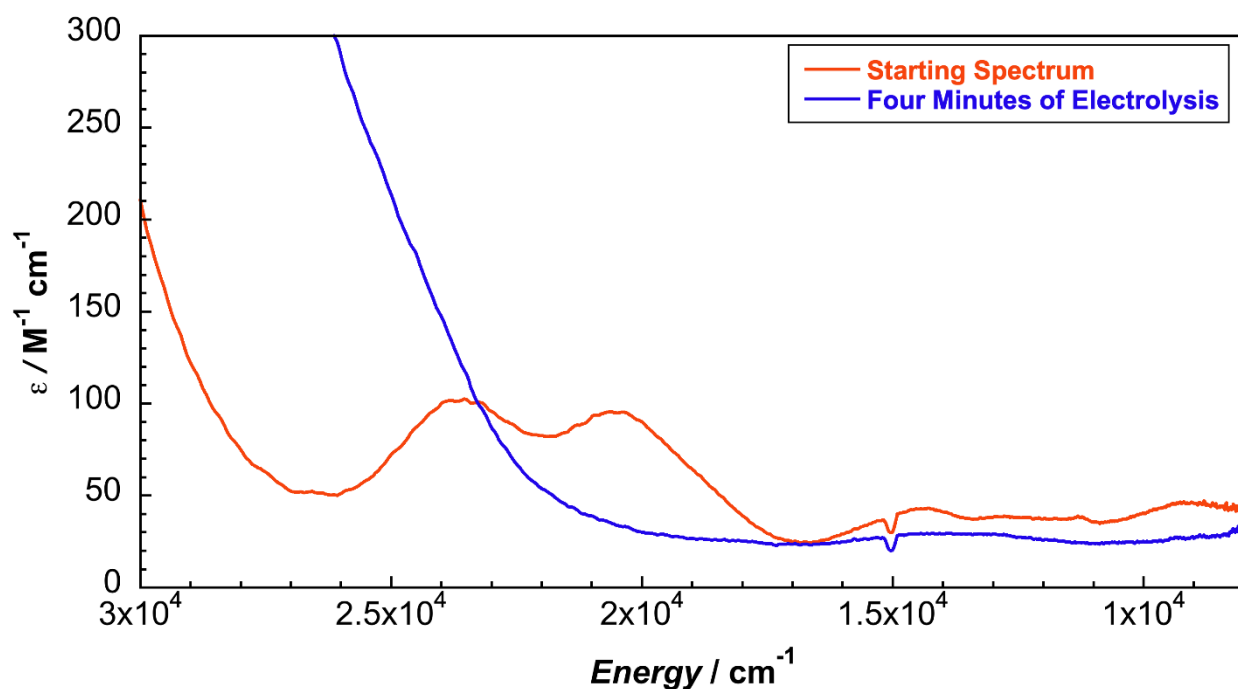


**Figure S66.** Starting and ending UV-vis-NIR spectra for four minutes of controlled potential electrolysis at 0.70 V vs.  $\text{Fc}^{+/0}$  of  $\text{Ni}^{\text{II}}(\text{IB})\text{Cl}_2$  in 0.1 M TBAPF<sub>6</sub> in DMA solution.

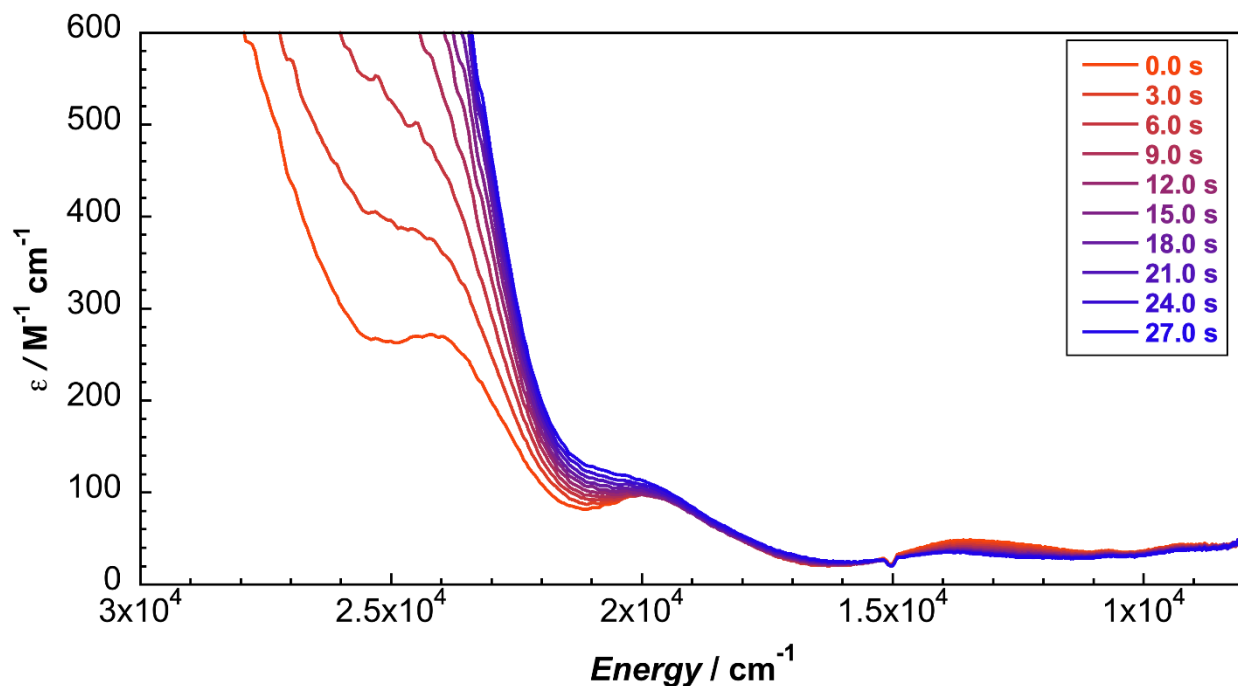


**Figure S67.** UV-vis-NIR spectral changes during the first 30 s of controlled potential electrolysis at  $-1.60 \text{ V}$  vs.  $\text{Fc}^{+/0}$  of  $\text{Ni}^{\text{II}}(\text{IB})\text{Br}_2$  in  $0.1 \text{ M}$  TBAPF<sub>6</sub> in DMA solution.

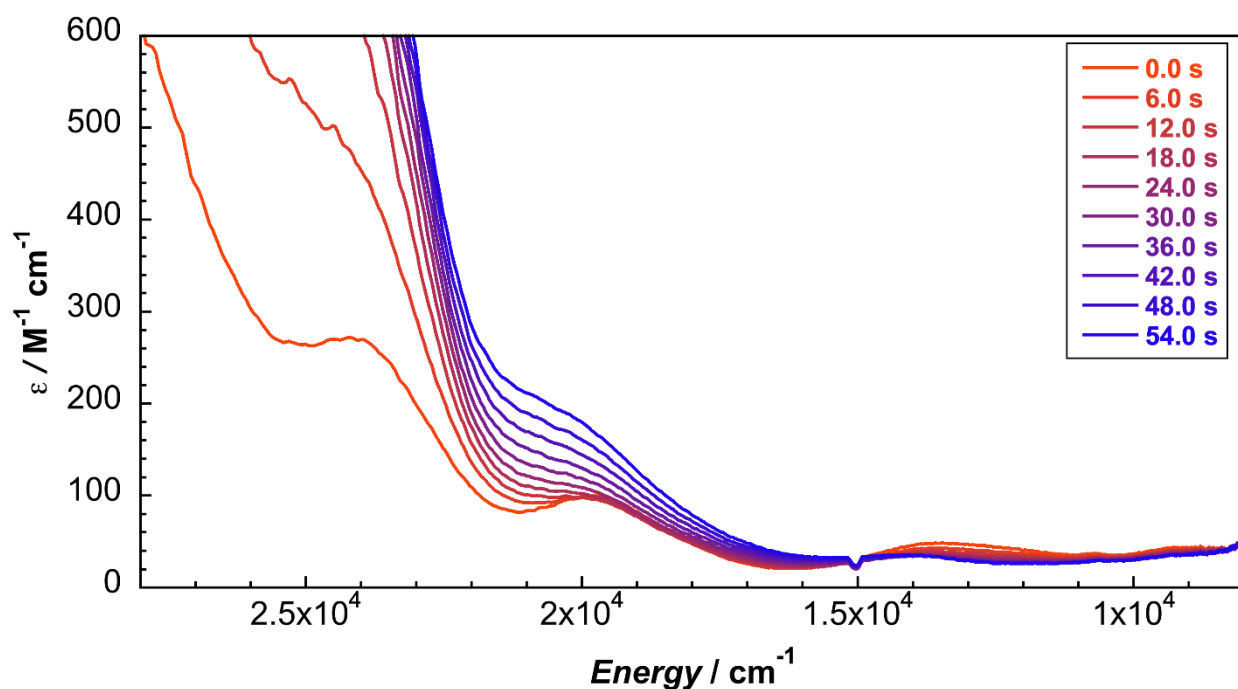


**Figure S68.** UV-vis-NIR spectral changes during the first 55 s of controlled potential electrolysis at  $-1.60 \text{ V}$  vs.  $\text{Fc}^{+/0}$  of  $\text{Ni}^{\text{II}}(\text{IB})\text{Br}_2$  in  $0.1 \text{ M}$  TBAPF<sub>6</sub> in DMA solution.

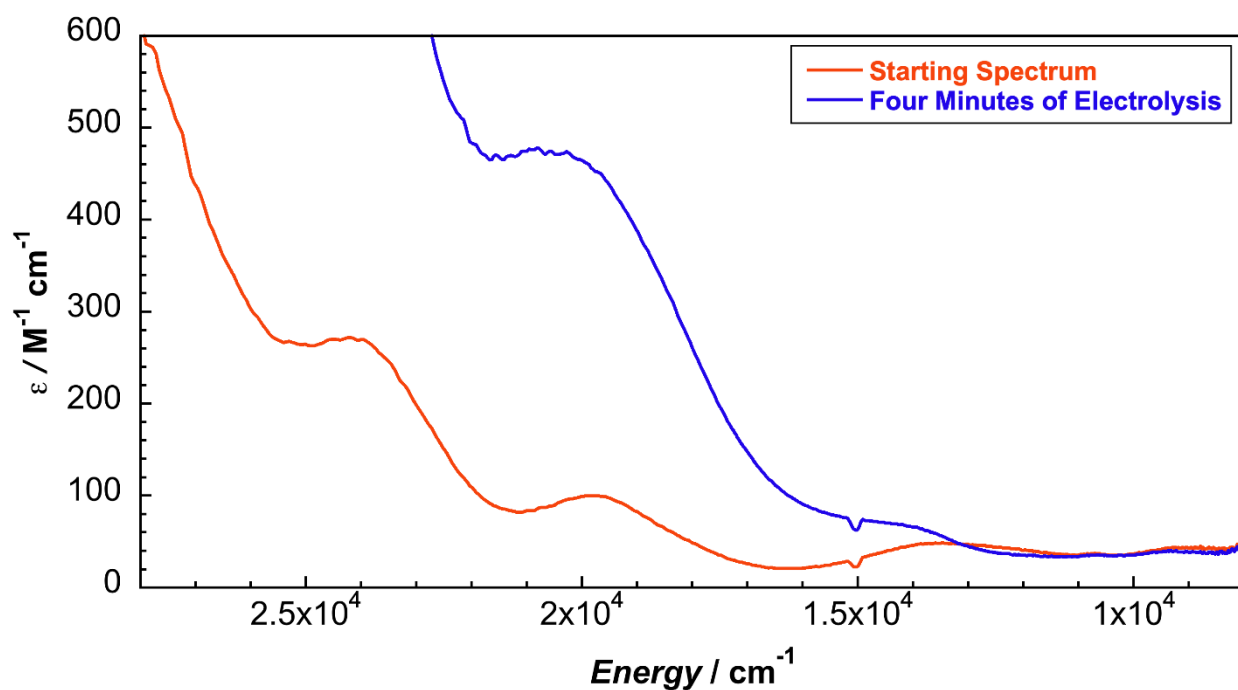


**Figure S69.** Starting and ending UV-vis-NIR spectra for four minutes of controlled potential electrolysis at  $-1.60$  V vs.  $\text{Fc}^{+/0}$  of  $\text{Ni}^{\text{II}}(\text{IB})\text{Br}_2$  in  $0.1$  M  $\text{TBAPF}_6$  in DMA solution.

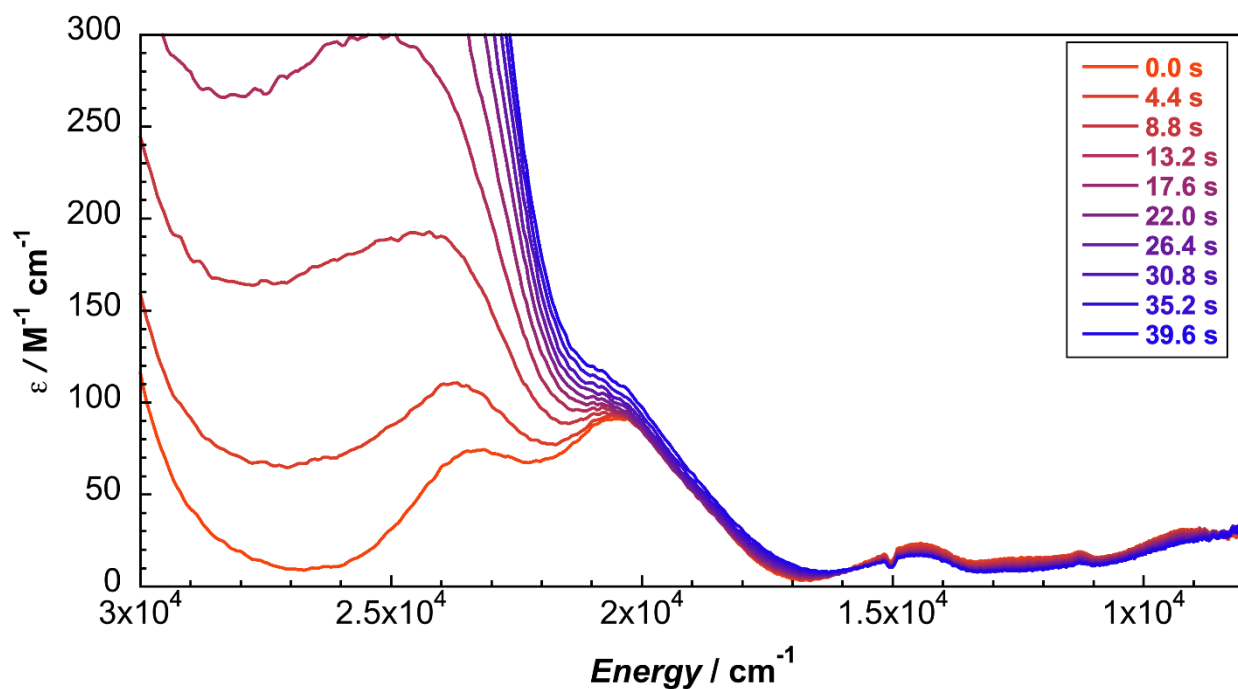


**Figure S70.** UV-vis-NIR spectral changes during the first  $40$  s of controlled potential electrolysis at  $-1.80$  V vs.  $\text{Fc}^{+/0}$  of  $\text{Ni}^{\text{II}}(\text{IB})\text{Cl}_2$  in  $0.1$  M  $\text{TBAPF}_6$  in DMA solution.

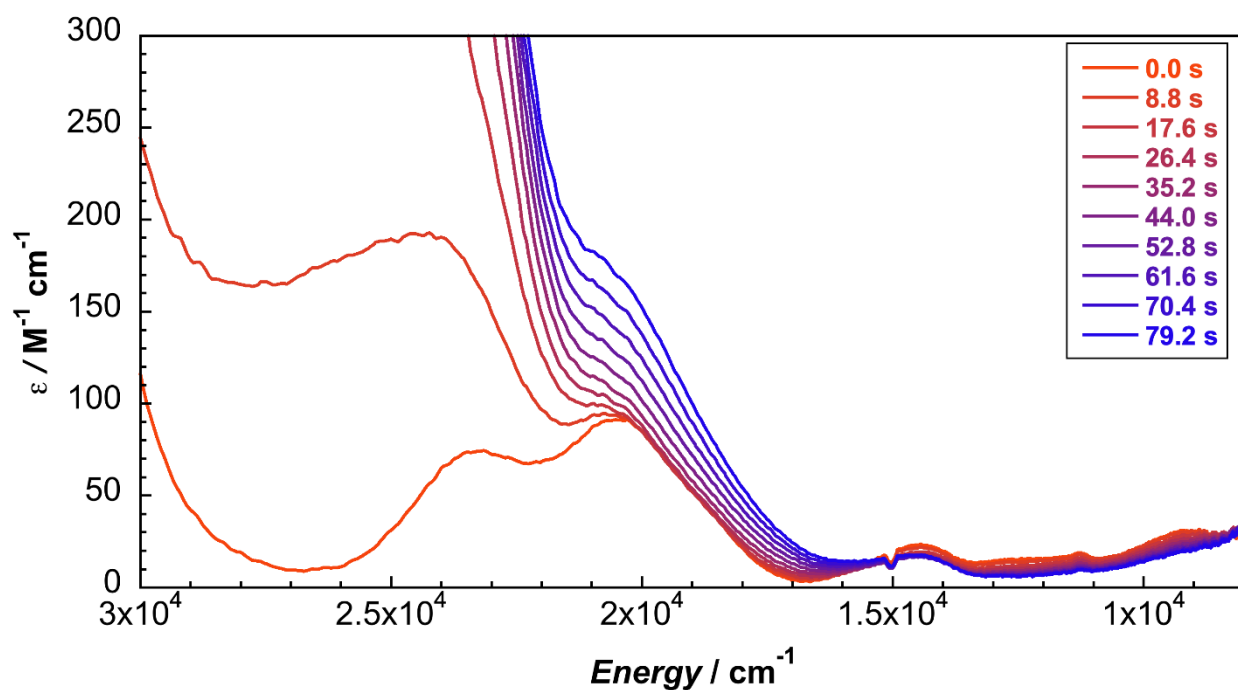


**Figure S71.** UV-vis-NIR spectral changes during the first 40 s of controlled potential electrolysis at  $-1.80$  V vs.  $\text{Fc}^{+/0}$  of  $\text{Ni}^{\text{II}}(\text{IB})\text{Cl}_2$  in  $0.1$  M  $\text{TBAPF}_6$  in DMA solution.

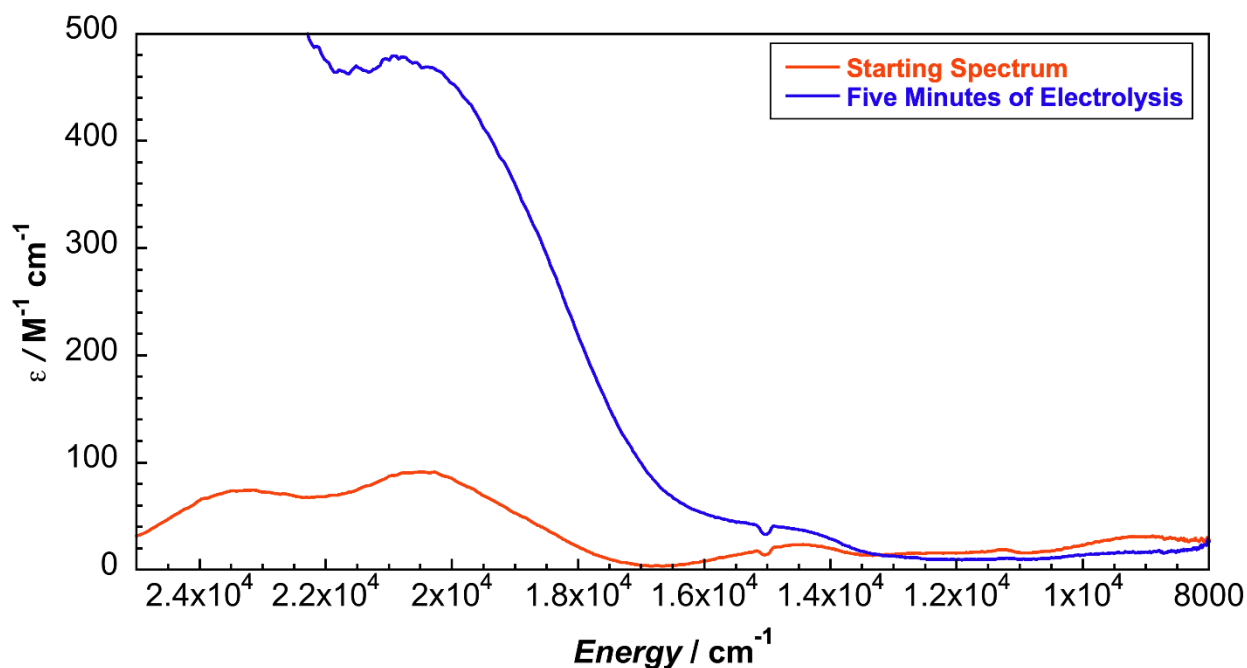


**Figure S72.** Starting and ending UV-vis-NIR spectra for four minutes of controlled potential electrolysis at  $-1.80$  V vs.  $\text{Fc}^{+/0}$  of  $\text{Ni}^{\text{II}}(\text{IB})\text{Cl}_2$  in  $0.1$  M  $\text{TBAPF}_6$  in DMA solution.

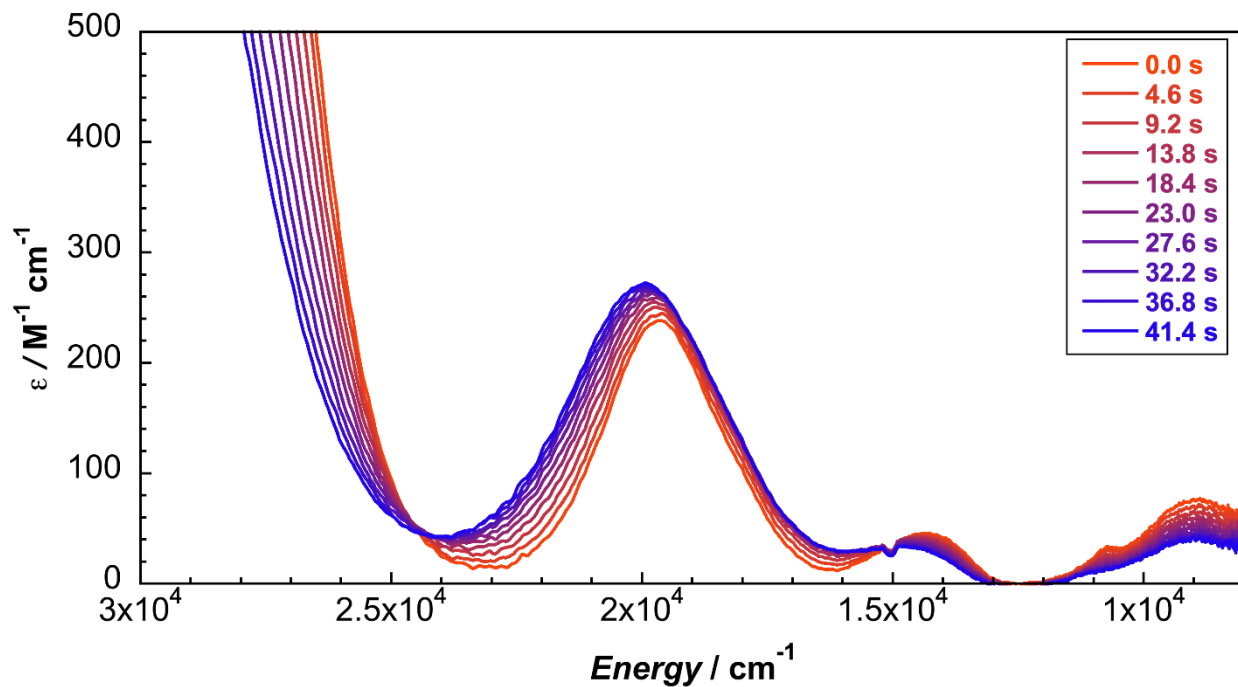


**Figure S73.** UV-vis-NIR spectral changes during the first 40 s of controlled potential electrolysis at  $-1.50 \text{ V}$  vs.  $\text{Fc}^{+/0}$  of  $\text{Ni}^{\text{II}}(\text{1B})\text{Br}_2$  in  $0.2 \text{ M}$  TBAPF<sub>6</sub> in DCM solution.

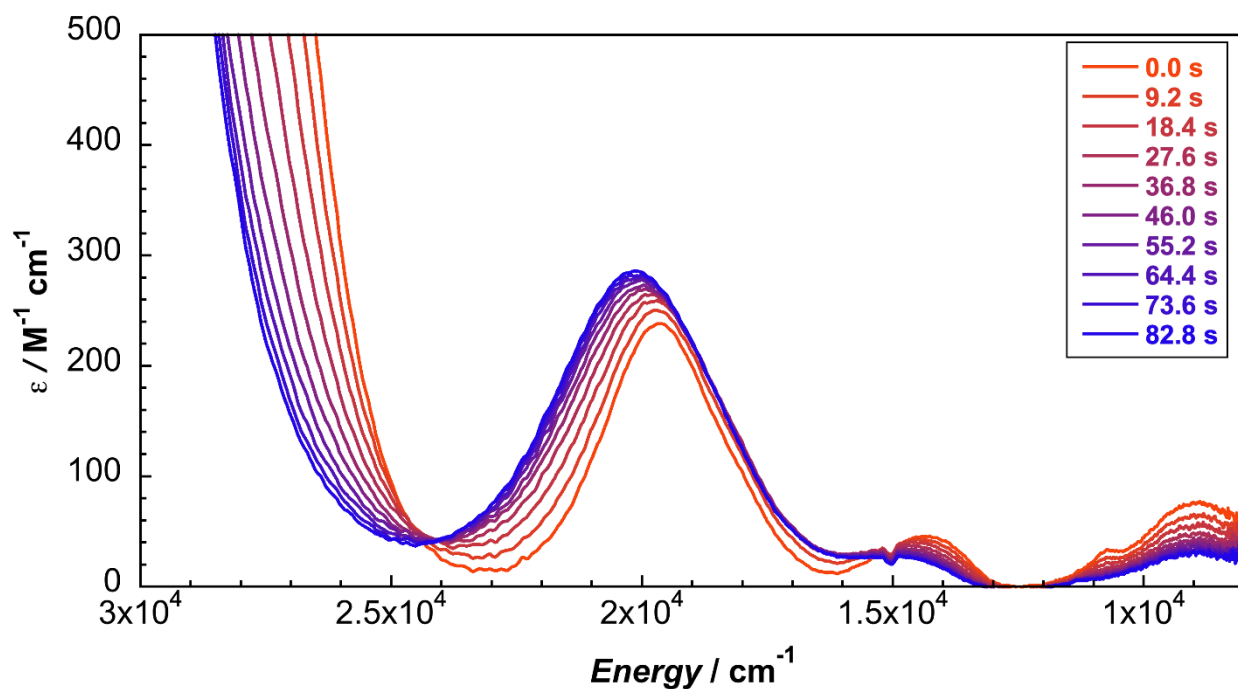


**Figure S74.** UV-vis-NIR spectral changes during the first 80 s of controlled potential electrolysis at  $-1.50 \text{ V}$  vs.  $\text{Fc}^{+/0}$  of  $\text{Ni}^{\text{II}}(\text{1B})\text{Br}_2$  in  $0.2 \text{ M}$  TBAPF<sub>6</sub> in DCM solution.

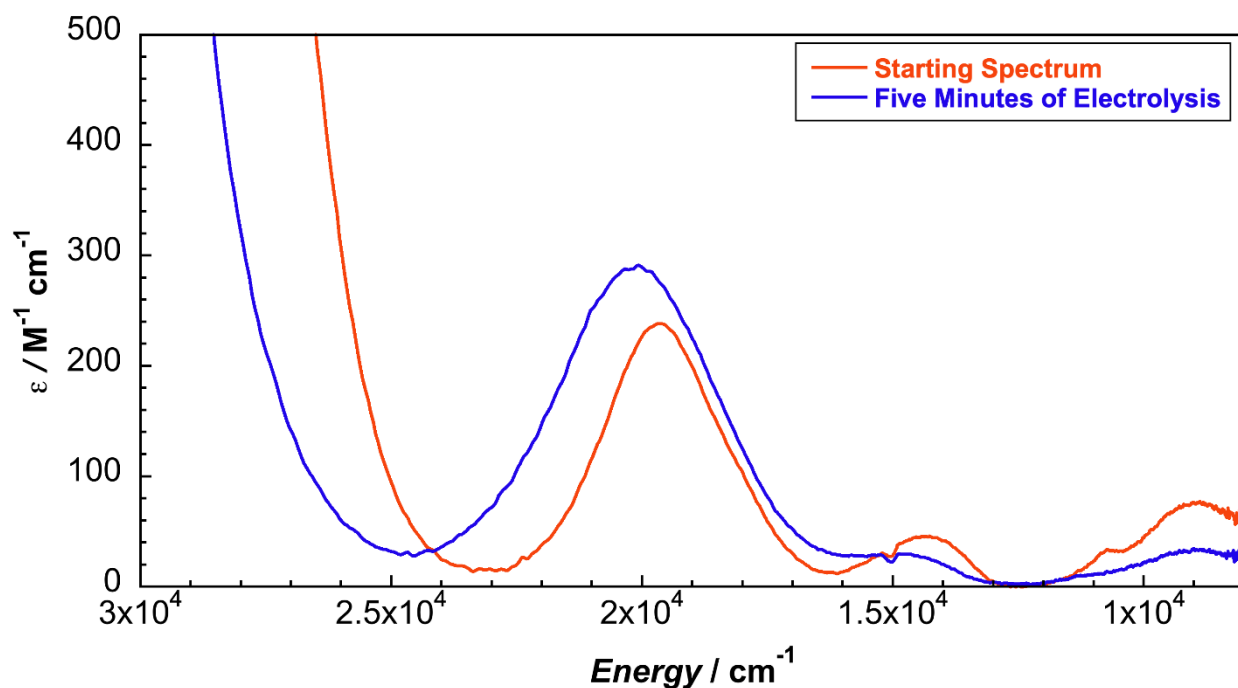


**Figure S75.** Starting and ending UV-vis-NIR spectra for five minutes of controlled potential electrolysis at  $-1.50$  V vs.  $\text{Fc}^{+/0}$  of  $\text{Ni}^{\text{II}}(\text{IB})\text{Br}_2$  in  $0.2$  M  $\text{TBAPF}_6$  in DCM solution.

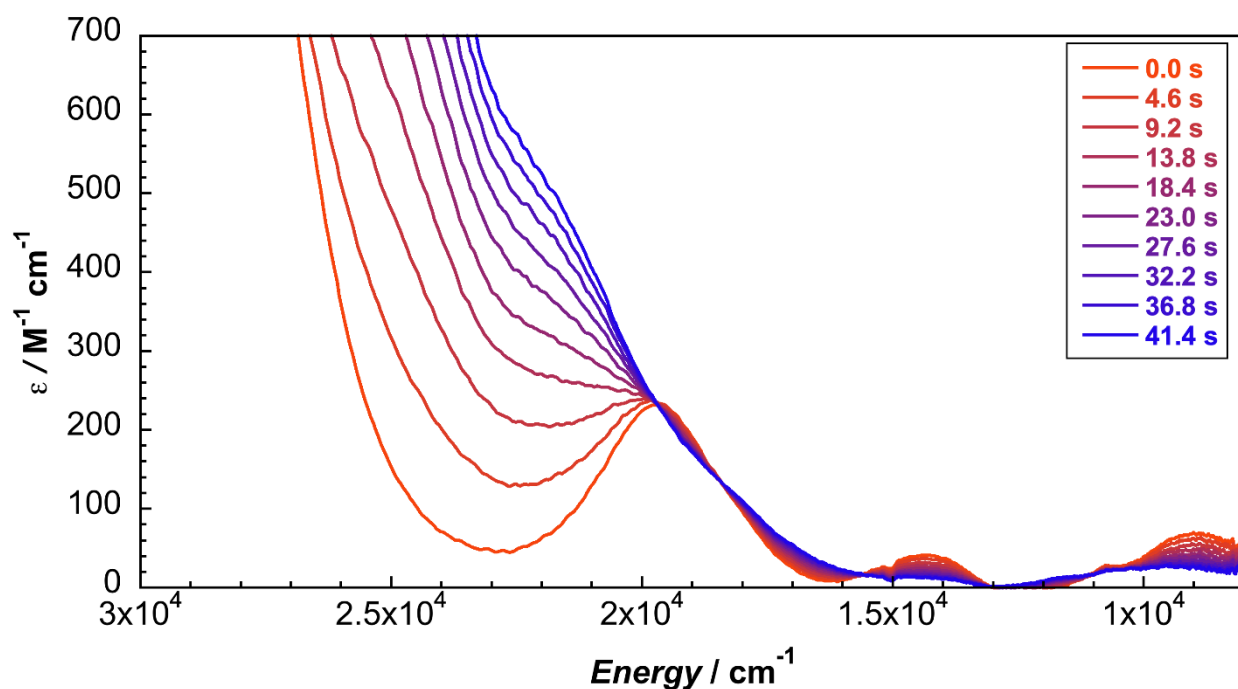


**Figure S76.** UV-vis-NIR spectral changes during the first  $40$  s of controlled potential electrolysis at  $1.20$  V vs.  $\text{Fc}^{+/0}$  of  $\text{Ni}^{\text{II}}(\text{IB})\text{Br}_2$  in  $0.2$  M  $\text{TBAPF}_6$  in DCM solution.



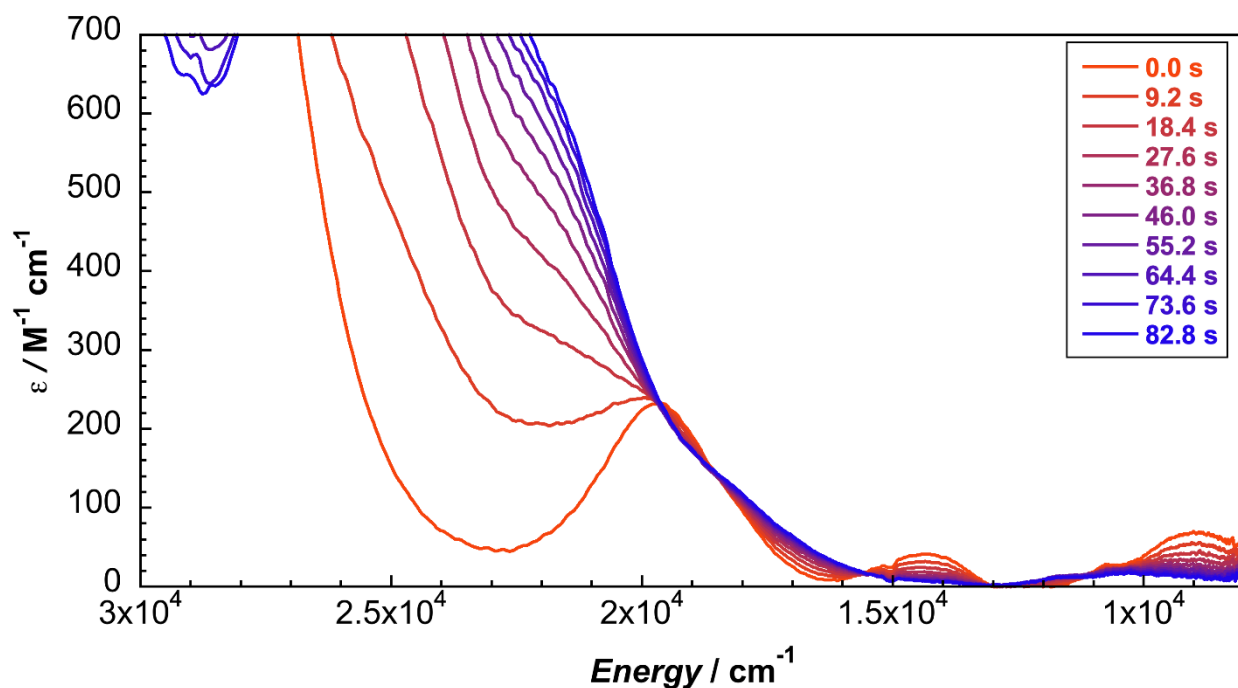


**Figure S77.** UV-vis-NIR spectral changes during the first 80 s of controlled potential electrolysis at 1.20 V vs.  $\text{Fc}^{+/0}$  of  $\text{Ni}^{\text{II}}(\text{IB})\text{Br}_2$  in 0.2 M  $\text{TBAPF}_6$  in DCM solution.

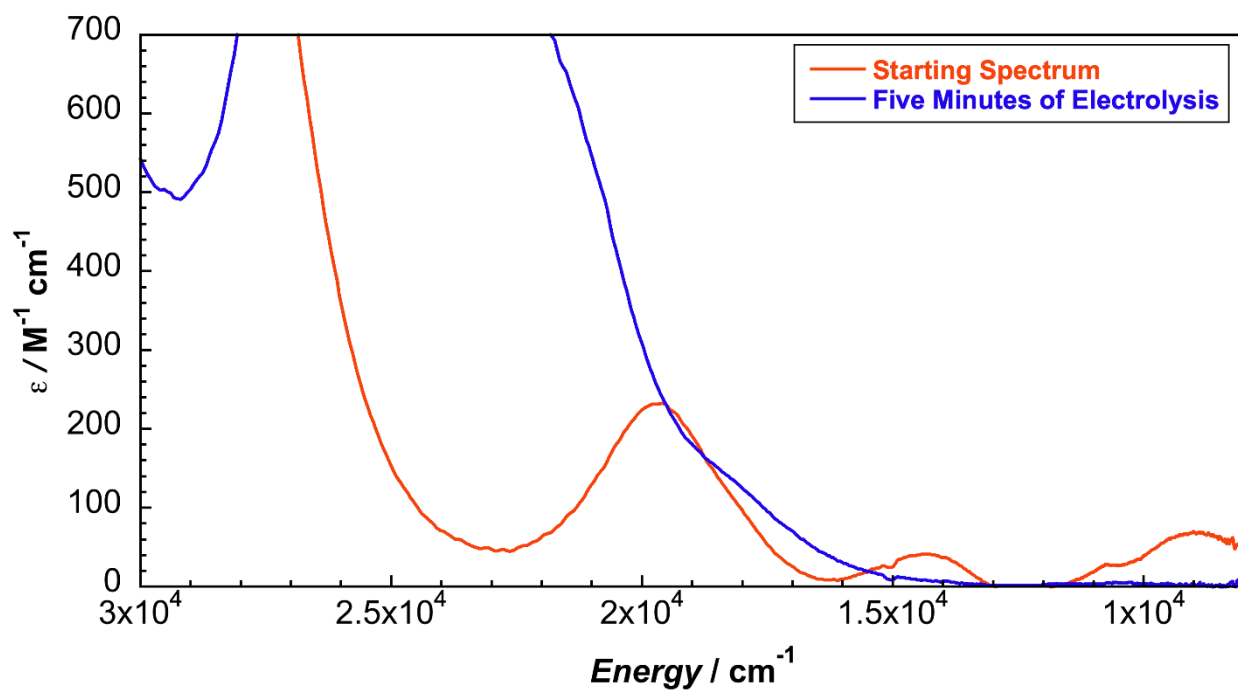


**Figure S78.** Starting and ending UV-vis-NIR spectra for five minutes of controlled potential electrolysis at 1.20 V vs.  $\text{Fc}^{+/0}$  of  $\text{Ni}^{\text{II}}(\text{IB})\text{Br}_2$  in 0.2 M  $\text{TBAPF}_6$  in DCM solution.

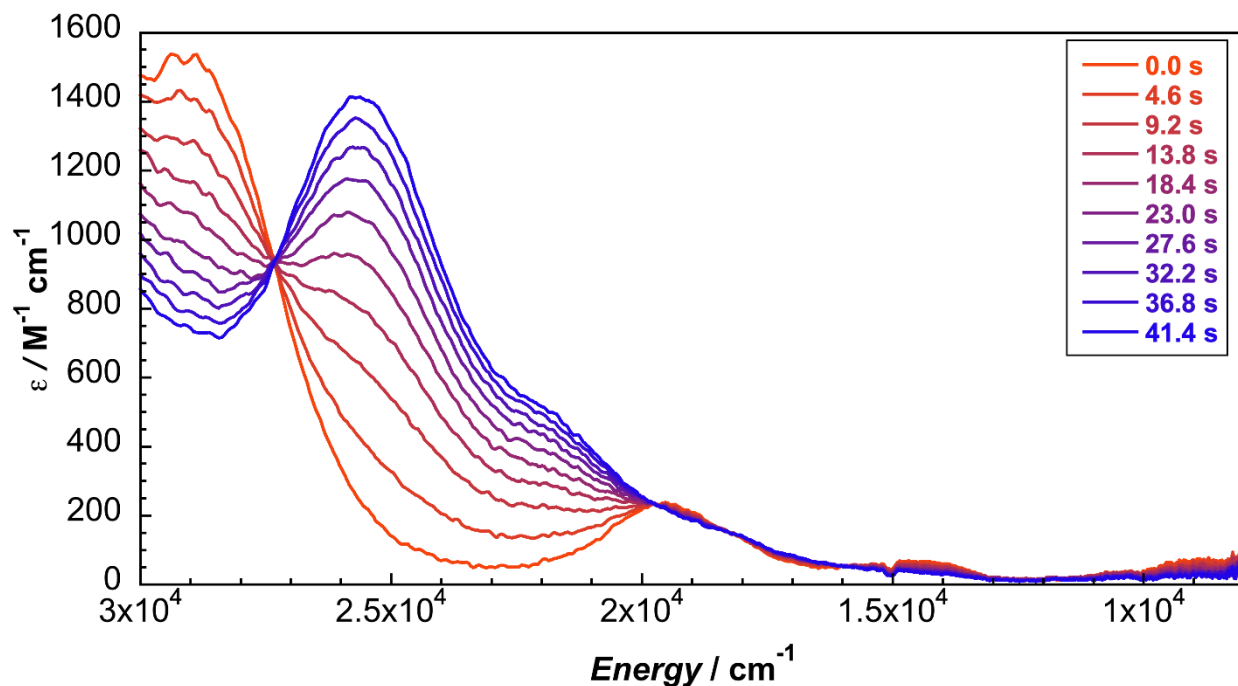


**Figure S79.** UV-vis-NIR spectral changes (diluted) during the first 40 s of controlled potential electrolysis at 1.20 V vs.  $\text{Fc}^{+/0}$  of  $\text{Ni}^{\text{II}}(\text{IB})\text{Br}_2$  in 0.1 M TBAPF<sub>6</sub> in DCM solution.

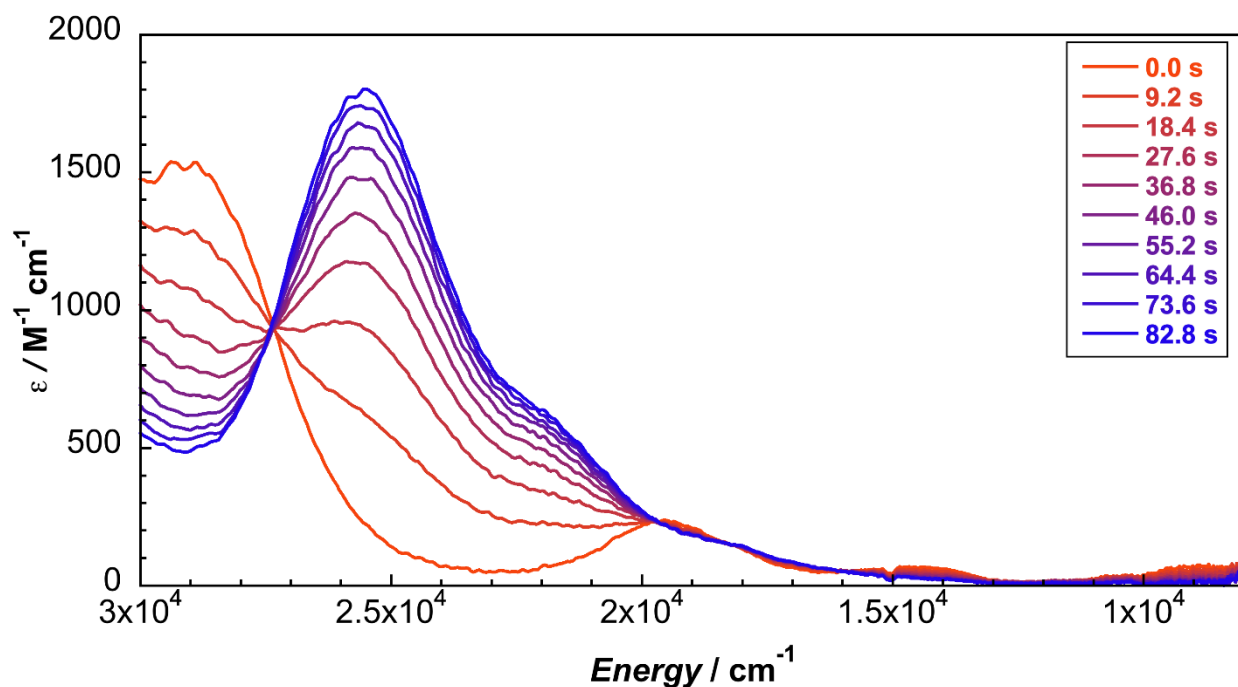


**Figure S80.** UV-vis-NIR spectral changes (diluted) during the first 80 s of controlled potential electrolysis at 1.20 V vs.  $\text{Fc}^{+/0}$  of  $\text{Ni}^{\text{II}}(\text{IB})\text{Br}_2$  in 0.1 M TBAPF<sub>6</sub> in DCM solution.

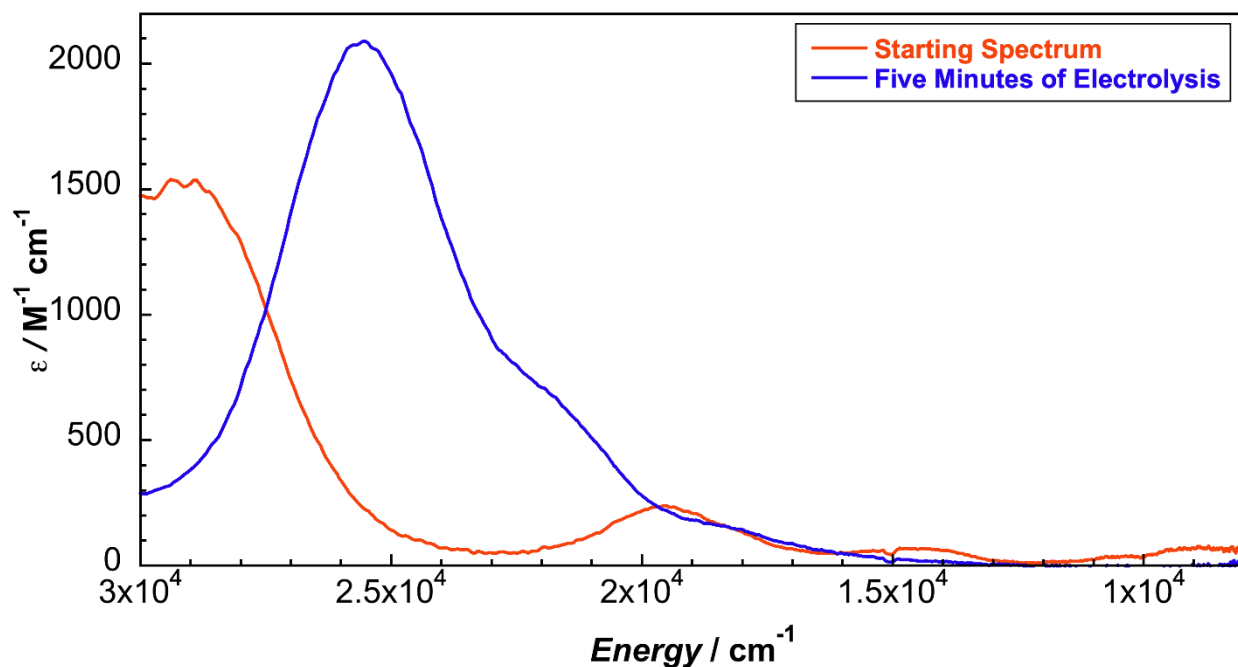


**Figure S81.** Starting and ending UV-vis-NIR spectra for five minutes of controlled potential electrolysis at 1.20 V vs.  $\text{Fc}^{+/0}$  of  $\text{Ni}^{\text{II}}(\text{1B})\text{Br}_2$  in 0.1 M  $\text{TBAPF}_6$  in DCM solution.

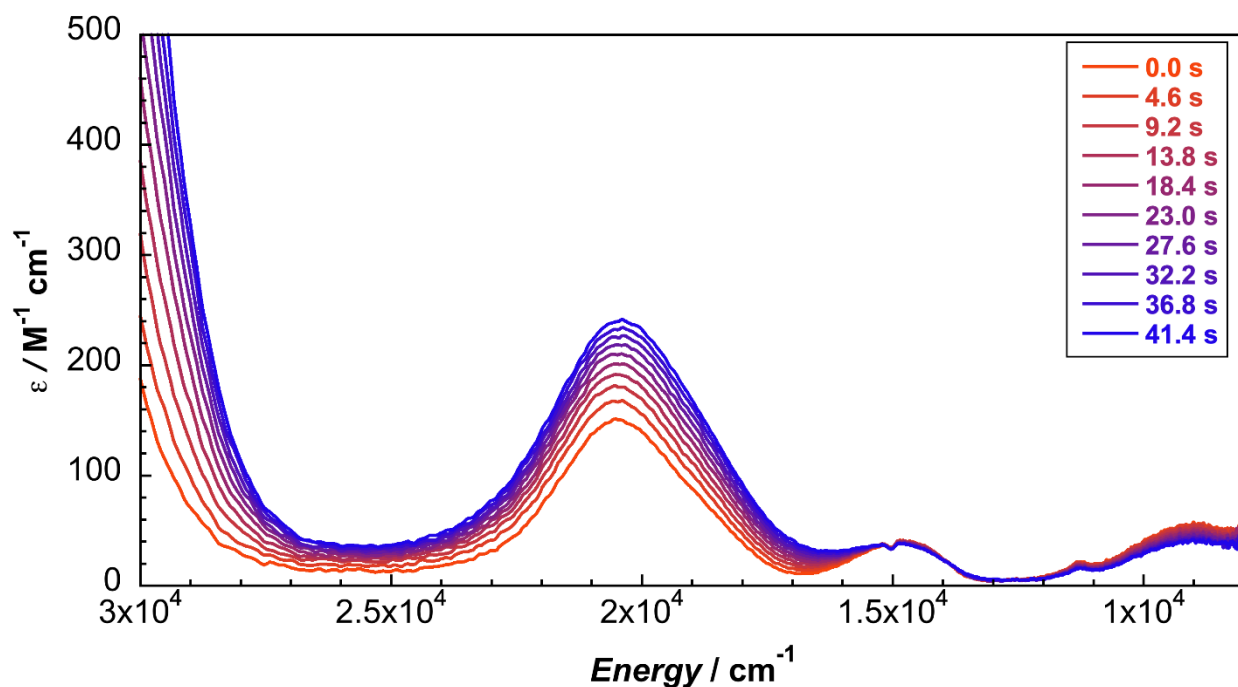


**Figure S82.** UV-vis-NIR spectral changes during the first 40 s of controlled potential electrolysis at  $-1.50$  V vs.  $\text{Fc}^{+/0}$  of  $\text{Ni}^{\text{II}}(\text{1B})\text{Cl}_2$  in 0.2 M  $\text{TBAPF}_6$  in DCM solution.

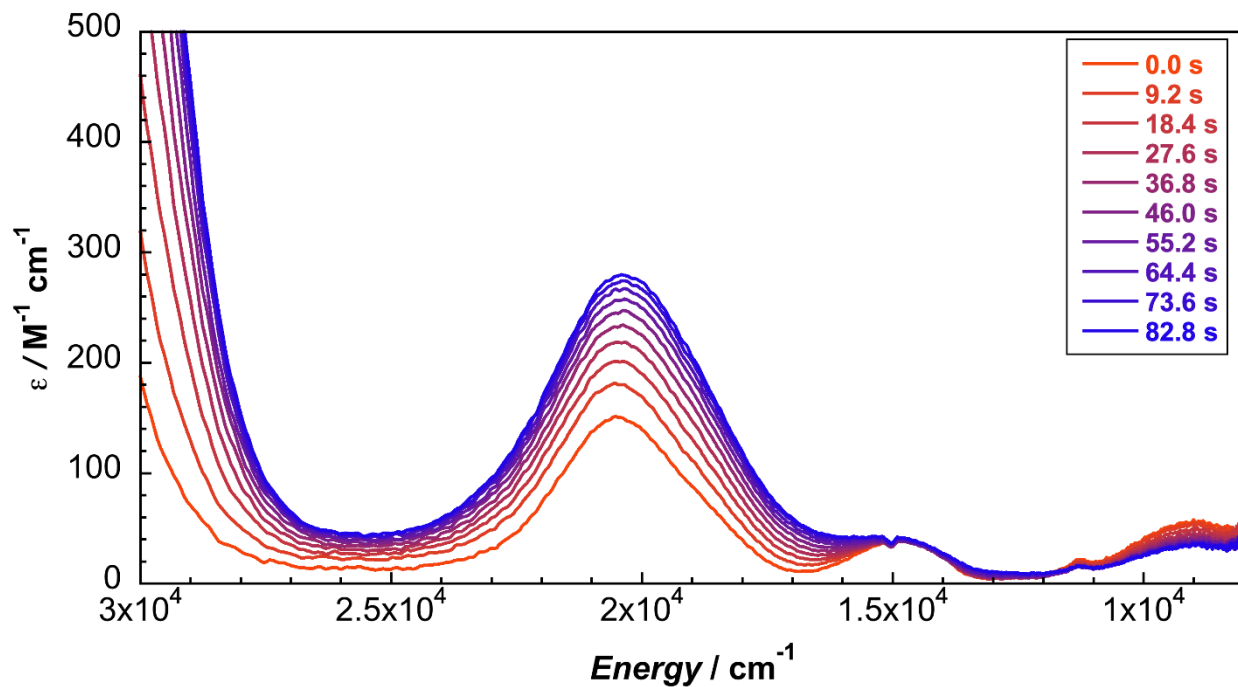


**Figure S83.** UV-vis-NIR spectral changes during the first 80 s of controlled potential electrolysis at  $-1.50$  V vs.  $\text{Fc}^{+/0}$  of  $\text{Ni}^{\text{II}}(\text{IB})\text{Cl}_2$  in  $0.2$  M  $\text{TBAPF}_6$  in DCM solution.

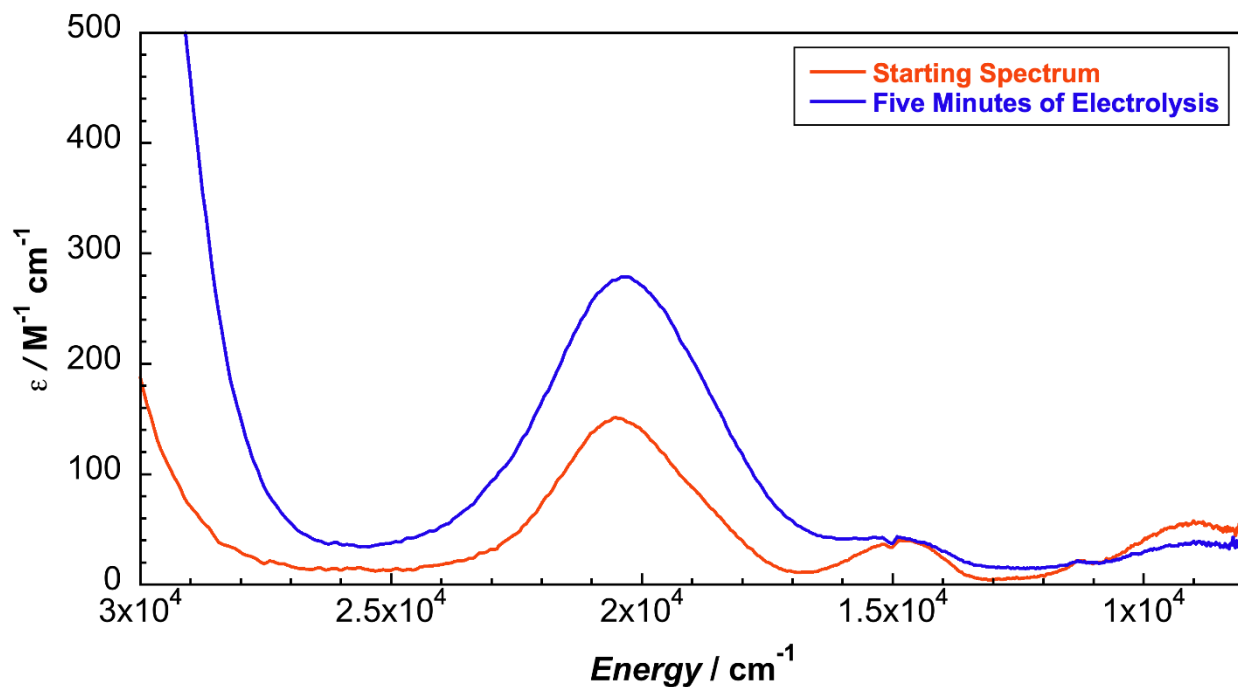


**Figure S84.** Starting and ending UV-vis-NIR spectra for five minutes of controlled potential electrolysis at  $-1.50$  V vs.  $\text{Fc}^{+/0}$  of  $\text{Ni}^{\text{II}}(\text{IB})\text{Cl}_2$  in  $0.2$  M  $\text{TBAPF}_6$  in DCM solution.

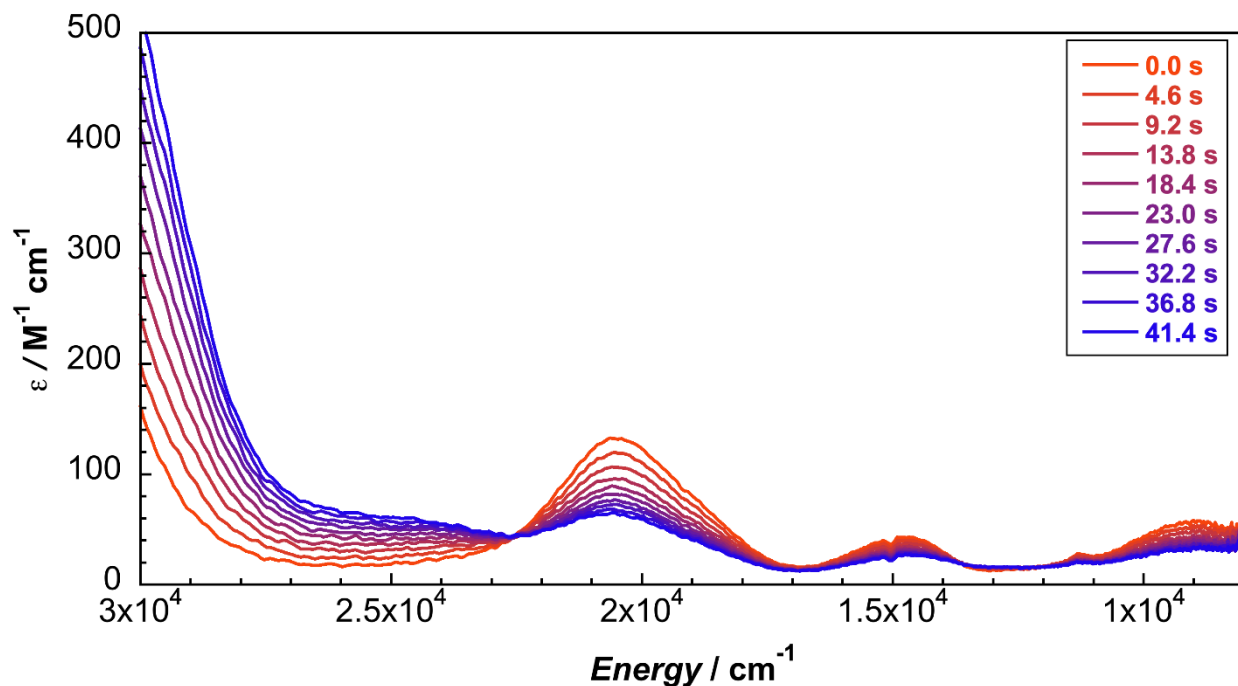


**Figure S85.** UV-vis-NIR spectral changes during the first 40 s of controlled potential electrolysis at 1.50 V vs.  $\text{Fc}^{+/0}$  of  $\text{Ni}^{\text{II}}(\text{IB})\text{Cl}_2$  in 0.2 M TBAPF<sub>6</sub> in DCM solution.

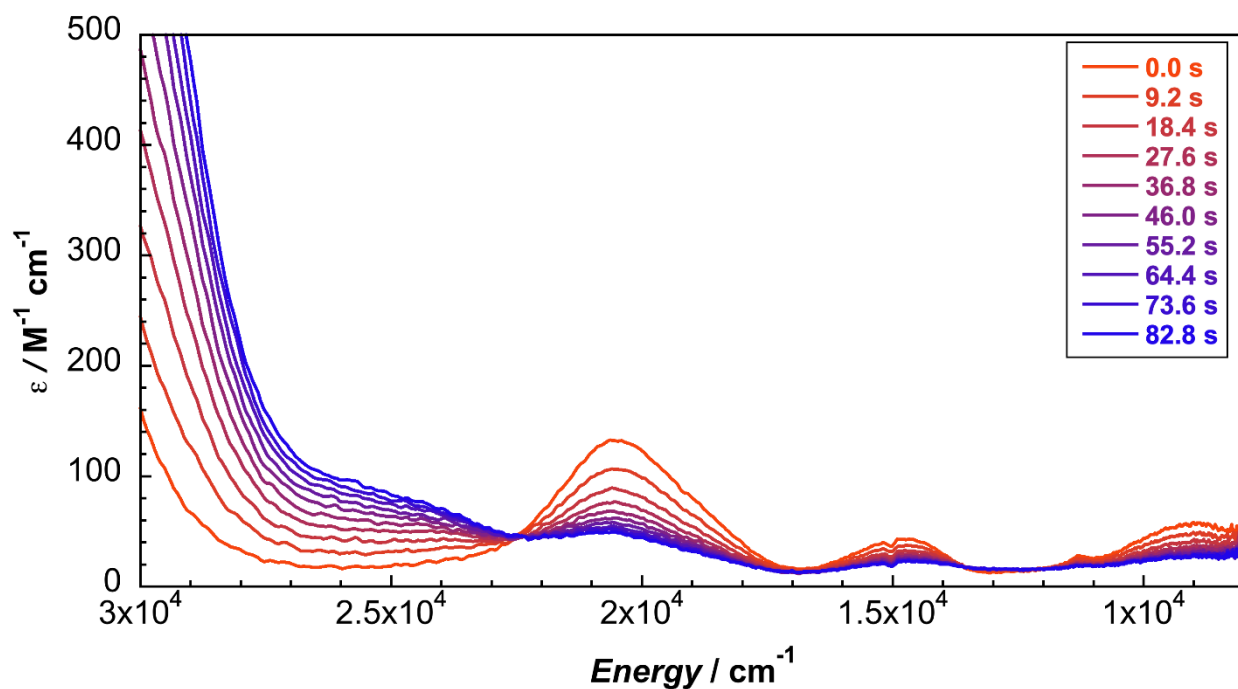


**Figure S86.** UV-vis-NIR spectral changes during the first 80 s of controlled potential electrolysis at 1.50 V vs.  $\text{Fc}^{+/0}$  of  $\text{Ni}^{\text{II}}(\text{IB})\text{Cl}_2$  in 0.2 M TBAPF<sub>6</sub> in DCM solution.

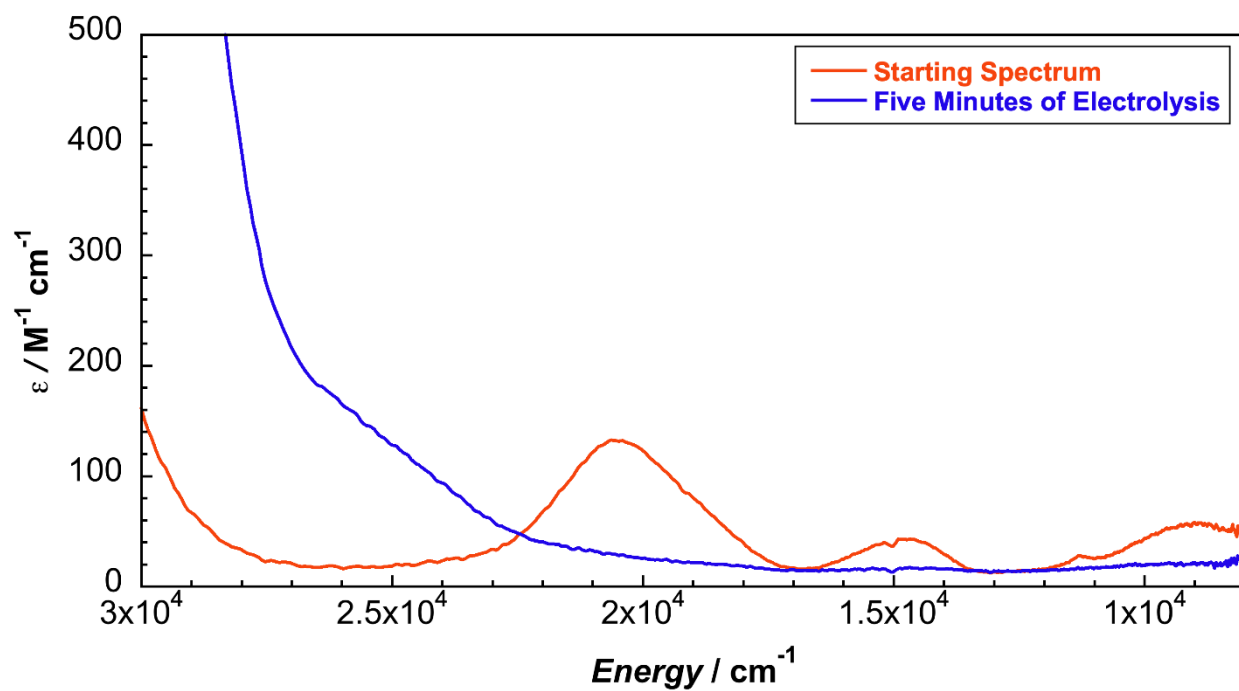


**Figure S87.** Starting and ending UV-vis-NIR spectra for five minutes of controlled potential electrolysis at 1.50 V vs.  $\text{Fc}^{+/0}$  of  $\text{Ni}^{\text{II}}(\text{1B})\text{Cl}_2$  in 0.2 M  $\text{TBAPF}_6$  in DCM solution.

## S7. X-Ray Crystallographic Data

### Collection and Refinement of Zinc(II) bis(chloride) (3a*R*,3a'*R*,8a*S*,8a'*S*)-2,2'-(cyclopropane-1,1-diyl)bis(3a,8a-dihydro- 8*H*-indeno[1,2-*d*]oxazole) [Zn(II)(IB)Cl<sub>2</sub>]

Low-temperature diffraction data ( $\phi$ - and  $\omega$ -scans) were collected on a Bruker AXS KAPPA APEX II diffractometer coupled to a PHOTON 100 CMOS detector with graphite monochromated Mo  $K_{\alpha}$  radiation ( $\lambda = 0.71073$  Å) for the structure of compound **Zn<sup>II</sup>(IB)Cl<sub>2</sub>**. The structure was solved by direct methods using SHELXL<sup>20</sup> and refined against  $F^2$  on all data by full-matrix least squares with SHELXL-2019<sup>21</sup> using established refinement techniques.<sup>22</sup> All non-hydrogen atoms were refined anisotropically. All hydrogen atoms were included into the model at geometrically calculated positions and refined using a riding model. The isotropic displacement parameters of all hydrogen atoms were fixed to 1.2 times the  $U$  value of the atoms they are linked to (1.5 times for methyl groups). All disordered atoms were refined with the help of similarity restraints on the 1,2- and 1,3-distances and displacement parameters as well as rigid bond restraints for anisotropic displacement parameters. **Zn<sup>II</sup>(IB)Cl<sub>2</sub>** crystallizes in the orthorhombic space group  $P2_12_12_1$  with one molecule in the asymmetric unit. A Dow Next Generation Instrumentation Grant supported this work performed by the X-Ray Crystallography Facility (XRCF) in the Beckman Institute (BI) at Caltech.

The B Level Alert results from a very small ESD value (0.003). Since the Flack value (0.05) is very small, the absolute configuration of the molecule is correct. We attempted to add TWIN and BASF and refine the structure, which did not remove the alert.

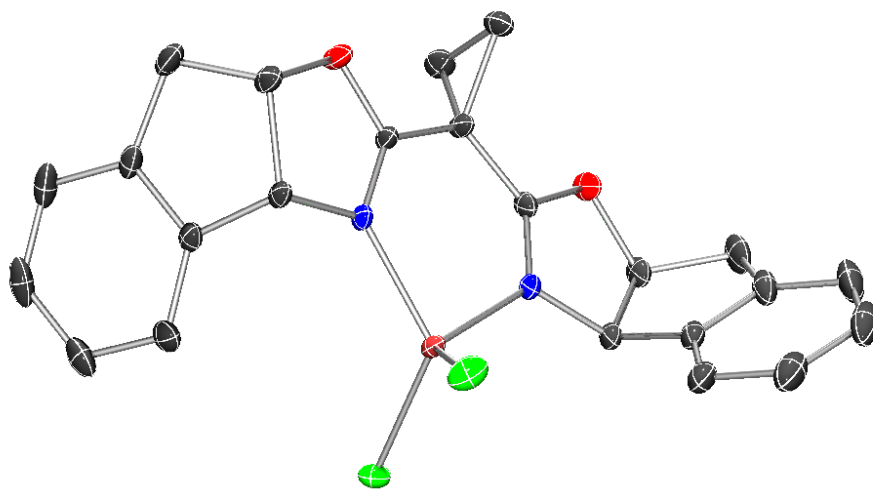


**Figure S88.** Molecular structure of the asymmetric unit of **Zn<sup>II</sup>(1B)Cl<sub>2</sub>**. Thermal ellipsoids set at 50% probability. Hydrogens omitted for clarity.



**Table S3.** Crystal data and structure refinement for **Zn(1B)Cl<sub>2</sub>**.

Empirical formula	C <sub>23</sub> H <sub>20</sub> N <sub>2</sub> O <sub>2</sub> Cl <sub>2</sub> Zn	
Formula weight	492.68	
Temperature	100(2) K	
Wavelength	0.71073 Å	
Crystal system	orthorhombic	
Space group	P2 <sub>1</sub> 2 <sub>1</sub> 2 <sub>1</sub>	
Unit cell dimensions	a = 9.323(3) Å	α = 90°.
	b = 10.617(3) Å	β = 90°.
	c = 21.782(3) Å	γ = 90°.
Volume	2156.1(9) Å <sup>3</sup>	
Z	4	
Density (calculated)	1.518 g/cm <sup>3</sup>	
Absorption coefficient	1.401 mm <sup>-1</sup>	
F(000)	1008.0	
Crystal size	0.200 x 0.250 x 0.300 mm <sup>3</sup>	
Theta range for data collection	3.74 to 72.68°.	
Index ranges	-15 ≤ h ≤ 15, -17 ≤ k ≤ 17, -36 ≤ l ≤ 33	
Reflections collected	54043	
Independent reflections	10439 [R <sub>int</sub> = 0.0392]	
Completeness to theta = 50.5°	99.40 %	
Absorption correction	Semi-empirical from equivalents	
Max. and min. transmission	0.7471 and 0.6611	
Refinement method	Full-matrix least-squares on F <sup>2</sup>	
Data / restraints / parameters	10439 / 0 / 271	
Goodness-of-fit on F <sup>2</sup>	1.066	
Final R indices [I > 2σ(I)]	R <sub>1</sub> = 0.0314, wR <sub>2</sub> = 0.0775	
R indices (all data)	R <sub>1</sub> = 0.0349, wR <sub>2</sub> = 0.0789	
Extinction coefficient	n/a	
Largest diff. peak and hole	1.03 and -0.43 e Å <sup>-3</sup>	

## S8. TDDFT and CASSCF+NEVPT2 Results and Inputs

### Density Functional Theory

All DFT calculations were carried out using ORCA 5.0.3.<sup>23</sup> The structures were optimized using the BP86 functional,<sup>9</sup> the hybrid basis set def2-TZVP/def2-TZVPP(Ni),<sup>24</sup> and the D3BJ dispersion correction.<sup>25,26</sup> The effect of solvation on geometry optimizations was included by employing the conductor-like polarizable continuum model (CPCM)<sup>27,28</sup> with a dielectric constant of  $\epsilon = 38$  to model DMA solvent. The calculations were accelerated by resolution-of-identity approximation (RI).<sup>29</sup>

For the equilibrium geometries, the terms contributing to Gibbs free energy were calculated as follows:

$$G = E_{el} + G_{solv} + [E_{ZPVE} + RT - RT \ln Q], \quad (3)$$

where:

- i)  $E_{el}$  is the *in vacuo* electronic energy, calculated using RI-TPSSH-D3BJ method,
- ii)  $G_{solv}$  is the free energy of solvation; calculated using the conductor-like polarizable continuum model (CPCM),
- iii)  $[E_{ZPVE} + RT - RT \ln Q]$  corresponds to the thermal enthalpic and entropic contributions to the solute energy with  $E_{ZPVE}$  and  $Q$  being the zero-point vibrational energy and the molecular partition function, respectively; obtained from frequency calculations with the rigid rotor/harmonic oscillator approximation (for  $p = 1$  bar,  $T = 298$  K).

The standard one-electron reduction potentials ( $E^\circ$  in V) were calculated from the change of the Gibbs free energy from eq. 3 upon  $1e^-$  reduction of the solute,  $Ox(aq) + e^- \rightarrow Red(aq)$ :

$$E^\circ [V] = G_{Ox} [eV] - G_{Red} [eV] + \Delta E^\circ_{abs}(\text{reference}) [eV], \quad (4)$$

where  $G_{Ox}/G_{Red}$  are the Gibbs free energies of the oxidized/reduced state of a solute, and  $\Delta E^\circ_{abs}(\text{reference})$  is the absolute potential of a reference electrode, which is required to compare computations with experiment. We have referenced the potentials to the  $Fc^{+/0}$  absolute potential

calculated using the same methodology as for the calculations of the Gibbs free energies of the Ni catalysts (*vide infra*), yielding a value of  $-4.55$  eV in DMA solvent.

### **Time-Dependent Density Functional Theory**

To compare computed electronic absorption spectra with experimental UV-vis-NIR spectra, we have performed TD-DFT calculations using TPSSh<sup>30,31</sup> on top of the DFT optimized (BP86) geometries.

### **Multiconfiguration Self-Consistent Field (MCSCF) Calculations**

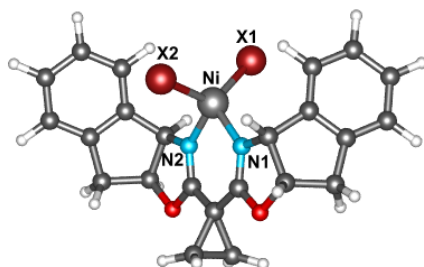
As implemented in the ORZ code, multiconfigurational/multireference approximations to wave function theory: CASSCF/MS-CASPT2<sup>32–37</sup> were performed in combination with the ANO-RCC basis set<sup>38,39</sup> for DFT-optimized structures of Ni catalysts. The ANO-RCC basis set, contracted to ANO-RCC-VTZP for Ni and coordinating atoms and ANO-RCC-VDZP for the rest was used. The second-order Douglas–Kroll–Hess (DKH2) one-electron spin-less Hamiltonian was applied for all WFT-based calculations to allow for spin-free relativistic effects.<sup>40–42</sup> The complete active space used in CASSCF calculations is specified in **Figure S91**, with the largest active space investigated herein comprising 22 electrons in 12 orbitals (denoted as 22e,12o) for **Ni<sup>II</sup>(IB)X<sub>2</sub>** complexes. This active space includes 5 x Ni<sub>3d</sub>, 3 x halide<sub>3p/4p</sub> (per each halide; i.e., 6 orbitals for dihalide complexes), and 1 x IB <sub>$\sigma$ -bonding</sub> orbitals.

Optimized structures of all studied complexes are provided in a separate zip file.

### S.8.1. Ground- and Excited-States Calculations with DFT/TDDFT.

Three different DFT functionals with varying amounts of exact exchange were used for comparison of the calculated bond distances of  $\text{Ni}^{\text{II}}(\text{IB})\text{Cl}_2$  and  $\text{Ni}^{\text{II}}(\text{IB})\text{Br}_2$  ground states (**Table S4**) and TDDFT electronic transition energies (**Table S5**). We note that the TPSSh functional provides the best overall agreement (considering bond lengths, transition energies, and oscillator strengths) and is used throughout this study for comparison to experiment.

**Table S4:** Comparison of selected bond distances and angles from X-ray crystallography with computed values at various DFT levels (BP86, TPSSh, and B3LYP).



#### $\text{Ni}^{\text{II}}(\text{IB})\text{Cl}_2$ :

Bond Length (Å)				
Bond	Crystal Structure	BP86	TPSSh	B3LYP
Ni-Cl1	2.2254(6)	2.24	2.25	2.27
Ni-Cl2	2.2330(6)	2.24	2.25	2.28
Ni-N1	1.987(1)	1.96	1.98	2.00
Ni-N2	1.971(1)	1.96	1.97	1.99
Bond Angle (°)				
Angle	Crystal Structure	BP86	TPSSh	B3LYP
Cl1-Ni-Cl2	115.80(2)	129	130	126
Cl1-Ni-N1	118.49(4)	117	119	122
Cl1-Ni-N2	98.70(4)	98	102	103
Cl2-Ni-N1	105.42(4)	98	98	98
Cl2-Ni-N2	126.48(4)	117	102	112
N1-Ni-N2	90.52(5)	92	92	91

#### $\text{Ni}^{\text{II}}(\text{IB})\text{Br}_2$ :

Bond Length (Å)				
Bond	Crystal Structure	BP86	TPSSh	B3LYP
Ni-Br1	2.358(1)	2.39	2.40	2.43
Ni-Br2	2.3749(9)	2.37	2.39	2.42
Ni-N1	1.974(5)	1.95	1.97	1.99
Ni-N2	1.981(5)	1.96	1.97	1.99
Bond Angle (°)				
Angle	Crystal Structure	BP86	TPSSh	B3LYP
Br1-Ni-Br2	117.13(4)	127	132	124
Br1-Ni-N1	124.1(1)	111	111	112
Br1-Ni-N2	101.1(1)	97	99	98
Br2-Ni-N1	100.2(1)	101	100	102
Br2-Ni-N2	122.2(1)	122	115	125
N1-Ni-N2	90.8(2)	92	93	92

An appreciable Ni<sup>II</sup>–X covalency is observed in these calculated Ni<sup>II</sup> ground states, with Mulliken spin populations of ~0.17e (summation over Cl atoms) and ~0.19e (summation over Br atoms) resulting from mixing of halide 2*p*/3*p* and Ni 3*d* orbitals. The slightly higher covalency of **Ni<sup>II</sup>(IB)Br<sub>2</sub>** is apparent from the smaller 3*d* orbital character in the β-LUMOs (β-LUMO: 75.5% vs. 73.8%, β-LUMO+1: 73.9% vs. 73.1% for **Ni<sup>II</sup>(IB)Cl<sub>2</sub>** vs. **Ni<sup>II</sup>(IB)Br<sub>2</sub>**). β-LUMO energies are destabilized and less negative for **Ni<sup>II</sup>(IB)Cl<sub>2</sub>** vs. **Ni<sup>II</sup>(IB)Br<sub>2</sub>** (**Figure S89**; β-LUMO: –3.13 eV vs. –3.35 eV, β-LUMO+1: –2.85 eV vs. –2.97 eV, respectively). Since the covalency difference is small, the destabilized β-LUMO energies likely arise from the shorter Ni<sup>II</sup>–X bonds and the resulting stronger ligand field of the chloride ligands (2.25 Å (Ni–Cl) vs. 2.40 Å (Ni–Br); **Table S4**).

**Table S5.** TDDFT predicted electronic transitions and their energies for **Ni<sup>II</sup>(IB)Cl<sub>2</sub>** and **Ni<sup>II</sup>(IB)Br<sub>2</sub>** using BP86, TPSSh, and B3LYP functionals.

Predicted Transition	Predicted Transition Energies (cm <sup>-1</sup> )					
	Ni <sup>II</sup> (IB)Cl <sub>2</sub>			Ni <sup>II</sup> (IB)Br <sub>2</sub>		
	BP86	TPSSh	B3LYP	BP86	TPSSh	B3LYP
<sup>3</sup> T <sub>1</sub> (F): <sup>3</sup> B <sub>1</sub> (F) → <sup>3</sup> A <sub>2</sub> (F)	5860	7629	6096	5408	7242	5823
<sup>3</sup> T <sub>1</sub> (F): <sup>3</sup> B <sub>1</sub> (F) → <sup>3</sup> B <sub>2</sub> (F)	8259	10 056	8188	7865	9730	7998
<sup>3</sup> T <sub>2</sub> : <sup>3</sup> B <sub>1</sub> (F) → <sup>3</sup> B <sub>2</sub>	10 474	14 393	12 418	10 003	13 924	12 080
<sup>3</sup> T <sub>2</sub> : <sup>3</sup> B <sub>1</sub> (F) → <sup>3</sup> A <sub>1</sub>	13 366	14 991	12 693	12 854	14 972	12 868
<sup>3</sup> T <sub>1</sub> (P): <sup>3</sup> B <sub>1</sub> (F) → <sup>3</sup> A <sub>2</sub> (P)	13 575	17 116	15 481	13 340	16 834	15 420
<sup>3</sup> T <sub>1</sub> (P): <sup>3</sup> B <sub>1</sub> (F) → <sup>3</sup> B <sub>1</sub> (P)	14 788	18 462	16 565	13 736	17 529	15 814
LMCT	16 214	25 014	29 283	15 173	22 628	25 301
LMCT	16 736	25 082	29 443	15 613	23 086	26 003
LMCT	17 317	25 737	29 699	15 837	23 212	26 564

The six lowest-energy transitions from **Table S5** correspond to ligand field transitions (**Figure S89**), four of which are also observed in experiment and can be used to compare energies. Namely, from the <sup>3</sup>T<sub>1</sub>(F) state, the experimental <sup>3</sup>B<sub>1</sub>(F) → <sup>3</sup>A<sub>2</sub>(F) transition (band 1) is observed at ~2000 cm<sup>-1</sup> (Cl) and ~2200 cm<sup>-1</sup> (Br) in the vibrational CD data; these transitions are highly overestimated in TDDFT (TPSSh/CPCM) with energies of ~7600 cm<sup>-1</sup> (Cl) and ~7200 cm<sup>-1</sup> (Br). The <sup>3</sup>B<sub>1</sub>(F) → <sup>3</sup>A<sub>1</sub> (band 3) maxima are at ~8200 cm<sup>-1</sup> (Cl) and ~8000 cm<sup>-1</sup> (Br) in experiment and at ~10 100 cm<sup>-1</sup> (Cl) and ~9700 cm<sup>-1</sup> (Br) in the calculation. Finally, two bands arising from the <sup>3</sup>T<sub>1</sub>(P) excited state are observed experimentally: <sup>3</sup>B<sub>1</sub>(F) → <sup>3</sup>B<sub>1</sub>(P) (band 5) and <sup>3</sup>B<sub>1</sub>(F) → <sup>3</sup>A<sub>2</sub>(P) (band 7). The TDDFT predicted energy of band 5 is again too high (band 5: ~14 900 cm<sup>-1</sup>

(experiment, Cl) and  $\sim 14\,500\text{ cm}^{-1}$  (experiment, Br) vs.  $18\,500\text{ cm}^{-1}$  (TDDFT, Cl) and  $\sim 17\,500\text{ cm}^{-1}$  (TDDFT, Br)). Conversely, band 7 is underestimated in TDDFT, leading to an incorrect predicted ordering of the  $^3T_1(\text{P})$  states (band 7:  $\sim 20\,100\text{ cm}^{-1}$  (experiment, Cl) and  $\sim 19\,400\text{ cm}^{-1}$  (experiment, Br) vs.  $17\,100\text{ cm}^{-1}$  (TDDFT, Cl) and  $\sim 16\,800\text{ cm}^{-1}$  (TDDFT, Br)). The  $^3B_1(\text{F}) \rightarrow ^3A_2(\text{P})$  band is, however, correctly predicted as the transition with the highest oscillator strength.

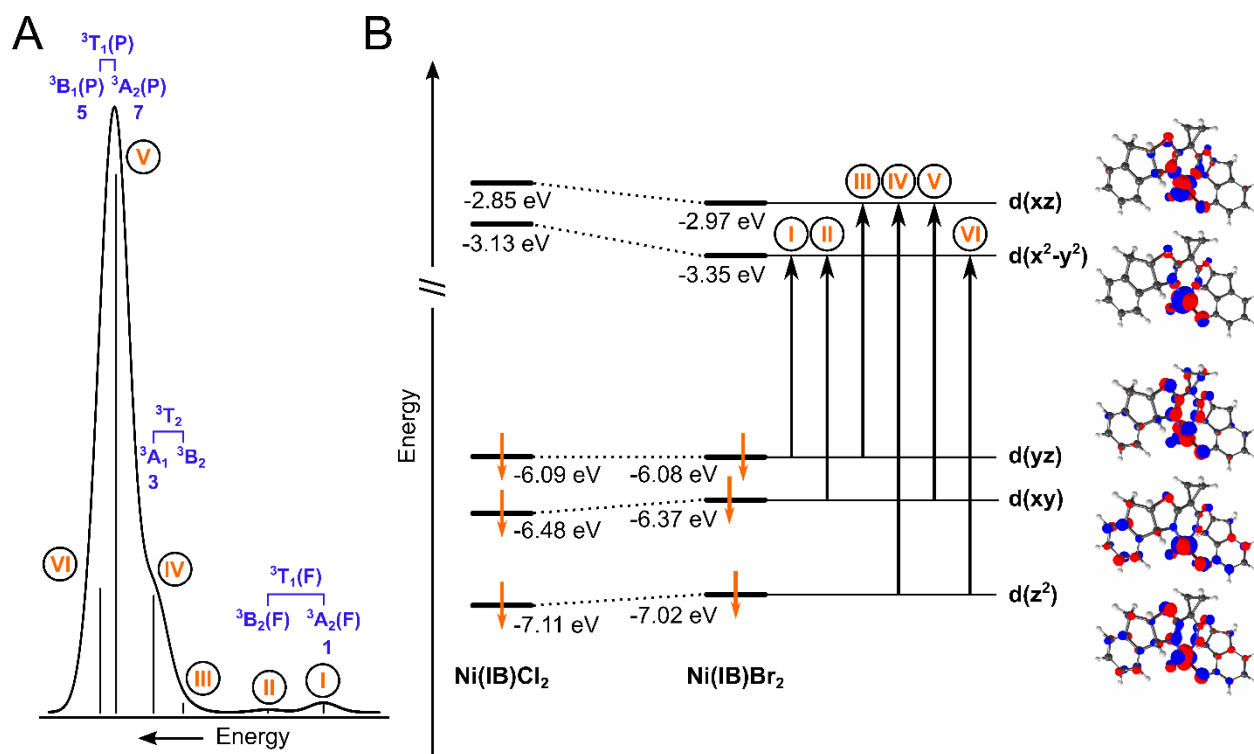


**Figure S89.** TDDFT calculations for  $\text{Ni}^{\text{II}}(\text{IB})\text{X}_2$  precatalysts. (A) An illustrative spectrum for  $\text{Ni}^{\text{II}}(\text{IB})\text{Br}_2$  (TPSSH/CPCM). Transition assignments from group theory (blue text) are provided along with bands numbered as in experiment. (B) Individual transitions from A depicted on the 3d  $\beta$ -orbital manifold of  $\text{Ni}^{\text{II}}(\text{IB})\text{Br}_2$  (right). Comparison between 3d  $\beta$ -orbital manifolds of  $\text{Ni}^{\text{II}}(\text{IB})\text{Cl}_2$  vs.  $\text{Ni}^{\text{II}}(\text{IB})\text{Br}_2$  demonstrating destabilization of the  $\beta$ -LUMOs due to differences in Cl vs. Br ligand field strength.

In addition to correlating TDDFT calculations to experimental precatalyst spectra, they can be further utilized to understand the equilibria discussed in **Section 2.4**. The TDDFT calculated spectra of  $\text{Ni}^{\text{II}}(\text{IB})\text{X}_2$  complexes do not change significantly with different CPCM dielectric constants (e.g., DMA ( $\epsilon = 38$ ) or DCM ( $\epsilon = 9$ ), **Figures S92-S93**), consistent with weak experimental solvatochromism of the ligand field bands for these neutral complexes (**Figures S3-S4** and **S6-S7**). Calculated spectra also do not display the additional  $\sim 23\,000\text{ cm}^{-1}$  band observed in DMA; this band is proposed to originate from a five-coordinate  $\text{Ni}^{\text{II}}(\text{IB})(\text{DMA})\text{X}_2$  species.

Indeed, calculated spectra for five-coordinate species exhibit a significant blue shift for the most intense calculated ligand field band (band 7,  $^3B_1(F) \rightarrow ^3A_2(P)$ ) by  $\sim 3000 - 4000 \text{ cm}^{-1}$  (**Figures S130-S131**). For this species, DMA preferentially coordinates to  $\text{Ni}^{\text{II}}$  via the oxygen atom, consistent with literature precedent<sup>43</sup> (see the comparison between TDDFT calculated spectra of oxygen- and nitrogen-coordinated DMA species,  $\text{Ni}^{\text{II}}(\text{IB})(\text{O-DMA})\text{X}_2$  and  $\text{Ni}^{\text{II}}(\text{IB})(\text{N-DMA})\text{X}_2$ , in **Figures S94-S95**). The computed free energies (in CPCM) of  $\text{Ni}^{\text{II}}(\text{IB})(\text{DMA})\text{X}_2$  formation are only  $\sim 4 \text{ kcal mol}^{-1}$  ( $\text{X} = \text{Cl}$ ) and  $\sim 6 \text{ kcal mol}^{-1}$  ( $\text{X} = \text{Br}$ ), qualitatively consistent with a possible equilibrium between  $\text{Ni}^{\text{II}}(\text{IB})\text{X}_2$  and  $\text{Ni}^{\text{II}}(\text{IB})(\text{DMA})\text{X}_2$  at room temperature and further consistent with strongly temperature-dependent UV-vis-NIR data (**Figure 4**). While the computed free energies are higher than those derived experimentally, this difference likely stems from deviations in solvation free energies, and/or solute and solvent entropic contributions to the calculated free energies, which are difficult to capture accurately as the problem involves multi-molecular association process. As such, the disagreement is only  $\sim 3.7 \text{ kcal mol}^{-1}$  ( $\text{Ni}(\text{IB})\text{Cl}_2$ ) and  $\sim 5.8 \text{ kcal mol}^{-1}$  ( $\text{Ni}(\text{IB})\text{Br}_2$ ), which does not seem to be unprecedented for current state-of-the-art computational modeling techniques.<sup>44</sup>

**Table S6.** Calculated formation energies of precatalyst structures proposed to be involved under different reaction conditions. All energies are in units of  $\text{kcal mol}^{-1}$ .

Equilibrium Reaction	$\Delta H(\text{gas-phase})$	$\Delta G(\text{gas-phase})$	$\Delta G(\text{CPCM})$
$\text{Ni}^{\text{II}}(\text{IB})\text{Cl}_2 + \text{DMA} \rightleftharpoons \text{Ni}^{\text{II}}(\text{IB})(\text{DMA})\text{Cl}_2$	-5.2	10.1	4.0
$\text{Ni}^{\text{II}}(\text{IB})\text{Br}_2 + \text{DMA} \rightleftharpoons \text{Ni}^{\text{II}}(\text{IB})(\text{DMA})\text{Br}_2$	-5.8	10.9	5.8
$2 \text{ Ni}^{\text{II}}(\text{IB})\text{Cl}_2 \rightleftharpoons [\text{Ni}^{\text{II}}(\text{IB})\text{Cl}_2]_2 \text{ dimer}$	-15.1	-6.5	-0.7
$2 \text{ Ni}^{\text{II}}(\text{IB})\text{Br}_2 \rightleftharpoons [\text{Ni}^{\text{II}}(\text{IB})\text{Br}_2]_2 \text{ dimer}$	-14.7	-4.7	1.1
$3 \text{ Ni}^{\text{II}}(\text{IB})\text{Cl}_2 \rightleftharpoons [\text{Ni}^{\text{II}}(\text{IB})\text{Cl}_2]_3 \text{ trimer}$	-24.4	-12.0	-3.5
$3 \text{ Ni}^{\text{II}}(\text{IB})\text{Br}_2 \rightleftharpoons [\text{Ni}^{\text{II}}(\text{IB})\text{Br}_2]_3 \text{ trimer}$	-22.5	-9.0	-0.7

The concentration-dependent electronic absorption data for  $\text{Ni}^{\text{II}}(\text{IB})\text{Cl}_2$  in DCM (**Figure S16**) suggest there is also an appreciable equilibrium between  $\text{Ni}^{\text{II}}(\text{IB})\text{Cl}_2$  and an aggregated species (e.g., dimer or trimer). Concentration-dependent data are not observed for  $\text{Ni}^{\text{II}}(\text{IB})\text{Br}_2$  up to  $\sim 150 \text{ mM}$  (*vide supra*, **Section 2.4**, **Figure S19**). For comparison, we have calculated the energy of  $[\text{Ni}^{\text{II}}(\text{IB})\text{X}_2]_2 \mu\text{-X}$  dimer and  $[\text{Ni}^{\text{II}}(\text{IB})\text{X}_2]_3 \mu\text{-X}$  trimer formation. From the calculated free

energies, the  $[\text{Ni}^{\text{II}}(\text{IB})\text{Cl}_2]_3$  and  $[\text{Ni}^{\text{II}}(\text{IB})\text{Br}_2]_3$  trimers are predicted to be the most thermodynamically stable species ( $\Delta G(\text{CPCM}) = -3.5 \text{ kcal mol}^{-1}$  and  $-0.7 \text{ kcal mol}^{-1}$  vs. the monomer for  $X = \text{Cl}$  and  $\text{Br}$ , respectively) (**Table S7**), and should thus be accessible at room temperature. While still negative, the calculated free energy of trimer formation is less negative for  $X = \text{Br}$ , in qualitative accord with experimental observations.

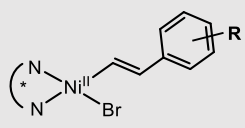
Finally, the calculated TDDFT spectra of the trimers qualitatively resemble the monomeric species (**Figures S96-S97**), but with blue-shifted ligand field bands relative to the monomers. This compares well with the experimental spectrum of the oligomeric species obtained from the variable-concentration and variable-temperature spectra of  $\text{Ni}^{\text{II}}(\text{IB})\text{Cl}_2$  (**Section 2.4**), with experimental and computed spectra overlaid in **Figure S132**.

**Table S7:** Calculated standard reduction potentials of various Ni-indabox complexes using DFT (TPSSH) methodology. All reduction potentials of the Ni complexes are referenced to the absolute potential of the reference electrode ( $\text{Fc}^{+/0}$ ).

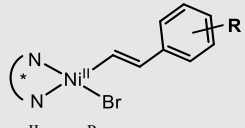
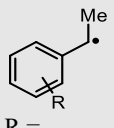
Reference electrode	
Ferrocenium / Ferrocene ( $\text{Fc}^{+/0}$ )	4.55 V
$\text{Ni}^{\text{III}}$ Oxidation State	Reduction potential (vs. $\text{Fc}^{+/0}$ )
$\text{Ni}^{\text{III}}(\text{IB})\text{Cl}_2 / \text{Ni}^{\text{II}}(\text{IB})\text{Cl}_2$	1.41 V
$\text{Ni}^{\text{III}}(\text{IB})\text{Br}_2 / \text{Ni}^{\text{II}}(\text{IB})\text{Br}_2$	1.42 V
$\text{Ni}^{\text{II}}$ Oxidation State	Reduction potential (vs. $\text{Fc}^{+/0}$ )
$\text{Ni}^{\text{II}}(\text{IB})\text{Cl}_2 / \text{Ni}^{\text{I}}(\text{IB})\text{Cl}_2$	-1.24 V
$\text{Ni}^{\text{II}}(\text{IB})\text{Cl}_2 / \text{Ni}^{\text{I}}(\text{IB})\text{Cl} + \text{Cl}$	-1.48 V
$\text{Ni}^{\text{II}}(\text{IB})\text{Cl} / \text{Ni}^{\text{I}}(\text{IB})\text{Cl}$	-0.20 V
$\text{Ni}^{\text{II}}(\text{IB})\text{Br}_2 / \text{Ni}^{\text{I}}(\text{IB})\text{Br}_2$	-1.11 V
$\text{Ni}^{\text{II}}(\text{IB})\text{Br}_2 / \text{Ni}^{\text{I}}(\text{IB})\text{Br} + \text{Br}$	-1.39 V
$\text{Ni}^{\text{II}}(\text{IB})\text{Br} / \text{Ni}^{\text{I}}(\text{IB})\text{Br}$	-0.13 V
$\text{Ni}^{\text{I}}$ Oxidation State	Reduction potential (vs. $\text{Fc}^{+/0}$ )
$\text{Ni}^{\text{I}}(\text{IB})\text{Cl} / \text{Ni}^0(\text{IB})\text{Cl}$	-3.10 V
$\text{Ni}^{\text{I}}(\text{IB})\text{Cl} / \text{Ni}^0(\text{IB}) + \text{Cl}$	-3.97 V
$\text{Ni}^{\text{I}}(\text{IB})\text{Br} / \text{Ni}^0(\text{IB})\text{Br}$	-3.07 V
$\text{Ni}^{\text{I}}(\text{IB})\text{Br} / \text{Ni}^0(\text{IB}) + \text{Br}$	-3.87 V



**Table S8:** Ni-3*d* atomic orbital character in the  $\beta$ -LUMO of  $\text{Ni}^{\text{II}}(\text{IB})\text{Cl}_2$ ,  $\text{Ni}^{\text{II}}(\text{IB})\text{Br}_2$  and  $\alpha$ -HOMO of different  $\text{Ni}^{\text{II}}(\text{IB})(\text{Vn})\text{Br}$  complexes (Vn = substituted *p*-vinylbenzene derivative).

$\text{Ni}^{\text{II}}(\text{IB})\text{X}_2$ ( $S = 1$ ); X =	$\beta$ -LUMO Ni-3 <i>d</i> orbital character
Cl	75.5 %
Br	73.8 %
 $\text{Ni}^{\text{II}}(\text{IB})(^{\text{R}}\text{Vn})\text{Br}$ ( $S = 0$ ); R =	
<i>p</i> -CF <sub>3</sub>	64.3 %
<i>p</i> -CN	64.9 %
<i>p</i> -CO <sub>2</sub> Me	62.4 %
<i>p</i> -Me	42.5 %
<i>p</i> -NMe <sub>2</sub>	9.9 %
<i>p</i> -OMe	27.6 %
<i>p</i> -OTs	57.0 %
Pyp-OMe	42.7 %

**Table S9:** Calculated oxidation potentials of various  $\text{Ni}^{\text{II}}(\text{IB})(\text{Vn})\text{Br}$  and benzyl-C(sp<sup>3</sup>) radicals (Vn = substituted *p*-vinylbenzene derivative). All oxidation potentials are referenced to the absolute potential of the reference electrode ( $\text{Fc}^{+/0}$ ).

 $\text{Ni}^{\text{II}}(\text{IB})(^{\text{R}}\text{Vn})\text{Br}$ ( $S = 0$ ); R =		Oxidation Potential (vs. $\text{Fc}^{+/0}$ )
<i>p</i> -CF <sub>3</sub>		−0.17 V
<i>p</i> -CN		−0.23 V
<i>p</i> -CO <sub>2</sub> Me		−0.19 V
<i>p</i> -Me		−0.29 V
<i>p</i> -NMe <sub>2</sub>		+0.14 V
<i>p</i> -OMe		−0.20 V
<i>p</i> -OTs		−0.29 V
Pyp-OMe		−0.47 V
 R =		Oxidation Potential (vs. $\text{Fc}^{+/0}$ )
H		+0.17 V
<i>p</i> -Br		+0.23 V
<i>p</i> -CF <sub>3</sub>		+0.48 V
<i>p</i> -F		+0.16 V
<i>p</i> -NMe <sub>2</sub>		−0.72 V
<i>p</i> -OMe		−0.32 V
<i>p</i> -Cl- <i>m</i> -Cl		+0.36 V

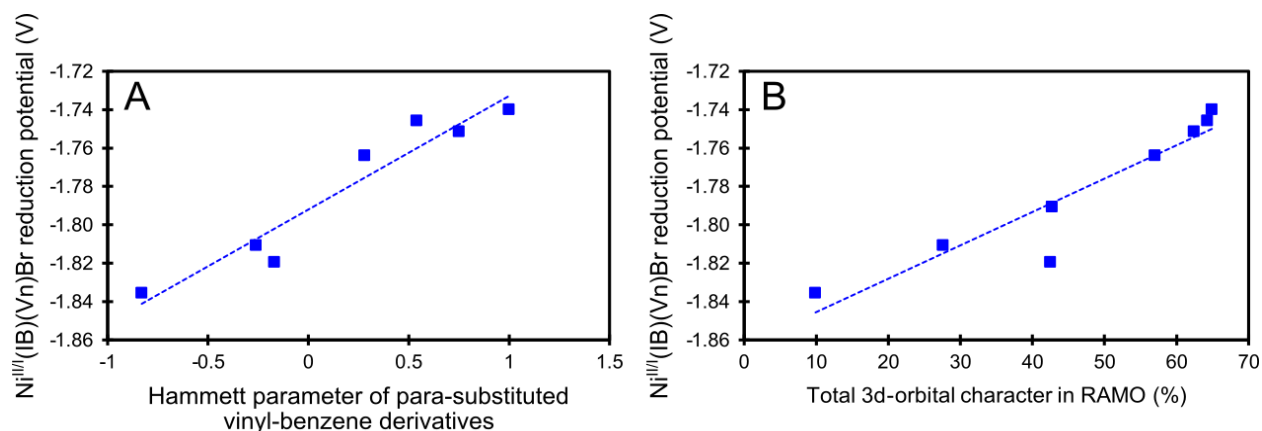


**Figure S90:** (A) Calculated  $\text{Ni}^{\text{II/I}}$  reduction potentials of the  $\text{Ni}^{\text{II}}(\text{IB})(\text{Vn})\text{Br}$  species (coupled to halide dissociation) vs. the vinyl substituent Hammett parameters. (B) Calculated  $\text{Ni}^{\text{II/I}}$  reduction potentials of the  $\text{Ni}^{\text{II}}(\text{IB})(\text{Vn})\text{Br}$  species (coupled to halide dissociation) vs. the 3d-orbital character in the  $\text{Ni}^{\text{II}}$   $d(x^2-y^2)$  RAMO.

## S8.2. Ground- and Excited-States Calculations with CASSCF/CASPT2

The ground-state wave function character of  $\text{Ni}^{\text{II}}(\text{IB})\text{Cl}_2$  and  $\text{Ni}^{\text{II}}(\text{IB})\text{Br}_2$  depends on the active space variation in CASSCF calculations (**Figure S91**). Regardless of active space size, the ground state is exclusively high spin (at the  $\Delta H$  level, the lowest-energy low-spin states are  $\sim 36\text{--}49$  kcal  $\text{mol}^{-1}$  (CASSCF) and  $\sim 28\text{--}39$  kcal  $\text{mol}^{-1}$  (CASPT2) higher in energy). An appreciable multiconfigurational character is observed, however, with a minimal active space (8e,5o; consisting of five Ni 3d orbitals), with contributions to the ground state configuration interaction (CI) vector from several different  $3d^8$   $\text{Ni}^{\text{II}}$  electronic configurations (**Tables S24** and **S30**). With the 22e,12o active space (five Ni 3d orbitals, six halide 2p/3p orbitals, and the Ni(II)  $\sigma$  bonding orbital), the ground-state solution is single-referent, with the highest weight of a single configuration in the CI vector of  $\sim 95\%$  for both  $\text{Ni}^{\text{II}}(\text{IB})\text{Cl}_2$  and  $\text{Ni}^{\text{II}}(\text{IB})\text{Br}_2$  (**Tables S28** and **S34**). This configuration corresponds to an  $S = 1$  triplet ground state with unpaired electrons in the  $d(x^2-y^2)$  and  $d(xz)$  orbitals. The orbital compositions also reflect the covalent interaction between the halide 2p/3p atomic orbitals and the Ni 3d orbitals, with Mulliken spin populations of  $\sim 0.14e$  (summation over Cl atoms) and  $\sim 0.17e$  (summation over Br atoms).

With this optimized active space, we have calculated the UV-vis-NIR absorption, CD, and MCD spectra of  $\text{Ni}^{\text{II}}(\text{IB})\text{Cl}_2$  and  $\text{Ni}^{\text{II}}(\text{IB})\text{Br}_2$  (**Figure 8** and **S142**). These calculations generally support assignments of experimental data given in **Section 2.1** (**Table 4**). Individual states can be

assigned based on the configuration state function with the largest weight in the CI vector, in conjunction with the location of the  $3d$  holes. For example, the ground-state wave functions for both complexes can be described as having  $\sim 95\%$  character of the configuration state function with holes in  $d(x^2-y^2)$  and  $d(xz)$  orbitals. From group theory, this corresponds to the  ${}^3B_1$  state in  $C_{2v}$  (i.e., direct product between  $A_1$  and  $B_1$ ). The first observed transition, calculated at  $\sim 2000\text{ cm}^{-1}$  ( $\text{Ni}^{\text{II}}(\text{IB})\text{Cl}_2$ ) and  $\sim 1800\text{ cm}^{-1}$  ( $\text{Ni}^{\text{II}}(\text{IB})\text{Br}_2$ ), has  $\sim 82\%$  and  $\sim 84\%$  character of the configuration state function with holes in  $d(yz)$  and  $d(xz)$  orbitals, corresponding to the  ${}^3B_1(\text{F}) \rightarrow {}^3A_2$  transition (band 1 in **Table 1**), matching the energy in the experimental vibrational CD ( $\sim 2200\text{ cm}^{-1}$  for both complexes). The next computed transition ( $\sim 3300\text{ cm}^{-1}$  and  $\sim 3000\text{ cm}^{-1}$  for  $\text{Ni}^{\text{II}}(\text{IB})\text{Cl}_2$  and  $\text{Ni}^{\text{II}}(\text{IB})\text{Br}_2$ ) is assigned as the forbidden  ${}^3B_1(\text{F}) \rightarrow {}^3B_2(\text{F})$  transition and is not observed in experiment. In the  ${}^3T_2$  manifold (in  $T_d$ ), we observe band 2 ( ${}^3B_1(\text{F}) \rightarrow {}^3B_1/{}^3B_2$ ; calculated:  $\sim 7400\text{ cm}^{-1}$  (Cl) and  $\sim 7200\text{ cm}^{-1}$  (Br), experimental:  $\sim 6200\text{ cm}^{-1}$  (Cl) and  $\sim 6600\text{ cm}^{-1}$  (Br)) and band 3 ( ${}^3B_1(\text{F}) \rightarrow {}^3A_1$ ; calculated:  $\sim 9800\text{ cm}^{-1}$  (Cl) and  $\sim 9300\text{ cm}^{-1}$  (Br), experimental:  $\sim 8000\text{ cm}^{-1}$  (Cl) and  $\sim 8200\text{ cm}^{-1}$  (Br)), as well as the forbidden  ${}^3B_1(\text{F}) \rightarrow {}^3B_1/{}^3B_2$  transition (calculated:  $10\,800\text{ cm}^{-1}$  (Cl) and  $10\,200\text{ cm}^{-1}$  (Br)). Note we cannot unambiguously differentiate between  ${}^3B_1/{}^3B_2$  assignments in all cases, as the states with holes in different orbitals mix in the multiconfigurational wavefunctions and exhibit similar CI weights. The most intense transition in the low-energy region, band 4 (experimental:  $10\,270\text{ cm}^{-1}$  (Cl) and  $10\,150\text{ cm}^{-1}$  (Br), calculated:  $\sim 12\,700\text{ cm}^{-1}$  (Cl) and  $\sim 12\,400\text{ cm}^{-1}$  (Br)), is assigned as the double-electron  ${}^3B_1(\text{F}) \rightarrow {}^3A_2(\text{F})$  transition with the holes in the  $d(z^2)$  and  $d(xy)$  orbitals. Finally, transitions to the  ${}^3T_1(\text{P})$  manifold (in  $T_d$ ) are calculated in the range of  $\sim 16\,100\text{ cm}^{-1}$  to  $\sim 21\,600\text{ cm}^{-1}$  (experiment:  $\sim 14\,500\text{ cm}^{-1}$  to  $\sim 20\,100\text{ cm}^{-1}$ ) with the same ordering as experiment (band 5:  ${}^3B_1(\text{F}) \rightarrow {}^3B_1(\text{P})/{}^3B_2(\text{P})$ , band 6:  ${}^3B_1(\text{F}) \rightarrow {}^3B_1(\text{P})/{}^3B_2(\text{P})$ , and the most intense band 7:  ${}^3T_1(\text{P}): {}^3B_1(\text{F}) \rightarrow {}^3A_2(\text{P})$ ) (see **Tables S22** and **S23** for tabulated energies and assignments).

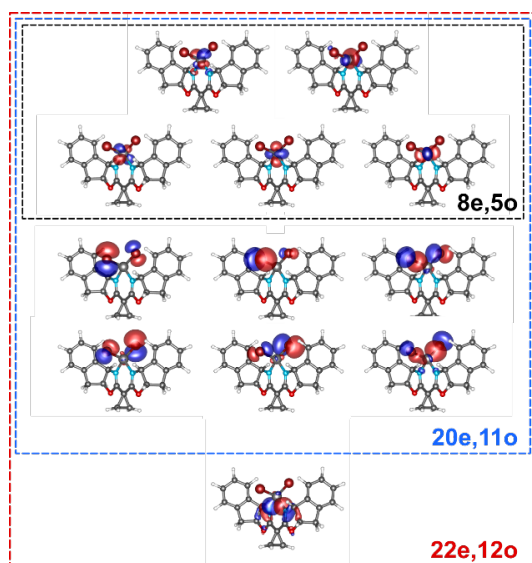


**Figure S91:** Different active spaces investigated in the multireference calculations. The largest active space comprising 22 electrons in 12 orbitals (denoted as 22e,12o) includes 5 x  $\text{Ni}_{3d}$  (*black box*), 3 x  $\text{Halide}_{3p/4p}$  (per each halide; i.e., 6 orbitals for dihalide complexes, *blue box*), and 1 x  $\text{IB}_{\sigma\text{-bonding}}$  orbitals (*red box*).

### S8.3. Additional Figures

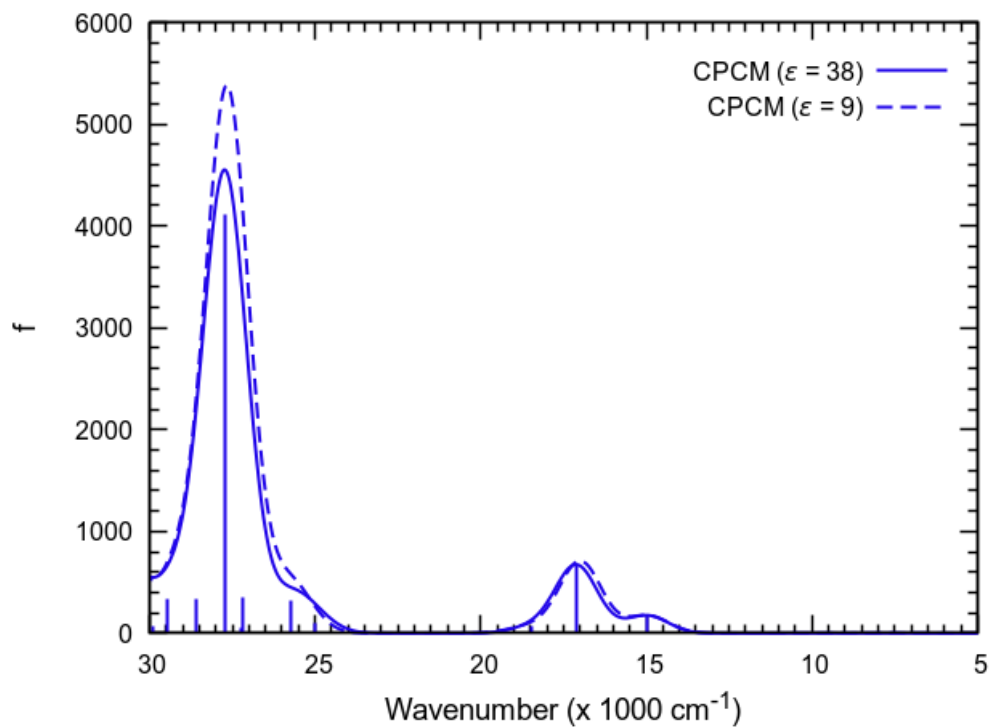


**Figure S92:** Calculated UV-vis-NIR spectra of  $\text{Ni}^{\text{II}}(\text{1B})\text{Cl}_2$  at the TDDFT (TPSSh) level.

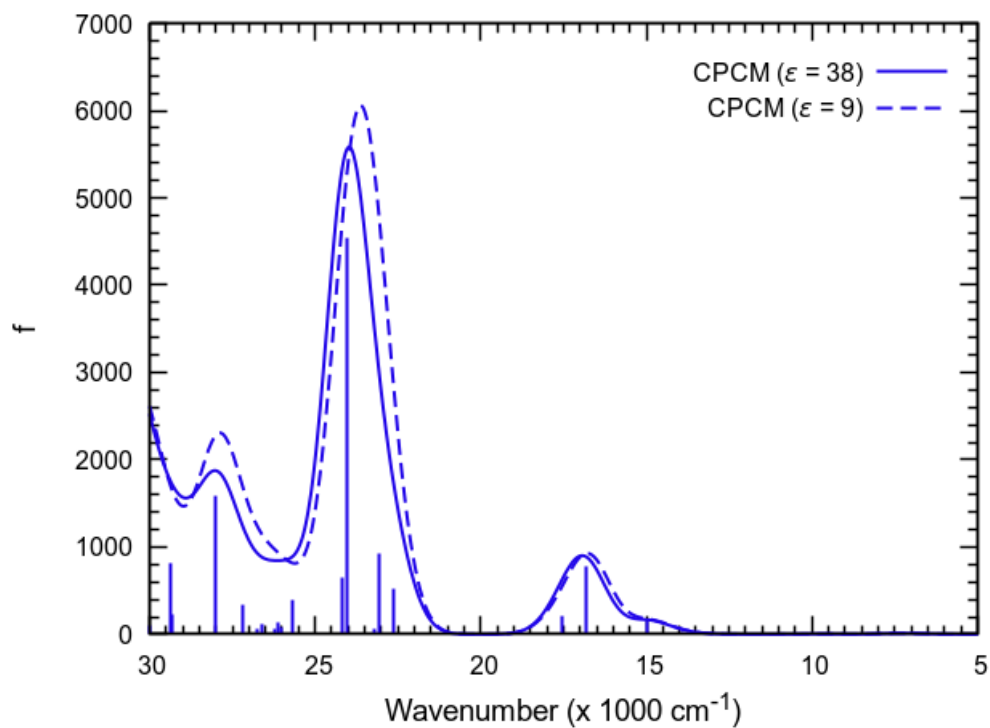


**Figure S93:** Calculated UV-vis-NIR spectra of  $\text{Ni}^{\text{II}}(\text{1B})\text{Br}_2$  at the TDDFT (TPSSh) level.

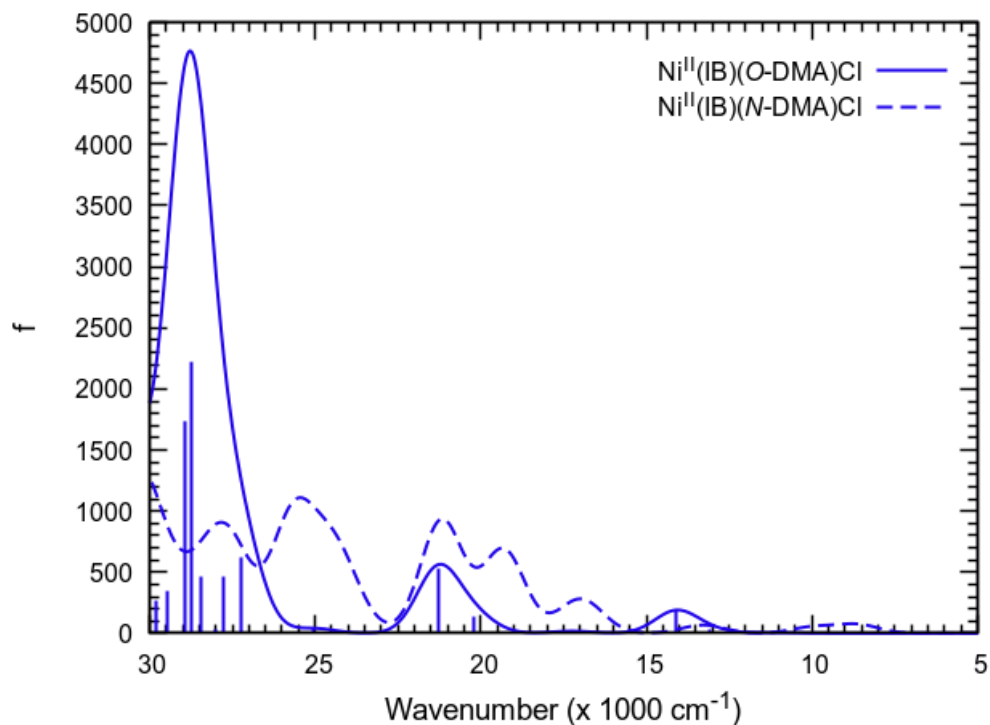


**Figure S94:** Calculated UV-vis-NIR spectra of solvent(DMA)-bound complexes  $\text{Ni}^{\text{II}}(\text{1B})(\text{O-DMA})\text{Cl}_2$  and  $\text{Ni}^{\text{II}}(\text{1B})(\text{N-DMA})\text{Cl}_2$  at the TDDFT (TPSSH) level and CPCM solvation model ( $\epsilon = 38$ ).

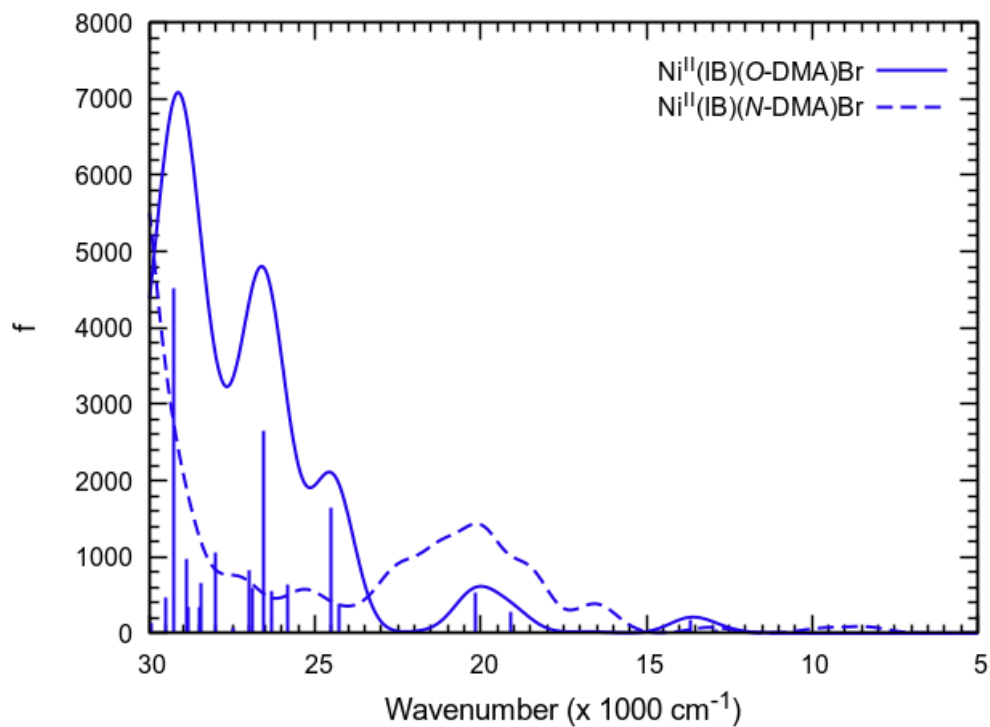


**Figure S95:** Calculated UV-vis-NIR spectra of solvent(DMA)-bound complexes  $\text{Ni}^{\text{II}}(\text{1B})(\text{O-DMA})\text{Br}_2$  and  $\text{Ni}^{\text{II}}(\text{1B})(\text{N-DMA})\text{Br}_2$  at the TDDFT (TPSSH) level and CPCM solvation model ( $\epsilon = 38$ ).

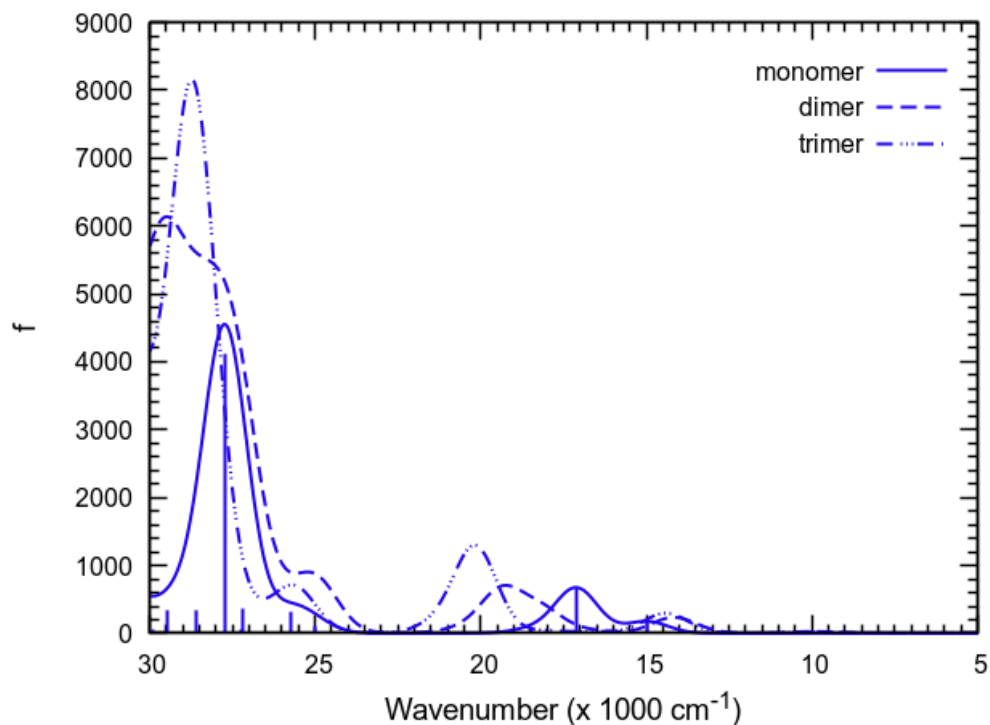


**Figure S96:** Calculated UV-vis-NIR spectra  $\text{Ni}^{\text{II}}(\text{1B})\text{Cl}_2$  in its monomeric, dimeric, and trimeric forms at the TDDFT (TPSSH) level and CPCM solvation model ( $\epsilon = 38$ ).

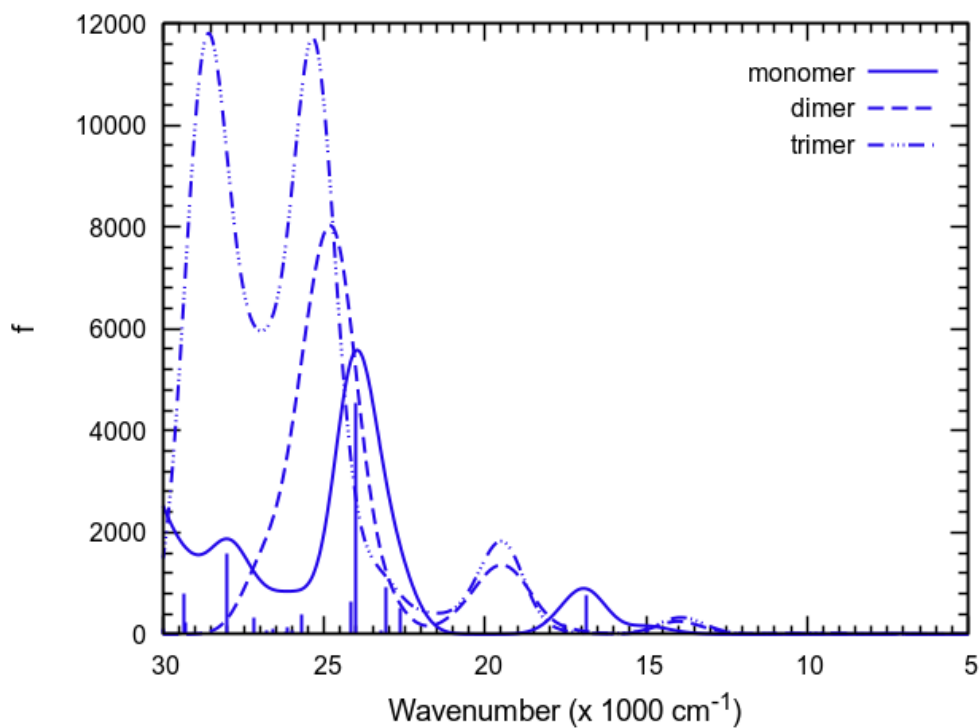


**Figure S97:** Calculated UV-vis-NIR spectra of  $\text{Ni}^{\text{II}}(\text{1B})\text{Br}_2$  in its monomeric, dimeric, and trimeric forms at the TDDFT (TPSSH) level and CPCM solvation model ( $\epsilon = 38$ ).

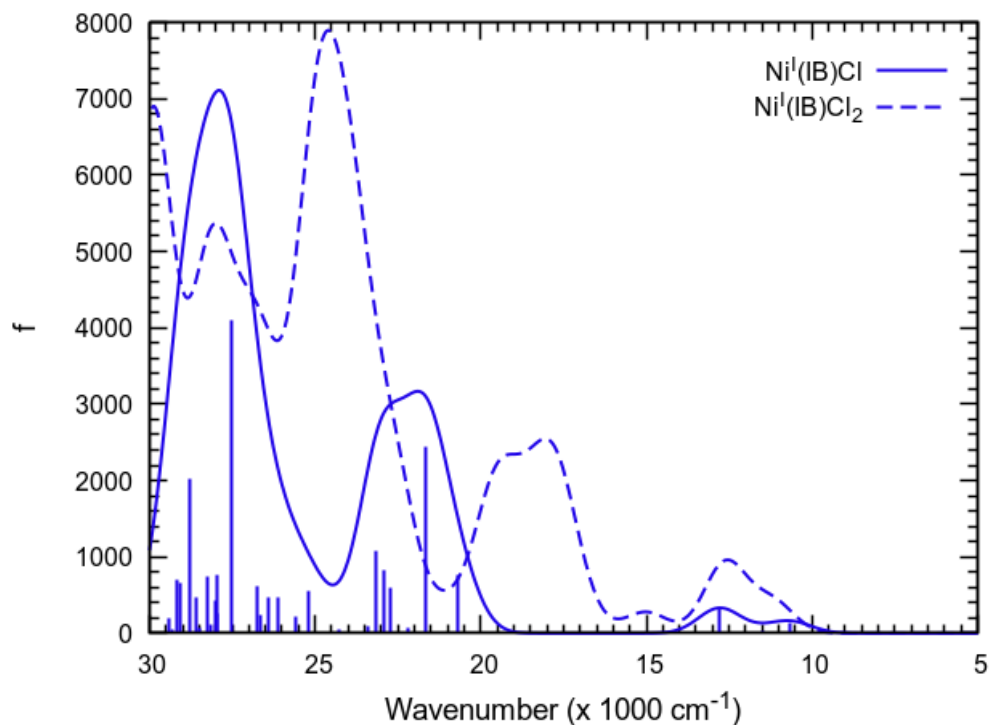


**Figure S98:** Calculated UV-vis-NIR spectra of  $\text{Ni}^{\text{I}}(\text{1B})\text{Cl}_2$  and  $\text{Ni}^{\text{I}}(\text{1B})\text{Cl}$  at the TDDFT (TPSSh) level and CPCM solvation model ( $\epsilon = 38$ ).

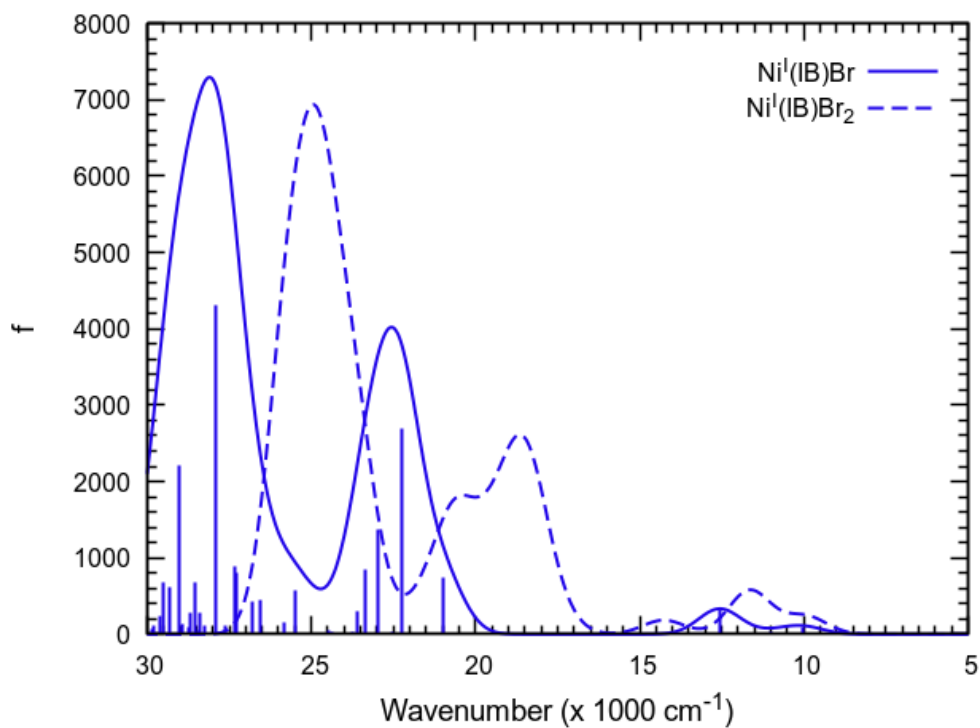


**Figure S99:** Calculated UV-vis-NIR spectra of  $\text{Ni}^{\text{I}}(\text{1B})\text{Br}_2$  and  $\text{Ni}^{\text{I}}(\text{1B})\text{Br}$  at the TDDFT (TPSSh) level and CPCM solvation model ( $\epsilon = 38$ ).



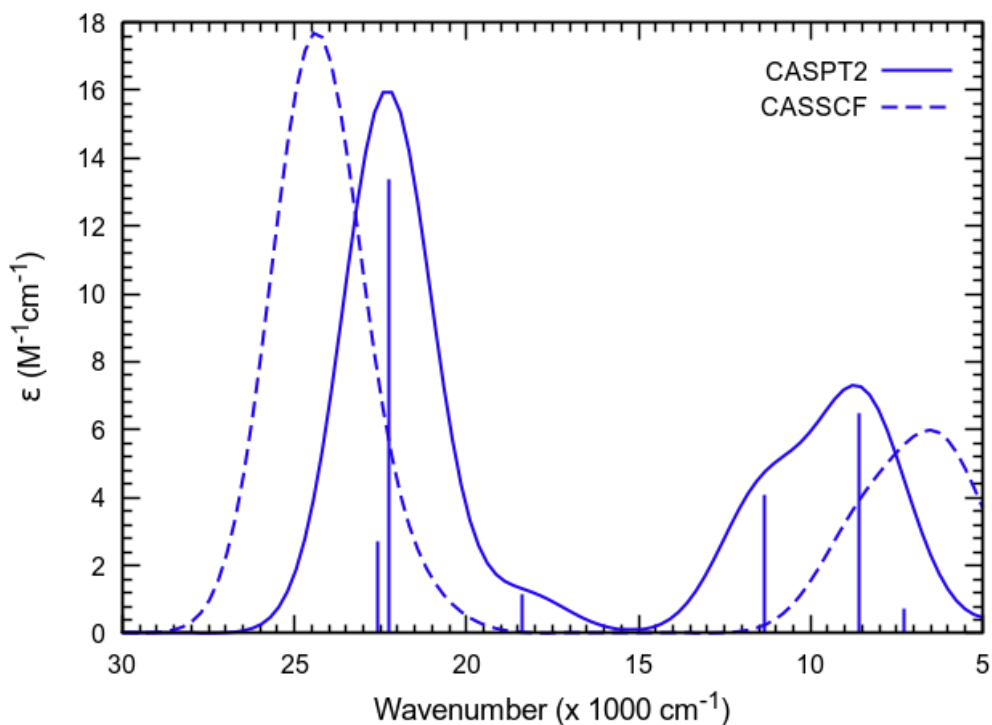


**Figure S100:** Calculated UV-vis-NIR spectra of  $\text{Ni}^{\text{II}}(\text{1B})\text{Cl}_2$  at the CASSCF and MS-CASPT2 levels with 8e,5o active space (*cf.* Figure S91) in the gas phase.

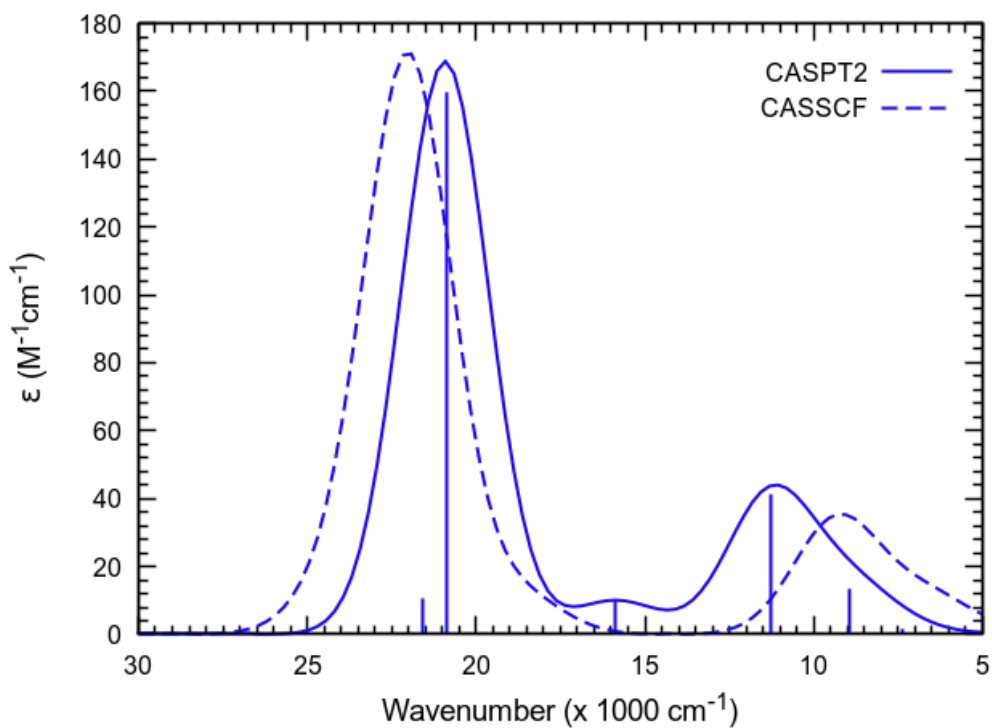


**Figure S101:** Calculated UV-vis-NIR spectra of  $\text{Ni}^{\text{II}}(\text{1B})\text{Cl}_2$  at the CASSCF and MS-CASPT2 levels with 20e,11o active space (*cf.* Figure S91) in the gas phase.

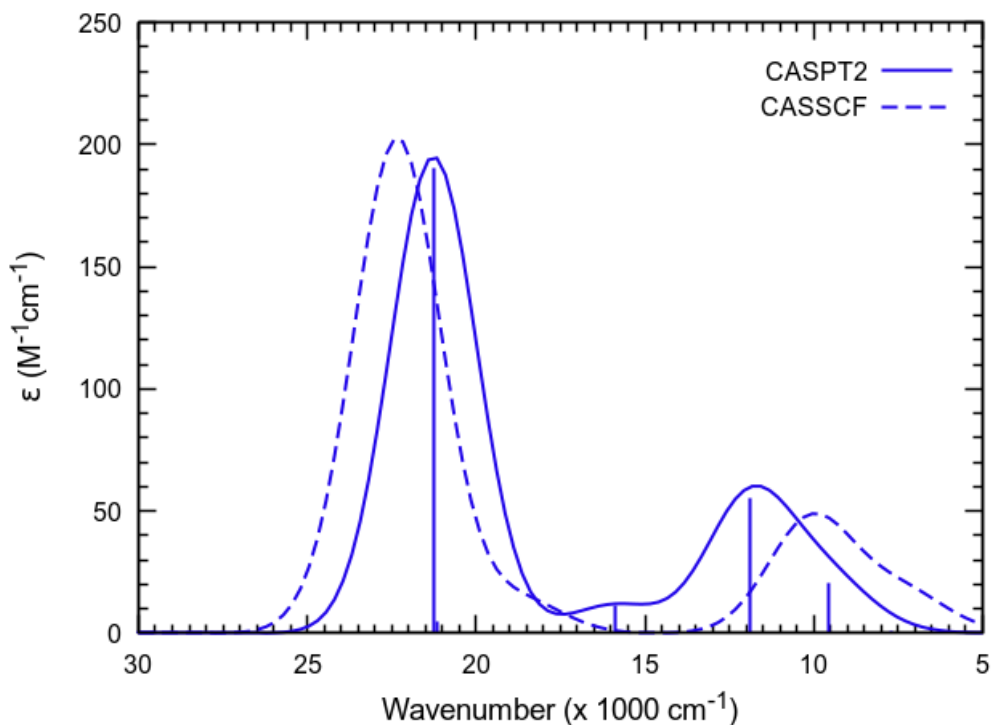


**Figure S102:** Calculated UV-vis-NIR spectra of  $\text{Ni}^{\text{II}}(\text{1B})\text{Cl}_2$  at the CASSCF and MS-CASPT2 levels with 22e,12o active space (*cf.* Figure S91) in the gas phase.

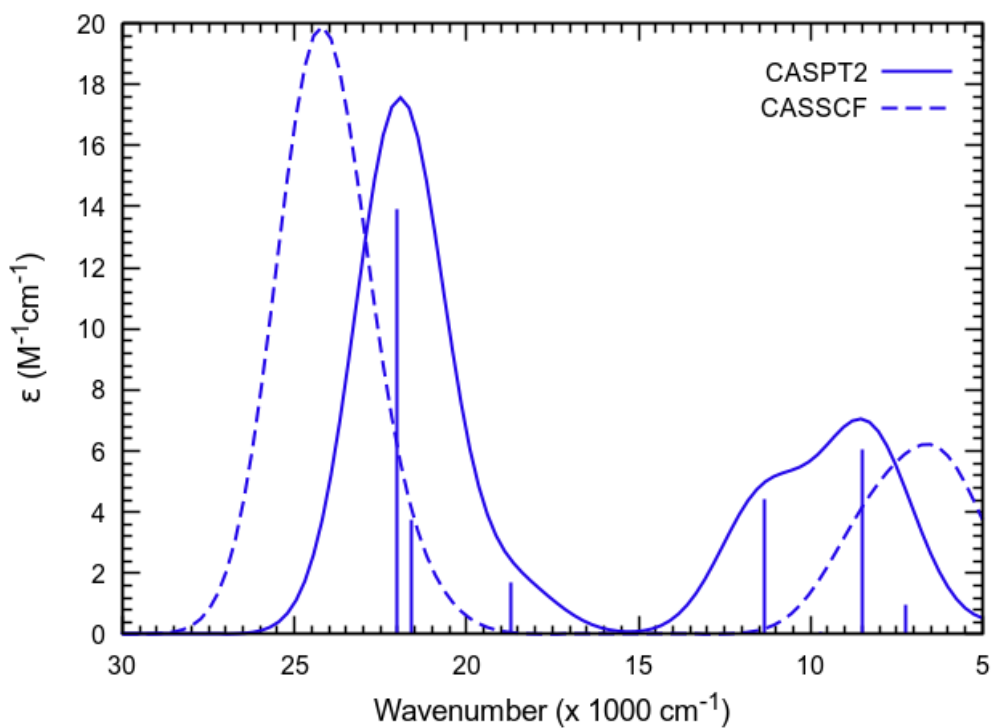


**Figure S103:** Calculated UV-vis-NIR spectra of  $\text{Ni}^{\text{II}}(\text{1B})\text{Br}_2$  at the CASSCF and MS-CASPT2 levels with 8e,5o active space (*cf.* Figure S91) in the gas phase.

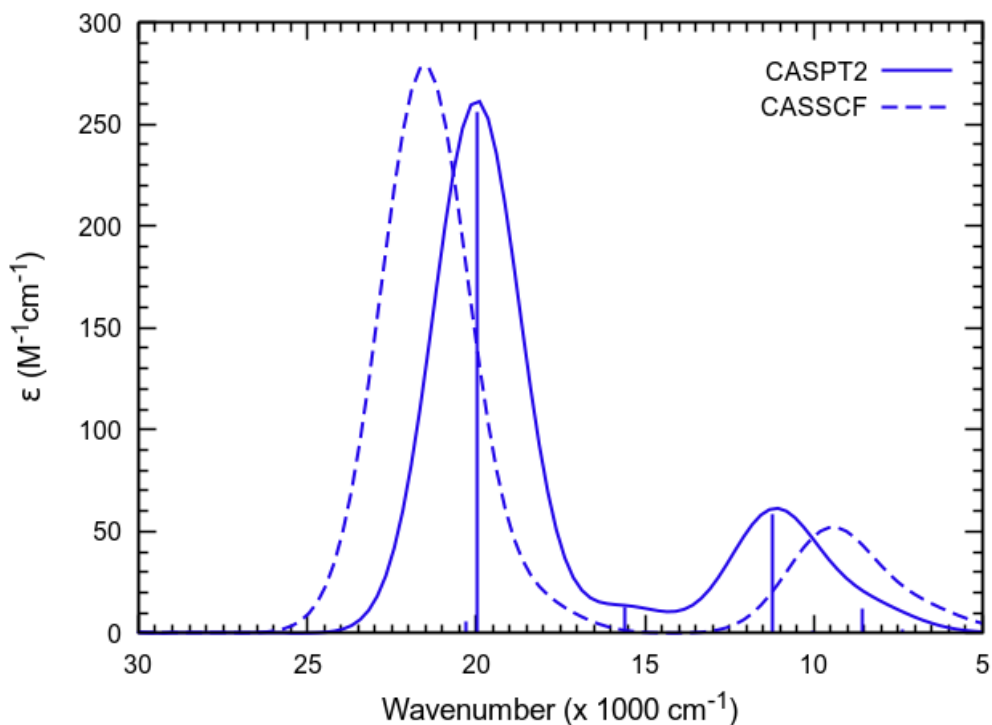


**Figure S104:** Calculated UV-vis-NIR spectra of  $\text{Ni}^{\text{I}}(\text{IB})\text{Br}_2$  at the CASSCF and MS-CASPT2 levels with 20e,11o active space (*cf.* Figure S91) in the gas phase.

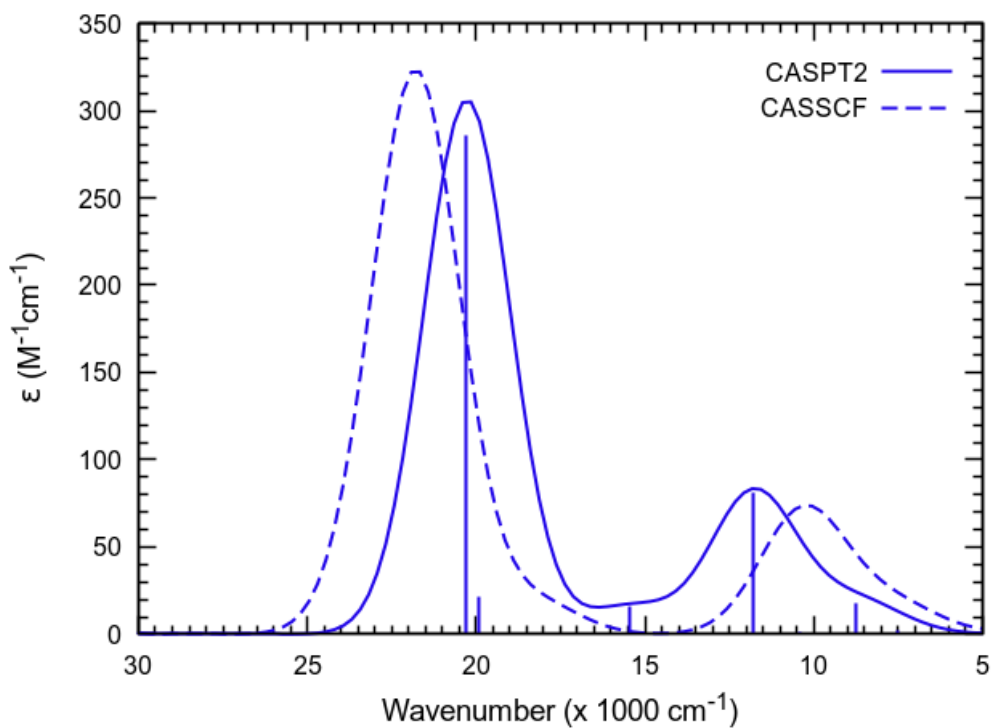


**Figure S105:** Calculated UV-vis-NIR spectra of  $\text{Ni}^{\text{II}}(\text{IB})\text{Br}_2$  at the CASSCF and MS-CASPT2 levels with 22e,12o active space (*cf.* Figure S91) in the gas phase.

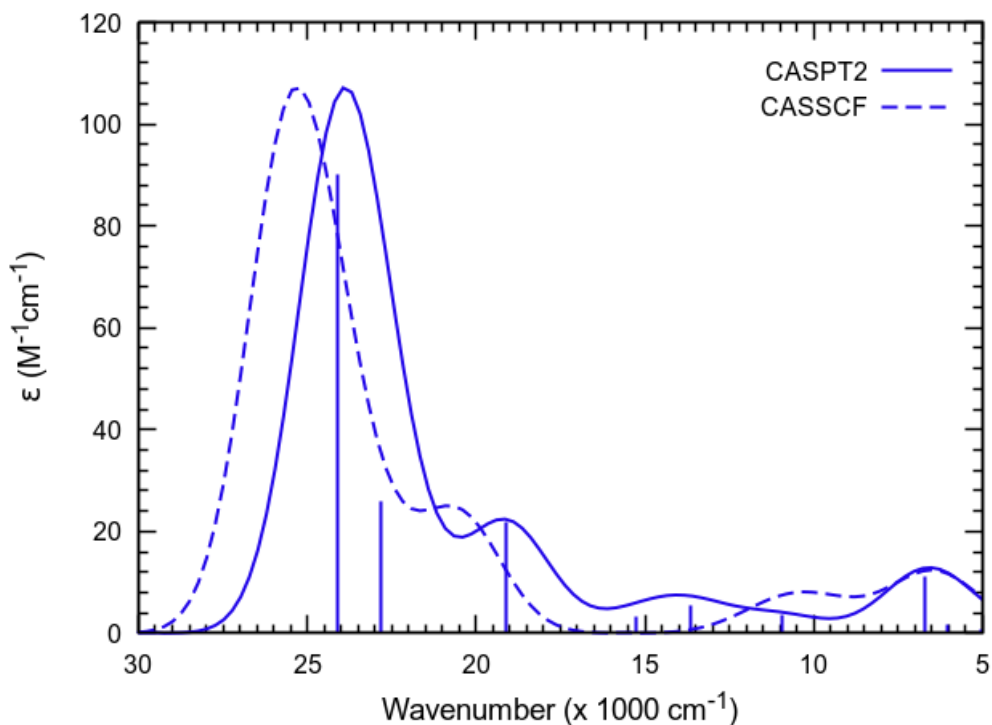


**Figure S106:** Calculated UV-vis-NIR spectra of solvent(DMA)-bound complex  $\text{Ni}^{\text{II}}(\text{1B})(\text{O-DMA})\text{Cl}_2$  at the CASSCF and MS-CASPT2 levels with 22e,12o active space (*cf.* Figure S91).

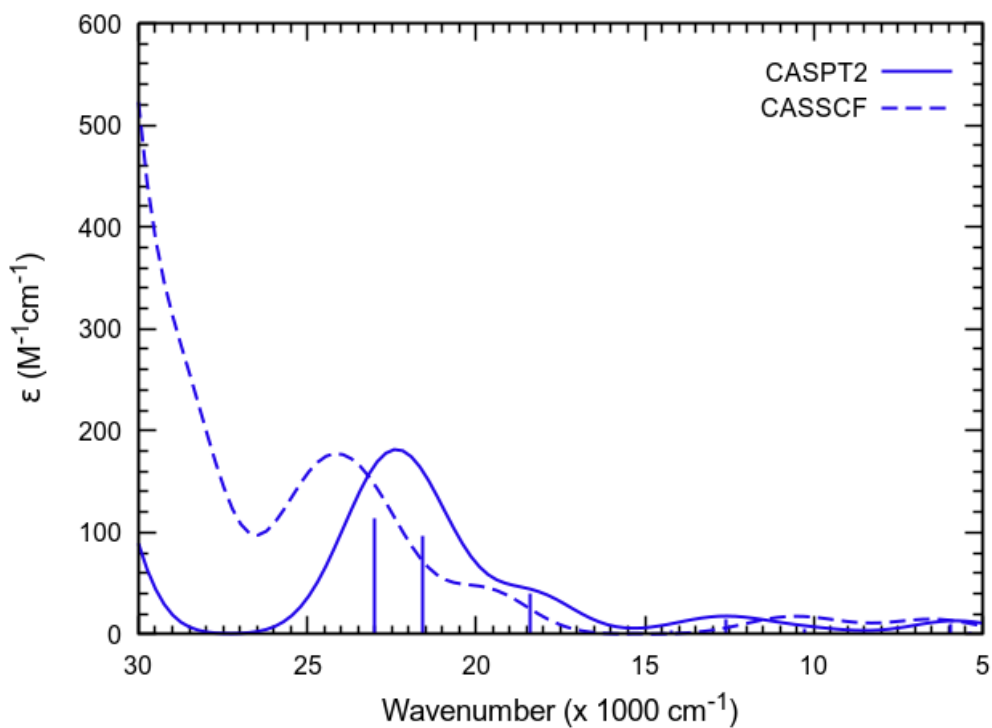


**Figure S107:** Calculated UV-vis-NIR spectra of solvent(DMA)-bound complex  $\text{Ni}^{\text{II}}(\text{1B})(\text{O-DMA})\text{Br}_2$  at the CASSCF and MS-CASPT2 levels with 22e,12o active space (*cf.* Figure S91).

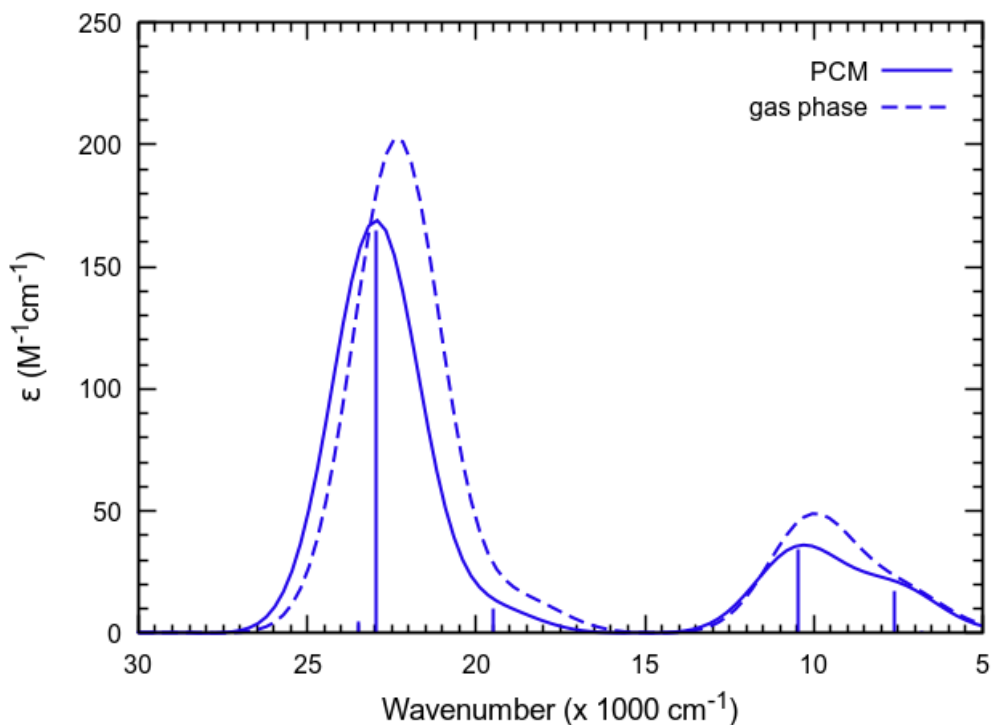


**Figure S108:** Calculated UV-vis-NIR spectra of  $\text{Ni}^{\text{II}}(\text{1B})\text{Cl}_2$  at the CASSCF level with 22e,12o active space (*cf.* Figure S91) in the gas phase vs. PCM ( $\epsilon = 38$ ) solvation model.

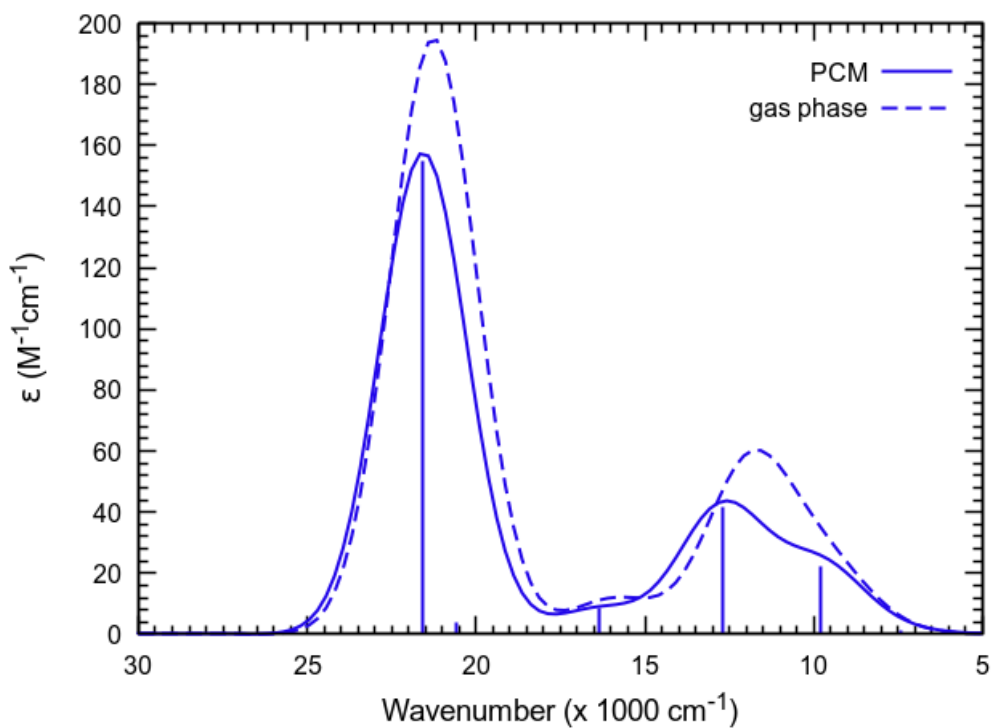


**Figure S109:** Calculated UV-vis-NIR spectra of  $\text{Ni}^{\text{II}}(\text{1B})\text{Cl}_2$  at the MS-CASPT2 level with 22e,12o active space (*cf.* Figure S91) in the gas phase vs. PCM ( $\epsilon = 38$ ) solvation model.

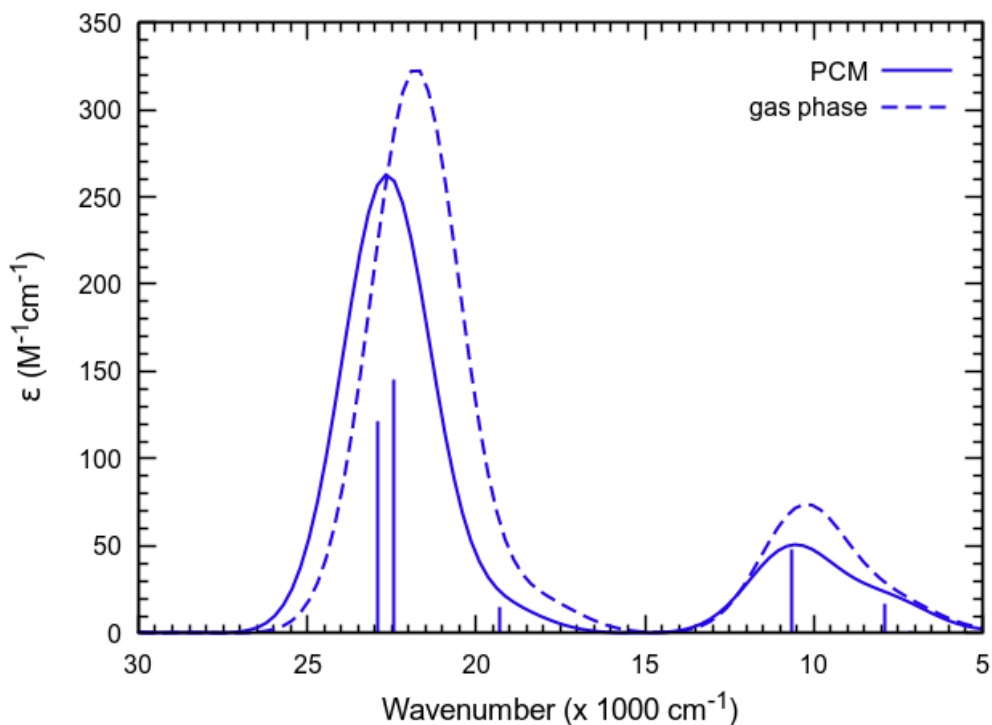


**Figure S110:** Calculated UV-vis-NIR spectra of  $\text{Ni}^{\text{II}}(\text{1B})\text{Br}_2$  at the CASSCF level with 22e,12o active space (*cf.* Figure S91) in the gas phase vs. PCM ( $\epsilon = 38$ ) solvation model.

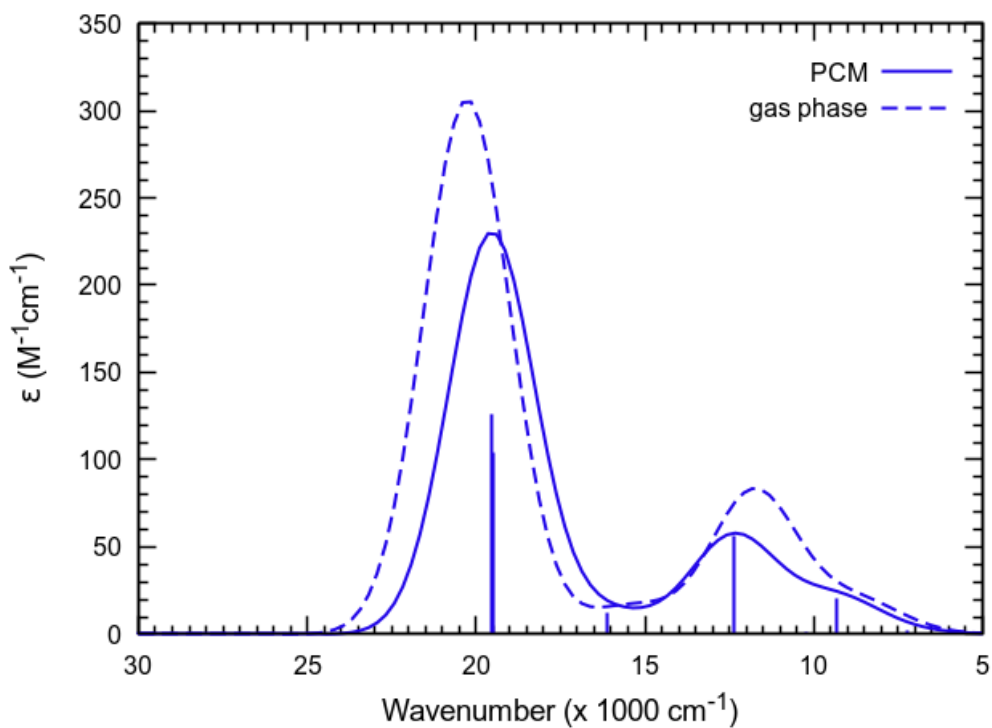


**Figure S111:** Calculated UV-vis-NIR spectra of  $\text{Ni}^{\text{II}}(\text{1B})\text{Br}_2$  at the MS-CASPT2 level with 22e,12o active space (*cf.* Figure S91) in the gas phase vs. PCM ( $\epsilon = 38$ ) solvation model.

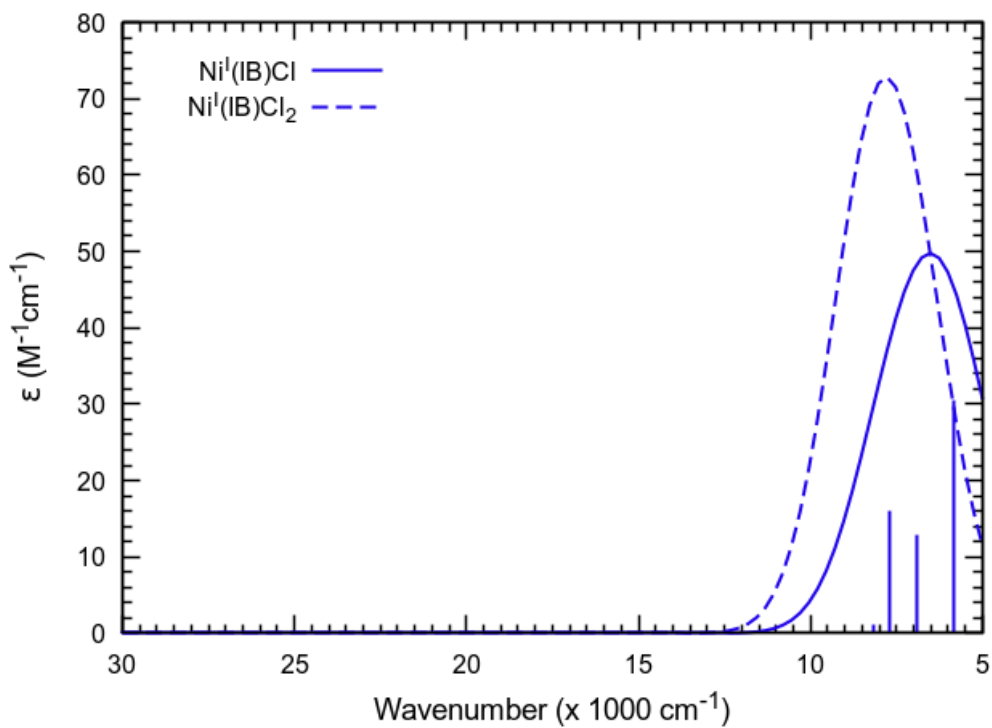


**Figure S112:** Calculated UV-vis-NIR spectra of  $\text{Ni}^{\text{I}}(\text{1B})\text{Cl}_2$  and  $\text{Ni}^{\text{I}}(\text{1B})\text{Cl}$  at the CASSCF level with 23e,12o and 17e,9o active spaces.

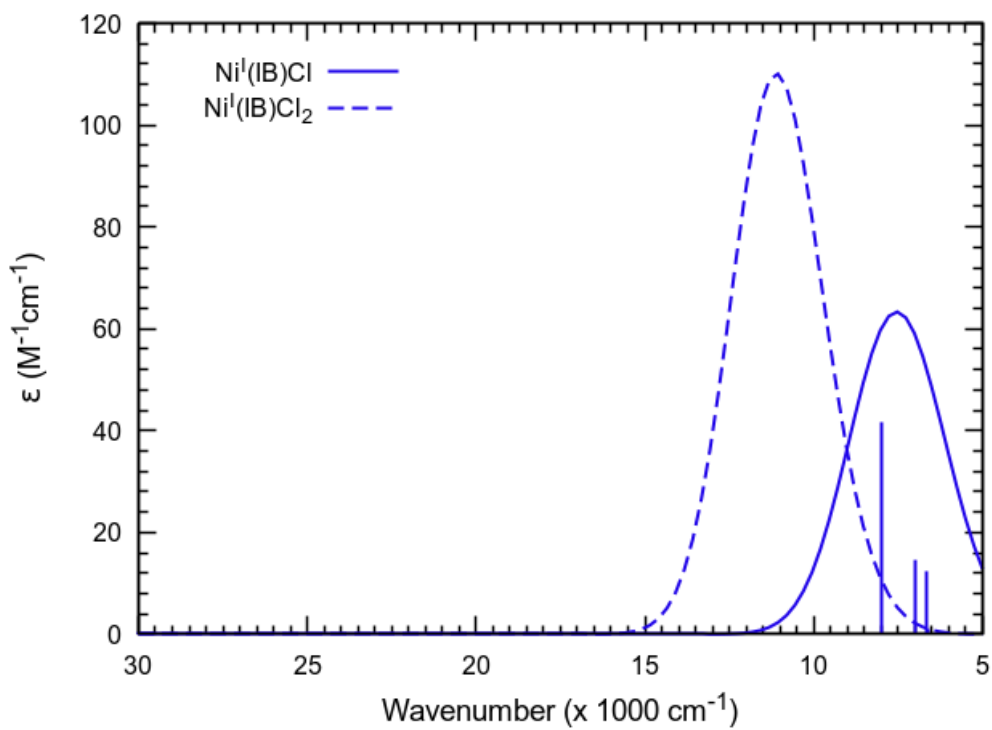


**Figure S113:** Calculated UV-vis-NIR spectra of  $\text{Ni}^{\text{I}}(\text{1B})\text{Cl}_2$  and  $\text{Ni}^{\text{I}}(\text{1B})\text{Cl}$  at the MS-CASPT2 level with 23e,12o and 17e,9o active spaces.

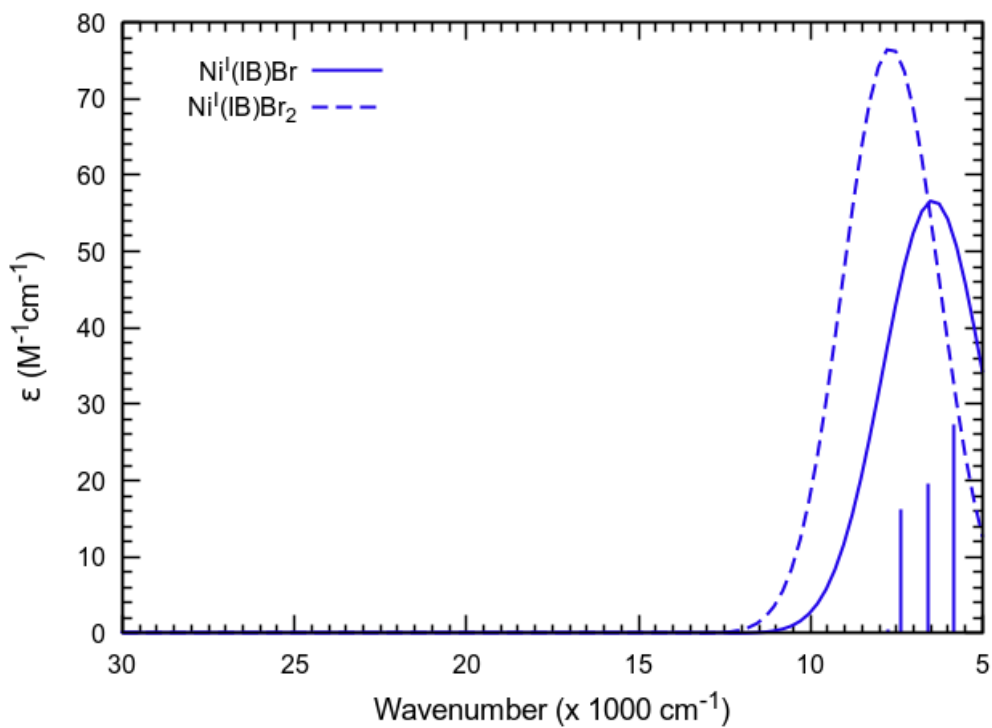


**Figure S114:** Calculated UV-vis-NIR spectra of  $\text{Ni}^{\text{I}}(\text{1B})\text{Br}_2$  and  $\text{Ni}^{\text{I}}(\text{1B})\text{Br}$  at the CASSCF level with 23e,12o and 17e,9o active spaces.

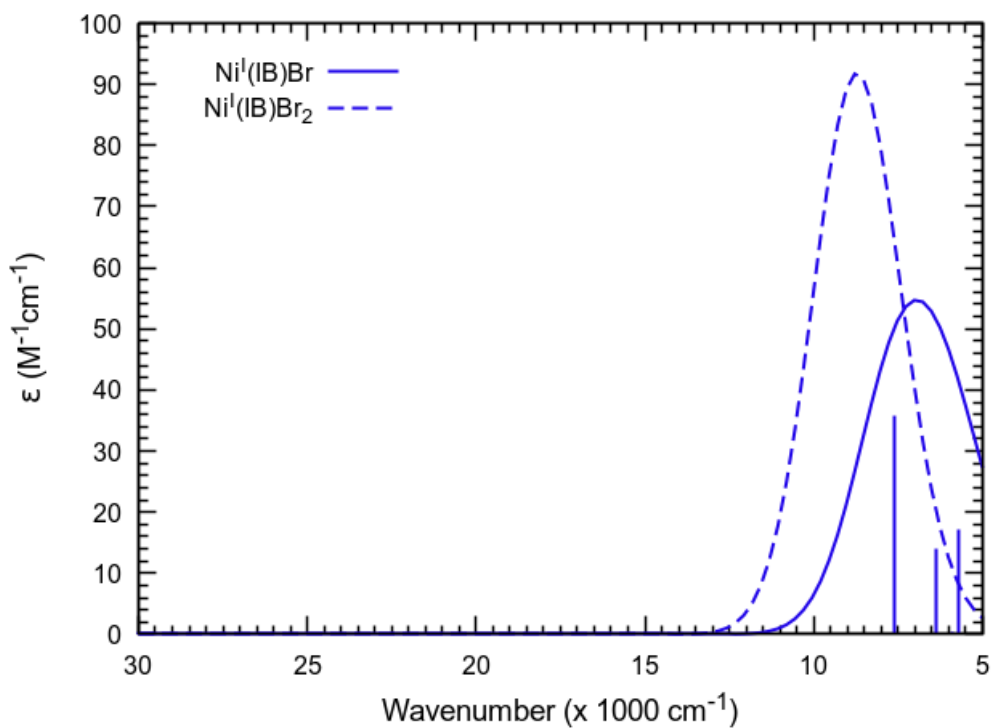


**Figure S115:** Calculated electronic absorption spectra of  $\text{Ni}^{\text{I}}(\text{1B})\text{Br}_2$  and  $\text{Ni}^{\text{I}}(\text{1B})\text{Br}$  at the MS-CASPT2 level with 23e,12o and 17e,9o active spaces.



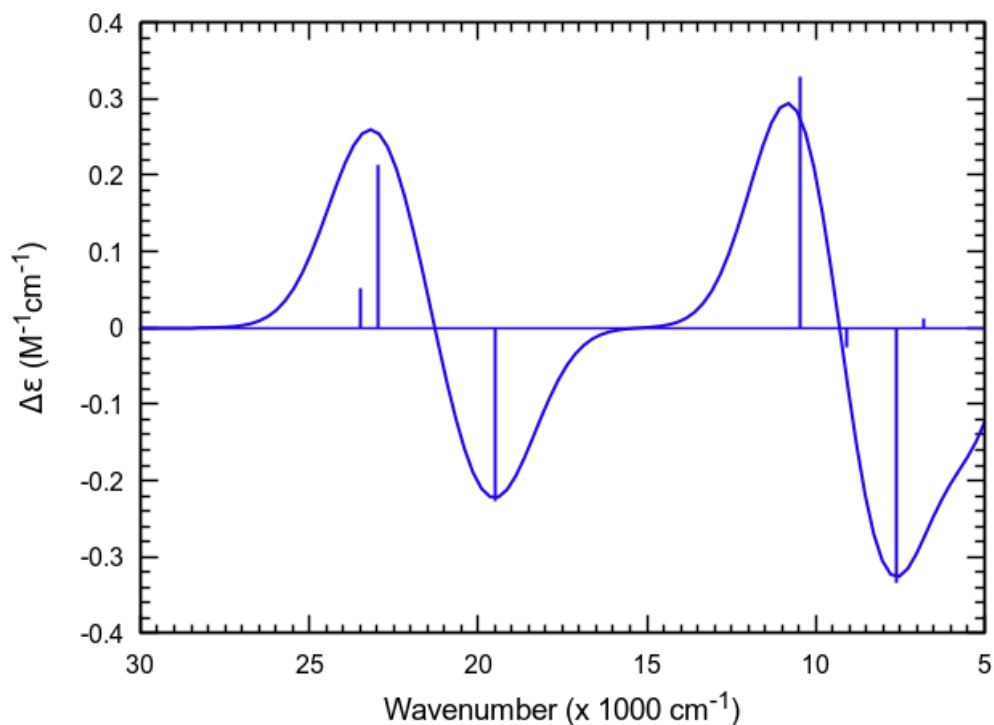


**Figure S116:** Calculated circular dichroism spectrum of  $\text{Ni}^{\text{II}}(\text{1B})\text{Cl}_2$  at the CASSCF level with 22e,12o active space (*cf.* Figure S91).

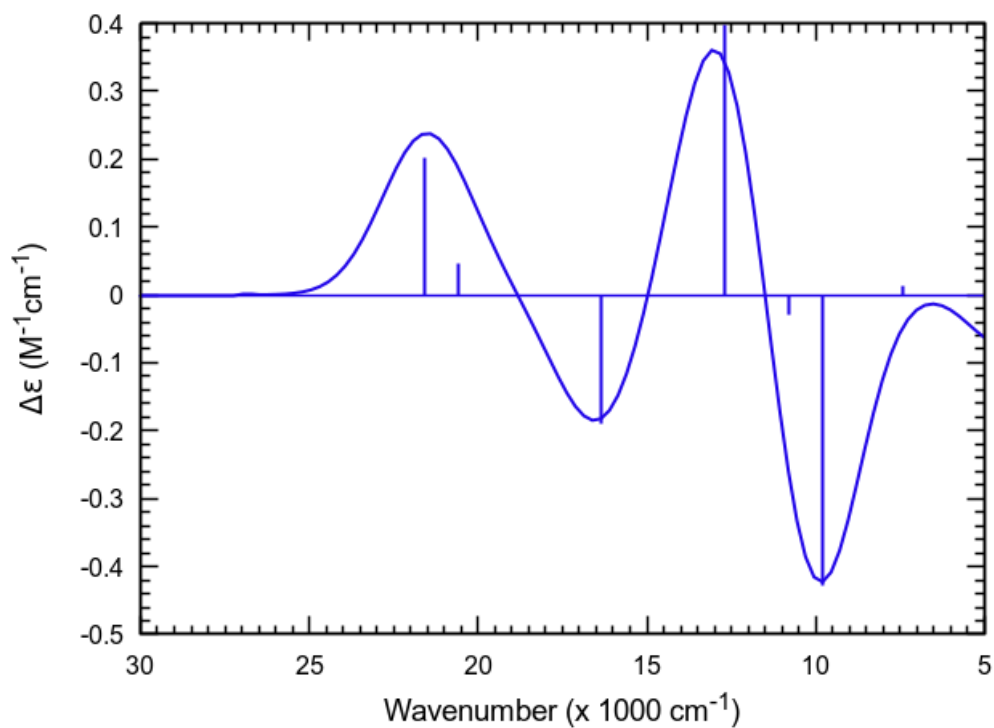


**Figure S117:** Calculated circular dichroism spectrum of  $\text{Ni}^{\text{II}}(\text{1B})\text{Cl}_2$  at the MS-CASPT2 level with 22e,12o active space (*cf.* Figure S91).

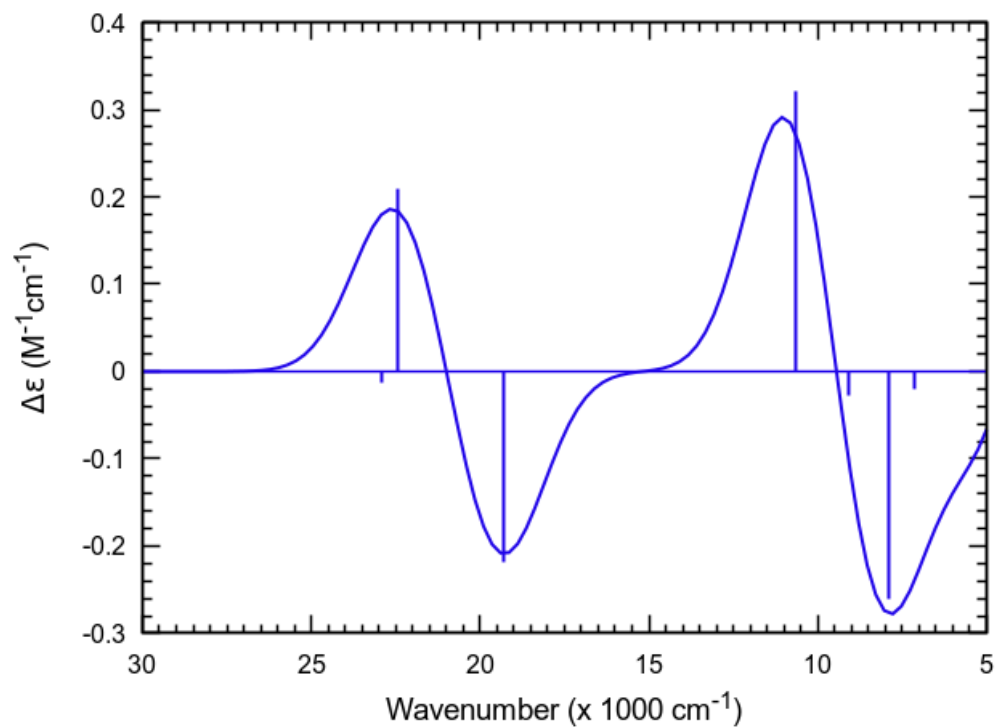


**Figure S118:** Calculated circular dichroism spectrum of **Ni(II)Br<sub>2</sub>** at the CASSCF level with 22e,12o active space (*cf.* Figure S91).

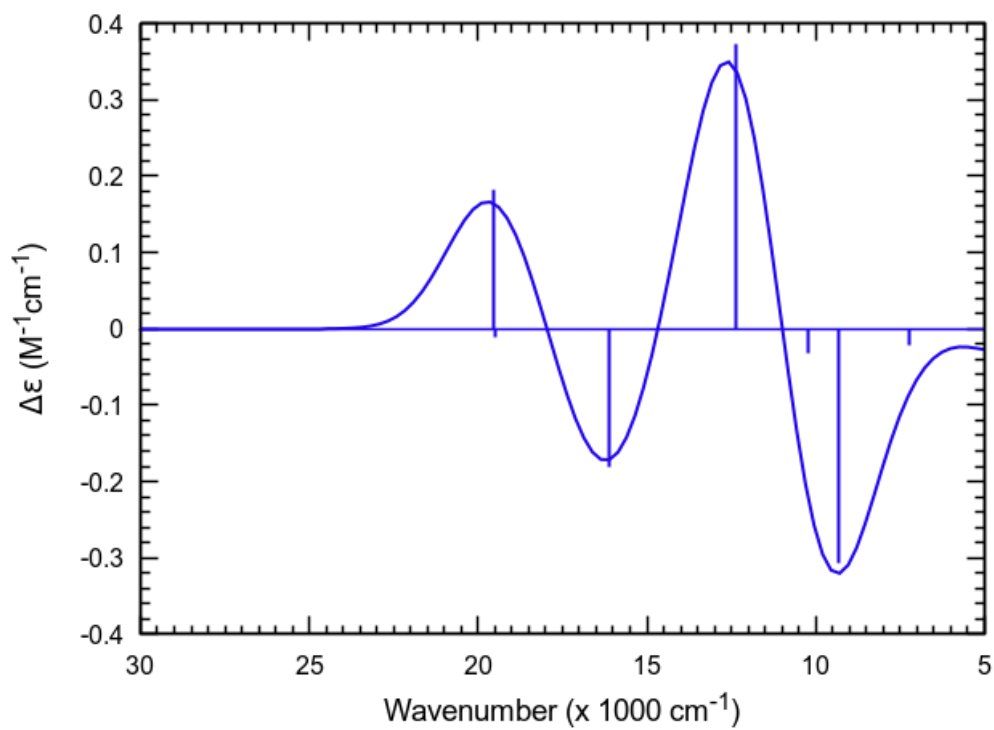


**Figure S119:** Calculated circular dichroism spectrum of **Ni(II)Br<sub>2</sub>** at the MS-CASPT2 level with 22e,12o active space (*cf.* Figure S91).

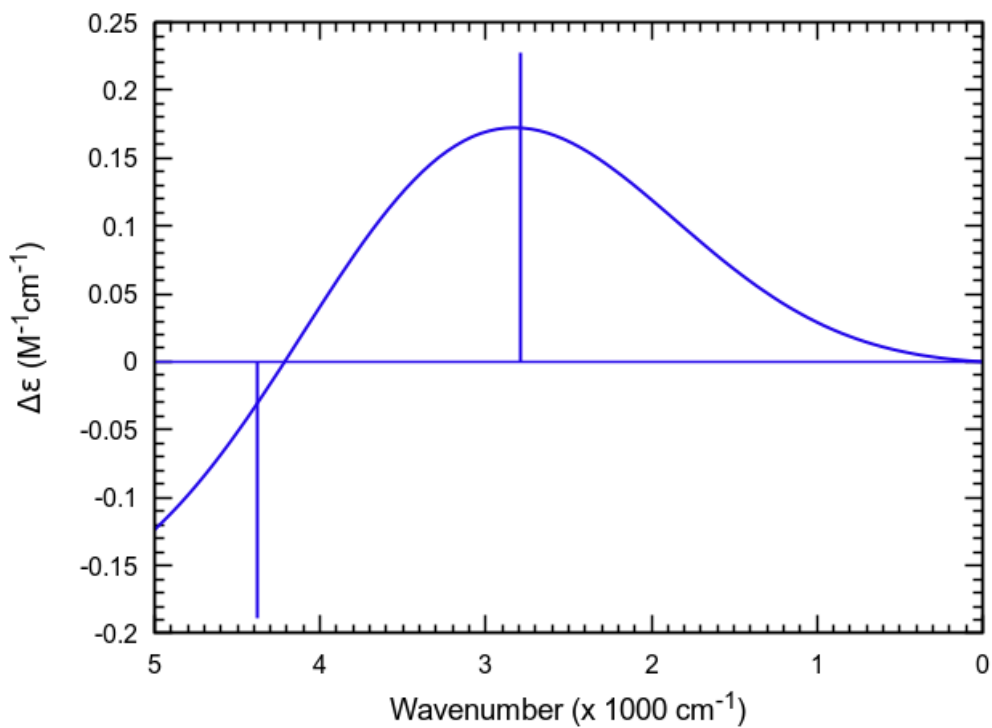


**Figure S120:** Calculated circular dichroism spectrum of  $\text{Ni}^{\text{II}}(\text{1B})\text{Cl}_2$  at the CASSCF level with 22e,12o active space (*cf.* Figure S91) in the 0-5000  $\text{cm}^{-1}$  energy region.

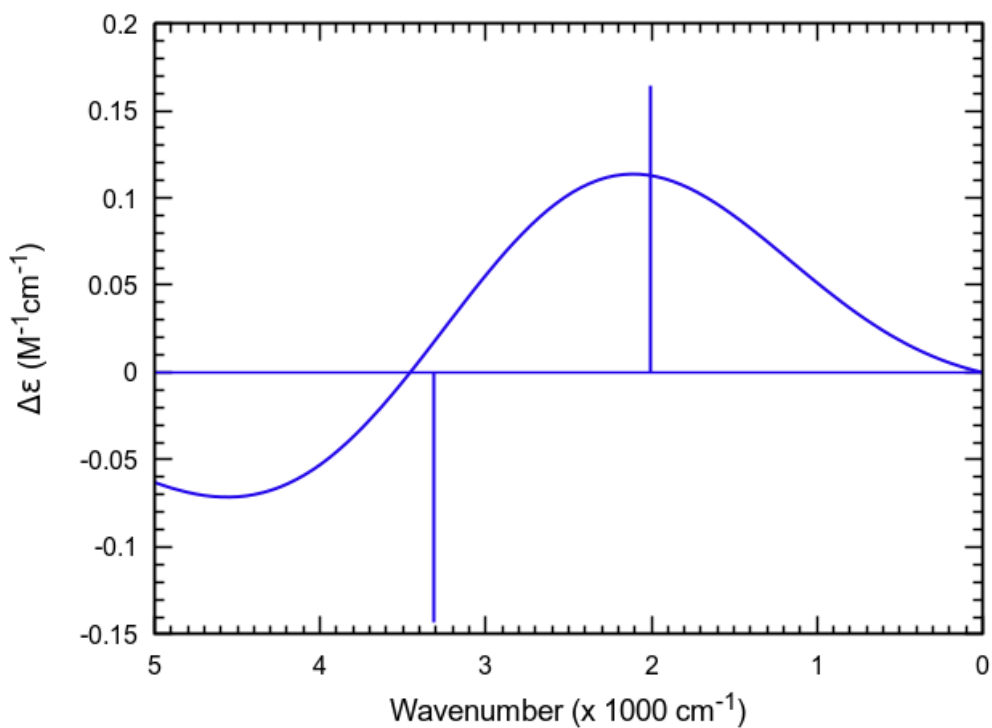


**Figure S121:** Calculated circular dichroism spectrum of  $\text{Ni}^{\text{II}}(\text{1B})\text{Cl}_2$  at the MS-CASPT2 level with 22e,12o active space (*cf.* Figure S91) in the 0-5000  $\text{cm}^{-1}$  energy region.

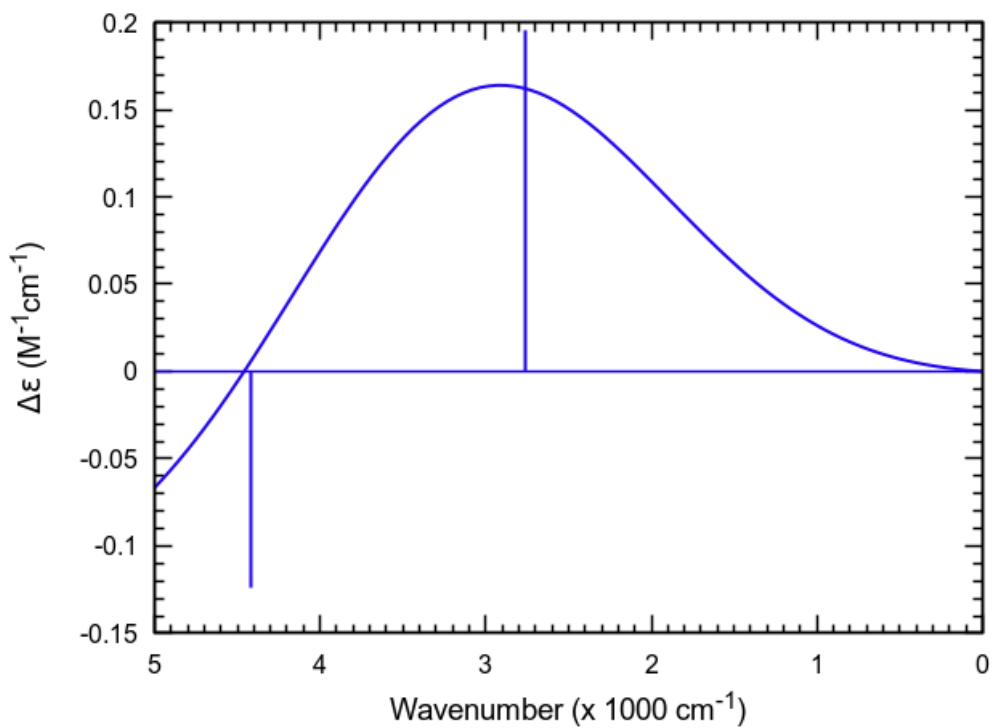


**Figure S122:** Calculated circular dichroism spectrum of  $\text{Ni}^{\text{II}}(\text{1B})\text{Br}_2$  at the CASSCF level with 22e,12o active space (*cf.* Figure S91) in the 0-5000  $\text{cm}^{-1}$  energy region.

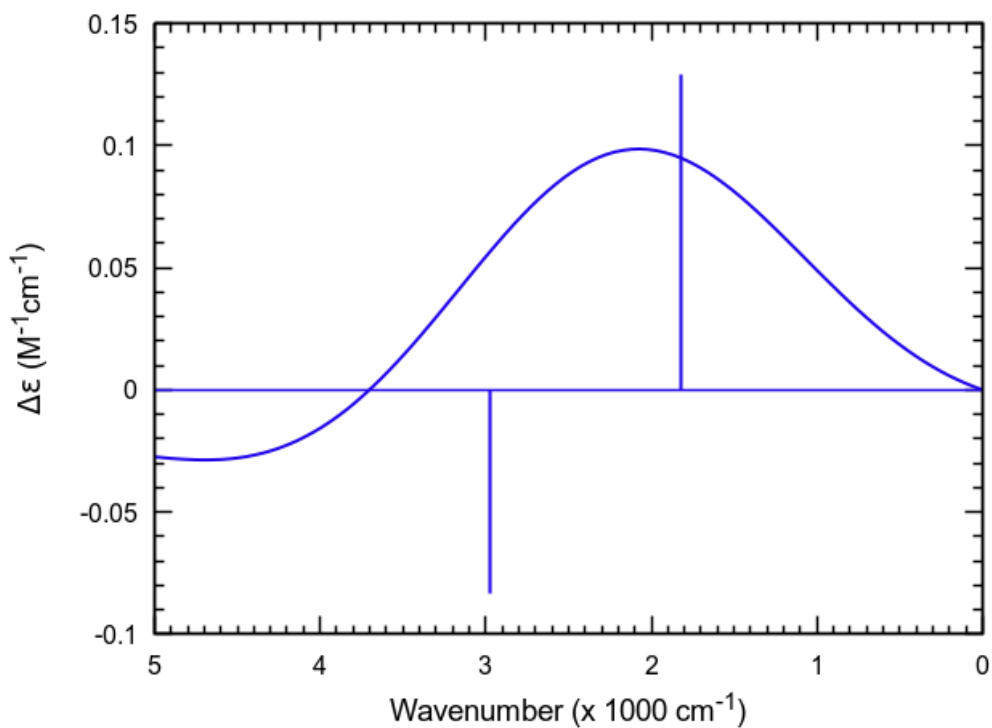


**Figure S123:** Calculated circular dichroism spectrum of  $\text{Ni}^{\text{II}}(\text{1B})\text{Br}_2$  at the MS-CASPT2 level with 22e,12o active space (*cf.* Figure S91) in the 0-5000  $\text{cm}^{-1}$  energy region.

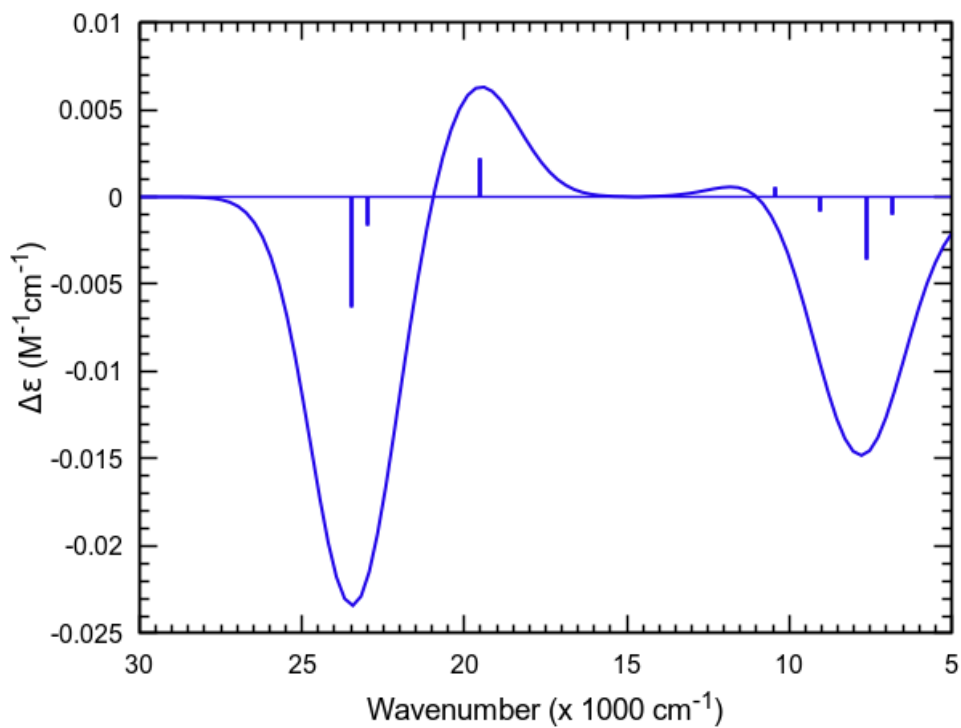


**Figure S124:** Calculated magnetic circular dichroism spectrum of  $\text{Ni}^{\text{II}}(\text{1B})\text{Cl}_2$  at the CASSCF level with 22e,12o active space (*cf.* Figure S91).

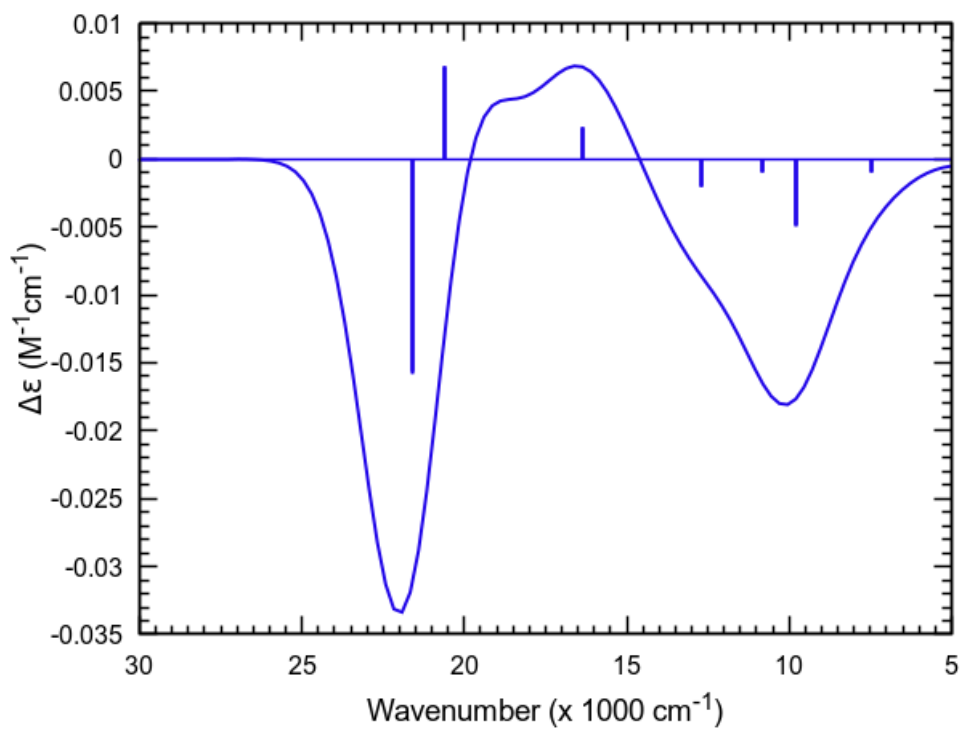


**Figure S125:** Calculated magnetic circular dichroism spectrum of  $\text{Ni}^{\text{II}}(\text{1B})\text{Cl}_2$  at the MS-CASPT2 level with 22e,12o active space (*cf.* Figure S91).

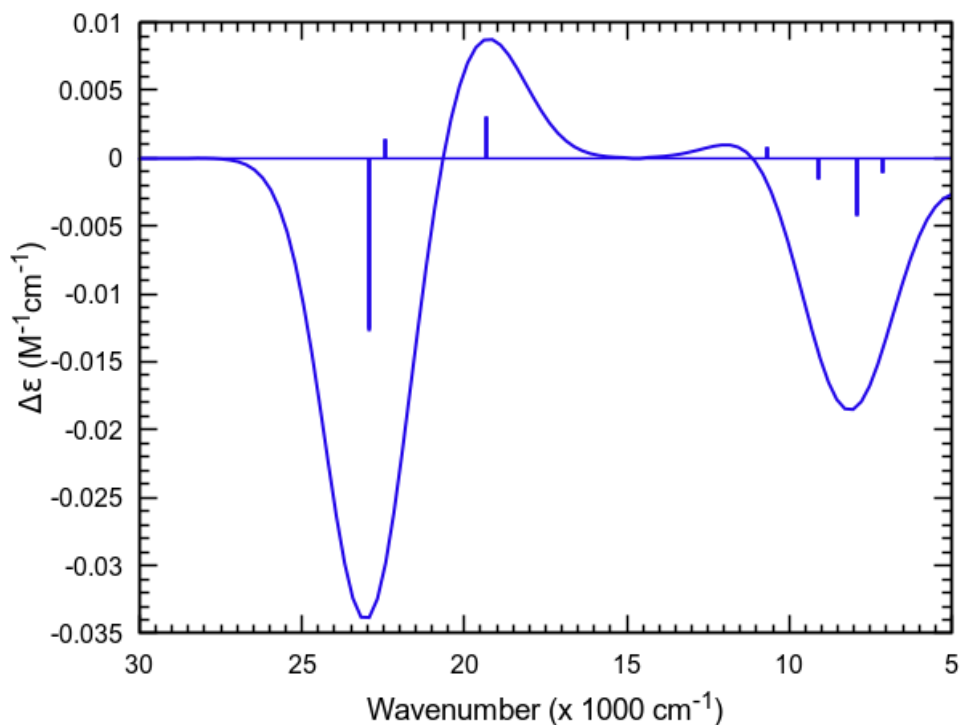


**Figure S126:** Calculated magnetic circular dichroism spectrum of  $\text{Ni}^{\text{II}}(\text{1B})\text{Br}_2$  at the CASSCF level with 22e,12o active space (*cf.* Figure S91).

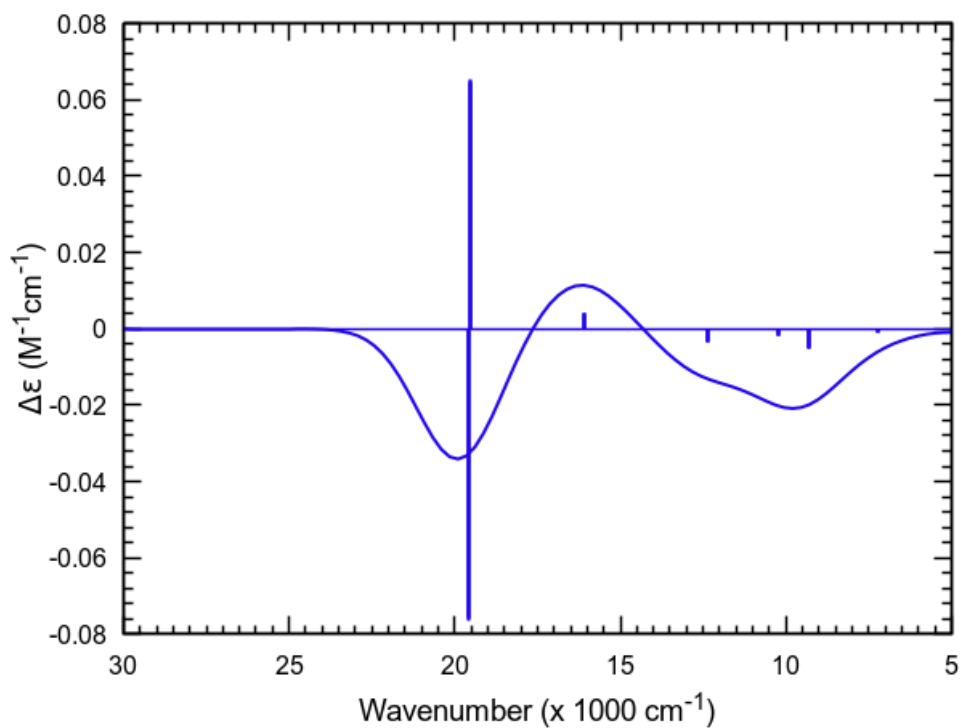


**Figure S127:** Calculated magnetic circular dichroism spectrum of  $\text{Ni}^{\text{II}}(\text{1B})\text{Br}_2$  at the MS-CASPT2 level with 22e,12o active space (*cf.* Figure S91).

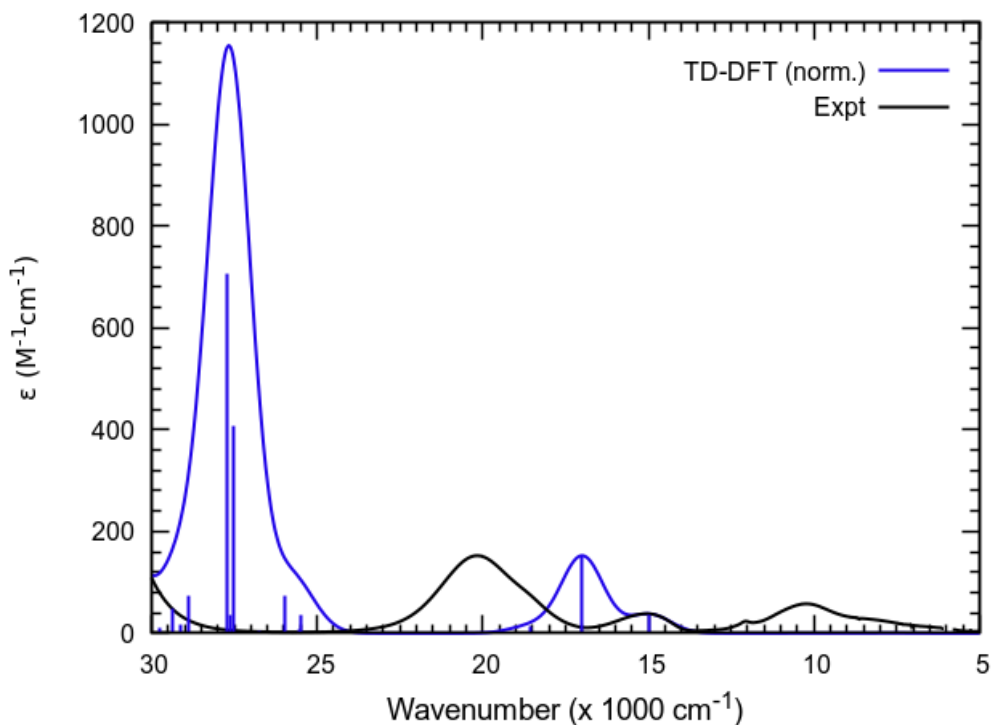


**Figure S128:** Comparison of experimental vs. calculated UV-vis-NIR spectrum of  $\text{Ni}^{\text{II}}(\text{1B})\text{Cl}_2$  at the TDDFT (TPSSH) level with CPCM solvation model ( $\epsilon = 38$ ).

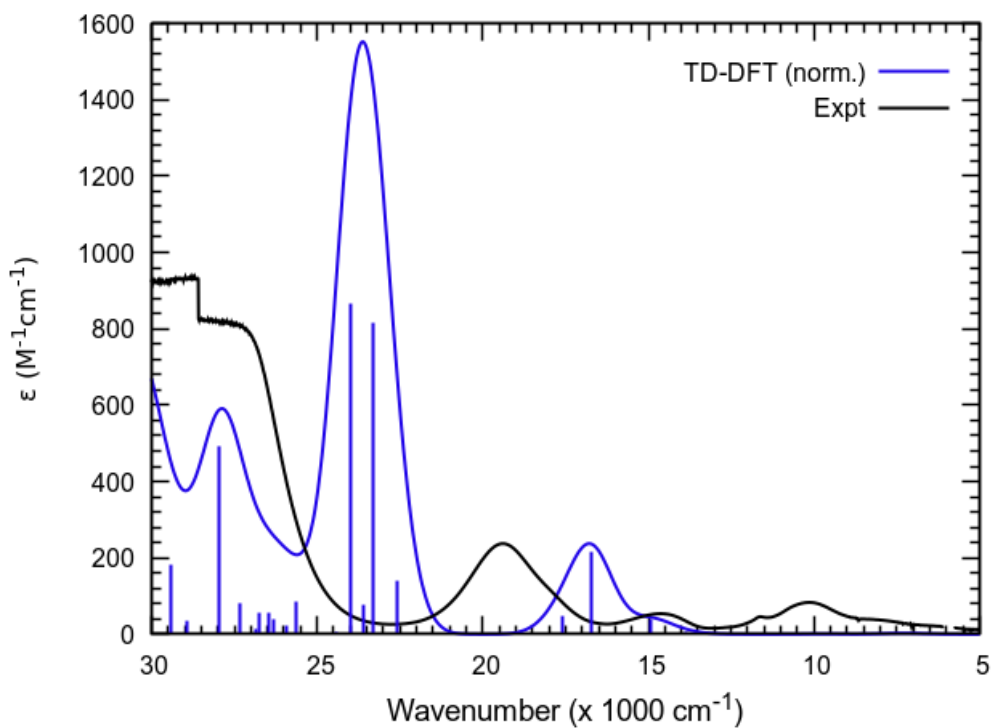


**Figure S129:** Comparison of experimental vs. calculated UV-vis-NIR spectrum of  $\text{Ni}^{\text{II}}(\text{1B})\text{Br}_2$  at the TDDFT (TPSSH) level with CPCM solvation model ( $\epsilon = 38$ ).

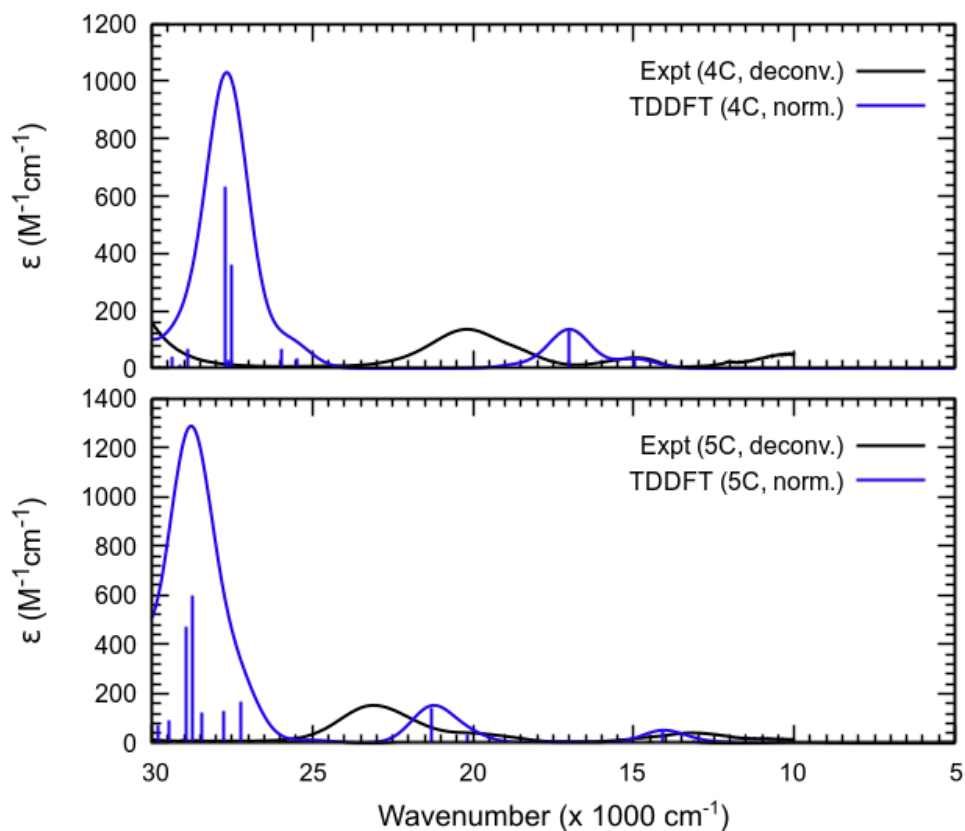


**Figure S130:** Comparison of UV-vis-NIR spectra of four-coordinate  $\text{Ni}^{\text{II}}(\text{1B})\text{Cl}_2$  (4C) and five-coordinate (5C)  $\text{Ni}^{\text{II}}(\text{1B})(\text{DMA})\text{Cl}_2$ , as deconvolved from variable-temperature UV-vis-NIR spectra in **Figure 7** vs. calculated spectra of  $\text{Ni}^{\text{II}}(\text{1B})\text{Cl}_2$  and  $\text{Ni}^{\text{II}}(\text{1B})(\text{O-DMA})\text{Cl}_2$  at the TDDFT (TPSSH) level with CPCM solvation model ( $\epsilon = 38$ ).



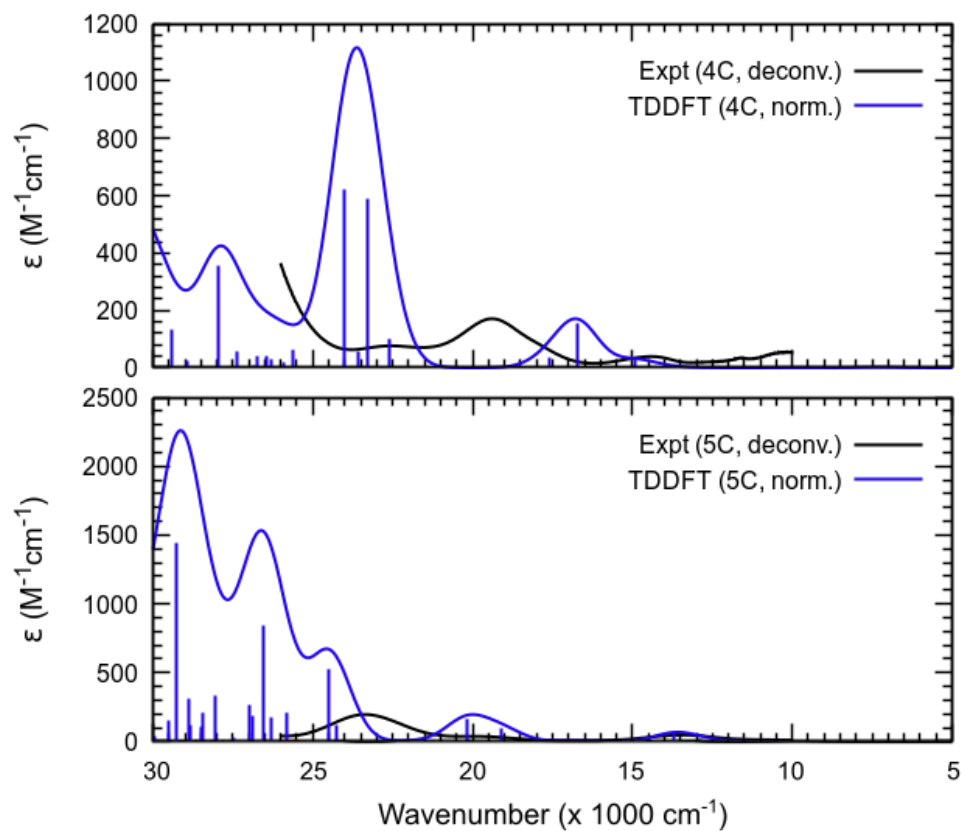


**Figure S131:** Comparison of UV-vis-NIR spectra of four-coordinate  $\text{Ni}^{\text{II}}(\text{1B})\text{Br}_2$  (4C) and five-coordinate (5C)  $\text{Ni}^{\text{II}}(\text{1B})(\text{DMA})\text{Br}_2$ , as deconvolved from variable-temperature UV-vis-NIR vs. calculated spectra of  $\text{Ni}^{\text{II}}(\text{1B})\text{Br}_2$  and  $\text{Ni}^{\text{II}}(\text{1B})(\text{O-DMA})\text{Br}_2$  at the TDDFT (TPSSH) level with CPCM solvation model ( $\epsilon = 38$ ).

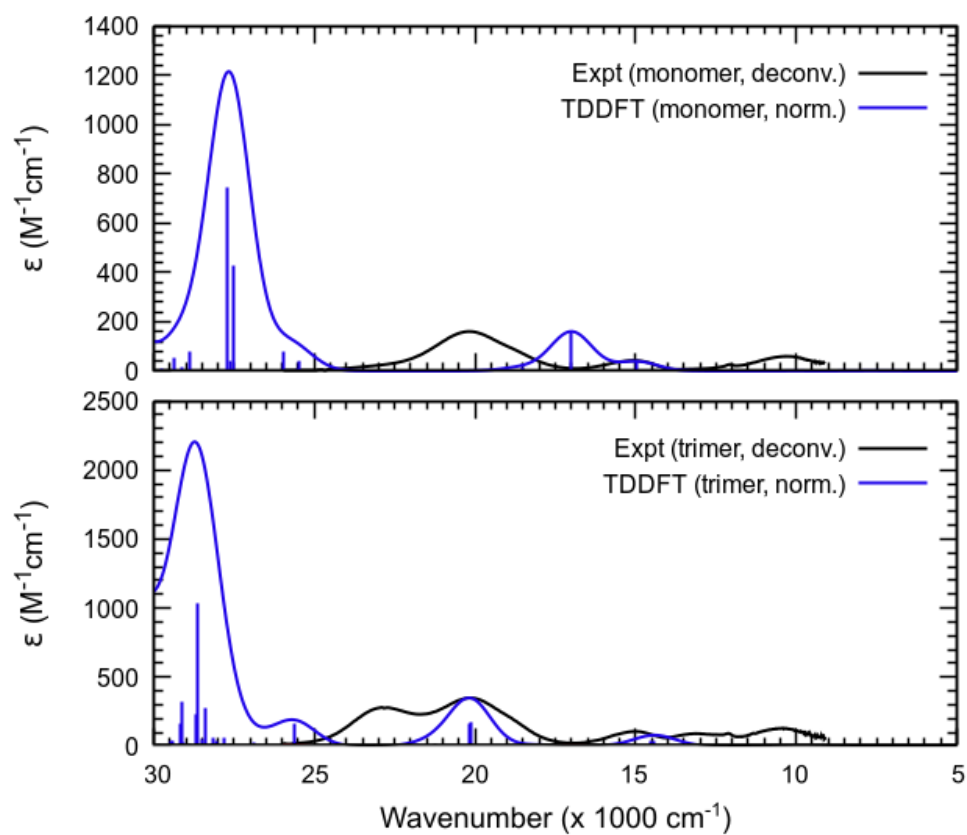


**Figure S132:** Comparison of UV-vis-NIR spectra of  $\text{Ni}^{\text{II}}(\text{1B})\text{Cl}_2$  monomer and trimer, as deconvolved from variable-temperature UV-vis-NIR in **Figure 7** vs. calculated spectra of  $\text{Ni}^{\text{II}}(\text{1B})\text{Cl}_2$  monomer and trimer at the TDDFT (TPSSH) level with CPCM solvation model ( $\epsilon = 38$ ).

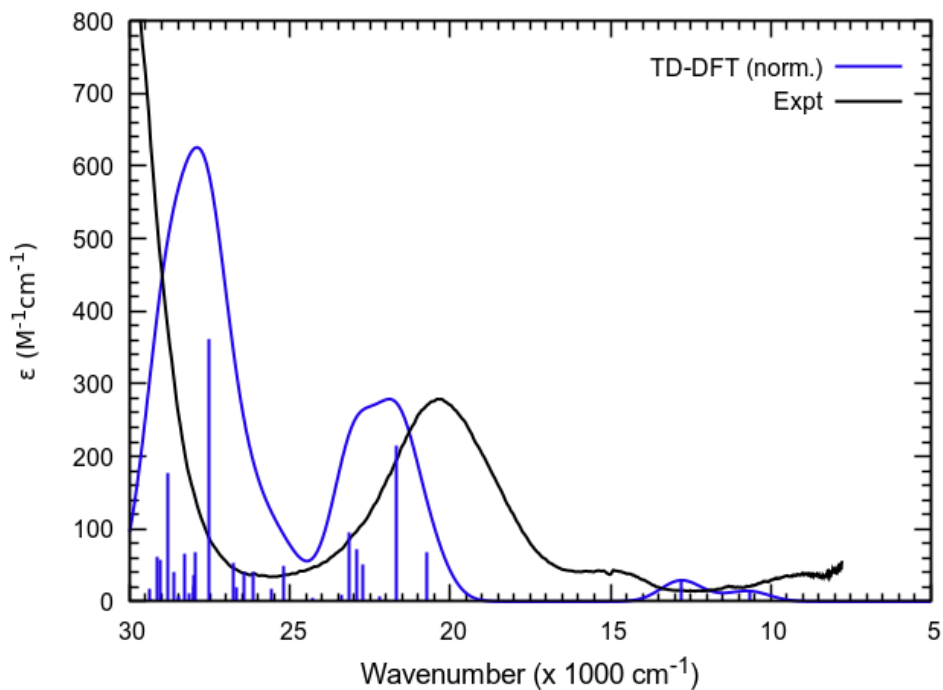


**Figure S133:** Comparison of experimental UV-vis-NIR spectrum of  $\text{Ni}^{\text{II}}(\text{1B})\text{Cl}_2$  collected after five minutes of controlled potential electrolysis at  $-1.50 \text{ V}$  vs.  $\text{Fc}^{+/0}$  in DCM vs. calculated UV-vis-NIR spectrum of  $\text{Ni}^{\text{I}}(\text{1B})\text{Cl}$  at the TDDFT (TPSSH/CPCM) level.

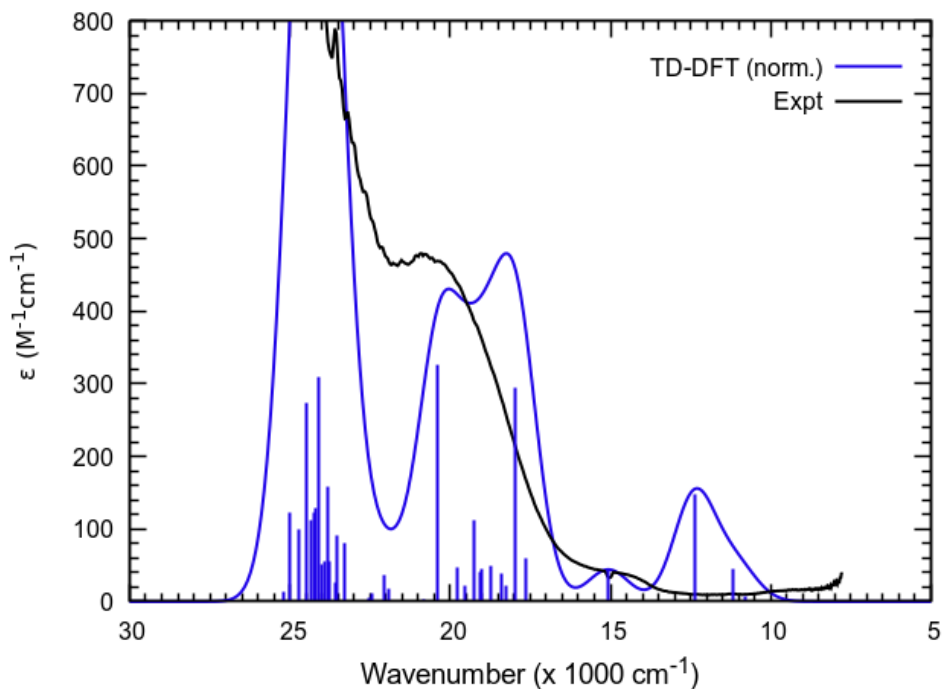


**Figure S134:** Comparison of experimental UV-vis-NIR spectrum of  $\text{Ni}^{\text{II}}(\text{1B})\text{Cl}_2$  collected after five minutes of controlled potential electrolysis at  $-1.80 \text{ V}$  vs.  $\text{Fc}^{+/0}$  in DMA vs. calculated UV-vis-NIR spectrum of  $\text{Ni}^{\text{I}}(\text{1B})(\text{O-DMA})\text{Cl}$  at the TDDFT (TPSSH/CPCM) level.

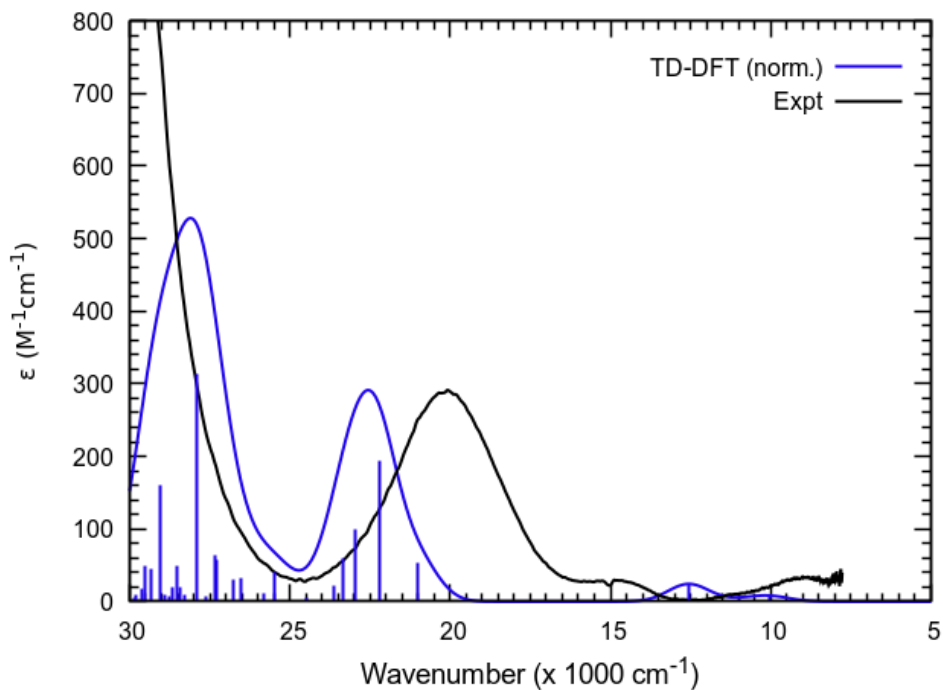


**Figure S135:** Comparison of experimental UV-vis-NIR spectrum of  $\text{Ni}^{\text{II}}(\text{1B})\text{Br}_2$  collected after five minutes of controlled potential electrolysis at  $-1.50 \text{ V}$  vs.  $\text{Fc}^{+/0}$  in DCM vs. calculated UV-vis-NIR spectrum of  $\text{Ni}^{\text{I}}(\text{1B})\text{Br}$  at the TDDFT (TPSSH/CPCM) level.

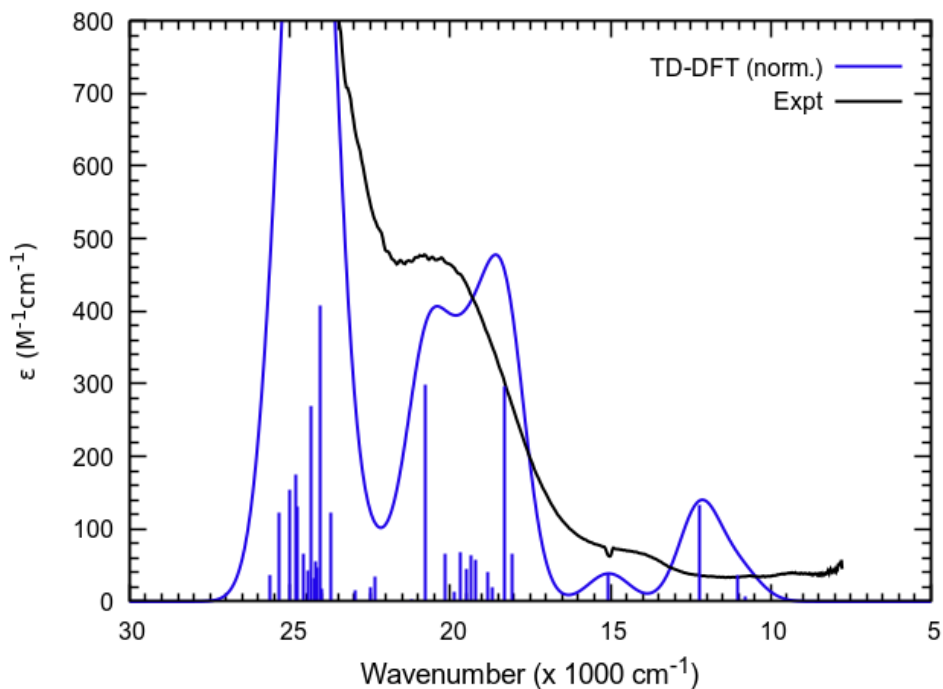


**Figure S136:** Comparison of experimental UV-vis-NIR spectrum of  $\text{Ni}^{\text{II}}(\text{1B})(\text{O-DMA})\text{Br}_2$  collected after four minutes of controlled potential electrolysis at  $-1.60 \text{ V}$  vs.  $\text{Fc}^{+/0}$  in DMA vs. calculated UV-vis-NIR spectrum of  $\text{Ni}^{\text{I}}(\text{1B})(\text{O-DMA})\text{Br}$  at the TDDFT (TPSSH/CPCM) level.

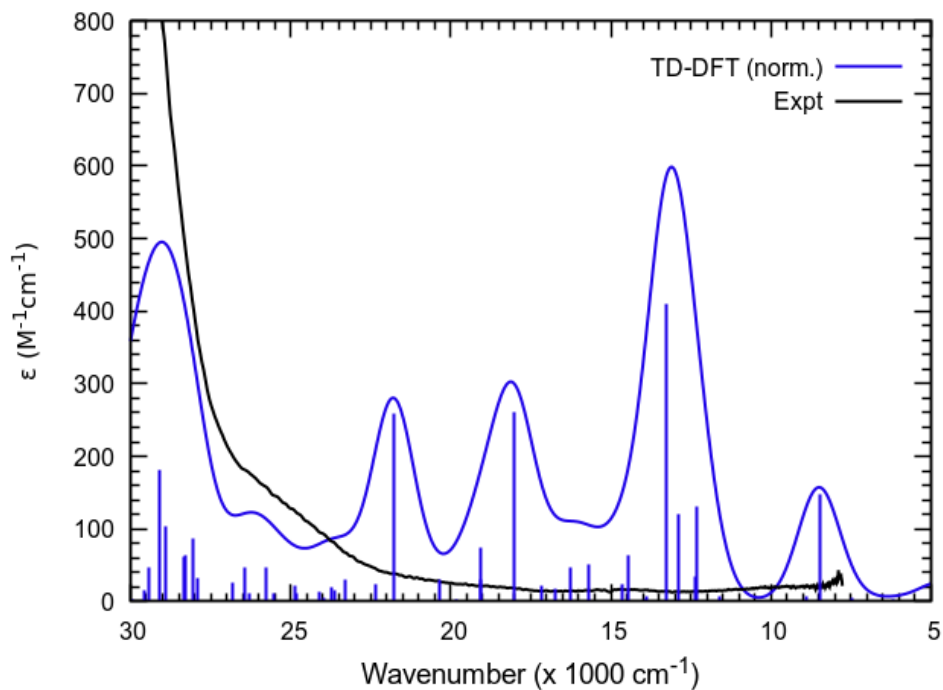


**Figure S137:** Comparison of experimental UV-vis-NIR spectrum of  $\text{Ni}^{\text{II}}(\text{1B})\text{Cl}_2$  collected after five minutes of controlled potential electrolysis at 1.50 V vs.  $\text{Fc}^{+/0}$  in DCM vs. calculated UV-vis-NIR spectrum of  $\text{Ni}^{\text{III}}(\text{1B})\text{Cl}_2$  at the TDDFT (TPSSH/CPCM) level.

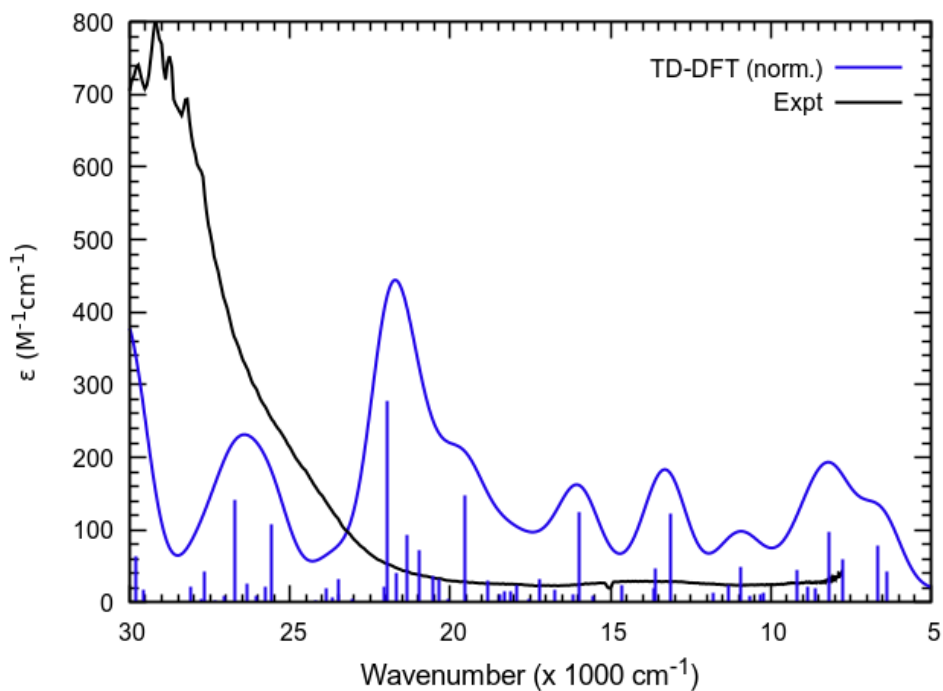


**Figure S138:** Comparison of experimental UV-vis-NIR spectrum of  $\text{Ni}^{\text{II}}(\text{1B})(\text{O-DMA})\text{Cl}_2$  collected after four minutes of controlled potential electrolysis at 0.70 V vs.  $\text{Fc}^{+/0}$  in DMA vs. calculated UV-vis-NIR spectrum of  $\text{Ni}^{\text{III}}(\text{1B})(\text{O-DMA})\text{Cl}_2$  at the TDDFT (TPSSH/CPCM) level.

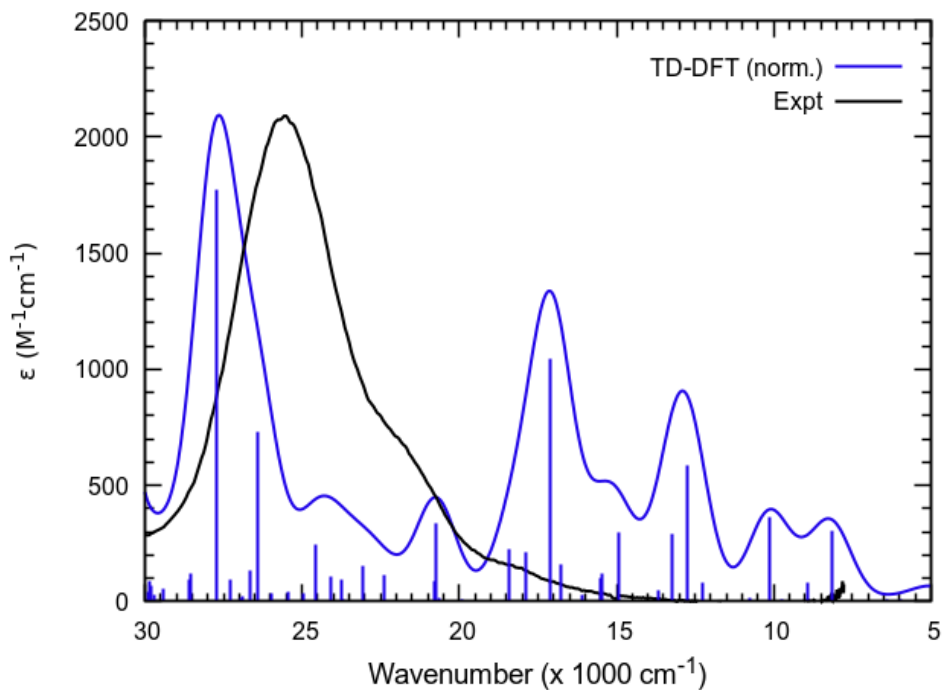


**Figure S139:** Comparison of experimental UV-vis-NIR spectrum of  $\text{Ni}^{\text{II}}(\text{1B})\text{Br}_2$  collected after five minutes of controlled potential electrolysis at 1.20 V vs.  $\text{Fc}^{+/0}$  in DCM vs. calculated UV-vis-NIR spectrum of  $\text{Ni}^{\text{III}}(\text{1B})\text{Br}_2$  at the TDDFT (TPSSH/CPCM) level.

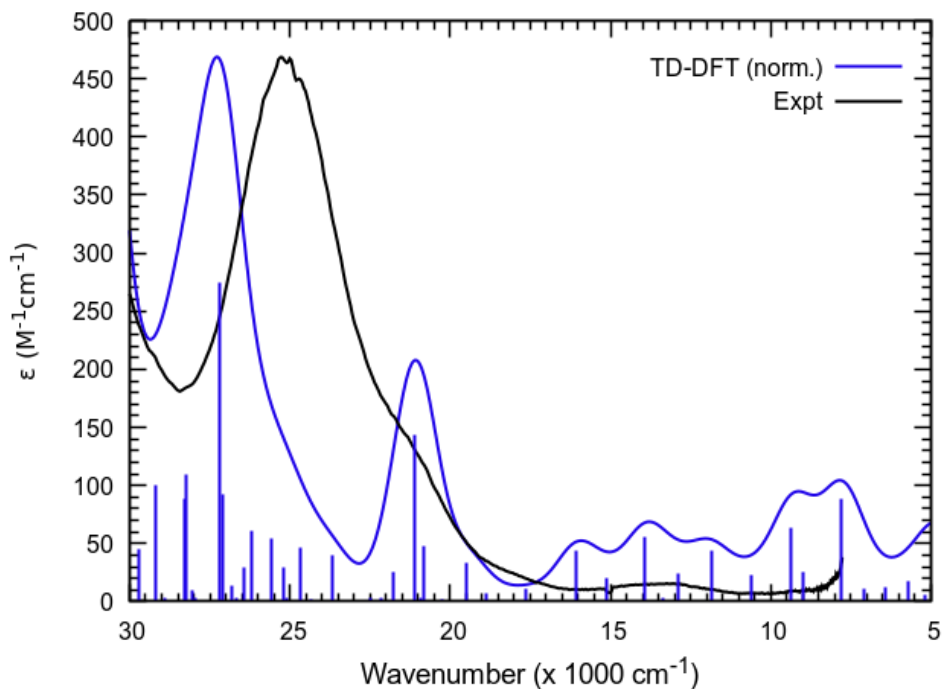


**Figure S140:** Comparison of experimental UV-vis-NIR spectrum of  $\text{Ni}^{\text{II}}(\text{1B})(\text{O-DMA})\text{Br}_2$  collected after four minutes of controlled potential electrolysis at 0.24 V vs.  $\text{Fc}^{+/0}$  in DMA vs. calculated UV-vis-NIR spectrum of  $\text{Ni}^{\text{III}}(\text{1B})(\text{O-DMA})\text{Br}_2$  at the TDDFT (TPSSH/CPCM) level.

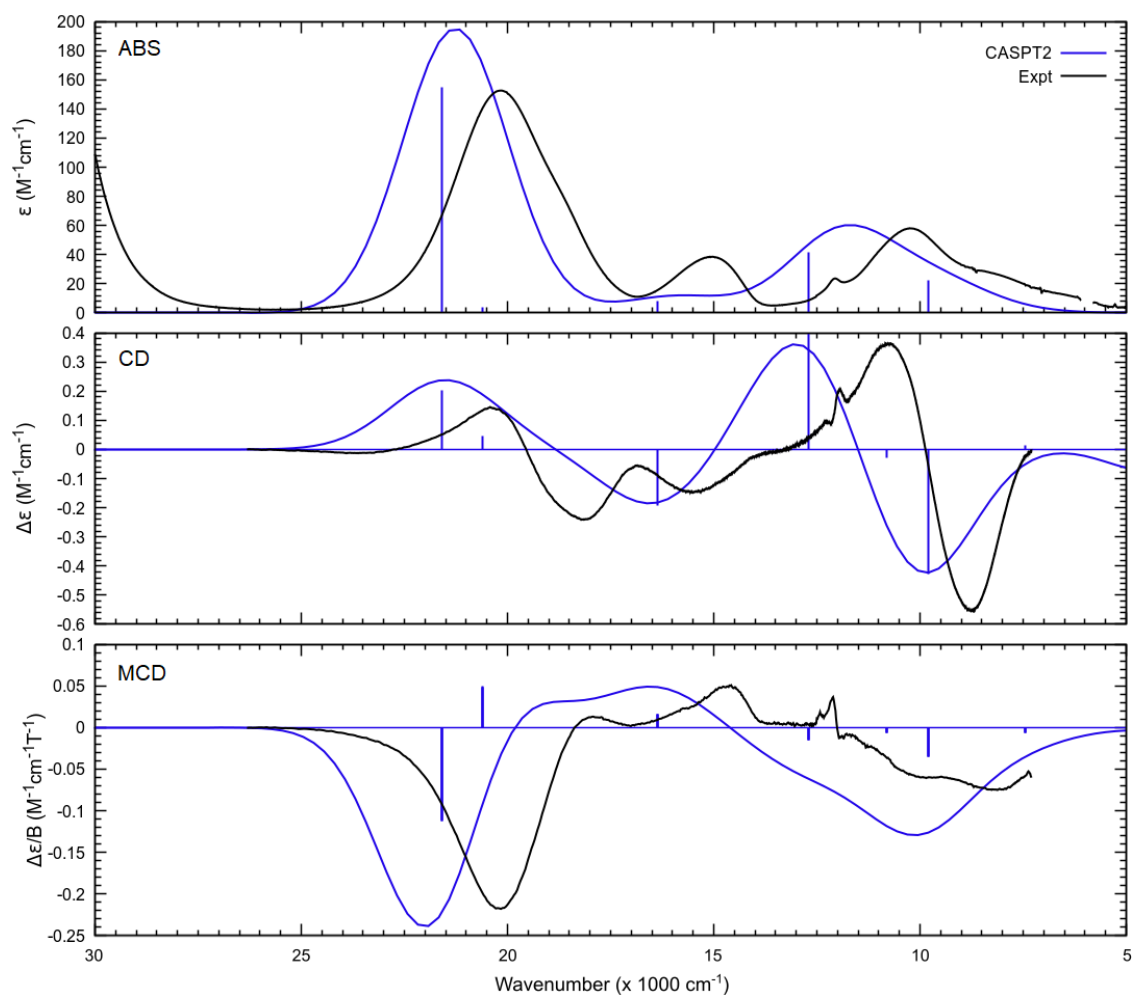


**Figure S141:** Comparison of the experimental UV-vis-NIR (ABS), circular dichroism (CD), and magnetic circular dichroism (MCD) of  $\text{Ni}^{\text{II}}(\text{1B})\text{Cl}_2$  vs. calculated spectra at the MS-CASPT2 level with 22e,12o active space (*cf.* Figure S91) with PCM solvation model ( $\epsilon = 38$ ).

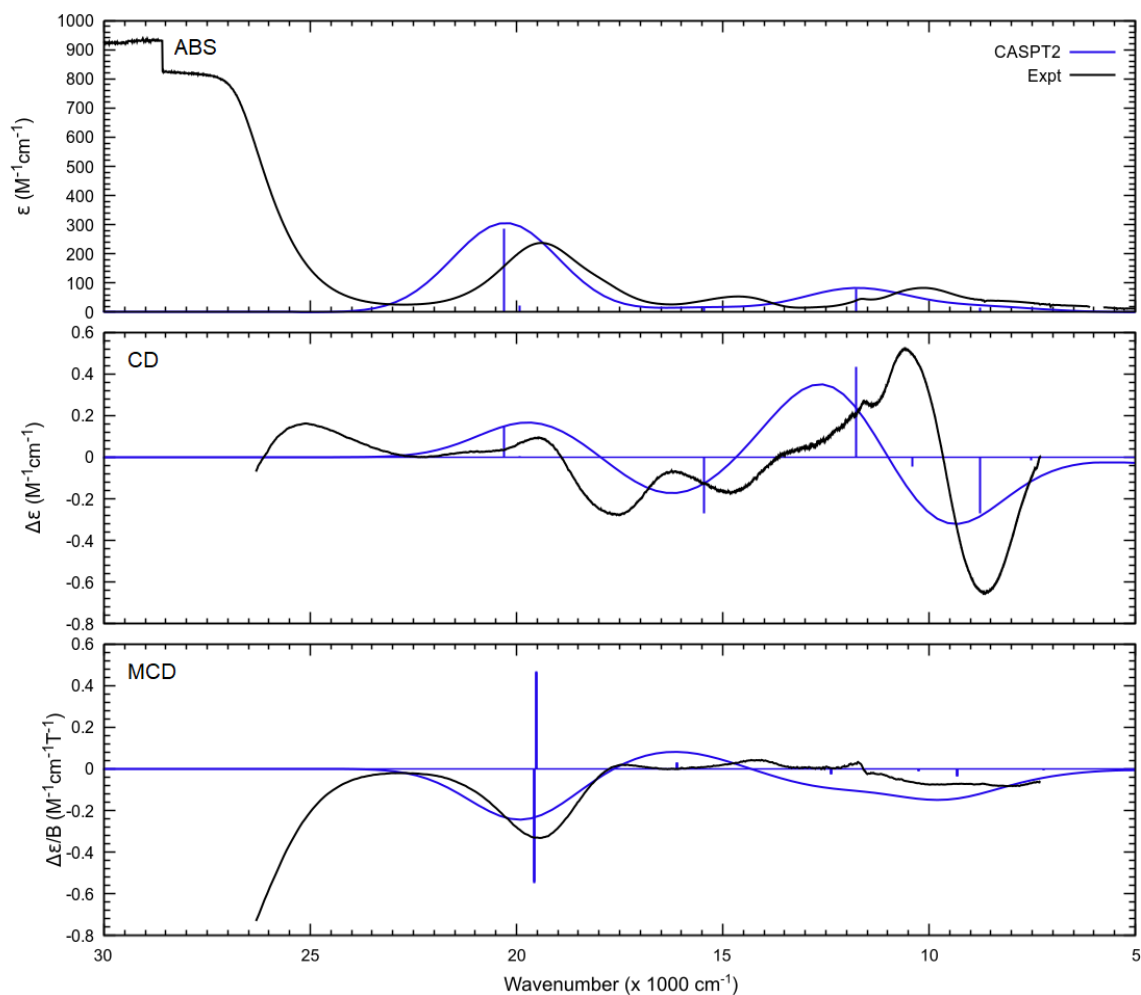


**Figure S142:** Comparison of the experimental UV-vis-NIR (ABS), circular dichroism (CD), and magnetic circular dichroism (MCD) of  $\text{Ni}^{\text{II}}(\text{1B})\text{Br}_2$  vs. calculated spectra at the MS-CASPT2 level with 22e,12o active space (*cf.* Figure S91) with PCM solvation model ( $\epsilon = 38$ ).



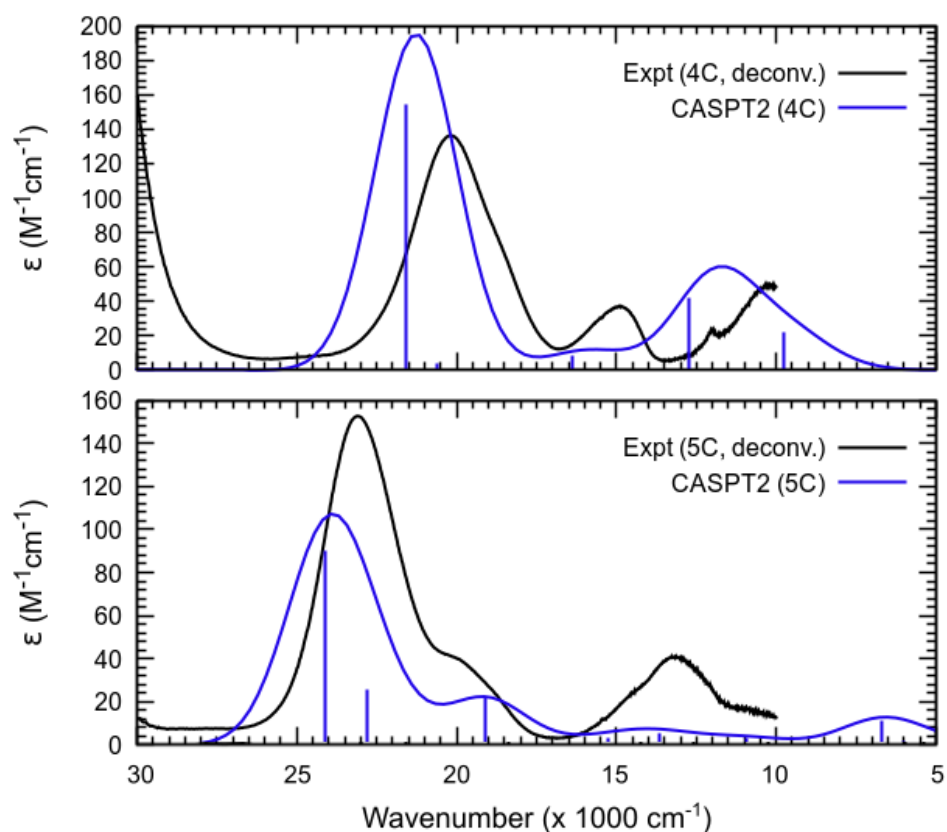


**Figure S143:** Comparison of UV-vis-NIR spectra of four-coordinate (4C)  $\text{Ni}^{\text{II}}(\text{IB})\text{Cl}_2$  and five-coordinate (5C)  $\text{Ni}^{\text{II}}(\text{IB})(\text{DMA})\text{Cl}_2$ , as deconvolved from variable-temperature UV-vis-NIR spectra in **Figure 7** in the main text vs. calculated spectra of  $\text{Ni}^{\text{II}}(\text{IB})\text{Cl}_2$  and  $\text{Ni}^{\text{II}}(\text{IB})(\text{O-DMA})\text{Cl}_2$  at the MS-CASPT2 level with 22e,12o active space (*cf.* Figure S91) with PCM solvation model ( $\epsilon = 38$ ).

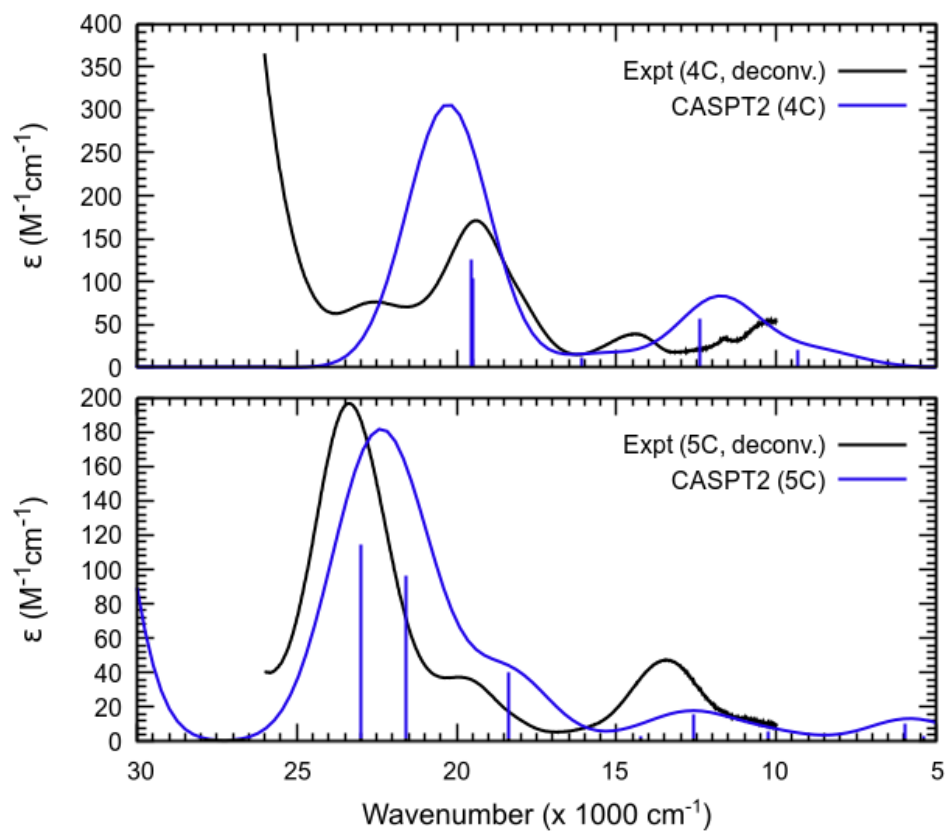


**Figure S144:** Comparison of UV-vis-NIR spectra of four-coordinate (4C)  $\text{Ni}^{\text{II}}(\text{IB})\text{Br}_2$  and five-coordinate (5C)  $\text{Ni}^{\text{II}}(\text{IB})(\text{DMA})\text{Br}_2$ , as deconvolved from variable-temperature UV-vis-NIR spectra vs. calculated spectra of  $\text{Ni}^{\text{II}}(\text{IB})\text{Br}_2$  and  $\text{Ni}^{\text{II}}(\text{IB})(O\text{-DMA})\text{Br}_2$  at the MS-CASPT2 level with 22e,12o active space (*cf.* Figure S91) with PCM solvation model ( $\epsilon = 38$ ).

### S.8.4. Additional Tables

**Table S10:** Calculated electronic transitions for  $\text{Ni}^{\text{II}}(\text{IB})\text{Cl}_2$  at the TDDFT (TPSSh) level in the gas phase.

Transition	Energy (eV)	Energy ( $\text{cm}^{-1}$ )	Energy ( $\text{kcal.mol}^{-1}$ )	Oscillator Strength
1	0.97	7854	22.5	0.0000886
2	1.21	9746	27.9	0.0000010
3	1.71	13795	39.4	0.0000004
4	1.83	14721	42.1	0.0008692
5	1.97	15883	45.4	0.0034545
6	2.36	19030	54.4	0.0003510

**Table S11:** Calculated electronic transitions for  $\text{Ni}^{\text{II}}(\text{IB})\text{Cl}_2$  at the TDDFT (TPSSh) level with CPCM solvation model ( $\epsilon = 38$ ).

Transition	Energy (eV)	Energy ( $\text{cm}^{-1}$ )	Energy ( $\text{kcal.mol}^{-1}$ )	Oscillator Strength
1	0.95	7629	21.8	0.0000112
2	1.25	10056	28.8	0.0000052
3	1.78	14393	41.1	0.0000114
4	1.86	14991	42.9	0.0012049
5	2.12	17116	48.9	0.0046184
6	2.29	18462	52.8	0.0004352

**Table S12:** Calculated electronic transitions for  $\text{Ni}^{\text{II}}(\text{IB})\text{Br}_2$  at the TDDFT (TPSSh) level in the gas phase.

Transition	Energy (eV)	Energy ( $\text{cm}^{-1}$ )	Energy ( $\text{kcal.mol}^{-1}$ )	Oscillator Strength
1	0.92	7423	21.2	0.0000991
2	1.17	9443	27.0	0.0000183
3	1.63	13183	37.7	0.0000467
4	1.81	14569	41.7	0.0009624
5	1.92	15485	44.3	0.0032813
6	2.22	17943	51.3	0.0006201

**Table S13:** Calculated electronic transitions for  $\text{Ni}^{\text{II}}(\text{IB})\text{Br}_2$  at the TDDFT (TPSSh) level with CPCM solvation model ( $\epsilon = 38$ ).

Transition	Energy (eV)	Energy ( $\text{cm}^{-1}$ )	Energy ( $\text{kcal.mol}^{-1}$ )	Oscillator Strength
1	0.90	7242	20.7	0.0000853
2	1.21	9730	27.8	0.0000262
3	1.73	13924	39.8	0.0001327
4	1.86	14972	42.8	0.0010470
5	2.09	16834	48.1	0.0053356
6	2.17	17529	50.1	0.0014775

**Table S14:** Calculated electronic transitions for  $\text{Ni}^{\text{II}}(\text{IB})(O\text{-DMA})\text{Cl}_2$  at the TDDFT (TPSSh) level with CPCM solvation model ( $\epsilon = 38$ ).

Transition	Energy (eV)	Energy ( $\text{cm}^{-1}$ )	Energy ( $\text{kcal.mol}^{-1}$ )	Oscillator Strength
1	1.37	11067	31.6	0.0000380
2	1.63	13109	37.5	0.0001836
3	1.75	14100	40.3	0.0012619
4	2.14	17242	49.3	0.0001261
5	2.50	20197	57.7	0.0009458
6	2.64	21286	60.9	0.0036666

**Table S15:** Calculated electronic transitions for  $\text{Ni}^{\text{II}}(\text{IB})(O\text{-DMA})\text{Br}_2$  at the TDDFT (TPSSh) level with CPCM solvation model ( $\epsilon = 38$ ).

Transition	Energy (eV)	Energy ( $\text{cm}^{-1}$ )	Energy ( $\text{kcal.mol}^{-1}$ )	Oscillator Strength
1	1.41	11365	32.5	0.0000307
2	1.60	12885	36.8	0.0003500
3	1.70	13690	39.1	0.0012969
4	2.08	16766	47.9	0.0001541

5	2.37	19099	54.6	0.0019739
6	2.50	20181	57.7	0.0036730

**Table S16:** Calculated electronic transitions for  $\text{Ni}^{\text{II}}(\text{IB})\text{Cl}_2$  trimer at the TDDFT (TPSSh) level with CPCM solvation model ( $\epsilon = 38$ ).

Transition	Energy (eV)	Energy ( $\text{cm}^{-1}$ )	Energy ( $\text{kcal.mol}^{-1}$ )	Oscillator Strength
1	1.21	9746	27.9	0.0000724
2	1.24	9985	28.5	0.0000660
3	1.72	13901	39.7	0.0000486
4	1.73	13963	39.9	0.0001179
5	1.74	13999	40.0	0.0001099
6	1.74	14072	40.2	0.0000733
7	1.79	14445	41.3	0.0009064
8	1.80	14515	41.5	0.0008827
9	2.05	16497	47.2	0.0001656
10	2.24	18069	51.7	0.0000526
11	2.24	18075	51.7	0.0002236
12	2.50	20132	57.6	0.0045479
13	2.50	20187	57.7	0.0040941
14	2.52	20297	58.0	0.0001275
15	2.63	21184	60.6	0.0001433
16	2.64	21259	60.8	0.0004167
17	2.65	21361	61.1	0.0001756
18	2.66	21422	61.2	0.0002617

**Table S17:** Calculated electronic transitions for  $\text{Ni}^{\text{II}}(\text{IB})\text{Br}_2$  trimer at the TDDFT (TPSSh) level with CPCM solvation model ( $\epsilon = 38$ ).

Transition	Energy (eV)	Energy ( $\text{cm}^{-1}$ )	Energy ( $\text{kcal.mol}^{-1}$ )	Oscillator Strength
1	1.18	9478	27.1	0.0000722
2	1.19	9567	27.4	0.0000716
3	1.64	13229	37.8	0.0002195
4	1.66	13348	38.2	0.0002605
5	1.67	13433	38.4	0.0001369
6	1.68	13560	38.8	0.0000610
7	1.74	14022	40.1	0.0009517
8	1.75	14094	40.3	0.0009310
9	1.98	15958	45.6	0.0001217
10	2.22	17893	51.2	0.0001162
11	2.22	17919	51.2	0.0003179
12	2.40	19353	55.3	0.0030564
13	2.41	19404	55.5	0.0065833
14	2.42	19492	55.7	0.0016736
15	2.51	20257	57.9	0.0019291
16	2.52	20294	58.0	0.0008290
17	2.54	20463	58.5	0.0001849
18	2.55	20547	58.7	0.0002717

**Table S18:** Calculated electronic transitions for  $\text{Ni}^{\text{II}}(\text{IB})\text{Cl}_2$  at the MS-CASPT2 level with 22e,12o active space (*cf.* Figure S91) in the gas phase.

Transition	Energy (eV)	Energy ( $\text{cm}^{-1}$ )	Energy ( $\text{kcal.mol}^{-1}$ )	Oscillator Strength	Assignment from CI vector
1	0.31	2519	7.2	0.0000111	$^3\text{B}_1(\text{F}) \rightarrow ^3\text{A}_2(\text{F})$
2	0.40	3198	9.1	0.0000026	$^3\text{B}_1(\text{F}) \rightarrow ^3\text{B}_2(\text{F})$
3	0.95	7698	22.0	0.0000127	$^3\text{B}_1(\text{F}) \rightarrow ^3\text{B}_2$
4	1.19	9584	27.4	0.0002858	$^3\text{B}_1(\text{F}) \rightarrow ^3\text{A}_1$
5	1.37	11014	31.5	0.0000022	$^3\text{B}_1(\text{F}) \rightarrow ^3\text{B}_1$
6	1.48	11896	34.0	0.0007678	$^3\text{B}_1(\text{F}) \rightarrow ^3\text{A}_2$
7	1.97	15903	45.5	0.0001611	$^3\text{B}_1(\text{F}) \rightarrow ^3\text{B}_2(\text{P})$
8	2.62	21148	60.5	0.0000661	$^3\text{B}_1(\text{F}) \rightarrow ^3\text{B}_1(\text{P})$
9	2.64	21267	60.8	0.0026258	$^3\text{B}_1(\text{F}) \rightarrow ^3\text{A}_2(\text{P})$

**Table S19:** Calculated electronic transitions for  $\text{Ni}^{\text{II}}(\text{IB})\text{Br}_2$  at the MS-CASPT2 level with 22e,12o active space (*cf.* Figure S91) in the gas phase.

Transition	Energy (eV)	Energy ( $\text{cm}^{-1}$ )	Energy ( $\text{kcal.mol}^{-1}$ )	Oscillator Strength	Assignment from CI vector
1	0.29	2347	6.7	0.0000201	$^3\text{B}_1(\text{F}) \rightarrow ^3\text{A}_2(\text{F})$
2	0.36	2897	8.3	0.0000030	$^3\text{B}_1(\text{F}) \rightarrow ^3\text{B}_2(\text{F})$
3	0.93	7513	21.5	0.0000254	$^3\text{B}_1(\text{F}) \rightarrow ^3\text{B}_2$
4	1.09	8755	25.0	0.0002450	$^3\text{B}_1(\text{F}) \rightarrow ^3\text{A}_1$
5	1.29	10392	29.7	0.0000199	$^3\text{B}_1(\text{F}) \rightarrow ^3\text{B}_1$
6	1.46	11779	33.7	0.0011246	$^3\text{B}_1(\text{F}) \rightarrow ^3\text{A}_2$
7	1.92	15464	44.2	0.0002214	$^3\text{B}_1(\text{F}) \rightarrow ^3\text{B}_2(\text{P})$
8	2.47	19914	56.9	0.0002996	$^3\text{B}_1(\text{F}) \rightarrow ^3\text{B}_1(\text{P})$
9	2.52	20296	58.0	0.0039389	$^3\text{B}_1(\text{F}) \rightarrow ^3\text{A}_2(\text{P})$

**Table S20:** Calculated electronic transitions for  $\text{Ni}^{\text{II}}(\text{IB})(\text{O-DMA})\text{Cl}_2$  at the MS-CASPT2 level with 22e,12o active space (*cf.* Figure S91) in the gas phase.

Transition	Energy (eV)	Energy ( $\text{cm}^{-1}$ )	Energy ( $\text{kcal.mol}^{-1}$ )	Oscillator Strength	Assignment from CI vector
1	0.62	5037	14.4	0.0000128	$^3\text{B}_1(\text{F}) \rightarrow ^3\text{A}_2(\text{F})$
2	0.75	6028	17.2	0.0000218	$^3\text{B}_1(\text{F}) \rightarrow ^3\text{B}_2(\text{F})$
3	0.83	6705	19.2	0.0001529	$^3\text{B}_1(\text{F}) \rightarrow ^3\text{A}_1$
4	1.36	10946	31.3	0.0000486	$^3\text{B}_1(\text{F}) \rightarrow ^3\text{A}_2$
5	1.69	13646	39.0	0.0000757	$^3\text{B}_1(\text{F}) \rightarrow ^3\text{B}_1$
6	1.89	15254	43.6	0.0000459	$^3\text{B}_1(\text{F}) \rightarrow ^3\text{B}_2$
7	2.37	19121	54.7	0.0003030	$^3\text{B}_1(\text{F}) \rightarrow ^3\text{B}_2(\text{P})$
8	2.83	22819	65.2	0.0003569	$^3\text{B}_1(\text{F}) \rightarrow ^3\text{B}_1(\text{P})$
9	2.99	24093	68.9	0.0012445	$^3\text{B}_1(\text{F}) \rightarrow ^3\text{A}_2(\text{P})$

**Table S21:** Calculated electronic transitions for  $\text{Ni}^{\text{II}}(\text{IB})(\text{O-DMA})\text{Br}_2$  at the MS-CASPT2 level with 22e,12o active space (*cf.* Figure S91) in the gas phase.

Transition	Energy (eV)	Energy ( $\text{cm}^{-1}$ )	Energy ( $\text{kcal.mol}^{-1}$ )	Oscillator Strength	Assignment from CI vector
1	0.66	5327	15.2	0.0000056	$^3\text{B}_1(\text{F}) \rightarrow ^3\text{B}_2(\text{F})$
2	0.67	5384	15.4	0.0000415	$^3\text{B}_1(\text{F}) \rightarrow ^3\text{A}_2(\text{F})$
3	0.74	5949	17.0	0.0001407	$^3\text{B}_1(\text{F}) \rightarrow ^3\text{A}_1$
4	1.27	10267	29.4	0.0000762	$^3\text{B}_1(\text{F}) \rightarrow ^3\text{B}_2$
5	1.56	12604	36.0	0.0002137	$^3\text{B}_1(\text{F}) \rightarrow ^3\text{B}_1$
6	1.76	14221	40.7	0.0000444	$^3\text{B}_1(\text{F}) \rightarrow ^3\text{B}_2(\text{P})$
7	2.28	18389	52.6	0.0005522	$^3\text{B}_1(\text{F}) \rightarrow ^3\text{A}_2$
8	2.68	21581	61.7	0.0013306	$^3\text{B}_1(\text{F}) \rightarrow ^3\text{B}_1(\text{P})$
9	2.85	22989	65.7	0.0015792	$^3\text{B}_1(\text{F}) \rightarrow ^3\text{A}_2(\text{P})$

**Table S22:** Calculated electronic transitions for  $\text{Ni}^{\text{II}}(\text{IB})\text{Cl}_2$  at the MS-CASPT2 level with 22e,12o active space (*cf.* Figure S91) with PCM solvation model ( $\epsilon = 38$ ).

Transition	Energy (eV)	Energy ( $\text{cm}^{-1}$ )	Energy ( $\text{kcal.mol}^{-1}$ )	Oscillator Strength	Assignment from CI vector
1	0.25	2009	5.7	0.0000077	$^3\text{B}_1(\text{F}) \rightarrow ^3\text{A}_2(\text{F})$
2	0.41	3318	9.5	0.0000029	$^3\text{B}_1(\text{F}) \rightarrow ^3\text{B}_2(\text{F})$
3	0.92	7443	21.3	0.0000187	$^3\text{B}_1(\text{F}) \rightarrow ^3\text{B}_1/^3\text{B}_2$
4	1.21	9786	28.0	0.0003087	$^3\text{B}_1(\text{F}) \rightarrow ^3\text{A}_1$
5	1.34	10810	30.9	0.0000043	$^3\text{B}_1(\text{F}) \rightarrow ^3\text{B}_1/^3\text{B}_2$
6	1.58	12709	36.3	0.0005755	$^3\text{B}_1(\text{F}) \rightarrow ^3\text{A}_2$
7	2.03	16354	46.8	0.0001158	$^3\text{B}_1(\text{F}) \rightarrow ^3\text{B}_1(\text{P})/^3\text{B}_2(\text{P})$
8	2.56	20607	58.9	0.0000561	$^3\text{B}_1(\text{F}) \rightarrow ^3\text{B}_1(\text{P})/^3\text{B}_2(\text{P})$
9	2.68	21586	61.7	0.0021345	$^3\text{B}_1(\text{F}) \rightarrow ^3\text{A}_2(\text{P})$

**Table S23:** Calculated electronic transitions for  $\text{Ni}^{\text{II}}(\text{IB})\text{Br}_2$  at the MS-CASPT2 level with 22e,12o active space (*cf.* Figure S91) with PCM solvation model ( $\epsilon = 38$ ).

Transition	Energy (eV)	Energy ( $\text{cm}^{-1}$ )	Energy ( $\text{kcal.mol}^{-1}$ )	Oscillator Strength	Assignment from CI vector
1	0.23	1824	5.2	0.0000192	$^3\text{B}_1(\text{F}) \rightarrow ^3\text{A}_2(\text{F})$
2	0.37	2974	8.5	0.0000031	$^3\text{B}_1(\text{F}) \rightarrow ^3\text{B}_2(\text{F})$
3	0.90	7229	20.7	0.0000244	$^3\text{B}_1(\text{F}) \rightarrow ^3\text{B}_1/^3\text{B}_2$
4	1.16	9322	26.7	0.0002802	$^3\text{B}_1(\text{F}) \rightarrow ^3\text{A}_1$
5	1.27	10244	29.3	0.0000139	$^3\text{B}_1(\text{F}) \rightarrow ^3\text{B}_1/^3\text{B}_2$
6	1.54	12382	35.4	0.0007781	$^3\text{B}_1(\text{F}) \rightarrow ^3\text{A}_2$
7	2.00	16112	46.1	0.0001711	$^3\text{B}_1(\text{F}) \rightarrow ^3\text{B}_1(\text{P})/^3\text{B}_2(\text{P})$
8	2.42	19514	55.8	0.0014311	$^3\text{B}_1(\text{F}) \rightarrow ^3\text{B}_1(\text{P})/^3\text{B}_2(\text{P})$
9	2.43	19561	55.9	0.0017455	$^3\text{B}_1(\text{F}) \rightarrow ^3\text{A}_2(\text{P})$

**Table S24:** Calculated electronic transitions for  $\text{Ni}^{\text{II}}(\text{IB})\text{Cl}_2$  at the CASSCF level with 8e,5o active space (*cf.* Figure S91) in the gas phase. Active Space Orbitals (in order for CI vector notation below):  $3d_{xy}(\text{Ni})$ ,  $3d_{x^2-y^2}(\text{Ni})$ ,  $3d_{z^2}(\text{Ni})$ ,  $3d_{yz}(\text{Ni})$ ,  $3d_{xz}(\text{Ni})$ . Starred CI vectors refer to the determinants that are already present in the particular state with the flipped alpha/beta orbitals.

State	Multiplicity	Energy (eV)	Energy ( $\text{cm}^{-1}$ )	Energy ( $\text{kcal.mol}^{-1}$ )	CI Vector	Contribution
1	3	0	0	0	12221	14.8%
					21221	68.8%
2	3	0.28	2285	6.5	12221	11.5%
					22121	45.4%
					22211	20.7%
3	3	0.43	3489	10.0	21122	13.3%
					21221	11.5%
					22211	52.3%
4	3	0.71	5740	16.4	12221	10.2%
					21122	12.7%
					21212	19.1%
					22112	24.5%
5	3	0.77	6218	17.8	11222	48.0%
					12122	17.3%
					21122	24.6%
6	3	0.90	7284	20.8	12122	50.9%
					12212	31.5%
7	3	1.05	8470	24.2	12122	11.0%
					12212	22.0%
					21122	11.2%
					21212	30.7%
					22112	21.8%
8	1	2.11	17002	48.6	20222	16.8%
					22220	57.7%
9	1	2.12	17122	49	21221	29.1%
					21221*	29.1%
10	1	2.35	18967	54.2	22121	19.4%
					22121*	19.4%
11	1	2.50	20173	57.7	22211	19.9%
					22211*	19.9%
12	1	2.69	21689	62.0	11222	10.8%
					11222*	10.8%
					21212	11.8%
					21212*	11.8%
					22022	23.3%
13	3	2.71	21871	62.5	12221	27.4%
					21122	31.4%
14	3	3.02	24338	69.6	11222	24.1%
					12212	34.2%
					21212	24.4%
15	1	3.29	26503	75.8	20222	23.5%
					21122	14.8%
					21122*	14.8%
					22220	11.1%
16	1	3.33	26869	76.8	20222	11.3%
					21122	13.2%
					21122*	13.2%
17	1	3.44	27777	79.4	11222	11.7%
					11222*	11.7%
					21212	15.8%
					21212*	15.8%
18	1	3.46	27897	79.8	12221	15.5%
					12221*	15.5%
19	1	3.62	29166	83.4	12221*	19.0%

					12221*	19.0%
					22202	14.4%
20	1	3.75	30285	86.6	22112	10.8%
					22112*	10.8%
21	1	3.89	31379	89.7	22022	36.5%
					22202	11.2%
22	1	4.00	32286	92.3	02222	32.0%
					22202	21.9%
23	1	4.05	32690	93.5	12212	19.4%
					12212*	19.4%
					22112	13.3%
					22112*	13.3%

**Table S25:** Calculated electronic transitions for  $\text{Ni}^{\text{II}}(\text{IB})\text{Cl}_2$  at the MS-CASPT2 level with 8e,5o active space (*cf.* Figure S91) in the gas phase. Active Space Orbitals (in order for CI vector notation below):  $3d_{xy}(\text{Ni})$ ,  $3d_{x^2-y^2}(\text{Ni})$ ,  $3d_{z^2}(\text{Ni})$ ,  $3d_{yz}(\text{Ni})$ ,  $3d_{xz}(\text{Ni})$ . Starred CI vectors refer to the determinants that are already present in the particular state with the flipped alpha/beta orbitals.

State	Multiplicity	Energy (eV)	Energy ( $\text{cm}^{-1}$ )	Energy ( $\text{kcal.mol}^{-1}$ )	CI Vector	Contribution
1	3	0	0	0	12221	14.8%
					21221	68.8%
2	3	0.29	2311	6.6	12221	11.5%
					22121	45.4%
					22211	20.7%
3	3	0.46	3715	10.6	21122	13.3%
					21221	11.5%
					22211	52.3%
4	3	0.90	7278	20.8	12221	10.2%
					21122	12.7%
					21212	19.1%
					22112	24.5%
5	3	1.07	8608	24.6	11222	48.0%
					12122	17.3%
					21122	24.6%
6	3	1.24	9972	28.5	12122	50.9%
					12212	31.5%
7	3	1.41	11363	32.5	12122	11.0%
					12212	22.0%
					21122	11.2%
					21212	30.7%
					22112	21.8%
8	1	1.70	13722	39.2	21221	29.1%
					21221*	29.1%
9	1	1.72	13860	39.6	20222	16.8%
					22220	57.7%
10	1	1.96	15800	45.2	22121	19.4%
					22121*	19.4%
11	1	2.16	17455	49.9	22211	19.9%
					22211*	19.9%
12	3	2.28	18378	52.5	12221	27.4%
					21122	31.4%
13	1	2.44	19651	56.2	11222	10.8%
					11222*	10.8%
					21212	11.8%
					21212*	11.8%
					22022	23.3%
14	3	2.76	22241	63.6	11222	24.1%
					12212	34.2%
					21212	24.4%
15	3	2.80	22597	64.6	12221	25.8%
					22112	37.4%



16	1	2.84	22867	65.4	22121	16.5%
					20222	23.5%
					21122	14.8%
					21122*	14.8%
17	1	2.92	23513	67.2	22220	11.1%
					20222	11.3%
					21122	13.2%
					21122*	13.2%
18	1	3.16	25464	72.8	11222	11.7%
					11222*	11.7%
					21212	15.8%
					21212*	15.8%
19	1	3.24	26114	74.7	12221	15.5%
					12221*	15.5%
20	1	3.31	26733	76.4	12221	19.0%
					12221*	19.0%
					22202	14.4%
21	1	3.46	27920	79.8	22112	10.8%
					22112*	10.8%
22	1	3.85	31036	88.7	22022	36.5%
					22202	11.2%
23	1	4.04	32606	93.2	02222	32.0%
					22202	21.9%
24	1	4.08	32901	94.1	12212	19.4%
					12212*	19.4%
					22112	13.3%
					22112*	13.3%

**Table S26:** Calculated electronic transitions for  $\text{Ni}^{\text{II}}(\text{IB})\text{Cl}_2$  at the CASSCF level with 20e, 11o active space (*cf.* Figure S91) in the gas phase. Active Space Orbitals (in order for CI vector notation below): 3p(Cl), 3d<sub>xy</sub>(Ni), 3p(Cl), 3d<sub>z2</sub>(Ni), 3d<sub>yz</sub>(Ni), 3p(Cl), 3p(Cl), 3p(Cl), 3p(Cl), 3d<sub>x2-y2</sub>(Ni), 3d<sub>xz</sub>(Ni). Starred CI vectors refer to the determinants that are already present in the particular state with the flipped alpha/beta orbitals.

State	Multiplicity	Energy (eV)	Energy (cm <sup>-1</sup> )	Energy (kcal.mol <sup>-1</sup> )	CI Vector	Contribution
1	3	0	0	0	2222222211	95.1%
2	3	0.34	2715	7.8	2122222212	15.4%
					2222122221	80.5%
3	3	0.49	3990	11.4	2122222221	54.6%
					2222122212	38.6%
4	3	0.75	6047	17.3	2122122222	22.1%
					2221122222	21.7%
					2221222221	27.1%
					2222122212	19.4%
5	3	0.83	6684	19.1	2221222212	91.7%
6	3	1.03	8271	23.6	2122122222	61.2%
					2221122222	25.2%
7	3	1.15	9310	26.6	2121222222	57.7%
					2122222212	33.7%
8	1	1.76	14173	40.5	2222222202	39.6%
					2222222220	41.3%
9	1	1.78	14354	41.0	2222222211	39.8%
					2222222211*	39.8%
10	1	2.01	16236	46.4	2222122221	31.4%
					2222122221*	31.4%
					2222222202	11.3%
11	1	2.20	17770	50.8	2122222221	14.1%
					2122222221*	14.1%
					2222122212	25.1%
					2222122212*	25.1%
12	3	2.33	18758	53.6	2122222221	26.4%
					2221122222	21.5%

					22212222221	12.8%
					22221222212	33.3%
13	1	2.36	19003	54.3	22212222212	13.9%
					22212222212*	13.9%
					22220222222	41.3%
					22222222202	10.1%
14	3	2.73	21999	62.9	21212222222	39.6%
					21222222212	41.8%
15	1	2.74	22126	63.3	20222222222	13.0%
					22212222212	16.8%
					22212222212*	16.8%
					22222222202	13.0%
					22222222220	14.1%
16	1	2.77	22352	63.9	21222222221	17.4%
					21222222221*	17.4%
					22221222212	16.7%
					22221222212*	16.7%
17	1	2.84	22941	65.6	21222222212	37.3%
					21222222212*	37.3%
18	1	2.99	24096	68.9	21221222222	25.9%
					21221222222*	25.9%
19	3	2.99	24117	69.0	21221222222	12.4%
					22211222222	24.1%
					22212222221	52.6%
20	1	3.29	26541	75.9	20222222222	24.1%
					22212222212	10.7%
					22212222212*	10.7%
					22220222222	20.4%
21	1	3.32	26745	76.5	21221222222	13.6%
					21221222222*	13.6%
					21222222221	10.3%
					21222222221*	10.3%
					22212222221	13.7%
					22212222221*	13.7%
22	1	3.70	29826	85.3	22211222222	20.8%
					22211222222*	20.8%
					22212222221	18.4%
					22212222221*	18.4%
23	1	3.81	30748	87.9	21212222222	35.0%
					21212222222*	35.0%
24	1	3.90	31430	89.9	20222222222	24.0%
					22202222222	44.0%

**Table S27:** Calculated electronic transitions for  $\text{Ni}^{\text{II}}(\text{IB})\text{Cl}_2$  at the MS-CASPT2 level with 20e,11o active space (*cf.* Figure S91) in the gas phase. Active Space Orbitals (in order for CI vector notation below): 3p(Cl), 3d<sub>xy</sub>(Ni), 3p(Cl), 3d<sub>z2</sub>(Ni), 3d<sub>yz</sub>(Ni), 3p(Cl), 3p(Cl), 3p(Cl), 3p(Cl), 3d<sub>x2-y2</sub>(Ni), 3d<sub>xz</sub>(Ni). Starred CI vectors refer to the determinants that are already present in the particular state with the flipped alpha/beta orbitals.

State	Multiplicity	Energy (eV)	Energy (cm <sup>-1</sup> )	Energy (kcal.mol <sup>-1</sup> )	CI Vector	Contribution
1	3	0	0	0	22222222211	95.1%
2	3	0.28	2226	6.4	21222222212	15.4%
					22221222221	80.5%
3	3	0.39	3110	8.9	21222222221	54.6%
					22221222212	38.6%
4	3	0.91	7365	21.1	21221222222	22.1%
					22211222222	21.7%
					22212222221	27.1%
					22221222212	19.4%
5	3	1.11	8930	25.5	22212222212	91.7%
6	3	1.32	10615	30.4	21221222222	61.2%
					22211222222	25.2%

7	1	1.32	10618	30.4	2222222211 2222222211*	39.8% 39.8%
8	1	1.38	11126	31.8	2222222202 2222222220	39.6% 41.3%
9	3	1.40	11286	32.3	2121222222 2122222212	57.7% 33.7%
10	1	1.58	12724	36.4	2222122221 2222122221* 2222222202	31.4% 31.4% 11.3%
11	1	1.90	15329	43.8	2122222221 2122222221* 2222122212 2222122212*	14.1% 14.1% 25.1% 25.1%
12	3	1.97	15867	45.4	2122222221 2221122222 2221222221 2222122212	26.4% 21.5% 12.8% 33.3%
13	1	2.07	16696	47.7	2221222212 2221222212* 2222022222 2222222202	13.9% 13.9% 41.3% 10.1%
14	1	2.28	18427	52.7	2022222222 2221222212 2221222212* 2222222202 2222222220	13.0% 16.8% 16.8% 13.0% 14.1%
15	1	2.37	19136	54.7	2122222221 2122222221* 2222122212 2222122212*	17.4% 17.4% 16.7% 16.7%
16	1	2.47	19930	57.0	2122222212 2122222212*	37.3% 37.3%
17	3	2.59	20886	59.7	2121222222 2122222212	39.6% 41.8%
18	3	2.68	21578	61.7	2122122222 2221122222 2221222221	12.4% 24.1% 52.6%
19	1	2.68	21615	61.8	2122122222 2122122222*	25.9% 25.9%
20	1	2.93	23600	67.5	2022222222 2221222212 2221222212* 2222022222	24.1% 10.7% 10.7% 20.4%
21	1	3.00	24194	69.2	2122122222 2122122222* 2122222221 2122222221* 2221222221 2221222221*	13.6% 13.6% 10.3% 10.3% 13.7% 13.7%
22	1	3.67	29584	84.6	2221122222 2221122222* 2221222221 2221222221*	20.8% 20.8% 18.4% 18.4%
23	1	3.81	30739	87.9	2022222222 2220222222	24.0% 44.0%
24	1	3.84	30939	88.5	2121222222 2121222222*	35.0% 35.0%

**Table S28:** Calculated electronic transitions for  $\text{Ni}^{\text{II}}(\text{IB})\text{Cl}_2$  at the CASSCF level with 22e,12o active space (cf. Figure S91) in the gas phase. Active Space Orbitals (in order for CI vector notation below):  $3d_{z^2}(\text{Ni})$ ,

$\sigma$ -bonding(IB), 3p(Cl), 3p(Cl), 3p(Cl), 3p(Cl), 3p(Cl), 3p(Cl),  $3d_{xy}(\text{Ni})$ ,  $3d_{yz}(\text{Ni})$ ,  $3d_{x^2-y^2}(\text{Ni})$ ,  $3d_{xz}(\text{Ni})$ . Starred CI vectors refer to the determinants that are already present in the particular state with the flipped alpha/beta orbitals.

State	Multiplicity	Energy (eV)	Energy (cm <sup>-1</sup> )	Energy (kcal.mol <sup>-1</sup> )	CI Vector	Contribution
1	3	0	0	0	22222222211	95.2%
2	3	0.36	2927	8.4	222222221212	14.8%
					222222222121	81.6%
3	3	0.54	4359	12.5	222222221221	58.4%
					222222222112	37.3%
4	3	0.82	6647	19.0	12222222122	24.8%
					122222222221	19.9%
					222222221122	30.5%
					222222222112	18.6%
5	3	0.91	7369	21.1	12222222212	94.9%
6	3	1.11	8979	25.7	122222222122	25.3%
					222222221122	49.1%
					222222221221	12.4%
7	3	1.25	10063	28.8	12222221222	58.9%
					222222221212	33.4%
8	1	1.66	13412	38.3	222222222202	33.9%
					222222222220	43.9%
9	1	1.71	13770	39.4	22222222211	40.6%
					222222222211*	40.6%
10	1	1.96	15821	45.2	222222222121	29.9%
					222222222121*	29.9%
					222222222202	10.3%
11	1	2.19	17686	50.6	222222221221	15.0%
					222222221221*	15.0%
					222222222112	22.5%
					222222222112*	22.5%
12	3	2.32	18714	53.5	12222222122	27.5%
					122222222221	12.6%
					222222221221	22.4%
					222222222112	29.4%
13	1	2.36	19047	54.5	222222222022	41.2%
					222222222202	14.4%
14	1	2.70	21752	62.2	12222222212	19.3%
					12222222212*	19.3%
					222222222022	15.4%
					222222222202	12.6%
					222222222220	17.0%
15	1	2.73	22012	62.9	222222221221	20.8%
					222222221221*	20.8%
					222222222112	16.8%
					222222222112*	16.8%
16	3	2.77	22317	63.8	12222221222	38.5%
					222222221212	45.5%
17	1	2.84	22880	65.4	222222221212*	34.5%
					222222221212*	34.5%
18	3	2.95	23789	68.0	12222222122	18.1%
					122222222221	59.2%
					222222222112	13.7%
19	1	2.98	24022	68.7	222222221122	24.9%
					222222221122*	24.9%
20	1	3.25	26195	74.9	12222222212	10.5%
					122222222212*	10.5%
					222222222022	11.8%
					222222222022	24.3%
21	1	3.26	26333	75.3	12222222221	13.7%
					122222222221*	13.7%

					222222221122	14.7%
					222222221122*	14.7%
22	1	3.65	29428	84.1	12222222122	22.2%
					12222222122*	22.2%
					12222222221	21.3%
					12222222221*	21.3%
23	1	3.84	30986	88.6	122222221222	28.4%
					122222221222*	28.4%
					222222220222	17.2%
24	1	3.90	31440	89.9	022222222222	29.9%
					122222221222	12.9%
					122222221222*	12.9%
					222222220222	21.5%

**Table S29:** Calculated electronic transitions for  $\text{Ni}^{\text{II}}(\text{IB})\text{Cl}_2$  at the MS-CASPT2 level with 22e,12o active space (*cf.* Figure S91) in the gas phase. Active Space Orbitals (in order for CI vector notation below):  $3d_{z^2}(\text{Ni})$ ,  $\sigma\text{-bonding}(\text{IB})$ ,  $3p(\text{Cl})$ ,  $3p(\text{Cl})$ ,  $3p(\text{Cl})$ ,  $3p(\text{Cl})$ ,  $3p(\text{Cl})$ ,  $3p(\text{Cl})$ ,  $3d_{xy}(\text{Ni})$ ,  $3d_{yz}(\text{Ni})$ ,  $3d_{x^2-y^2}(\text{Ni})$ ,  $3d_{xz}(\text{Ni})$ . Starred CI vectors refer to the determinants that are already present in the particular state with the flipped alpha/beta orbitals.

State	Multiplicity	Energy (eV)	Energy ( $\text{cm}^{-1}$ )	Energy ( $\text{kcal.mol}^{-1}$ )	CI Vector	Contribution
1	3	0.00	0	0.0	222222222211	95.2%
2	3	0.31	2519	7.2	222222221212	14.8%
					2222222222121	81.6%
3	3	0.40	3198	9.1	222222221221	58.4%
					222222222112	37.3%
4	3	0.95	7698	22.0	12222222122	24.8%
					122222222221	19.9%
					222222221122	30.5%
					222222222112	18.6%
5	3	1.19	9584	27.4	122222222212	94.9%
6	1	1.33	10705	30.6	222222222211	40.6%
					222222222211*	40.6%
7	1	1.34	10782	30.8	222222222202	33.9%
					222222222220	43.9%
8	3	1.37	11014	31.5	12222222122	25.3%
					222222221122	49.1%
					222222221221	12.4%
9	3	1.47	11896	34.0	122222221222	58.9%
					222222221212	33.4%
10	1	1.60	12913	36.9	2222222222121	29.9%
					2222222222121*	29.9%
					222222222202	10.3%
11	1	1.92	15489	44.3	222222221221	15.0%
					222222221221*	15.0%
					222222222112	22.5%
					222222222112*	22.5%
12	3	1.97	15903	45.5	12222222122	27.5%
					122222222221	12.6%
					222222221221	22.4%
					222222222112	29.4%
13	1	2.11	16996	48.6	222222222202	41.2%
					222222222202	14.4%
14	1	2.31	18650	53.3	122222222212	19.3%
					122222222212*	19.3%
					222222220222	15.4%
					222222222202	12.6%
					222222222220	17.0%
15	1	2.35	18973	54.2	222222221221	20.8%
					222222221221*	20.8%
					222222222112	16.8%

					22222222112*	16.8%
16	1	2.54	20503	58.6	222222221212	34.5%
					222222221212*	34.5%
17	3	2.62	21148	60.5	12222222122	18.1%
					12222222221	59.2%
					222222221122	13.7%
18	3	2.64	21267	60.8	122222221222	38.5%
					222222221212	45.5%
19	1	2.73	21980	62.8	222222221122	24.9%
					222222221122*	24.9%
20	1	2.88	23216	66.4	122222222212	10.5%
					122222222212*	10.5%
					222222220222	11.8%
					222222222022	24.3%
21	1	2.96	23867	68.2	122222222221	13.7%
					122222222221*	13.7%
					222222221122	14.7%
					222222221122*	14.7%
22	1	3.51	28319	81.0	122222222122	22.2%
					122222222122*	22.2%
					122222222221	21.3%
					122222222221*	21.3%
23	1	3.82	30811	88.1	022222222222	29.9%
					122222221222	12.9%
					122222221222*	12.9%
					222222220222	21.5%
24	1	3.85	31076	88.9	122222221222	28.4%
					122222221222*	28.4%
					222222220222	17.2%

**Table S30:** Calculated electronic transitions for  $\text{Ni}^{\text{II}}(\text{IB})\text{Br}_2$  at the CASSCF level with 8e,5o active space (*cf.* Figure S91) in the gas phase. Active Space Orbitals (in order for CI vector notation below):  $3d_{xy}(\text{Ni})$ ,  $3d_{z^2}(\text{Ni})$ ,  $3d_{yz}(\text{Ni})$ ,  $3d_{x^2-y^2}(\text{Ni})$ ,  $3d_{xz}(\text{Ni})$ . Starred CI vectors refer to the determinants that are already present in the particular state with the flipped alpha/beta orbitals.

State	Multiplicity	Energy (eV)	Energy ( $\text{cm}^{-1}$ )	Energy ( $\text{kcal.mol}^{-1}$ )	CI Vector	Contribution
1	3	0	0	0	21221	28.6%
					22121	30.7%
					22211	38.3%
2	3	0.27	2196	6.3	12212	10.6%
					21221	13.1%
					22121	58.9%
					22211	10.1%
3	3	0.41	3328	9.5	12221	73.2%
					21122	10.2%
					22112	11.8%
4	3	0.72	5785	16.5	12122	24.9%
					21221	14.1%
					22112	37.3%
					22211	11.3%
5	3	0.77	6194	17.7	21122	12.1%
					21212	73.7%
					22112	10.2%
6	3	0.87	7057	20.2	12122	31.1%
					21212	17.5%
					22112	32.2%
7	3	1.03	8287	23.7	11222	81.1%
8	1	2.08	16807	48.1	22220	59.3%
9	1	2.12	17133	49.0	21221	11.7%
					21221*	11.7%
					22121	14.5%

					22121*	14.5%
					22211	15.6%
					22211*	15.6%
10	1	2.35	18932	54.1	22121	24.0%
					22121*	24.0%
11	1	2.48	20002	57.2	12221	27.1%
					12221*	27.1%
12	1	2.69	21687	62.0	02222	14.3%
					20222	20.9%
					22022	14.0%
					22112	14.7%
					22112*	14.7%
					22202	18.4%
13	3	2.74	22076	63.1	12221	18.5%
					21122	36.8%
					21221	19.9%
14	3	2.97	23995	68.6	12212	26.3%
					21122	23.2%
					22211	29.0%
15	1	3.32	26765	76.5	21122	16.9%
					21122*	16.9%
					22220	12.8%
16	1	3.37	27191	77.7	12221	11.1%
					12221*	11.1%
					20222	10.7%
					22022	28.9%
17	1	3.44	27738	79.3	21221	21.9%
					21221*	21.9%
					22211	12.0%
					22211*	12.0%
18	1	3.48	28030	80.1	11222	17.6%
					11222*	17.6%
					12122	14.9%
					12122*	14.9%
19	1	3.58	28855	82.5	12122	18.4%
					12122*	18.4%
					22211	13.6%
					22211*	13.6%
20	1	3.74	30163	86.2	20222	17.3%
					22022	17.1%
21	1	3.83	30865	88.2	20222	12.3%
					21122	17.9%
					21122*	17.9%
22	1	3.95	31849	91.1	02222	42.0%
					22202	27.5%
23	1	3.99	32147	91.9	12212	25.8%
					12212*	25.8%

**Table S31:** Calculated electronic transitions for  $\text{Ni}^{\text{II}}(\text{IB})\text{Br}_2$  at the MS-CASPT2 level with 8e,5o active space (*cf.* Figure S91) in the gas phase. Active Space Orbitals (in order for CI vector notation below):  $3d_{xy}(\text{Ni})$ ,  $3d_{z^2}(\text{Ni})$ ,  $3d_{yz}(\text{Ni})$ ,  $3d_{x^2-y^2}(\text{Ni})$ ,  $3d_{xz}(\text{Ni})$ . Starred CI vectors refer to the determinants that are already present in the particular state with the flipped alpha/beta orbitals.

State	Multiplicity	Energy (eV)	Energy ( $\text{cm}^{-1}$ )	Energy ( $\text{kcal.mol}^{-1}$ )	CI Vector	Contribution
1	3	0	0	0	21221	28.6%
					22121	30.7%
					22211	38.3%
2	3	0.28	2250	6.4	12212	10.6%
					21221	13.1%
					22121	58.9%
					22211	10.1%

3	3	0.46	3741	10.7	12221	73.2%
					21122	10.2%
					22112	11.8%
4	3	0.90	7246	20.7	12122	24.9%
					21221	14.1%
					22112	37.3%
					22211	11.3%
5	3	1.05	8490	24.3	21122	12.1%
					21212	73.7%
					22112	10.2%
6	3	1.20	9717	27.8	12122	31.1%
					21212	17.5%
					22112	32.2%
7	3	1.41	11353	32.5	11222	81.1%
8	1	1.69	13632	39.0	21221	11.7%
					21221*	11.7%
					22121	14.5%
					22121*	14.5%
					22211	15.6%
					22211*	15.6%
9	1	1.69	13654	39.0	22220	59.3%
10	1	1.96	15826	45.2	22121	24.0%
					22121*	24.0%
11	1	2.14	17297	49.5	12221	27.1%
					12221*	27.1%
12	3	2.32	18688	53.4	12221	18.5%
					21122	36.8%
					21221	19.9%
13	1	2.45	19725	56.4	2222	14.3%
					20222	20.9%
					22022	14.0%
					22112	14.7%
					22112*	14.7%
					22202	18.4%
14	3	2.68	21600	61.8	12212	26.3%
					21122	23.2%
					22211	29.0%
15	3	2.73	22027	63.0	12122	25.6%
					12212	45.7%
					21122	11.9%
					21221	10.6%
16	1	2.86	23089	66.0	21122	16.9%
					21122*	16.9%
					22220	12.8%
17	1	2.96	23864	68.2	12221	11.1%
					12221*	11.1%
					20222	10.7%
					22022	28.9%
18	1	3.21	25883	74.0	11222	17.6%
					11222*	17.6%
					12122	14.9%
					12122*	14.9%
19	1	3.25	26223	75.0	21221	21.9%
					21221*	21.9%
					22211	12.0%
					22211*	12.0%
20	1	3.30	26590	76.0	12122	18.4%
					12122*	18.4%
					22211	13.6%
					22211*	13.6%
21	1	3.49	28114	80.4	20222	17.3%



22	1	3.76	30312	86.7	22022	17.1%
					20222	12.3%
					21122	17.9%
					21122*	17.9%
23	1	3.98	32092	91.8	02222	42.0%
					22202	27.5%
24	1	4.00	32278	92.3	12212	25.8%
					12212*	25.8%

**Table S32:** Calculated electronic transitions for  $\text{Ni}^{\text{II}}(\text{IB})\text{Br}_2$  at the CASSCF level with 20e,11o active space (*cf.* Figure S91) in the gas phase. Active Space Orbitals (in order for CI vector notation below): 4p(Br), 4p(Br), 4p(Br), 4p(Br), 4p(Br), 4p(Br),  $3d_{z^2}$  (Ni),  $3d_{x^2-y^2}$  (Ni),  $3d_{yz}$  (Ni),  $3d_{xy}$  (Ni),  $3d_{xz}$  (Ni). Starred CI vectors refer to the determinants that are already present in the particular state with the flipped alpha/beta orbitals.

State	Multiplicity	Energy (eV)	Energy (cm <sup>-1</sup> )	Energy (kcal.mol <sup>-1</sup> )	CI Vector	Contribution
1	3	0	0	0	22222221221	91.0%
2	3	0.33	2680	7.7	22222221212	11.5%
					22222222121	77.2%
3	3	0.51	4117	11.8	22222221122	33.8%
					22222222211	53.7%
4	3	0.78	6313	18.0	22222212122	27.7%
					22222212221	20.0%
					22222221122	25.9%
					22222222112	18.3%
5	3	0.85	6893	19.7	22222211222	85.1%
6	3	1.03	8279	23.7	22222212122	20.7%
					22222222112	59.9%
7	3	1.18	9518	27.2	22222212212	61.1%
					22222221212	31.3%
8	1	1.67	13471	38.5	22222220222	13.4%
					22222221221	20.1%
					22222221221*	20.1%
					22222222220	18.9%
9	1	1.71	13771	39.4	22222220222	20.5%
					22222221221	16.6%
					22222221221*	16.6%
					22222222220	26.9%
10	1	1.95	15742	45.0	2222222121	27.3%
					2222222121*	27.3%
11	1	2.15	17361	49.6	22222221122	22.4%
					22222221122*	22.4%
					22222222211	13.2%
					22222222211*	13.2%
12	3	2.27	18344	52.4	22222212122	26.1%
					22222212221	10.6%
					22222221122	29.5%
					22222222211	24.1%
13	1	2.30	18529	53.0	22222211222	11.2%
					22222211222*	11.2%
					22222220222	14.1%
					22222220222	40.4%
14	1	2.63	21199	60.6	22222211222	10.5%
					22222211222*	10.5%
					22222222220	13.6%
15	3	2.67	21511	61.5	22222212212	36.6%
					22222221212	44.6%
16	1	2.68	21641	61.9	22222222211	12.5%
					22222222211*	12.5%
17	1	2.75	22206	63.5	22222221212	31.3%
					22222221212*	31.3%
18	3	2.88	23192	66.3	22222212122	21.2%

					22222212221	52.5%
					22222222112	13.8%
19	1	2.90	23360	66.8	22222222112*	22.1%
					22222222112*	22.1%
20	1	3.15	25389	72.6	22222222022	20.2%
					22222222202	17.5%
21	1	3.18	25648	73.3	22222222112	13.0%
					22222222112*	13.0%
22	1	3.56	28691	82.0	22222212122	18.4%
					22222212122*	18.4%
					22222212221	19.4%
					22222212221*	19.4%
23	1	3.69	29798	85.2	22222212212	35.8%
					22222212212*	35.8%
24	1	3.76	30366	86.8	22222202222	35.0%
					22222222202	29.1%

**Table S33:** Calculated electronic transitions for  $\text{Ni}^{\text{II}}(\text{IB})\text{Br}_2$  at the MS-CASPT2 level with 20e,11lo active space (*cf.* Figure S91) in the gas phase. Active Space Orbitals (in order for CI vector notation below): 4p(Br), 4p(Br), 4p(Br), 4p(Br), 4p(Br), 4p(Br),  $3d_{z^2}$  (Ni),  $3d_{x^2-y^2}$  (Ni),  $3d_{yz}$  (Ni),  $3d_{xy}$  (Ni),  $3d_{xz}$  (Ni). Starred CI vectors refer to the determinants that are already present in the particular state with the flipped alpha/beta orbitals.

State	Multiplicity	Energy (eV)	Energy ( $\text{cm}^{-1}$ )	Energy ( $\text{kcal.mol}^{-1}$ )	CI Vector	Contribution
1	3	0	0	0	22222221221	91.0%
2	3	0.26	2079	5.9	22222221212	11.5%
					22222222121	77.2%
3	3	0.39	3167	9.1	22222221122	33.8%
					22222222211	53.7%
4	3	0.91	7349	21.0	22222212122	27.7%
					22222212221	20.0%
					22222221122	25.9%
					22222222112	18.3%
5	3	1.06	8560	24.5	22222211222	85.1%
6	1	1.24	10028	28.7	22222220222	13.4%
					22222221221	20.1%
					22222221221*	20.1%
					22222222220	18.9%
7	1	1.24	10030	28.7	22222220222	20.5%
					22222221221	16.6%
					22222221221*	16.6%
					22222222220	26.9%
8	3	1.25	10053	28.7	22222212122	20.7%
					22222222112	59.9%
9	3	1.39	11201	32.0	22222212212	61.1%
					22222221212	31.3%
10	1	1.51	12143	34.7	22222222121	27.3%
					22222222121*	27.3%
11	1	1.82	14704	42.0	22222221122	22.4%
					22222221122*	22.4%
					22222222211	13.2%
					22222222211*	13.2%
12	3	1.94	15617	44.7	22222212122	26.1%
					22222212221	10.6%
					22222221122	29.5%
					22222222211	24.1%
13	1	1.99	16012	45.8	22222211222	11.2%
					22222211222*	11.2%
					22222220222	14.1%
					22222220222	40.4%
14	1	2.17	17532	50.1	22222211222	10.5%

					22222211222*	10.5%
					22222222220	13.6%
15	1	2.24	18059	51.6	22222222211	12.5%
					22222222211*	12.5%
16	1	2.34	18847	53.9	2222221212	31.3%
					2222221212*	31.3%
17	3	2.48	19978	57.1	22222212212	36.6%
					2222221212	44.6%
18	3	2.52	20307	58.1	22222212122	21.2%
					22222212221	52.5%
					22222222112	13.8%
19	1	2.54	20509	58.6	22222222112	22.1%
					22222222112*	22.1%
20	1	2.68	21649	61.9	22222222022	20.2%
					22222222202	17.5%
21	1	2.81	22697	64.9	22222222112	13.0%
					22222222112*	13.0%
22	1	3.34	26947	77.0	22222212122	18.4%
					22222212122*	18.4%
					22222212221	19.4%
					22222212221*	19.4%
23	1	3.53	28470	81.4	22222202222	35.0%
					22222222202	29.1%
24	1	3.57	28790	82.3	22222212212	35.8%
					22222212212*	35.8%
25	1	4.30	34683	99.2	21222222221	40.8%
					21222222221*	40.8%
26	1	4.32	34858	99.7	12222222221	30.8%
					12222222221*	30.8%

**Table S34:** Calculated electronic transitions for  $\text{Ni}^{\text{II}}(\text{IB})\text{Br}_2$  at the CASSCF level with 22e,12o active space (*cf.* Figure S91) in the gas phase. Active Space Orbitals (in order for CI vector notation below): 4p(Br),  $3d_{z^2}$ (Ni),  $3d_{yz}$ (Ni), 4p(Br),  $3d_{xy}$ (Ni), 4p(Br), 4p(Br), 4p(Br), 4p(Br),  $\sigma$ -bonding(IB),  $3d_{x^2-y^2}$ (Ni),  $3d_{xz}$ (Ni). Starred CI vectors refer to the determinants that are already present in the particular state with the flipped alpha/beta orbitals.

State	Multiplicity	Energy (eV)	Energy ( $\text{cm}^{-1}$ )	Energy ( $\text{kcal.mol}^{-1}$ )	CI Vector	Contribution
1	3	0	0	0	222222222211	94.90%
2	3	0.36	2905	8.3	221222222221	83.60%
					222212222212	12.00%
3	3	0.56	4481	12.8	221222222212	29.70%
					222212222221	61.30%
4	3	0.86	6945	19.9	211222222222	19.40%
					212222222212	11.90%
					212222222221	15.90%
					221212222222	25.00%
					221222222212	21.80%
5	3	0.95	7636	21.8	212222222212	85.10%
6	3	1.12	9006	25.7	211222222222	27.10%
					221212222222	42.80%
					222212222221	13.10%
7	3	1.28	10305	29.5	212212222222	57.80%
					222212222212	28.40%
8	1	1.57	12703	36.3	222222222202	23.40%
					222222222220	36.70%
9	1	1.63	13161	37.6	222222222211	33.60%
					222222222211*	33.60%
10	1	1.89	15250	43.6	221222222221	28.80%
					221222222221*	28.80%
					222222222202	11.00%
11	1	2.14	17221	49.2	221222222212	23.00%

					221222222212*	23.00%
					222212222221	14.50%
					222212222221*	14.50%
12	3	2.26	18259	52.2	211222222222	30.90%
					212222222221	10.90%
					221222222212	27.20%
					222212222221	17.70%
13	1	2.28	18403	52.6	220222222222	36.30%
					222222222202	19.70%
14	1	2.57	20736	59.3	212222222212	16.30%
					212222222212*	16.30%
					222222222202	12.80%
					222222222220	12.20%
15	1	2.63	21178	60.6	221222222212	15.10%
					221222222212*	15.10%
					222212222221	11.80%
					222212222221*	11.80%
16	3	2.69	21733	62.1	212212222222	38.10%
					222212222212	42.90%
17	1	2.74	22116	63.2	222212222212	34.90%
					222212222212*	34.90%
18	3	2.83	22834	65.3	211222222222	12.90%
					212222222221	57.90%
					221212222222	14.60%
19	1	2.88	23193	66.3	221212222222	20.70%
					221212222222*	20.70%
20	1	3.08	24831	71.0	220222222222	21.50%
21	1	3.11	25108	71.8	212222222221	11.70%
					212222222221*	11.70%
					221212222222	14.40%
					221212222222*	14.40%
22	1	3.47	27986	80.0	211222222222	17.30%
					211222222222*	17.30%
					212222222221	22.50%
					212222222221*	22.50%
23	1	3.72	29966	85.7	202222222222	12.00%
					212212222222	22.00%
					212212222222*	22.00%
					222202222222	22.00%
24	1	3.75	30246	86.5	202222222222	17.60%
					212212222222	16.70%
					212212222222*	16.70%
					222202222222	21.20%

**Table S35:** Calculated electronic transitions for  $\text{Ni}^{\text{II}}(\text{IB})\text{Br}_2$  at the MS-CASPT2 level with 22e,12o active space (*cf.* Figure S91) in the gas phase. Active Space Orbitals (in order for CI vector notation below): 4p(Br),  $3d_{z^2}$  (Ni),  $3d_{yz}$  (Ni), 4p(Br),  $3d_{xy}$  (Ni), 4p(Br), 4p(Br), 4p(Br), 4p(Br),  $\sigma$ -bonding(IB),  $3d_{x^2-y^2}$  (Ni),  $3d_{xz}$  (Ni). Starred CI vectors refer to the determinants that are already present in the particular state with the flipped alpha/beta orbitals.

State	Multiplicity	Energy (eV)	Energy ( $\text{cm}^{-1}$ )	Energy ( $\text{kcal.mol}^{-1}$ )	CI Vector	Contribution
1	3	0	0	0	222222222211	94.9%
2	3	0.29	2347	6.7	221222222221	83.6%
					222212222212	12.0%
3	3	0.36	2897	8.3	221222222212	29.7%
					222212222221	61.3%
4	3	0.93	7513	21.5	211222222222	19.4%
					212222222212	11.9%
					212222222221	15.9%
					221212222222	25.0%
					221222222212	21.8%

5	3	1.09	8755	25.0	21222222212	85.1%
6	1	1.22	9827	28.1	22222222202	23.4%
					22222222220	36.7%
7	1	1.27	10214	29.2	22222222211	33.6%
					22222222211*	33.6%
8	3	1.29	10392	29.7	21122222222	27.1%
					22121222222	42.8%
					22221222221	13.1%
9	3	1.46	11780	33.7	21221222222	57.8%
					22221222212	28.4%
10	1	1.52	12242	35.0	22122222221	28.8%
					22122222221*	28.8%
					22222222202	11.0%
11	1	1.84	14840	42.4	22122222212	23.0%
					22122222212*	23.0%
					22221222221	14.5%
					22221222221*	14.5%
12	3	1.92	15465	44.2	21122222222	30.9%
					21222222221	10.9%
					22122222212	27.2%
					22221222221	17.7%
13	1	2.01	16196	46.3	22022222222	36.3%
					22222222202	19.7%
14	1	2.20	17759	50.8	21222222212	16.3%
					21222222212*	16.3%
					22222222202	12.8%
					22222222220	12.2%
15	1	2.23	18016	51.5	22122222212	15.1%
					22122222212*	15.1%
					22221222221	11.8%
					22221222221*	11.8%
16	1	2.41	19410	55.5	22221222212	34.9%
					22221222212*	34.9%
17	3	2.47	19914	56.9	21122222222	12.9%
					21222222221	57.9%
					22121222222	14.6%
18	3	2.52	20296	58.0	21221222222	38.1%
					22221222212	42.9%
19	1	2.56	20674	59.1	22121222222	20.7%
					22121222222*	20.7%
20	1	2.68	21577	61.7	22022222222	21.5%
21	1	2.77	22347	63.9	21222222221	11.7%
					21222222221*	11.7%
					22121222222	14.4%
					22121222222*	14.4%
22	1	3.20	25784	73.7	21122222222	17.3%
					21122222222*	17.3%
					21222222221	22.5%
					21222222221*	22.5%
23	1	3.47	27961	79.9	20222222222	17.6%
					21221222222	16.7%
					21221222222*	16.7%
					22220222222	21.2%
24	1	3.50	28265	80.8	20222222222	12.0%
					21221222222	22.0%
					21221222222*	22.0%
					22220222222	22.0%

**Table S36:** Calculated electronic transitions for **Ni<sup>II</sup>(IB)Cl<sub>2</sub>** at the CASSCF level with 22e,12o active space (*cf.* Figure S91) with the PCM solvation model ( $\epsilon = 38$ ). Active Space Orbitals (in order for CI vector

notation below):  $3d_{z^2}(\text{Ni})$ ,  $\sigma$ -bonding(IB),  $3p(\text{Cl})$ ,  $3p(\text{Cl})$ ,  $3p(\text{Cl})$ ,  $3p(\text{Cl})$ ,  $3p(\text{Cl})$ ,  $3p(\text{Cl})$ ,  $3d_{xy}(\text{Ni})$ ,  $3d_{yz}(\text{Ni})$ ,  $3d_{x^2-y^2}(\text{Ni})$ ,  $3d_{xz}(\text{Ni})$ . Starred CI vectors refer to the determinants that are already present in the particular state with the flipped alpha/beta orbitals.

State	Multiplicity	Energy (eV)	Energy (cm <sup>-1</sup> )	Energy (kcal.mol <sup>-1</sup> )	CI Vector	Contribution
1	3	0	0	0	22222222211	96.2%
2	3	0.35	2792	8.0	222222222121	85.6%
3	3	0.54	4376	12.5	122222222221	14.3%
					222222221221	55.3%
					222222222112	28.7%
4	3	0.85	6816	19.5	222222221122	45.7%
					222222221221	18.6%
					222222222112	27.7%
5	3	0.94	7618	21.8	122222222212	68.9%
					222222221212	29.7%
6	3	1.12	9061	25.9	122222222122	70.4%
					222222222112	11.3%
7	3	1.30	10448	29.9	122222221222	71.1%
					122222222212	11.1%
					222222221212	14.1%
8	1	1.67	13439	38.4	222222222202	24.7%
					222222222220	58.4%
9	1	1.76	14216	40.6	222222222211	42.8%
					222222222211*	42.8%
10	1	2.01	16236	46.4	222222222121	35.9%
					222222222121*	35.9%
11	1	2.27	18273	52.2	222222221221	20.8%
					222222221221*	20.8%
					2222222222112	20.1%
					222222222112*	20.1%
12	3	2.42	19515	55.8	122222222122	25.3%
					122222222221	40.7%
					222222222112	26.7%
13	1	2.48	19980	57.1	222222222202	39.6%
					222222222202	25.1%
14	1	2.81	22646	64.7	122222222212	15.6%
					122222222212*	15.6%
					222222222202	17.5%
					222222222220	13.3%
15	3	2.85	22957	65.6	122222221222	27.7%
					122222222212	14.5%
					222222221212	45.5%
16	1	2.86	23058	65.9	222222221221	13.8%
					222222221221*	13.8%
					2222222222112	25.5%
					222222222112*	25.5%
17	3	2.91	23474	67.1	122222222221	24.7%
					222222221122	41.8%
					222222221221	21.8%
18	1	3.03	24471	70.0	022222222222	12.3%
					122222222212	17.9%
					122222222212*	17.9%
					222222221212	16.9%
					222222221212*	16.9%
19	1	3.08	24824	71.0	122222222122	18.7%
					122222222122*	18.7%
					122222222221	25.1%
					122222222221*	25.1%
20	1	3.31	26704	76.4	122222222221	12.5%
					122222222221*	12.5%
					2222222221122	19.5%

21	1	3.38	27243	77.9	222222221122*	19.5%
					022222222222	17.9%
					222222221212	12.4%
					222222221212*	12.4%
22	1	3.65	29423	84.1	222222220222	33.0%
					122222221222	14.1%
					122222222122*	14.1%
					222222221122	20.7%
					222222221122*	20.7%
					222222221221	10.4%
23	1	3.91	31553	90.2	222222221221*	10.4%
					022222222222	19.8%
					122222221222	15.1%
					122222222122*	15.1%
24	1	3.95	31888	91.2	222222220222	32.1%
					022222222222	10.6%
					122222221222	24.5%
					122222221222*	24.5%
					222222220222	19.0%

**Table S37:** Calculated electronic transitions for  $\text{Ni}^{\text{II}}(\text{IB})\text{Cl}_2$  at the MS-CASPT2 level with 22e,12o active space (*cf.* Figure S91) with the PCM solvation model ( $\epsilon = 38$ ). Active Space Orbitals (in order for CI vector notation below):  $3d_{z^2}(\text{Ni})$ ,  $\sigma$ -bonding(IB),  $3p(\text{Cl})$ ,  $3p(\text{Cl})$ ,  $3p(\text{Cl})$ ,  $3p(\text{Cl})$ ,  $3p(\text{Cl})$ ,  $3p(\text{Cl})$ ,  $3d_{xy}(\text{Ni})$ ,  $3d_{yz}(\text{Ni})$ ,  $3d_{x^2-y^2}(\text{Ni})$ ,  $3d_{xz}(\text{Ni})$ . Starred CI vectors refer to the determinants that are already present in the particular state with the flipped alpha/beta orbitals.

State	Multiplicity	Energy (eV)	Energy ( $\text{cm}^{-1}$ )	Energy ( $\text{kcal.mol}^{-1}$ )	CI Vector	Contribution
1	3	0	0	0	222222222211	96.2%
2	3	0.25	2009	5.7	222222222121	85.6%
3	3	0.41	3318	9.5	122222222221	14.3%
					222222221221	55.3%
					2222222222112	28.7%
4	3	0.92	7443	21.3	222222221122	45.7%
					222222221221	18.6%
					2222222222112	27.7%
5	3	1.21	9786	28.0	122222222212	68.9%
					222222221212	29.7%
6	1	1.27	10276	29.4	222222222202	24.7%
					222222222220	58.4%
7	3	1.34	10810	30.9	122222222122	70.4%
					2222222222112	11.3%
8	1	1.39	11201	32.0	222222222211	42.8%
					222222222211*	42.8%
9	3	1.58	12709	36.3	122222221222	71.1%
					122222222212	11.1%
					222222221212	14.1%
10	1	1.62	13091	37.4	222222222121	35.9%
					222222222121*	35.9%
11	1	1.94	15665	44.8	222222221221	20.8%
					222222221221*	20.8%
					2222222222112	20.1%
					2222222222112*	20.1%
12	3	2.03	16355	46.8	122222222122	25.3%
					122222222221	40.7%
					2222222222112	26.7%
13	1	2.23	17988	51.4	222222222022	39.6%
					222222222202	25.1%
14	1	2.43	19610	56.1	122222222212	15.6%
					122222222212*	15.6%
					222222222202	17.5%
					222222222220	13.3%

15	1	2.47	19909	56.9	22222221221	13.8%
					22222221221*	13.8%
					22222222112	25.5%
					22222222112*	25.5%
16	3	2.55	20607	58.9	12222222221	24.7%
					222222221122	41.8%
					222222221221	21.8%
17	3	2.68	21586	61.7	12222221222	27.7%
					12222222212	14.5%
					222222221212	45.5%
18	1	2.80	22596	64.6	12222222122	18.7%
					12222222122*	18.7%
					12222222221	25.1%
					12222222221*	25.1%
19	1	2.81	22642	64.7	02222222222	12.3%
					12222222212	17.9%
					12222222212*	17.9%
					222222221212	16.9%
					222222221212*	16.9%
20	1	3.02	24323	69.5	12222222221	12.5%
					12222222221*	12.5%
					222222221122	19.5%
					222222221122*	19.5%
21	1	3.03	24426	69.8	02222222222	17.9%
					222222221212	12.4%
					222222221212*	12.4%
					222222222022	33.0%
22	1	3.51	28274	80.8	12222222122	14.1%
					12222222122*	14.1%
					222222221122	20.7%
					222222221122*	20.7%
					222222221221	10.4%
23	1	3.98	32106	91.8	222222221221*	10.4%
					02222222222	10.6%
					122222221222	24.5%
					122222221222*	24.5%
					222222220222	19.0%
24	1	4.03	32493	92.9	02222222222	19.8%
					122222221222	15.1%
					122222221222*	15.1%
					222222220222	32.1%

**Table S38:** Calculated electronic transitions for  $\text{Ni}^{\text{II}}(\text{IB})\text{Br}_2$  at the CASSCF level with 22e,12o active space (*cf.* Figure S91) with the PCM solvation model ( $\epsilon = 38$ ). Active Space Orbitals (in order for CI vector notation below): 4p(Br),  $3d_{xy}(\text{Ni})$ ,  $3d_{yz}(\text{Ni})$ , 4p(Br),  $3d_{z^2}(\text{Ni})$ , 4p(Br), 4p(Br), 4p(Br), 4p(Br),  $\sigma$ -bonding(IB),  $3d_{x^2-y^2}(\text{Ni})$ ,  $3d_{xz}(\text{Ni})$ . Starred CI vectors refer to the determinants that are already present in the particular state with the flipped alpha/beta orbitals.

State	Multiplicity	Energy (eV)	Energy ( $\text{cm}^{-1}$ )	Energy ( $\text{kcal.mol}^{-1}$ )	CI Vector	Contribution
1	3	0.00	0	0.0	22122222221	12.1%
					22222222211	82.7%
2	3	0.34	2764	7.9	21222222212	10.2%
					22122222221	76.5%
3	3	0.55	4419	12.6	21222222221	70.5%
					22122222212	23.1%
4	3	0.88	7127	20.4	21122222222	21.9%
					22121222222	10.2%
					22122222212	28.7%
					22221222212	14.2%
					22221222221	19.5%
5	3	0.98	7891	22.6	22121222222	19.3%



					222212222212	74.0%
6	3	1.13	9092	26.0	211222222222	35.7%
					212222222212	11.2%
					221212222222	22.6%
					221222222212	14.1%
7	3	1.32	10662	30.5	212212222222	72.5%
					212222222212	15.1%
8	1	1.59	12834	36.7	222222222202	16.4%
					222222222220	57.1%
9	1	1.70	13751	39.3	222222222211	35.4%
					222222222211*	35.4%
10	1	1.96	15807	45.2	221222222221	31.7%
					221222222221*	31.7%
11	1	2.23	17972	51.4	212222222221	23.3%
					212222222221*	23.3%
					222222222202	10.4%
12	3	2.40	19321	55.2	212222222221	16.0%
					221212222222	24.5%
					221222222212	24.0%
					222212222221	19.3%
13	1	2.44	19662	56.2	220222222222	17.0%
					221222222212	18.8%
					221222222212*	18.8%
					222222222202	12.1%
14	1	2.72	21953	62.8	222212222212	19.4%
					222212222212*	19.4%
					222222222202	19.7%
					222222222220	10.3%
15	3	2.78	22433	64.1	211222222222	22.1%
					212212222222	19.4%
					212222222212	22.0%
					222212222221	16.0%
16	1	2.80	22573	64.5	212222222221	11.6%
					212222222221*	11.6%
					220222222222	15.1%
					221222222212	12.9%
					221222222212*	12.9%
17	3	2.84	22911	65.5	212222222212	32.7%
					221212222222	11.9%
					222212222221	29.9%
18	1	2.98	24018	68.7	212222222212	30.4%
					212222222212*	30.4%
19	1	3.00	24223	69.3	222212222221	24.5%
					222212222221*	24.5%
20	1	3.21	25919	74.1	211222222222	27.9%
					211222222222*	27.9%
21	1	3.27	26397	75.5	220222222222	25.5%
					222202222222	13.2%
22	1	3.53	28445	81.3	221212222222	25.8%
					221212222222*	25.8%
23	1	3.84	30991	88.6	202222222222	33.5%
					212212222222	13.7%
					212212222222*	13.7%
					222202222222	18.4%
24	1	3.88	31256	89.4	202222222222	11.7%
					212212222222	24.8%
					212212222222*	24.8%
					222202222222	14.6%

**Table S39:** Calculated electronic transitions for  $\text{Ni}^{\text{II}}(\text{IB})\text{Br}_2$  at the MS-CASPT2 level with 22e,12o active space (*cf.* Figure S91) with the PCM solvation model ( $\epsilon = 38$ ). Active Space Orbitals (in order for CI vector notation below): 4p(Br),  $3d_{xy}(\text{Ni})$ ,  $3d_{yz}(\text{Ni})$ , 4p(Br),  $3d_{z^2}(\text{Ni})$ , 4p(Br), 4p(Br), 4p(Br), 4p(Br),  $\sigma$ -bonding(IB),  $3d_{x^2-y^2}(\text{Ni})$ ,  $3d_{xz}(\text{Ni})$ . Starred CI vectors refer to the determinants that are already present in the particular state with the flipped alpha/beta orbitals.

State	Multiplicity	Energy (eV)	Energy ( $\text{cm}^{-1}$ )	Energy ( $\text{kcal.mol}^{-1}$ )	CI Vector	Contribution
1	3	0	0	0	221222222221	12.1%
					222222222211	82.7%
2	3	0.23	1824	5.2	212222222212	10.2%
					221222222221	76.5%
3	3	0.37	2974	8.5	212222222221	70.5%
					221222222212	23.1%
4	3	0.90	7229	20.7	211222222222	21.9%
					221212222222	10.2%
					221222222212	28.7%
					222212222212	14.2%
					222212222221	19.5%
5	3	1.16	9322	26.7	221212222222	19.3%
					222212222212	74.0%
6	1	1.17	9428	27.0	222222222202	16.4%
					222222222220	57.1%
7	3	1.27	10244	29.3	211222222222	35.7%
					212222222212	11.2%
					221212222222	22.6%
					221222222212	14.1%
8	1	1.34	10828	31.0	222222222211	35.4%
					222222222211*	35.4%
9	3	1.54	12382	35.4	212212222222	72.5%
					212222222212	15.1%
10	1	1.55	12504	35.8	221222222221	31.7%
					221222222221*	31.7%
11	1	1.85	14932	42.7	212222222221	23.3%
					212222222221*	23.3%
					222222222202	10.4%
12	3	2.00	16112	46.1	212222222221	16.0%
					221212222222	24.5%
					221222222212	24.0%
					222212222221	19.3%
13	1	2.17	17475	50.0	220222222222	17.0%
					221222222212	18.8%
					221222222212*	18.8%
					222222222202	12.1%
14	1	2.31	18654	53.3	222212222212	19.4%
					222212222212*	19.4%
					222222222202	19.7%
					222222222220	10.3%
15	1	2.38	19223	55.0	212222222221	11.6%
					212222222221*	11.6%
					220222222222	15.1%
					221222222212	12.9%
					221222222212*	12.9%
16	3	2.42	19514	55.8	212222222212	32.7%
					221212222222	11.9%
					222212222221	29.9%
17	3	2.43	19561	55.9	211222222222	22.1%
					212212222222	19.4%
					212222222212	22.0%
					222212222221	16.0%
18	1	2.67	21572	61.7	222212222221*	24.5%
					222212222221*	24.5%

19	1	2.68	21602	61.8	21222222212	30.4%
					21222222212*	30.4%
20	1	2.88	23206	66.3	21122222222	27.9%
					21122222222*	27.9%
21	1	2.88	23248	66.5	22022222222	25.5%
					22220222222	13.2%
22	1	3.28	26468	75.7	22121222222	25.8%
					22121222222*	25.8%
23	1	3.77	30417	87.0	20222222222	11.7%
					21221222222	24.8%
					21221222222*	24.8%
					22220222222	14.6%
24	1	3.83	30905	88.4	20222222222	33.5%
					21221222222	13.7%
					21221222222*	13.7%
					22220222222	18.4%

**Table S40:** Calculated electronic transitions for  $\text{Ni}^{\text{II}}(\text{IB})(\text{O-DMA})\text{Cl}_2$  at the CASSCF level with 22e,12o active space (*cf.* Figure S91) in the gas phase. Active Space Orbitals (in order for CI vector notation below):  $3d_{z^2}(\text{Ni})$ ,  $\sigma$ -bonding(IB),  $3p(\text{Cl})$ ,  $3d_{xy}(\text{Ni})$ ,  $3p(\text{Cl})$ ,  $3p(\text{Cl})$ ,  $3p(\text{Cl})$ ,  $3p(\text{Cl})$ ,  $3d_{yz}(\text{Ni})$ ,  $3p(\text{Cl})$ ,  $3d_{x^2-y^2}(\text{Ni})$ ,  $3d_{xz}(\text{Ni})$ . Starred CI vectors refer to the determinants that are already present in the particular state with the flipped alpha/beta orbitals.

State	Multiplicity	Energy (eV)	Energy ( $\text{cm}^{-1}$ )	Energy ( $\text{kcal.mol}^{-1}$ )	CI Vector	Contribution
1	3	0.00	0	0.0	22222222211	97.2%
2	3	0.47	3779	10.8	22212222221	17.0%
					222222221221	75.4%
3	3	0.71	5746	16.4	12222222212	12.5%
					12222222221	12.1%
					22212222221	42.1%
4	3	0.81	6530	18.7	12222222212	41.2%
					12222222221	23.0%
					22212222212	10.7%
					22212222221	13.7%
5	3	1.15	9253	26.5	12212222222	19.7%
					12222222212	12.1%
					22212222212	45.1%
6	3	1.30	10472	29.9	12212222222	21.7%
					12222222212	18.0%
					12222222221	10.2%
					222122221222	40.7%
7	1	1.38	11098	31.7	22222222211	12.7%
					22222222211*	12.7%
					22222222220	54.4%
8	3	1.41	11407	32.6	12212222222	15.1%
					122222221222	55.3%
					222222221212	15.2%
9	1	1.74	14033	40.1	22222222202	18.2%
					222222222211	26.3%
					222222222211*	26.3%
					22222222220	16.4%
10	1	2.20	17724	50.7	222222221221	32.3%
					222222221221*	32.3%
11	1	2.35	18936	54.1	22212222221	21.8%
					22212222221*	21.8%
12	1	2.49	20107	57.5	12222222221	12.3%
					12222222221*	12.3%
					22212222221	16.7%
					22212222221*	16.7%
13	3	2.55	20561	58.8	122222221222	20.4%

					12222222221	13.9%
					22212222221	14.2%
					222222221212	24.1%
14	1	2.87	23165	66.2	222122222212	31.1%
					222122222212*	31.1%
15	3	2.95	23774	68.0	122222221222	11.7%
					122222222221	32.9%
					222122221222	27.2%
16	1	2.98	24028	68.7	222022222222	12.2%
					222222222202	45.8%
17	3	3.16	25516	73.0	122122222222	35.3%
					222122222212	16.0%
					222222221212	38.1%
18	1	3.25	26250	75.1	122222222212	16.6%
					122222222212*	16.6%
					122222222221	16.4%
					122222222221*	16.4%
19	1	3.46	27932	79.9	222222221212	28.0%
					222222221212*	28.0%
20	1	3.64	29386	84.0	022222222222	11.0%
					122122222222	14.3%
					122122222222*	14.3%
					222222220222	27.8%
21	1	3.69	29771	85.1	022222222222	13.9%
					222022222222	19.6%
					222122221222	11.7%
					222122221222*	11.7%
22	1	3.85	31022	88.7	222022222222	16.0%
					222222220222	19.3%
23	1	3.97	32008	91.5	022222222222	31.5%
					222022222222	10.5%
					222122221222	12.2%
					222122221222*	12.2%
24	1	4.02	32385	92.6	122122222222	15.5%
					122122222222*	15.5%
					122222221222	19.7%
					122222221222*	19.7%

**Table S41:** Calculated electronic transitions for  $\text{Ni}^{\text{II}}(\text{IB})(\text{O-DMA})\text{Cl}_2$  at the MS-CASPT2 level with 22e,12o active space (*cf.* Figure S91) in the gas phase. Active Space Orbitals (in order for CI vector notation below):  $3d_{z^2}(\text{Ni})$ ,  $\sigma\text{-bonding}(\text{IB})$ ,  $3p(\text{Cl})$ ,  $3d_{xy}(\text{Ni})$ ,  $3p(\text{Cl})$ ,  $3p(\text{Cl})$ ,  $3p(\text{Cl})$ ,  $3p(\text{Cl})$ ,  $3d_{yz}(\text{Ni})$ ,  $3p(\text{Cl})$ ,  $3d_{x^2-y^2}(\text{Ni})$ ,  $3d_{xz}(\text{Ni})$ . Starred CI vectors refer to the determinants that are already present in the particular state with the flipped alpha/beta orbitals.

State	Multiplicity	Energy (eV)	Energy ( $\text{cm}^{-1}$ )	Energy ( $\text{kcal.mol}^{-1}$ )	CI Vector	Contribution
1	3	0.00	0	0.0	222222222211	97.2%
2	3	0.62	5037	14.4	222122222221	17.0%
					222222221221	75.4%
3	3	0.75	6028	17.2	122222222212	12.5%
					122222222221	12.1%
					222122222221	42.1%
4	3	0.83	6705	19.2	122222222212	41.2%
					122222222221	23.0%
					222122222212	10.7%
					222122222221	13.7%
5	1	0.97	7849	22.4	222222222211	12.7%
					222222222211*	12.7%
					222222222220	54.4%
6	3	1.36	10946	31.3	122122222222	19.7%
					122222222212	12.1%
					222122222212	45.1%

7	1	1.40	11258	32.2	22222222202	18.2%
					22222222211	26.3%
					22222222211*	26.3%
					22222222220	16.4%
8	3	1.69	13646	39.0	12212222222	21.7%
					12222222212	18.0%
					12222222221	10.2%
					222122221222	40.7%
9	3	1.89	15254	43.6	12212222222	15.1%
					122222221222	55.3%
					222222221212	15.2%
10	1	1.97	15903	45.5	222222221221	32.3%
					222222221221*	32.3%
11	1	2.20	17749	50.7	22212222221	21.8%
					22212222221*	21.8%
12	1	2.31	18662	53.4	12222222221	12.3%
					12222222221*	12.3%
					22212222221	16.7%
					22212222221*	16.7%
13	3	2.37	19121	54.7	122222221222	20.4%
					12222222221	13.9%
					22212222221	14.2%
					222222221212	24.1%
14	1	2.63	21223	60.7	22202222222	12.2%
					22222222202	45.8%
15	1	2.73	22054	63.1	22212222212	31.1%
					22212222212*	31.1%
16	3	2.83	22819	65.2	122222221222	11.7%
					12222222221	32.9%
					222122221222	27.2%
17	3	2.99	24093	68.9	12212222222	35.3%
					22212222212	16.0%
					222222221212	38.1%
18	1	3.24	26150	74.8	12222222212	16.6%
					12222222212*	16.6%
					12222222221	16.4%
					12222222221*	16.4%
19	1	3.36	27077	77.4	222222221212	28.0%
					222222221212*	28.0%
20	1	3.64	29352	83.9	02222222222	13.9%
					22202222222	19.6%
					222122221222	11.7%
					222122221222*	11.7%
21	1	3.82	30786	88.0	02222222222	11.0%
					12212222222	14.3%
					12212222222*	14.3%
					222222220222	27.8%
22	1	4.05	32697	93.5	22202222222	16.0%
					222222220222	19.3%
23	1	4.13	33320	95.3	12212222222	15.5%
					12212222222*	15.5%
					122222221222	19.7%
					122222221222*	19.7%
24	1	4.20	33887	96.9	02222222222	31.5%
					22202222222	10.5%
					222122221222	12.2%
					222122221222*	12.2%

**Table S42:** Calculated electronic transitions for  $\text{Ni}^{\text{II}}(\text{IB})(\text{O-DMA})\text{Br}_2$  at the CASSCF level with 22e,12o active space (*cf.* Figure S91) in the gas phase. Active Space Orbitals (in order for CI vector notation below):

$3d_{z^2}(\text{Ni})$ ,  $\sigma$ -bonding(IB),  $4p(\text{Br})$ ,  $4p(\text{Br})$ ,  $4p(\text{Br})$ ,  $4p(\text{Br})$ ,  $4p(\text{Br})$ ,  $3d_{yz}(\text{Ni})$ ,  $4p(\text{Br})$ ,  $3d_{xy}(\text{Ni})$ ,  $3d_{xz}(\text{Ni})$ ,  $3d_{x^2-y^2}(\text{Ni})$ . Starred CI vectors refer to the determinants that are already present in the particular state with the flipped alpha/beta orbitals.

State	Multiplicity	Energy (eV)	Energy (cm <sup>-1</sup> )	Energy (kcal.mol <sup>-1</sup> )	CI Vector	Contribution
1	3	0	0	0	22222222211	96.9%
2	3	0.53	4297	12.3	222222222112	73.1%
					222222222121	16.2%
3	3	0.75	6027	17.2	122222222221	27.1%
					222222212212	48.2%
4	3	0.81	6529	18.7	122222222221	44.6%
					222222212212	31.2%
					222222212221	11.6%
5	3	1.14	9203	26.3	122222222122	23.1%
					122222222221	11.2%
					222222212221	34.4%
6	1	1.31	10570	30.2	222222222202	22.8%
					222222222211	29.2%
					222222222211*	29.2%
7	3	1.32	10684	30.5	122222222212	17.8%
					222222212122	53.7%
8	3	1.45	11658	33.3	122222212222	57.8%
					122222222122	17.4%
					222222212221	10.9%
9	1	1.62	13066	37.4	222222222202	34.9%
					222222222220	41.6%
10	1	2.15	17313	49.5	222222222112	19.0%
					222222222112*	19.0%
11	1	2.27	18309	52.3	122222222221	17.0%
					122222222221*	17.0%
12	1	2.42	19518	55.8	222222212212	29.3%
					222222212212*	29.3%
13	3	2.45	19731	56.4	122222222122	21.4%
					122222222212	14.8%
					222222212221	28.0%
14	1	2.70	21816	62.4	222222212221	33.3%
					222222212221*	33.3%
15	1	2.75	22157	63.3	222222222202	20.6%
					222222222220	25.5%
16	3	2.86	23063	65.9	122222222212	37.0%
					222222212122	33.4%
17	3	3.08	24869	71.1	122222212222	19.1%
					122222222122	19.9%
					222222222121	38.6%
18	1	3.16	25468	72.8	122222222212	26.4%
					122222222212*	26.4%
19	1	3.22	25981	74.3	222222222121	20.8%
					222222222121*	20.8%
20	1	3.52	28428	81.3	022222222222	13.9%
					122222212222	14.9%
					122222212222*	14.9%
					222222202222	11.8%
					222222212122	10.7%
					222222212122*	10.7%
21	1	3.58	28902	82.6	222222202222	29.7%
22	3	3.58	28908	82.7	222212222212	47.7%
					222212222221	34.8%
23	1	3.71	29960	85.7	122222212222	11.3%
					122222212222*	11.3%
					222222212122	13.0%
					222222212122*	13.0%

24	1	3.74	30162	86.2	222212222212 222212222212*	29.9% 29.9%
25	1	3.87	31230	89.3	022222222222 122222222122 122222222122* 222222222022	17.8% 12.9% 12.9% 13.0%
26	1	3.91	31566	90.3	122222222122 122222222122* 222222222022	17.3% 17.3% 17.0%
27	3	3.93	31722	90.7	222212222212 222212222221	43.7% 42.2%
28	1	4.01	32376	92.6	222212222212 222212222212* 222212222221 222212222221*	11.7% 11.7% 30.8% 30.8%
29	3	4.11	33131	94.7	222122222212 222122222221	63.5% 24.8%
30	1	4.14	33432	95.6	222122222212 222122222212* 222122222221 222122222221*	25.3% 25.3% 13.1% 13.1%
31	3	4.20	33838	96.7	222212222221 222221222212 222221222221 222222221212	15.2% 28.4% 28.1% 15.6%
32	3	4.34	34977	100.0	222212212222	57.9%

**Table S43:** Calculated electronic transitions for  $\text{Ni}^{\text{II}}(\text{IB})(\text{O-DMA})\text{Br}_2$  at the MS-CASPT2 level with 22e,12o active space (*cf.* Figure S91) in the gas phase. Active Space Orbitals (in order for CI vector notation below):  $3d_{z^2}(\text{Ni})$ ,  $\sigma$ -bonding(IB),  $4p(\text{Br})$ ,  $4p(\text{Br})$ ,  $4p(\text{Br})$ ,  $4p(\text{Br})$ ,  $4p(\text{Br})$ ,  $3d_{yz}(\text{Ni})$ ,  $4p(\text{Br})$ ,  $3d_{xy}(\text{Ni})$ ,  $3d_{xz}(\text{Ni})$ ,  $3d_{x^2-y^2}(\text{Ni})$ . Starred CI vectors refer to the determinants that are already present in the particular state with the flipped alpha/beta orbitals.

State	Multiplicity	Energy (eV)	Energy ( $\text{cm}^{-1}$ )	Energy ( $\text{kcal.mol}^{-1}$ )	CI Vector	Contribution
1	3	0	0	0	222222222211	96.9%
2	3	0.66	5327	15.2	222222222112 222222222121	73.1% 16.2%
3	3	0.67	5384	15.4	122222222221 222222212212	27.1% 48.2%
4	3	0.74	5949	17.0	122222222221 222222212212 222222212221	44.6% 31.2% 11.6%
5	1	0.95	7681	22.0	222222222202 222222222211 222222222211*	22.8% 29.2% 29.2%
6	3	1.27	10267	29.4	122222222122 122222222221 222222212221	23.1% 11.2% 34.4%
7	1	1.28	10329	29.5	222222222202 222222222220	34.9% 41.6%
8	3	1.56	12604	36.0	122222222212 222222212122	17.8% 53.7%
9	3	1.76	14221	40.7	122222212222 122222222122 222222212221	57.8% 17.4% 10.9%
10	1	1.90	15301	43.7	222222222112 222222222112*	19.0% 19.0%
11	1	2.10	16899	48.3	122222222221 122222222221*	17.0% 17.0%
12	1	2.22	17876	51.1	222222212212 222222212212*	29.3% 29.3%

13	3	2.28	18389	52.6	12222222122	21.4%
					12222222212	14.8%
					222222212221	28.0%
14	1	2.33	18791	53.7	22222222202	20.6%
					22222222220	25.5%
15	1	2.49	20055	57.3	222222212221	33.3%
					222222212221*	33.3%
16	3	2.68	21581	61.7	12222222212	37.0%
					222222212122	33.4%
17	3	2.85	22989	65.7	122222212222	19.1%
					122222222122	19.9%
					222222222121	38.6%
18	1	3.00	24230	69.3	222222222121	20.8%
					222222222121*	20.8%
19	1	3.02	24327	69.6	122222222212	26.4%
					122222222212*	26.4%
20	1	3.27	26380	75.4	122222212222	11.3%
					122222212222*	11.3%
					222222212122	13.0%
					222222212122*	13.0%
21	1	3.42	27553	78.8	022222222222	13.9%
					122222212222	14.9%
					122222212222*	14.9%
					222222202222	11.8%
					222222212122	10.7%
					222222212122*	10.7%
22	1	3.46	27869	79.7	222222202222	29.7%
23	1	3.64	29368	84.0	222212222212	29.9%
					222212222212*	29.9%
24	1	3.73	30084	86.0	122222222122	17.3%
					122222222122*	17.3%
					222222222022	17.0%
25	1	3.78	30500	87.2	022222222222	17.8%
					122222222122	12.9%
					122222222122*	12.9%
					222222222022	13.0%
26	3	3.96	31915	91.3	222212222212	47.7%
					222212222221	34.8%
27	1	4.16	33525	95.9	222212222212	11.7%
					222212222212*	11.7%
					222212222221	30.8%
					222212222221*	30.8%
28	3	4.22	34056	97.4	222212222212	43.7%
					222212222221	42.2%



## S.9. References

- (1) Hofstra, J. L. Development and Mechanistic Studies of Ni-Catalyzed Asymmetric Reductive Cross-Coupling Reactions.
- (2) Hofstra, J. L.; Cherney, A. H.; Ordner, C. M.; Reisman, S. E. Synthesis of Enantioenriched Allylic Silanes via Nickel-Catalyzed Reductive Cross-Coupling. *J. Am. Chem. Soc.* **2018**, *140* (1), 139–142. <https://doi.org/10.1021/jacs.7b11707>.
- (3) Wang, Y.; Rogers, E. I.; Compton, R. G. The Measurement of the Diffusion Coefficients of Ferrocene and Ferrocenium and Their Temperature Dependence in Acetonitrile Using Double Potential Step Microdisk Electrode Chronoamperometry. *Journal of Electroanalytical Chemistry* **2010**, *648* (1), 15–19. <https://doi.org/10.1016/j.jelechem.2010.07.006>.
- (4) Bard, A. J.; Faulkner, L. R. *Electrochemical Methods: Fundamentals and Applications*, 2nd ed.; Wiley: New York, 2001.
- (5) Gerloch, M.; Hanton, L. R.; Manning, M. R. Tetrahedral Complexes of Nickel(II): Electronic Spectra,  $\gamma$  and  $\pi$  Bonding, And the Electroneutrality Principle. *Inorganica Chimica Acta* **1981**, *48*, 205–214. [https://doi.org/10.1016/S0020-1693\(00\)90092-6](https://doi.org/10.1016/S0020-1693(00)90092-6).
- (6) Koester, V. J.; Dunn, T. M. Electronic Spectrum of the Tetrachloronickelate(II) Complex at 2.2.Deg.K. *Inorg. Chem.* **1975**, *14* (8), 1811–1817. <https://doi.org/10.1021/ic50150a014>.
- (7) Fereday, R. J.; Hathaway, B. J.; Dudley, R. J. Polarised Single-Crystal Electronic Spectrum of Dichlorobis(Triphenylphosphine)Nickel(II). *J. Chem. Soc. A* **1970**, No. 0, 571–574. <https://doi.org/10.1039/J19700000571>.
- (8) Lever, A. B. P. *Inorganic Electronic Spectroscopy*, 2nd ed.; Elsevier, 1984.
- (9) Davies, J. E.; Gerloch, M.; Phillips, D. J. Phosphine  $\pi$ -Acceptor Properties in Dihalogenobis(Triphenylphosphine)-Nickel(II) and -Cobalt(II). *J. Chem. Soc., Dalton Trans.* **1979**, No. 11, 1836–1842. <https://doi.org/10.1039/DT9790001836>.
- (10) Goodgame, D. M. L.; Goodgame, M.; Cotton, F. A. Electronic Spectra of Some Tetrahedral Nickel(II) Complexes. *J. Am. Chem. Soc.* **1961**, *83* (20), 4161–4167. <https://doi.org/10.1021/ja01481a014>.
- (11) Espinoza, E. M.; Clark, J. A.; Soliman, J.; Derr, J. B.; Morales, M.; Vullev, V. I. Practical Aspects of Cyclic Voltammetry: How to Estimate Reduction Potentials When Irreversibility Prevails. *J. Electrochem. Soc.* **2019**, *166* (5), H3175–H3187. <https://doi.org/10.1149/2.0241905jes>.
- (12) Bard, A. J.; Faulkner, L. R.; White, H. S. *Electrochemical Methods: Fundamentals and Applications*, 3rd ed.; John Wiley & Sons, Inc.: Hoboken, NJ, USA, 2022.
- (13) Wang, J.; Tian, Y.; Zhao, Y.; Zhuo, K. A Volumetric and Viscosity Study for the Mixtures of 1-n-Butyl-3-Methylimidazolium Tetrafluoroborate Ionic Liquid with Acetonitrile, Dichloromethane, 2-Butanone and N, N – Dimethylformamide. *Green Chem.* **2003**, *5* (5), 618–622. <https://doi.org/10.1039/B303735E>.
- (14) Grande, M. del C.; García, M.; Marschoff, C. M. Density and Viscosity of Anhydrous Mixtures of Dimethylsulfoxide with Acetonitrile in the Range (298.15 to 318.15) K. *J. Chem. Eng. Data* **2009**, *54* (2), 652–658. <https://doi.org/10.1021/je8001909>.
- (15) Pal, A.; Kumar, A. Excess Molar Volumes and Kinematic Viscosities for Binary Mixtures of Dipropylene Glycol Monobutyl Ether and Dipropylene Glycol Tert-Butyl Ether with 2-Pyrrolidinone, N-Methyl-2-Pyrrolidinone, N,N-Dimethylformamide, and N,N-Dimethylacetamide at 298.15 K. *J. Chem. Eng. Data* **2005**, *50* (3), 856–862. <https://doi.org/10.1021/je049657g>.

- (16) Tang, T.; Jones, E.; Wild, T.; Hazra, A.; Minter, S. D.; Sigman, M. S. Investigating Oxidative Addition Mechanisms of Allylic Electrophiles with Low-Valent Ni/Co Catalysts Using Electroanalytical and Data Science Techniques. *J. Am. Chem. Soc.* **2022**, *144* (43), 20056–20066. <https://doi.org/10.1021/jacs.2c09120>.
- (17) Ju, L.; Lin, Q.; LiBretto, N. J.; Wagner, C. L.; Hu, C. T.; Miller, J. T.; Diao, T. Reactivity of (Bi-Oxazoline)Organonickel Complexes and Revision of a Catalytic Mechanism. *J. Am. Chem. Soc.* **2021**, *143* (36), 14458–14463. <https://doi.org/10.1021/jacs.1c07139>.
- (18) Zhou, Y.-Y.; Uyeda, C. Reductive Cyclopropanations Catalyzed by Dinuclear Nickel Complexes. *Angewandte Chemie International Edition* **2016**, *55* (9), 3171–3175. <https://doi.org/10.1002/anie.201511271>.
- (19) Turro, R. F.; Wahlman, J. L. H.; Tong, Z. J.; Chen, X.; Yang, M.; Chen, E. P.; Hong, X.; Hadt, R. G.; Yang, Y.-F.; Houk, K. N.; Reisman, S. E. Mechanistic Investigation of Ni-Catalyzed Reductive Cross-Coupling of Alkenyl and Benzyl Electrophiles. *Submitted and Uploaded to ChemRxiv* **2023**.
- (20) Sheldrick, G. M. Phase Annealing in SHELX-90: Direct Methods for Larger Structures. *Acta Crystallogr A Found Crystallogr* **1990**, *46* (6), 467–473. <https://doi.org/10.1107/S0108767390000277>.
- (21) Sheldrick, G. M. Crystal Structure Refinement with It SHELXL. *Acta Crystallographica Section C* **2015**, *71* (1), 3–8. <https://doi.org/10.1107/S2053229614024218>.
- (22) Müller, P. Practical Suggestions for Better Crystal Structures. *Crystallography Reviews* **2009**, *15* (1), 57–83. <https://doi.org/10.1080/08893110802547240>.
- (23) Neese, F. The ORCA Program System. *WIREs Comput Mol Sci* **2012**, *2* (1), 73–78. <https://doi.org/10.1002/wcms.81>.
- (24) Weigend, F.; Ahlrichs, R. Balanced Basis Sets of Split Valence, Triple Zeta Valence and Quadruple Zeta Valence Quality for H to Rn: Design and Assessment of Accuracy. *Phys. Chem. Chem. Phys.* **2005**, *7* (18), 3297. <https://doi.org/10.1039/b508541a>.
- (25) Grimme, S.; Antony, J.; Ehrlich, S.; Krieg, H. A Consistent and Accurate Ab Initio Parametrization of Density Functional Dispersion Correction (DFT-D) for the 94 Elements H-Pu. *The Journal of Chemical Physics* **2010**, *132* (15), 154104. <https://doi.org/10.1063/1.3382344>.
- (26) Grimme, S.; Ehrlich, S.; Goerigk, L. Effect of the Damping Function in Dispersion Corrected Density Functional Theory. *J. Comput. Chem.* **2011**, *32* (7), 1456–1465. <https://doi.org/10.1002/jcc.21759>.
- (27) Barone, V.; Cossi, M. Quantum Calculation of Molecular Energies and Energy Gradients in Solution by a Conductor Solvent Model. *J. Phys. Chem. A* **1998**, *102* (11), 1995–2001. <https://doi.org/10.1021/jp9716997>.
- (28) Klamt, A.; Schüürmann, G. COSMO: A New Approach to Dielectric Screening in Solvents with Explicit Expressions for the Screening Energy and Its Gradient. *J. Chem. Soc., Perkin Trans. 2* **1993**, No. 5, 799–805. <https://doi.org/10.1039/P29930000799>.
- (29) Eichkorn, K.; Treutler, O.; Öhm, H.; Häser, M.; Ahlrichs, R. Auxiliary Basis Sets to Approximate Coulomb Potentials. *Chemical Physics Letters* **1995**, *240* (4), 283–290. [https://doi.org/10.1016/0009-2614\(95\)00621-A](https://doi.org/10.1016/0009-2614(95)00621-A).
- (30) Tao, J.; Perdew, J. P.; Staroverov, V. N.; Scuseria, G. E. Climbing the Density Functional Ladder: Nonempirical Meta-Generalized Gradient Approximation Designed for Molecules and Solids. *Phys. Rev. Lett.* **2003**, *91* (14), 146401. <https://doi.org/10.1103/PhysRevLett.91.146401>.

- (31) Staroverov, V. N.; Scuseria, G. E.; Tao, J.; Perdew, J. P. Comparative Assessment of a New Nonempirical Density Functional: Molecules and Hydrogen-Bonded Complexes. *The Journal of Chemical Physics* **2003**, *119* (23), 12129–12137. <https://doi.org/10.1063/1.1626543>.
- (32) Roos, B. O.; Taylor, P. R.; Sigbahn, P. E. M. A Complete Active Space SCF Method (CASSCF) Using a Density Matrix Formulated Super-CI Approach. *Chemical Physics* **1980**, *48* (2), 157–173. [https://doi.org/10.1016/0301-0104\(80\)80045-0](https://doi.org/10.1016/0301-0104(80)80045-0).
- (33) Siegbahn, P. E. M.; Almlöf, J.; Heiberg, A.; Roos, B. O. The Complete Active Space SCF (CASSCF) Method in a Newton–Raphson Formulation with Application to the HNO Molecule. *The Journal of Chemical Physics* **1981**, *74* (4), 2384–2396. <https://doi.org/10.1063/1.441359>.
- (34) Andersson, K. Different Forms of the Zeroth-Order Hamiltonian in Second-Order Perturbation Theory with a Complete Active Space Self-Consistent Field Reference Function. *Theoretica chimica acta* **1995**, *91* (1), 31–46. <https://doi.org/10.1007/BF01113860>.
- (35) Andersson, Kerstin.; Malmqvist, P. Aake.; Roos, B. O.; Sadlej, A. J.; Wolinski, Krzysztof. Second-Order Perturbation Theory with a CASSCF Reference Function. *J. Phys. Chem.* **1990**, *94* (14), 5483–5488. <https://doi.org/10.1021/j100377a012>.
- (36) Andersson, K.; Malmqvist, P.; Roos, B. O. Second-order Perturbation Theory with a Complete Active Space Self-consistent Field Reference Function. *The Journal of Chemical Physics* **1992**, *96* (2), 1218–1226. <https://doi.org/10.1063/1.462209>.
- (37) Finley, J.; Malmqvist, P.-Å.; Roos, B. O.; Serrano-Andrés, L. The Multi-State CASPT2 Method. *Chemical Physics Letters* **1998**, *288* (2), 299–306. [https://doi.org/10.1016/S0009-2614\(98\)00252-8](https://doi.org/10.1016/S0009-2614(98)00252-8).
- (38) Widmark, P.-O.; Malmqvist, P.-Å.; Roos, B. O. Density Matrix Averaged Atomic Natural Orbital (ANO) Basis Sets for Correlated Molecular Wave Functions. *Theoretica chimica acta* **1990**, *77* (5), 291–306. <https://doi.org/10.1007/BF01120130>.
- (39) Roos, B. O.; Lindh, R.; Malmqvist, P.-Å.; Veryazov, V.; Widmark, P.-O. New Relativistic ANO Basis Sets for Transition Metal Atoms. *J. Phys. Chem. A* **2005**, *109* (29), 6575–6579. <https://doi.org/10.1021/jp0581126>.
- (40) Douglas, M.; Kroll, N. M. Quantum Electrodynamical Corrections to the Fine Structure of Helium. *Annals of Physics* **1974**, *82* (1), 89–155. [https://doi.org/10.1016/0003-4916\(74\)90333-9](https://doi.org/10.1016/0003-4916(74)90333-9).
- (41) Hess, B. A. Relativistic Electronic-Structure Calculations Employing a Two-Component No-Pair Formalism with External-Field Projection Operators. *Phys. Rev. A* **1986**, *33* (6), 3742–3748. <https://doi.org/10.1103/PhysRevA.33.3742>.
- (42) Jansen, G.; Hess, B. A. Revision of the Douglas-Kroll Transformation. *Phys. Rev. A* **1989**, *39* (11), 6016–6017. <https://doi.org/10.1103/PhysRevA.39.6016>.
- (43) Sigel, H.; Martin, R. B. Coordinating Properties of the Amide Bond. Stability and Structure of Metal Ion Complexes of Peptides and Related Ligands. *Chem. Rev.* **1982**, *82* (4), 385–426. <https://doi.org/10.1021/cr00050a003>.
- (44) Bursch, M.; Mewes, J.-M.; Hansen, A.; Grimme, S. Best-Practice DFT Protocols for Basic Molecular Computational Chemistry\*\*. *Angewandte Chemie* **2022**, *134* (42), e202205735. <https://doi.org/10.1002/ange.202205735>.